

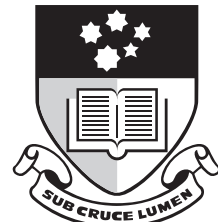
Ionospheric Scintillation Effects on Global Positioning System Receivers

By

Mark Frederick Knight

Thesis submitted for the degree of

Doctor of Philosophy



Department of Electrical and Electronic Engineering
Faculty of Engineering
The University of Adelaide
Adelaide, South Australia

December 2000

CONTENTS

ABSTRACT	VII
DECLARATION	IX
ACKNOWLEDGMENTS	XI
LIST OF FIGURES	XIII
LIST OF TABLES.....	XIX
ABBREVIATIONS	XXI
LIST OF SYMBOLS.....	XXIII
PUBLICATIONS.....	XXIX
1. INTRODUCTION	1
1.1. MOTIVATION	2
1.2. THESIS OUTLINE AND CONTRIBUTIONS	3
2. BACKGROUND	5
2.1. IONOSPHERIC SCINTILLATIONS	5
2.1.1. The ionosphere	5
2.1.2. Morphology of scintillations	7
2.1.3. Statistical characteristics of scintillations	10
2.1.4. Wide Band Scintillation Model	15
2.1.5. Phase screen model	16
2.1.5.1. Deterministic phase screen	17
2.1.5.2. Random phase screen	18

2.1.6. Summary	19
2.2. GLOBAL POSITIONING SYSTEM	20
2.2.1. Principles of GPS positioning.....	20
2.2.2. GPS receiver tracking loops.....	23
2.3. A REVIEW OF SCINTILLATION EFFECTS ON GPS	25
2.3.1. Carrier tracking loops.....	26
2.3.2. Code tracking loops	29
2.3.3. Codeless and Semi-Codeless receivers	30
2.3.4. Navigation data	30
2.3.5. Acquisition.....	31
2.3.6. Optimum tracking of the carrier phase.....	32
2.3.7. Scintillation effects on navigation.....	32
2.4. SUMMARY	33
3. CARRIER TRACKING LOOPS	35
3.1. CARRIER LOOP MODEL	36
3.2. THE IMPACT OF PHASE SCINTILLATIONS ON CARRIER PHASE TRACKING LOOPS	42
3.2.1. Phase tracking errors and thresholds.....	42
3.2.2. The effects of pre-detection filtering on phase errors	49
3.2.3. Carrier phase range errors	51
3.2.4. Doppler errors	54
3.2.5. Summary	55
3.3. THE IMPACT OF AMPLITUDE SCINTILLATIONS ON CARRIER PHASE TRACKING LOOPS	57
3.3.1. Background	58
3.3.2. Phase errors from the linear model	60
3.3.2.1. Amplitude scintillations only.....	60
3.3.2.2. Amplitude and phase scintillations.....	69
3.3.2.3. Amplitude scintillations and dynamics.....	72
3.3.2.4. Additional comments.....	73
3.3.3. Phase errors from the non-linear model	74
3.3.4. The effects of pre-detection filtering on phase errors	77
3.3.5. Summary	79
3.4. CARRIER LOOP TRACKING THRESHOLDS.....	81
3.4.1. Optimum loop bandwidths.....	85

3.4.2. WBMOD predictions of \mathbf{T} and S_4	87
3.4.3. Velocity and elevation angle effects	88
3.4.3.1. Elevation angle effects.....	88
3.4.3.2. Satellite and receiver velocity.....	91
3.4.4. Summary	94
3.5. THE IMPACT OF FADE DEPTH AND DURATION ON CYCLE SLIPS	96
3.5.1. 1 st Order loops.....	99
3.5.1.1. Constant velocity	105
3.5.2. 2 nd Order loops.....	106
3.5.2.1. Constant acceleration.....	108
3.5.3. Pre-detection filters	109
3.5.4. Summary	110
3.6. SCINTILLATION EFFECTS ON CARRIER PHASE DIFFERENTIAL GPS	111
3.7. CARRIER FREQUENCY TRACKING LOOPS	115
3.7.1. The impact of phase scintillations on frequency tracking loops.....	117
3.7.2. The impact of amplitude scintillations on frequency tracking loops	120
3.8. CONCLUSIONS	121
4. CODE TRACKING LOOPS.....	123
4.1. CODE LOOP MODEL	123
4.2. THE IMPACT OF PHASE SCINTILLATIONS ON CODE TRACKING LOOPS.....	130
4.3. THE IMPACT OF AMPLITUDE SCINTILLATIONS ON CODE TRACKING LOOPS.....	132
4.3.1. Slow amplitude fluctuations	138
4.4. FREQUENCY-SELECTIVE SCINTILLATION EFFECTS.....	143
4.5. CONCLUSIONS	152
5. CODELESS AND SEMI-CODELESS RECEIVERS.....	153
5.1. CODELESS PROCESSING TECHNIQUES	153
5.2. THEORETICAL ANALYSIS.....	155
5.3. THRESHOLD CURVES.....	158
5.4. SCINTILLATION MEASUREMENTS.....	160
5.4.1. Overview of scintillation data	160
5.4.1.1. Novatel Millennium™ data	160

5.4.2. A comparison of models with measurements	162
5.5. CONCLUSIONS.....	163
6. NAVIGATION DATA	165
6.1. BACKGROUND	165
6.2. THE IMPACT OF PHASE SCINTILLATIONS ON NAVIGATION DATA.....	168
6.3. THE IMPACT OF AMPLITUDE SCINTILLATIONS ON NAVIGATION DATA.....	170
6.4. THE COMBINED EFFECT OF SCINTILLATIONS ON NAVIGATION DATA.....	175
6.5. A NOTE ON WORD ERROR PROBABILITIES	177
6.6. CONCLUSIONS.....	179
7. ACQUISITION.....	181
7.1. ACQUISITION MODEL.....	181
7.2. DETECTION AND FALSE ALARM PROBABILITIES	182
7.2.1. Phase scintillation effects.....	187
7.2.2. Correlation sidelobes.....	190
7.3. ACQUISITION TIMES	193
7.3.1. Acquisition search strategy	193
7.3.2. Mean time to acquire.....	194
7.3.2.1. Amplitude correlation times	196
7.3.2.2. Short amplitude correlation times.....	197
7.3.2.3. Long amplitude correlation times	200
7.3.3. Independence.....	204
7.3.4. False alarms.....	206
7.4. CONCLUSIONS.....	207
8. OPTIMUM TRACKING OF THE CARRIER PHASE.....	209
8.1. WIENER FILTER APPROACH	209
8.1.1. Causal Wiener filters.....	210
8.1.2. Non-causal Wiener filters	217
8.1.3. Doppler errors	218
8.1.4. Optimum post-loop filters.....	222
8.2. DIRECT DETERMINATION OF THE MMSE	225

8.2.1. Doppler errors	227
8.3. CONCLUSIONS	229
9. SCINTILLATION EFFECTS ON NAVIGATION	231
9.1. PREDICTING THE PERFORMANCE OF A SINGLE LINK	231
9.2. PREDICTING THE PERFORMANCE OF MULTIPLE LINKS	233
9.3. PREDICTING NAVIGATIONAL ACCURACY	234
9.4. PREDICTIONS BASED ON WBMOD	238
9.5. CONCLUSIONS	245
10. SUMMARY	247
10.1. OVERVIEW.....	247
10.2. CONCLUSIONS	249
10.3. FURTHER RESEARCH.....	252
APPENDIX A: SCINTILLATION MODEL.....	255
APPENDIX B: GPS TRACKING LOOP SIMULATORS	265
APPENDIX C: TRACKING THRESHOLDS AND CYCLE SLIPS.....	269
APPENDIX D: THERMAL NOISE ERRORS.....	275
APPENDIX E: DOPPLER ERRORS	285
APPENDIX F: IONOSPHERIC PIERCE POINT VELOCITY	289
APPENDIX G: WBMOD PREDICTIONS OF F_C	295
BIBLIOGRAPHY	297

Abstract

The Global Positioning System (GPS) is used extensively in both the military and civilian communities for such diverse activities as navigation, surveying, remote sensing, asset management and precise timing. The tremendous popularity of GPS has stemmed from the low cost and small size of modern GPS receivers, and from the high accuracy and reliability of the system. This second factor has also resulted in GPS being considered as a sole means of navigation for critical safety of life applications such as precision approach and landing for aircraft and narrow channel navigation for ships.

A number of environmental factors are known to affect the performance of GPS, including electromagnetic interference, multipath, foliage attenuation, atmospheric delays and ionospheric scintillations. In this thesis, the effects of ionospheric scintillations on GPS will be examined.

Ionospheric scintillations are rapid variations in the amplitude and phase of transitionospheric radio signal resulting from density irregularities in the ionosphere. Scintillations have the capacity to affect both the accuracy and reliability of GPS systems by compromising the performance of the code and carrier tracking loops of a receiver. In order to quantify this effect, a widely used stochastic model of scintillation activity is combined with various tracking and acquisition models to produce a collection of receiver performance measures. These include the magnitude of the code and carrier range measurement errors, a measure of the tracking state of the carrier loop, the mean time to acquire, and the bit error probability for the navigation data. An advantage of the stochastic model chosen in this study is that it is linked to an existing predictive scintillation model which is based on large amounts of scintillation data collected over the previous 20 years or so. Consequently, by combining these models it is possible to predict the performance of a given receiver type at any future time and location.

Declaration

This work contains no material which has been accepted for the award of any other degree or diploma in any university or other tertiary institution and, to the best of my knowledge and belief, contains no material previously published or written by another person, except where due reference has been made in the text.

I give consent to this copy of my thesis, when deposited in the University of Adelaide library, being available for loan and photocopying.

Signature _____

Date _____

Acknowledgments

I wish to thank the following people for their assistance and support during my candidature.

My academic supervisor Professor Doug Gray of the Electrical and Electronic Engineering Department, the University of Adelaide, for his technical guidance, encouragement and support over the years.

My supervisor, Dr Anthony Finn of Surveillance Systems Division (SSD), Defence Science and Technology Organisation (DSTO) for providing me with an opportunity to pursue my research objectives as part of my work commitments to DSTO.

The senior management of Surveillance systems Division for providing a framework in which I could undertake further studies.

The Cooperative Research Centre for Sensor Signal and Information Processing (CSSIP) for the use of their facilities and for the knowledge gained through the various seminars and courses they have held.

My wife Lorraine for her patience and support over the last few years.

List of Figures

Figure 2.1-1: Typical daytime electron density profile for the mid-latitudes	6
Figure 2.1-2: Illustration of the equatorial Fountain Effect	7
Figure 2.1-3: Scintillation regions of the world	8
Figure 2.1-4: Example of the scintillation indices produced by WBMOD	16
Figure 2.1-5: Modelled diffraction patterns based on a thin screen diffraction model and an isolated Gaussian shaped irregularity	17
Figure 2.1-6: Scintillation statistics for a random, Gaussian distributed density layer	19
Figure 2.2-1: Architecture of a generic GPS receiver	23
Figure 2.2-2: Signal processing model of a generic code or carrier tracking loop	24
Figure 3.1-1: Model of a generic Costas phase locked loop	36
Figure 3.1-2: Non-linear baseband model of an I.Q Costas phase locked loop	39
Figure 3.1-3: Linear baseband model of an I.Q Costas phase locked loop	39
Figure 3.1-4: Closed loop transfer function model of a Costas phase locked loop	40
Figure 3.2-1: Threshold spectral strength as a function of the spectral index and the loop noise bandwidth for second and third order loops	45
Figure 3.2-2: Threshold spectral strength as a function of the loop noise bandwidth for second and third order loops	46
Figure 3.2-3: RMS phase scintillation errors as a function of spectral strength for a second order Costas phase locked loop	47
Figure 3.2-4: Mean time between cycle slips for a second order Costas phase locked loop in the presence of phase scintillations	48
Figure 3.2-5: The effects of pre-detection filtering on the RMS phase scintillation error for a second order Costas phase locked loop	51
Figure 3.2-6: Variance of the carrier phase range error as a function of the loop noise bandwidth for a second order Costas loop in the presence of phase scintillations	53
Figure 3.2-7: Variance of the Doppler error as a function of the loop noise bandwidth for a second order Costas loop in the presence of phase scintillations	55
Figure 3.3-1: Phase error variance as a function of S_4 for a first order I.Q Costas loop with an ideal AGC	64

Figure 3.3-2: Phase error variance as a function of S_4 from simulations for a first order I.Q Costas loop with an ideal AGC	64
Figure 3.3-3: Phase error variance as a function of S_4 for a first order I.Q Costas loop with a fast AGC	67
Figure 3.3-4: Phase error variance as a function of S_4 for a first order I.Q Costas loop with a slow AGC	68
Figure 3.3-5: $\sigma_{\phi_{ep}}^2(\tilde{A})$ for a first order I.Q Costas loop with both a fast and a slow AGC ..	70
Figure 3.3-6: $\sigma_{\hat{\phi}_p}^2$ as a function of S_4 for a first order I.Q Costas loop with both a fast and a slow AGC	72
Figure 3.3-7: Non-linear model of a first order Costas loop with phase scintillations translated back through the VCO and loop filter to the discriminator output.....	75
Figure 3.3-8: σ_{ϑ}^2 and $\sigma_{\phi_T}^2$ as a function of S_4 for a first order I.Q Costas loop with a fast AGC	77
Figure 3.3-9: The impact of pre-detection filtering on the power spectral density of amplitude scintillations	78
Figure 3.3-10: Scatter plot of the fade depth after pre-detection filtering versus the fade depth before filtering from simulated scintillation data	79
Figure 3.4-1: Normalised threshold amplitude as a function of the phase scintillation spectral strength for both an ideal and a fast AGC	83
Figure 3.4-2: The probability of losing lock for a 2 nd order Costas phase locked loop as a function of S_4 and the loop bandwidth	84
Figure 3.4-3: Tracking threshold as a function of T, S_4 , and loop bandwidth	85
Figure 3.4-4: Threshold loop noise bandwidth as a function of the phase scintillation spectral strength	86
Figure 3.4-5: T and S_4 values obtained from WBMOD for high solar activity	88
Figure 3.4-6: Mean and RMS of the geometry factors for T and S_{4w} obtained from WBMOD for a period of high solar activity.....	89
Figure 3.4-7: Effective scan velocity as a function of elevation angle	90
Figure 3.4-8: Ionospheric pierce point velocity due to satellite motion	92
Figure 3.4-9: Ionospheric pierce point speed as a function of elevation angle	93
Figure 3.5-1: Model of a phase locked loop for zero signal amplitude	97
Figure 3.5-2: Probability of a cycle slip as a function of the fade depth and duration for a first order Costas loop based on theory with $B_n = 15\text{Hz}$	102

Figure 3.5-3: Probability of a cycle slip as a function of the fade depth and duration for a first order Costas loop based on theory with $B_n = 5\text{Hz}$	102
Figure 3.5-4: Probability of a cycle slip as a function of the fade depth and duration for a first order Costas loop based on simulations with $B_n = 15\text{Hz}$	103
Figure 3.5-5: Probability of a cycle slip as a function of the fade depth and duration for a first order Costas loop based on simulations with $B_n = 5\text{Hz}$	103
Figure 3.5-6: Probability of a cycle slip as a function of the fade depth and duration for a first order Costas loop based on sims (Atan2(Q,I) and I.Q discriminators)	104
Figure 3.5-7: Loop filter for a second order phase locked loop	107
Figure 3.5-8: Probability of a cycle slip as a function of the fade depth and duration for a second order Atan(Q/I) Costas loop based on simulations	108
Figure 3.5-9: Signal amplitude after pre-detection filtering for a range of infinitely deep fades with varying durations	110
Figure 3.6-1: $\sigma_{\Delta\phi}$ as a function of f_o and the baseline length in the presence of phase scintillations	113
Figure 3.6-2: RMS phase error as a function of S_4 and the loop bandwidth	114
Figure 3.7-1: Representation of a generic frequency locked loop	115
Figure 3.7-2: Linear equivalent model of a frequency locked loop	116
Figure 3.7-3: Difference between the threshold spectral strength of a frequency locked loop and the threshold spectral strength of a Costas phase locked loop	119
Figure 4.1-1: Representation of a generic delay locked loop	124
Figure 4.1-2: Delay error function of an Early-Late power discriminator	125
Figure 4.1-3: Linear model of a delay locked loop with an Early-Late power discrim	128
Figure 4.3-1: Delay error variance as a function of S_4	140
Figure 4.4-1: Scintillation waveforms at the L1 frequency and 10 MHz above L1 under frequency-selective scintillation conditions	146
Figure 4.4-2: The impact of a single phase-changing screen with a power law in-situ density profile on 0.0978 μs pulses that are bandlimited to $\pm 10.23 \text{ MHz}$	147
Figure 4.4-3: Figure 4.4-2 normalised by the peak pulse height	147
Figure 4.4-4: The impact of a single phase-changing screen with a power law in-situ density profile on 0.978 μs pulses that are bandlimited to $\pm 1.023 \text{ MHz}$	148
Figure 4.4-5: Early-Late gate error function for bandlimited 0.0978 μs pulses	149
Figure 4.4-6: Figure 4.4-5 normalised by the peak discriminator error	149
Figure 4.4-7: Early-Late gate error function normalised by the peak discriminator error for 0.978 μs pulses	150

Figure 4.4-8: Delay errors and the amplitude scintillation waveform as a function of ground position for bandlimited 0.0978 μ s pulses	151
Figure 4.4-9: Delay errors and the amplitude scintillation waveform as a function of ground position for bandlimited 0.978 μ s pulses	151
Figure 5.2-1: The effect of a reduced amplitude threshold on the fade duration	158
Figure 5.3-1: Tracking thresholds for both codeless and semi-codeless receivers as a function of T and S_4	159
Figure 5.4-1: The percentage of time from 8:00pm to 10:00pm (local time) that the Novatel Millennium™ loses lock on one or more satellites at Parepare, Indonesia	161
Figure 5.4-2: The percentage of time that the L2 code and carrier loops lose lock as a function of S_4	163
Figure 6.2-1: of a bit error and a word error as a function of the phase error variance, $\sigma_{\phi_{ep}}^2$, for a first order loop	170
Figure 6.3-1: Probability of bit and word errors as a function of S_4 for $B_n = 2\text{Hz}$	174
Figure 6.3-2: Probability of bit and word errors as a function of S_4 for $B_n = 15\text{Hz}$	174
Figure 6.4-1: Probability of bit and word errors as a function of S_4 and $\sigma_{\phi_{ep}}^2$	176
Figure 6.5-1: Probability of a word error as a function of S_4 under the assumption that the amplitude is independent between successive epochs	178
Figure 7.1-1: A square-law acquisition detector for a GPS receiver	182
Figure 7.2-1: \bar{P}_d as a function of S_4 for five values of C/N_o	186
Figure 7.2-2: Equivalent C/N_o as a function of S_4 for five values of C/N_o	187
Figure 7.2-3: Threshold T as a function of f_o for a threshold variance of 1 rad ²	189
Figure 7.2-4: \bar{P}_{fa} for a peak sidelobe level of -22dB as a function of S_4	190
Figure 7.2-5: CDF and PDF of the sidelobe levels for the GPS Gold codes and the corresponding \bar{P}_{fa}	191
Figure 7.3-1: Mean acquisition time ratio as a function of S_4	198
Figure 7.3-2: RMS acquisition time ratio as a function of S_4	199
Figure 8.1-1: Wiener filter model of a phase locked loop	210
Figure 8.1-2: Phase error variance as a function of the spectral index for both causal and non-causal Wiener filters	218
Figure 8.1-3: Post-loop filtering schemes for loop phase estimates.....	223
Figure 8.2-1: Relationship between the two components of the mean square tracking error as a function of the loop noise bandwidth	226

Figure 8.2-2: Threshold values of T above which phase scintillation energy dominates over dynamics in the choice of an optimum loop bandwidth	228
Figure 9.3-1: Probability of a navigation or RAIM outage as a function of both the single link probability of losing lock and the number of visible satellites	236
Figure 9.4-1: Percentage of links that may be stressed to the point of losing lock from WBMOD. 23 Sept. 2000, 12:00 noon UTC, 90 th percentile, SSN=135, $K_p = 4 \cdot 3$, 10° mask angle, $C/N_o = 41.5$ dBHz, $B_n = 15$ Hz, Loop order = 3, Coded L1 loop	239
Figure 9.4-2: Percentage of links that may be stressed to the point of losing lock from WBMOD. 23 Sept. 2000, 12:00 noon UTC, 90 th percentile, SSN=135, $K_p = 4 \cdot 3$, 10° mask angle, $C/N_o = 44$ dBHz, $B_n = 15$ Hz, Loop order = 3, Coded L1 loop	240
Figure 9.4-3: Percentage of links that may be stressed to the point of losing lock from WBMOD. 23 Sept. 2000, 12:00 noon UTC, 90 th percentile, SSN=135, $K_p = 4 \cdot 3$, 10° mask angle, $C/N_o = 41.5$ dBHz, $B_n = 2$ Hz, Loop order = 3, Coded L1 loop	241
Figure 9.4-4: Percentage of links that may be stressed to the point of losing lock from WBMOD. 23 Sept. 2000, 12:00 noon UTC, 90 th percentile, SSN=135, $K_p = 4 \cdot 3$, 10° mask angle, $C/N_o = 44$ dBHz, $B_n = 2$ Hz, Loop order = 3, Coded L1 loop	241
Figure 9.4-5: Percentage of links that may be stressed to the point of losing lock from WBMOD. 23 Sept. 2000, 12:00 noon UTC, 90 th percentile, SSN=135, $K_p = 4 \cdot 3$, 0° mask angle, $C/N_o = 41.5$ dBHz, $B_n = 15$ Hz, Loop order = 3, Coded L1 loop	242
Figure 9.4-6: Percentage of links that may be stressed to the point of losing lock from WBMOD. 23 Oct. 2000, 12:00 noon UTC, 90 th percentile, SSN=135, $K_p = 4 \cdot 3$, 10° mask angle, $C/N_o = 41.5$ dBHz, $B_n = 15$ Hz, Loop order = 3, Coded L1 loop	243
Figure 9.4-7: Percentage of links that may be stressed to the point of losing lock from WBMOD. 23 Sept. 2000, 12:00 noon UTC, 90 th percentile, SSN=100, $K_p = 4 \cdot 3$, 10° mask angle, $C/N_o = 41.5$ dBHz, $B_n = 15$ Hz, Loop order = 3, Coded L1 loop	243
Figure 9.4-8: Percentage of links that may be stressed to the point of losing lock from WBMOD. 23 Sept. 2000, 12:00 noon UTC, 90 th percentile, SSN=135, $K_p = 4 \cdot 3$, 10° mask angle, $C/N_o = 41.5$ dBHz, $B_n = 0.2$ Hz, Loop order = 3, Semi-codeless L2 loop	244
Figure 9.4-9: Percentage of links that may be stressed to the point of losing lock from WBMOD. 23 Sept. 2000, 12:00 noon UTC, 65 th percentile, SSN=135, $K_p = 4 \cdot 3$, 10° mask angle, $C/N_o = 41.5$ dBHz, $B_n = 0.2$ Hz, Loop order = 3, Semi-codeless L2 loop	244
Figure A-1: Geometry of the thin phase screen diffraction model	258

Figure A-2: Sample realisation of in-situ phase, phase scintillations, and amplitude scintillations obtained from the Fresnel-Kirchoff diffraction model	262
Figure B-1: Simulink™ model of a Costas phase locked loop	266
Figure B-2: Simulink™ model of a delay locked loop	266
Figure B-3: Simulink model of a combined Costas phase locked loop / Delay locked loop channel	267
Figure C.1: 1σ phase error from all sources other than dynamics versus the steady state dynamic phase error at the tracking threshold of an I.Q Costas loop	271
Figure G-1: f_c as a function of elevation angle from WBMOD	296

List of Tables

Table 3.1-1: Costas loop discriminator functions	37
Table 3.1-2: Transfer functions and noise bandwidths of a phase locked loop	41
Table 3.7-1: Frequency locked loop discriminator functions	116
Table 4.1-1: Delay locked loop discriminator functions	124
Table 4.2-1: Conversion factors for code and carrier errors	131
Table E.1: Steady state tracking errors in the presence of dynamics	286

Abbreviations

ADO	Australian Defence Organisation
AGC	automatic gain control
AS	Anti-spoofing
BPSK	binary phase shift keying
C/A-Code	coarse/acquisition code
CDF	cumulative probability distribution function
CPDGPS	carrier phase differential GPS
CW	continuous wave
dB	decibel
DGPS	differential GPS
dip	dipole (Earth's magnetic axis)
DLL	delay locked loop
DoD	Department of Defense
DOP	dilution of precision
DSSS	direct sequence spread spectrum
ECEF	Earth centred Earth fixed
FLL	frequency locked loop
GDOP	geometric dilution of precision
GPS	Global Positioning System
HDOP	horizontal dilution of precision
I	inphase signal
IF	intermediate frequency
IID	independent and identically distributed
INS	inertial navigation system
IPP	ionospheric pierce point
J/S	jammer to signal ratio
L1 and L2	GPS L-band carrier frequencies
NCO	numerically controlled oscillator
P-Code	precision code
P(Y)-Code	The encrypted precision code (the Y-Code)

PDF	probability density function
PDI	pre-detection integration
PDOP	position dilution of precision
PLL	phase locked loop
PPS	Precise Positioning Service
PRN	pseudorandom noise
PSD	power spectral density
PVT	position, velocity and time
Q	quadrature signal
RF	radio frequency
RMS	root mean square
SA	Selective Availability
SNR	signal to noise ratio
SPS	Standard Positioning Service
TEC	total electron content
UERE	user equivalent range error
UTC	coordinated universal time
VCO	voltage controlled oscillator
WADGPS	Wide Area Differential GPS
WBMOD	Wide Band Scintillation Model
WGS-84	World Geodetic System 1984

List of Symbols

A	Signal amplitude
\tilde{A}	Signal amplitude after the Pre-Detection Integrate & dump (PDI) filters
\mathbf{A}	Quiescent (unperturbed) signal amplitude
\tilde{A}_N	Filtered amplitude normalised by the quiescent amplitude, \mathbf{A}
\tilde{A}_{Th}	Amplitude threshold for carrier lock
B_n	Loop noise bandwidth
\bar{B}_n	Design loop noise bandwidth
$B_n _o$	Optimum loop noise bandwidth
B_I	Bandwidth of the PDI filters
$C_k L$	Height integrated irregularity strength
C/N_o	Carrier to noise power density ratio
$C/N_o _{Eq}$	Equivalent C/N_o for codeless and semi-codeless receivers
d	Navigation data
$\text{Erfc}(x)$	Complementary error function
$F(s)$	Open loop transfer function
$F_o(s)$	Optimum open loop transfer function
f_{IF}, ω_{IF}	IF carrier frequency in Hz and radians/s respectively
f_n, ω_n	Loop natural frequency in Hz and radians/s respectively
$f_n _o, \omega_n _o$	Optimum loop natural frequency in Hz and radians/s respectively
f_o	Frequency corresponding to the ionospheric outer scale size
f_c	Fresnel cutoff frequency of the amplitude scintillation power spectrum
$f_A(A)$	Probability Density Function (PDF) of the amplitude, A
$f_{\tilde{A}}(\tilde{A})$	PDF of the amplitude after PDI filtering, \tilde{A}
$f_{\tilde{A}_N}(\tilde{A}_N)$	PDF of the normalised amplitude, \tilde{A}_N
$f_I(I)$	PDF of the signal intensity, I
$f_{\phi_p}(\phi_p)$	PDF of carrier phase scintillations, ϕ_p

$f_\vartheta(\varphi)$	PDF of the modulo π reduced phase tracking error, ϑ
$G(s)$	Transfer function of the PDI filters
g	AGC gain factor
g_N	Normalised AGC gain factor
$H(s)$	Closed loop transfer function
$H_o(s)$	Optimum closed loop transfer function
h_i	Height of the Ionospheric Pierce Point (IPP)
I	Signal intensity
I_N	Normalised signal intensity
I_E, I_P, I_L	Early, prompt and late I channel signals following the PDI filters
$I_n(x)$	Modified Bessel function of the first kind of order n
$K_X(\tau)$	Autocovarianec function of X
L	Loop order
l_o	Ionospheric outer scale size
m	Parameter of the Nakagami-m distribution
$N(\mu, \sigma)$	The Gaussian PDF with mean μ and variance σ^2
N_o	Power Spectral Density (PSD) of the thermal noise on the IF
N_C	Number of cells in the uncertainty region for acquisition
n	IF thermal noise term
n_d	Discriminator noise term
n_{dN}	Discriminator noise term normalised by the AGC
n_{IE}, n_{IP}, n_{IL}	Early, prompt and late I channel noise following the PDI filters
n_{QE}, n_{QP}, n_{QL}	Early, prompt and late Q channel noise following the PDI filters
P_d	Probability of detection for acquisition
\bar{P}_d	Average probability of detection
P_{fa}	Probability of false alarm for acquisition
\bar{P}_{fa}	Average probability of false alarm
P_e	Probability of a navigation data bit error
P_w	Probability of a navigation data word error
P_L	Probability of losing carrier lock
\bar{P}_L	Average probability of losing carrier lock
P_{CS}	Probability of a cycle slip

p	Spectral index (slope) of the phase scintillation power spectrum
p_E, p_P, p_L	Early, Prompt and Late PRN codes
Q_E, Q_P, Q_L	Early, prompt and late Q channel signals following the PDI filters
$Q(x)$	Gaussian probability integral
$R_X(\tau)$	Autocorrelation function of X
R_E, R_P, R_L	Early, prompt and late code autocorrelation functions
$\text{rect}(x)$	Rectangle function
S_4	Normalised (by the mean) standard deviation of the signal intensity
S_{4w}	S_4 predictions obtained from the weak scintillation model
$S_\phi(s)$	PSD of the carrier phase
$S_{\phi_d}(s)$	PSD of the dynamics component of the carrier phase
$S_{\phi_p}(s)$	PSD of the phase scintillation component of the carrier phase
$S_{n_d}(s)$	PSD of the discriminator noise term
$S_\tau(s)$	PSD of the code delay process
$\text{sinc}(x)$	Sinc function (ie. $\sin(\pi x)/\pi x$)
T	Period of the pre-detection integrate-and-dump filters
\mathbf{T}	Spectral strength of phase scintillations at a frequency of 1 Hz.
\bar{T}	Mean time to cycle slip
\bar{T}_{ACQ}	Mean time to acquire
T_c	PRN code chip width
$T_{CT}(x)$	Correlation time of x
T_d	Dwell time for acquisition
T_r	Time to re-visit a cell during acquisition
T_v	Verification time for acquisition
v_e	Effective scan velocity of the propagation path through the ionosphere
v_I	IPP velocity
v_d	Irregularity drift velocity
v_r	Component of the IPP velocity due to receiver motion
v_s	Component of the IPP velocity due to satellite motion
z_F	Radius of the first Fresnel zone
$\Gamma(x)$	Gamma function
$\Gamma(x, y)$	Incomplete Gamma function

γ	Slope of the delay error function (Section 4 only)
$\delta(t)$	Dirac Delta function
$\bar{\varepsilon}_T^2$	Total transient distortion produced by dynamics
η	Detection threshold for acquisition
ν	Carrier frequency (Hz)
ζ	Damping factor for a second order loop
ρ_e	The effective loop SNR
σ_{ACQ}	Standard Deviation (STD) of the acquisition time
σ_n	STD of the thermal noise on either the I or Q channels
σ_{n_d}	STD of the discriminator noise term
σ_{n_dN}	STD of the normalised discriminator noise term
σ_ϕ	STD of the carrier phase
σ_{ϕ_p}	STD of the carrier phase due to phase scintillations
σ_{ϕ_e}	STD of the carrier phase tracking error
σ_ϑ	STD of the modulo π reduced phase tracking error
$\sigma_{\phi_{ep}}$	STD of the carrier phase tracking error due to phase scintillations
σ_{ϕ_T}	STD of the carrier phase error due to thermal noise
σ_{τ_T}	STD of the delay error due to thermal noise
$\sigma_{\hat{\phi}_p}$	STD of the carrier phase range error due phase scintillations
$\sigma_{\omega_{ep}}$	STD of the Doppler error due phase scintillations
$\sigma_{\phi_e}^2 \Big _{Th}$	Linear model tracking error threshold
$\sigma_{\phi_T}^2 \Big _{Th}$	Component of the tracking error threshold associated with thermal noise
$\sigma_{\phi_e}^2 \Big _o$	Minimum phase error variance obtained by an optimisation process
τ	Fade duration (Section 3) or code delay (Section 4)
τ_d	Component of the code delay due to dynamics
τ_p	Component of the code delay due to phase scintillations
τ_o	Component of the code delay due to other sources
τ_ϵ	Code loop delay tracking error
$\hat{\tau}$	Code loop delay estimate
ϕ	Carrier phase process

ϕ_d	Component of the carrier phase process due to dynamics
ϕ_p	Component of the carrier phase process due to phase scintillations
ϕ_o	Component of the carrier phase process due to other phase noise
$\hat{\phi}$	Carrier loop phase estimate
ϕ_e	Carrier loop phase tracking error
ϕ_{er}	Carrier phase range error
$\hat{\phi}_p$	Contribution to the carrier phase range error from phase scintillations
ϕ_{ess}	Steady State carrier loop phase tracking error
$\phi_e _T$	The maximum phase error for linear operation of the discriminator
ϑ	Carrier phase error reduced modulo π
Θ	Position step (radians)
Ω	Velocity step (radians/s)
Λ	Acceleration step (radians/s ²)
χ^2_n	Chi-squared distribution with n degrees of freedom
ω_{ep}	Contribution to the Doppler error due to phase scintillations
Δ	Single difference operator for carrier phase DGPS
$\nabla\Delta$	Double difference operator for carrier phase DGPS
\otimes	Convolution operator
$[X(s)]_{pos}$	Laplace transform of $x(t)$ such that $x(t) = 0$ for $t < 0$
$[X(s)]^+$	Factorisation of $X(s)$ such that all poles & zeros are in the left half s plane
$[X(s)]^-$	Factorisation of $X(s)$ such that all poles & zeros are in the right half s plane

Publications

- Knight, M. F., Gray, D. A., "*Maximum Likelihood Estimation of Ionospheric Total Electron Content Using GPS*", ISSPA 96 - Fourth International Symposium on Signal Processing and its Applications, Gold Coast, Australia, 1996.
- Knight, M. F., Finn, A., "*The Impact of Ionospheric Scintillations on GPS Performance*", Proceedings of ION GPS-96, The Ninth International Technical Meeting of the Satellite Division of the Institute of Navigation, Kansas City, Missouri, 1996.
- Knight, M. F., Finn, A., "*The Effects of Ionospheric Scintillations on GPS*", Proceedings of ION GPS-98, The Eleventh International Technical Meeting of the Satellite Division of the Institute of Navigation, Nashville, Tennessee, 1998.
- Knight, M. F., Cervera, M., Finn, A., "*A Comparison of Predicted and Measured GPS Performance in an Ionospheric Scintillation Environment*", Proceedings of ION GPS-99, The Twelfth International Technical Meeting of the Satellite Division of the Institute of Navigation, Nashville, Tennessee, 1999.
- Knight, M. F., Cervera, M. A., Finn, A., "*A Comparison of Measured GPS Performance with Model Based Predictions in an Equatorial Scintillation Environment*", Proceedings of the IAIN World Congress, San Diego, California, 2000.
- Knight, M. F., Finn, A., Cervera, M. A., Thomas, R., "*The Performance of GPS in the Presence of Ionospheric Scintillations*", Proceedings of the 4th International Symposium on Satellite Navigation Technology & Applications, Brisbane, Australia, 1999.
- Cervera, M. A., Knight, M. F., "*Time Series Modelling of Intensity and Phase Scintillation at GPS Frequencies*", Proceedings of the International Beacon Satellite Symposium 97, Sopron, Hungary, 1997.
- Knight, M. F., Finn, A., Cervera, M. A., "*Ionospheric Effects on Global Positioning System Receivers*", DSTO Research Report, DSTO-RR-0121, 1998.
- Knight, M. F., Finn, A., "*The Performance of Global Positioning System Receivers in a Combined Navigation Warfare / Ionospheric Scintillation Environment*", DSTO Research Report, DSTO-RR-0151, 1999.
- Knight, M. F., Finn, A., "*Information Document on the Combined Impact of MSS Interference and Ionospheric Scintillations on GPS Receiver Performance*", International Telecommunications Union, Radiocommunication Study Groups, Doc. AUS/6, 1999.

Chapter 1

Introduction

The NAVSTAR Global Positioning System (GPS) is a satellite based radio navigation system that provides accurate three dimensional position, velocity and time information globally and continuously under all weather conditions. The GPS system can be conveniently divided into three segments; (i) the Space Segment which consists of the GPS satellites, (ii) the Control Segment which comprises a network of monitor stations and ground antennas, and (iii) the User Segment which consists of the GPS receivers and associated systems. Because of the high accuracy, low cost and portability of GPS receivers, applications for GPS are appearing in many different areas including air, land and sea navigation, surveying, geodesy, and military applications to name a few.

The accuracy and reliability of GPS is a function of both system and environmental factors. System factors are associated with the three GPS segments described above and include errors in the satellite clock and ephemeris information, hardware channel biases, satellite geometry effects and thermal noise errors. Environmental factors are associated with propagation phenomena and include electromagnetic interference from external sources, ionospheric effects (including those associated with both the quiescent and the disturbed ionosphere), tropospheric delays, obscuration and multipath. Depending on the circumstances, the most significant environmental factor can be the disturbed ionosphere. For GPS, the principal manifestation of a disturbed ionosphere is ionospheric scintillations.

Ionospheric scintillations are rapid variations in the amplitude and phase of transitionospheric radio signals resulting from density irregularities in the ionosphere. Scintillations show strong diurnal, seasonal, geographic and solar cycle dependence being at their most severe during the evening hours, in the months of the equinox, at equatorial latitudes and during the years of solar maximum. As we are currently at solar maximum

(year 2000), it is expected that both the frequency and severity of scintillation activity will remain at a high level over the coming year or so.

Scintillations affect GPS receivers at the tracking loop level and so have the potential to disrupt all GPS systems, including both single and dual frequency receivers and both stand-alone and differential systems. The errors introduced into the code and carrier tracking loops of a GPS receiver result in an increase in range measurement errors and under extreme conditions can lead to a complete loss of signal lock. Other effects include an increase in the probability of errors within the GPS navigation data and an increase in the time taken to acquire the GPS signal when a receiver is first turned on. However, as scintillations are unlikely to affect all of the satellites in a receiver's field of view simultaneously, their impact on navigational accuracy will be through a degradation in the geometry of the available constellation. Consequently, the coverage of both the satellites and the irregularities, as well as the intensity of scintillation activity will all contribute to the accuracy of the final position solution.

1.1. Motivation

GPS will become the primary navigation system for the Australian Defence Organisation (ADO) and will be installed on all air, sea and land based platforms, as well as forming an integral part of the guidance mechanisms of many weapons. The positional accuracy of GPS affords the possibility of enhancing many ADO operations, including navigation, precision approach and landing, logistic support, the management of assets, mine warfare, and the targeting and guidance of weapons. In addition, GPS allows combined operations between air, sea and land based forces to be executed with flexibility and precision through the use of a common reference grid and precise position, velocity and time information. The cost effectiveness, accuracy, reliability and convenience of GPS will ensure that it becomes an essential part of most military systems, replacing existing, more costly navigation systems. GPS has also found an enormous market in the civilian community in such diverse areas as aircraft and marine navigation, surveying, remote sensing, geodesy, geographic information systems (GIS), and precise timing.

The Surveillance Systems Division (SSD) of the Defence Science & Technology Organisation (DSTO) has been tasked with the job of assessing the impact of environmental factors on the performance of GPS systems. These factors include electromagnetic interference, multipath, foliage attenuation, atmospheric delays and

ionospheric scintillations. The areas that may be affected by equatorial scintillations cover nearly 50% of the earth's surface and include regions such as Northern Australia and South East Asia which are of considerable operational interest to the ADO. For this reason, SSD has an interest in quantifying the effects of scintillations on GPS performance and of developing tools to predict the occurrence of significant scintillation events. The results obtained from this study will also be of interest to civilian users, particularly those attempting to achieve high levels of accuracy in equatorial regions. This is especially true now that the United States Department of Defense has disabled Selective Availability¹ which, until recently, has been the largest source of error for civilian GPS users.

1.2. Thesis outline and contributions

The principal contribution of this research is to use a widely accepted stochastic model of scintillation activity to investigate the effects of scintillations on GPS receivers and systems. This model has the advantage of being closely linked to the Wide Band Scintillation Model (WBMOD²) which allows various statistical scintillation parameters to be predicted for a given time, location and satellite-receiver geometry. The individual contributions of this research can be summarised as follows:

Chapter 3

Expressions are derived for the variance of the *carrier phase tracking error* for a Costas carrier tracking loop as a function of various amplitude and phase scintillation parameters. These expressions are then used to determine the strength of scintillation activity that will cause a carrier loop to lose lock. The sensitivity of the scintillation parameters to geometrical factors such as the satellite elevation angle and satellite and receiver motion are also discussed.

Expressions are also derived for the variance of the *carrier phase range errors* for a Costas carrier tracking loop as a function of the scintillation parameters. These expressions are then used to determine the errors that would be experienced by a carrier phase differential GPS system over different baseline lengths.

¹ Selective Availability or SA is an error introduced by the US Department of Defense to intentionally degrade the accuracy of the civil GPS service.

² The Wide Band Scintillation Model or WBMOD combines empirically derived models of the global distribution and behaviour of ionospheric irregularities with a propagation model to predict the characteristics of scintillations on a user specified transionospheric link.

Chapter 4

Expressions are derived for the variance of the *code phase tracking errors* and the variance of the *code phase range errors (pseudorange errors)* for a code tracking loop as a function of scintillation parameters.

Chapter 5

Expressions are derived for the effects of scintillations on codeless and semi-codeless tracking loops. The predicted performance of a semi-codeless loop is then compared with the measured performance obtained from a receiver located in the equatorial region during a period of moderately high scintillation activity.

Chapter 6

Expressions are derived for the probability of a data bit error in the GPS navigation message as a result of scintillations. The likely effects of these errors on the performance of a receiver are also discussed.

Chapter 7

The effects of scintillations on acquisition are investigated for a square-law acquisition detector, and expressions are derived for the mean time to acquire the GPS signal under amplitude scintillation conditions.

Chapter 8

Optimum filters are derived for carrier phase tracking loops that minimise phase tracking errors in the presence of scintillations. The effects of dynamics on the structure of these optimum filters is also discussed.

Chapter 9

The problem of translating predictions of the impact of scintillations on individual satellite-receiver links to predictions of navigational accuracy are discussed. The utility of WBMOD for predicting the effects of scintillations on GPS and its limitations are also discussed and some examples are given.

Appendix A

A technique is described for generating simulated amplitude and phase scintillation data using a model based on a single, thin diffracting screen containing randomly distributed ionospheric irregularities. The simulated scintillation data obtained from this model is used throughout the thesis to validate the theoretical results.

Chapter 2

Background

This chapter is divided into three main sections. In Section 2.1, the morphology of ionospheric scintillations is discussed and various scintillation models are introduced. In Section 2.2, a brief overview of the GPS system is given and a model of GPS receiver code and carrier tracking loops is provided. Finally, in Section 2.3 relevant literature is reviewed and the problems to be addressed in this thesis are identified.

2.1. Ionospheric scintillations

Ionospheric scintillations are rapid variations in the amplitude and phase of transionospheric radio signals resulting from electron density irregularities in the ionosphere. Scintillations are therefore intimately linked to the underlying physical processes in the ionosphere that give rise to irregularities. In this section, these processes will be described along with the morphology of the associated scintillations. The models of scintillation activity that will be used in subsequent chapters will then be discussed, including; (i) a stochastic model based on data from previous solar maxima which will form the basis of most of the analytical work that follows, (ii) a model which combines various climatological irregularity models with a propagation model to produce predictions of scintillation strength and occurrence, and (iii) a propagation model based on a simple thin diffracting screen that enables simulated scintillation data to be generated for various simulation tests.

2.1.1. The ionosphere

The ionosphere is a region of the upper atmosphere in which the density of free electrons is large enough to have an appreciable effect on the propagation of radio waves [27], [80]. Although both the lower and upper boundaries of the ionosphere are not well defined, for most practical purposes they can be considered to occur at roughly 50km and 1000km

respectively. Below this is the neutral atmosphere (the troposphere) and above is the protonosphere that eventually merges with the interplanetary medium.

The ionosphere is formed by the ionising effects of solar X-ray and ultraviolet radiation on neutral gasses in the upper atmosphere. As solar radiation penetrates the atmosphere, its intensity is reduced through absorption while at the same time the density of the atmosphere (and hence its capacity to produce ions) increases. Together, these two effects lead to the formation of a region of maximum electron density, referred to as a Chapman layer [27], at altitudes between about 250km and 400km. A typical daytime electron density profile for a mid-latitude location is given in Figure 2.1-1. In this figure, it is apparent that the ionosphere forms into several layers, the largest of these being the F2-layer which extends from about 200 to 1000 km in height.

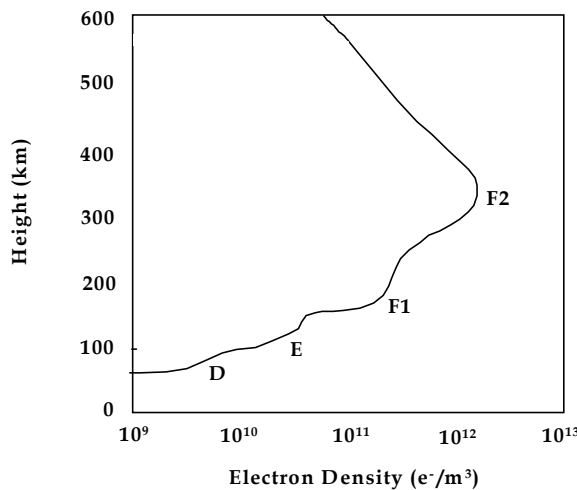


Figure 2.1-1: A typical daytime electron density profile for a mid-latitude location.

The peak density of the F2-layer undergoes large diurnal variations, reaching a maximum at approximately 1400hrs local time and a minimum just before dawn. The height of the F2-layer peak also shows a diurnal dependence, tending to fall at dawn and rise during the evening hours. At low geomagnetic latitudes, the F2-layer height continues to rise during the evening reaching a maximum height of approximately 500km at about 1900hrs local time. This effect is due to an upward $E \times B$ force created by an Eastward electric field in the E-layer that becomes enhanced soon after sunset. At these altitudes, the free ions recombine very slowly after dusk and so the plasma density remains relatively high. Under the influence of pressure gradients and gravity, the equatorial plasma in the heightened F2-layer is forced downwards along the magnetic field lines, creating regions of enhanced electron density at approximately 15 to 20 degrees either side of the

geomagnetic equator. These enhanced regions are referred to as the *Equatorial Anomaly*, and the process by which they are created is known as the *Fountain Effect* (see for example [49], [27] and the illustration in Figure 2.1-2). The Equatorial Anomaly is an important phenomenon in the study of scintillations as it is responsible for the formation of the plasma density irregularities that give rise to scintillations.

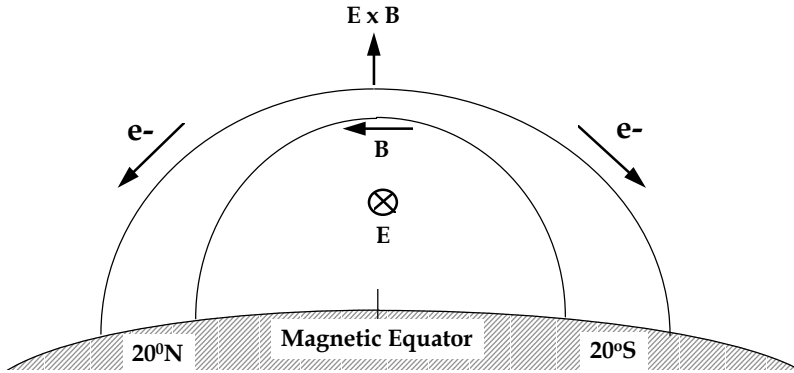


Figure 2.1-2: Illustration of the equatorial Fountain Effect which gives rise to the Equatorial Anomaly. E and B represent the electric and magnetic field vectors respectively.

2.1.2. Morphology of scintillations

Scintillations occur predominantly in the equatorial band that extends from about 20°S to 20°N of the magnetic equator, and in the auroral and polar cap regions (see Figure 2.1-3). The processes that produce scintillations in these two regions are quite different, leading to significant differences in the characteristics of the resulting scintillations.

Auroral and polar cap scintillations are mainly the result of geomagnetic storms¹ that are associated with solar flares² and coronal holes³. Unlike equatorial scintillations, they show little diurnal variation in their rate of occurrence, and can last from a few hours to many days, beginning at any time during the day [52]. Large and rapid variations in the plasma density are often associated with auroral and polar cap scintillations [10] and can lead to significant errors in differential GPS (DGPS) systems as well as rapid changes in the apparent range and range rate [52] & [53]. Auroral scintillations also show a seasonal dependence which is the reverse of that observed at low latitudes, being greatest from the

¹ Large variations in the strength and direction of the Earth's magnetic field.

² Sudden increases in the intensity of solar electromagnetic radiation associated with sunspot activity.

³ Low density regions of the solar corona that are associated with solar winds (high energy charged particles from the sun).

autumn equinox through winter to the spring equinox, and a minimum during the summer months [2]. Indeed, the geomagnetic disturbances that excite auroral and polar cap scintillations tend to suppress the onset of equatorial scintillations during solar maximum periods [3], [27] & [53]. Because geomagnetic storm activity is linked to solar activity through solar flares and coronal holes, auroral and polar cap scintillations also show a strong dependence on the 11 year solar cycle, being most intense during solar maximum periods, but almost non-existent during minima.

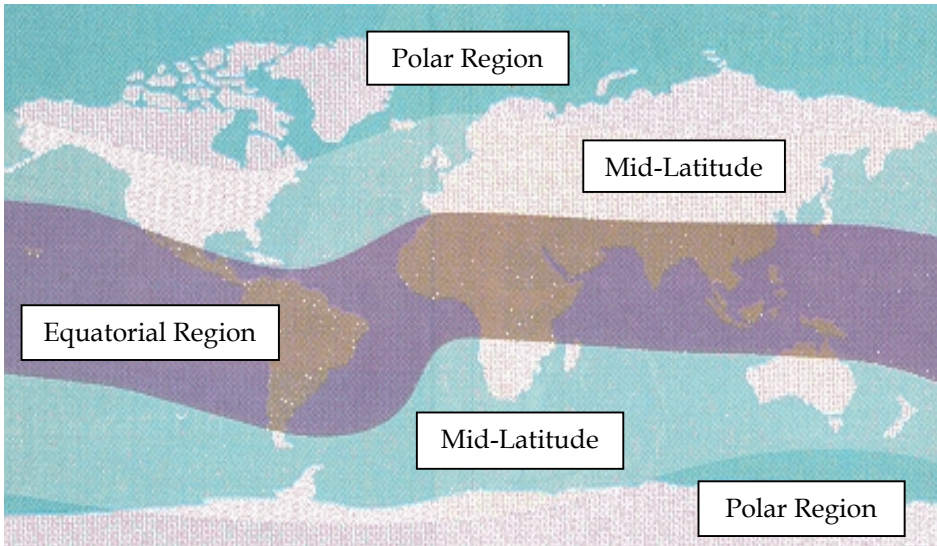


Figure 2.1-3: Map of the world showing the approximate locations of the polar, mid-latitude and equatorial regions. Scintillations are mainly confined to the equatorial and polar regions.

Equatorial scintillations, on the other hand, are produced by irregularities in the F-layer of the equatorial ionosphere following the passage of the evening terminator¹ and tend to disappear soon after midnight. In these regions, the most severe scintillations are associated with the crests of the equatorial anomaly which are centred approximately 15° either side of the magnetic equator [1]. As equatorial scintillations are coupled to the anomaly, they tend to be worse during the years of solar maximum when the anomaly is at its greatest. As we are currently at solar maximum (year 2000), it is expected that scintillation activity will now be at its greatest, and will remain so for at least a year or so.

Equatorial scintillations also show a strong seasonal dependence, being greatest during the months of April to August² in the Pacific longitude sector, but a minimum during these months in the American, African and Indian sectors. This situation is reversed

¹ The terminator is the boundary that divides day from night.

² Centred on the June Solstice.

during the months of September to March¹ [53]. During the seasons of high scintillation activity, the equinoctial months of March and September tend to suffer the highest levels of activity, although this does not appear to be true at all longitudes [8].

Equatorial scintillations are mainly produced by irregularities created by instabilities in the F-layer of the ionosphere during the evening hours. After sunset, the lower regions of the F-layer recombine more rapidly than the upper regions, leading to an unstable situation akin to a heavy fluid being supported on a lighter fluid². This situation eventually leads to the formation of bubbles of low density plasma which are forced upwards through the denser upper regions. As the bubbles grow, steep density gradients on the walls cause smaller irregularities to form [69]. At GPS frequencies, these smaller irregularities, which can be of the order of the Fresnel zone radius or less (< 300m), are responsible for scintillations [3]. The low density bubbles eventually form into irregularity patches, or *Plumes*, which can reach heights of up to 1500km at the magnetic equator. Once formed, the plumes extend along the magnetic field lines in a North-South direction for over 2000km, leading to an accumulation of irregularities in the Northern and Southern anomaly regions ($\pm 15^{\circ}$ to $\pm 20^{\circ}$ dip latitudes³). Because of the higher background densities in these regions, the irregularities tend to produce much stronger scintillation effects than at the magnetic equator. Irregularity plumes typically have East-West extents of between one and several hundred km's and tend to move in an Easterly direction with velocities of the order of 50 to 200 m/s [85]. Consequently, scintillations are often experienced in patches that can last for an hour or so with periods of little or no activity in between [3]. Eventually, in the absence of solar radiation, the irregularities begin to fade along with the associated scintillation activity. This usually occurs around local midnight, although at times scintillations can persist until early morning.

Scintillations can also occur during daylight hours and at mid-latitudes when Sporadic-E is present in the E-layer. Sporadic-E are thin layers of highly dense plasma at heights of about 100km in which large density gradients can exist. However, scintillations produced by Sporadic-E are much less common and less predictable than those produced by the F-layer processes described above.

¹ Centred on the December Solstice.

² This is referred to as a Rayleigh-Taylor instability.

³ “dip” refers to the Earth’s magnetic dipole or magnetic axis.

In the discussions that follow, only equatorial scintillations will be considered as they affect the largest number of people and tend to be more severe than their auroral counterparts [53]. In addition, the latitude band that is affected by equatorial scintillations covers approximately 50% of the Earth's surface, compared to only 7% for the auroral and polar cap regions. However, it should be mentioned that during intense magnetic storms, auroral disturbances can extend well into the mid-latitudes, disrupting GPS through both scintillation activity and large density gradients. An example of this was the magnetic storm in March 1989 during which auroral scintillation effects were felt over most of the continental United States causing narrow bandwidth receivers to frequently lose signal lock [52]. Such events are, however, quite uncommon.

2.1.3. Statistical characteristics of scintillations

Scintillations are produced by changes in the phase velocity of sections of a satellite signal wavefront as it propagates through irregularities in the ionosphere. As absorption in the ionosphere is negligible at L-band frequencies, the amplitude of the emergent wave is unaffected by the irregularities. However, as the wave propagates towards the ground, interference across the wavefront creates complex amplitude and phase diffraction patterns that are a function of both the range to the irregularities and the cross-range position. Scintillations are produced when these spatial diffraction patterns are transformed into temporal ones, either through relative motion between the receiver and the patterns, or by changes in the structure of the irregularities with time. Although diffraction is the principal cause of scintillations, weak focussing and defocusing through refraction can introduce additional amplitude and phase variations. However, for refractive effects to be significant at L-band frequencies, the density gradients in the ionosphere must be extremely large.

In this thesis, the effects of ionospheric scintillations are modelled as a complex modulation of the unperturbed GPS signal. Furthermore, the phase and amplitude components of this modulation are modelled as Wide Sense Stationary (WSS) stochastic processes that are produced by a random distribution of irregularities of different sizes. Consequently, they are defined in terms of their power spectral densities, probability density functions and variances. Although a deterministic model based on a collection of Gaussian shaped irregularities was also investigated [56], this approach was not taken any further as the resulting waveforms were found not to represent the vast majority of measured scintillation data.

The power spectral density of *phase* scintillations follows an inverse power law relationship of the form [76], [35]

$$S_{\phi_p}(f) = \frac{T}{(f_o^2 + f^2)^{p/2}} \text{ radians}^2/\text{Hz} \quad (2.1-1)$$

where T is the magnitude of the power spectral density at a frequency of 1Hz (as $f_o \ll 1$, $S_{\phi_p}(f=1) \approx T$), f is the frequency of phase fluctuations, f_o is a frequency that corresponds to the ionospheric *outer scale size*¹, and p is termed the spectral index and usually lies in the range 1 to 4, typically being 2.5 at equatorial latitudes [35]. The spectral strength can be represented by the following expression [13], [76]

$$T \propto G v_e^{(p-1)} \lambda^2 C_k L \sec(\theta) \quad (2.1-2)$$

where,

- G is a factor that depends on the direction of propagation of the radio wave and the geometry and orientation of the irregularities,
- v_e is the effective velocity of the propagation path through the contours of plasma density,
- λ is the carrier wavelength,
- $C_k L$ is referred to as the *height integrated irregularity strength* and is a measure of the strength of the irregularity spatial power spectrum at a scale size of 1km and the thickness of the irregularity layer, and
- θ is the off-vertical incidence angle of the propagation path at the irregularity layer.

The effective velocity, v_e , is a function of the velocity of the ionospheric pierce point² through the irregularity layer, v_I , the drift velocity of the irregularities, v_d (typically 50 to 200 m/s [85]), and the geometry and orientation of the irregularities. For GPS, the pierce point velocity, v_I , consists of a component due to receiver motion, v_r , and a component due to satellite motion, v_s (typically 60 to 450 m/s, depending on the elevation and azimuth angles of the satellites [9]). By changing v_I through receiver motion, the phase scintillation log spectrum will either be translated to the left or right, depending on the direction of motion of the receiver in relation to the vector sum of v_d

¹ $f_o = v_e / l_o$ where l_o is the outer scale size (maximum irregularity size) and v_e is the effective velocity.

² The ionospheric pierce point (IPP) is the point at which the satellite signal ray path intersects the ionosphere at the irregularity height. This is normally taken to be the height of the F2-layer peak which is roughly 400km.

and v_s and the geometry of the irregularities. However, the spectral index, p , will remain unchanged as it depends only on the spectrum of irregularity sizes in the ionosphere¹. Thus, receiver motion will shift the phase scintillation log spectrum along the frequency axis, but will not alter its slope. This effect, in conjunction with the higher levels of carrier loop stress experienced during receiver motion, has the potential to significantly alter a receiver's tolerance to scintillation activity.

The power spectral density of *amplitude* scintillations follows a similar power law relationship for high fluctuation frequencies, but is heavily attenuated at low frequencies. The cutoff frequency of the amplitude scintillation power spectrum (the *Fresnel cutoff frequency*) is given by [103]

$$f_c = \frac{v_e}{\sqrt{2}z_F} \text{ Hz} \quad (2.1-3)$$

where $z_F = \sqrt{\frac{\lambda z_1 z_2}{z_1 + z_2}}$ is the *Fresnel zone radius*, and z_1 and z_2 are the distances between the ionospheric irregularity layer and the satellite and receiver respectively. Notice that f_c is also the frequency that corresponds to the peak of the amplitude scintillation power spectrum [103]. Fresnel filtering occurs because amplitude scintillations are mainly produced by diffraction effects which are only significant when the irregularity scale size is of the order of the Fresnel zone radius. At typical ionospheric heights (~ 400 km for the F2-layer peak) and assuming vertical propagation, z_F is of the order of 276m at the GPS L1 frequency. For an irregularity drift velocity of 100m/s (a typical equatorial value) and assuming $v_I = 0$, the Fresnel cutoff frequency is approximately 0.26Hz.

Two commonly used measures of the strength of scintillation activity are the RMS phase, σ_{ϕ_p} , and the RMS intensity normalised by the mean, S_4 . The RMS phase is obtained from the integral of the power spectral density of phase scintillations as follows

$$\sigma_{\phi_p} = \sqrt{E\{\phi_p^2\}} = \sqrt{\int_{-\infty}^{\infty} S_{\phi_p}(f) df} \quad (2.1-4)$$

¹ For moderate levels of scintillation activity, p is related to the slope of the one dimensional irregularity spatial power spectrum, q , by $p \approx q + 1$. This approximation ignores the effects of diffraction on the phase.

where ϕ_p is the carrier phase (assumed to be zero-mean). Consequently, σ_{ϕ_p} is a function of T , p and the outer scale size parameter, f_o . In practice, however, the integral in Equation (2.1-4) is limited to some low frequency which is related to the coherent integration time of the receiver. Indeed, as the statistics of scintillations are only stationary for a few tens of seconds [35], this integral is unlikely to produce a realistic result if $1/f_o$ is much greater than a few tens of seconds.

The intensity scintillation index, S_4 , is the normalised RMS intensity and is given by

$$S_4 = \sqrt{\frac{E\{I^2\}}{E\{I\}^2} - 1} \quad (2.1-5)$$

where $I = A^2$ is the signal intensity. S_4 is also a function of T and p , but includes a *Fresnel filtering factor*, F ¹, and the Fresnel zone radius, z_F , which together account for the low frequency cutoff in the amplitude scintillation power spectrum. Under moderately disturbed ionospheric conditions, S_4 can be approximated by the following expression which is based on Rino's weak-scatter theory [13], [76]

$$\begin{aligned} S_{4w}^2 &\propto F z_F^{(p-1)} \lambda^2 C_k L \sec(\theta) \\ &\propto \frac{F z_F^{(p-1)}}{G v_e^{(p-1)}} \cdot T \end{aligned} \quad (2.1-6)$$

The following expression can be used to derive an approximate value for S_4 under strong scintillation conditions (assuming that refractive focusing effects do not occur) [13], [77]

$$S_4 = \sqrt{1 - \exp(-S_{4w}^2)} \quad (2.1-7)$$

Both σ_{ϕ_p} and S_{4w} show a simple dependence on the carrier frequency, v [13], [27]. For low to moderate levels of scintillation activity ($S_4 < 0.5$), S_4 scales with the carrier frequency as $v^{-(p+3)/4}$. Under strong scintillation conditions, S_4 is approximately equal to 1 at all frequencies (unless focusing occurs which may drive S_4 slightly higher than 1). The RMS phase, on the other hand, shows a v^{-1} dependence for both weak and strong

¹ The Fresnel filtering factor, F , is a function of the geometry and orientation of the irregularities, as well as the spectral index, p .

scintillations, unless the scintillation activity is exceptionally strong. Consequently, the GPS L2 frequency¹ is affected slightly more by scintillation activity than the higher GPS L1 frequency² (by a factor of about 1.4 for S_4 and 1.3 for σ_{ϕ_p}). This adds to the problem of the inherently higher level of susceptibility of the L2 channel as a result of the lower signal level of the L2 P-Code³ (the RMS carrier phase jitter resulting from thermal noise on the L2 P-Code is $\sqrt{2}$ times greater than the carrier jitter on the L1 P-Code, and twice as large as the carrier jitter on the C/A-Code for normal satellite signal levels).

Measurements of the probability density functions (PDF's) of scintillations have shown that phase scintillations follow a zero-mean Gaussian PDF, while amplitude scintillations follow the Nakagami-m PDF [64]. Although other distribution functions have been proposed for scintillations, the Gaussian / Nakagami-m distribution functions were found to provide the best fit based on chi-square tests of observed intensity and phase scintillation data [34], [101]. The Nakagami-m PDF is defined by the mean square amplitude, $\langle A^2 \rangle$, and by the m parameter which is a function of the strength of amplitude scintillation activity, *viz*

$$f_A(A) = \frac{2m^m \cdot A^{2m-1}}{\Gamma(m) \cdot \langle A^2 \rangle^m} e^{-m \cdot A^2 / \langle A^2 \rangle}, \quad A \geq 0 \quad (2.1-8)$$

where A is signal amplitude, $\Gamma()$ is the Gamma function and m is a parameter that is linked to the strength of scintillation activity by $m = 1/S_4^2$ [23]. The Nakagami-m PDF approximates the Gaussian PDF for small values of S_4 , and becomes equal to the Rayleigh PDF for $S_4 = 1$ (ie. for extremely strong scintillation activity). If the scintillation statistics are assumed to be stationary, then by conservation of energy, and assuming no absorption in the ionosphere, $\langle A^2 \rangle$ is independent of the strength of scintillation activity.

Phase scintillations follow a zero-mean Gaussian PDF and are therefore defined completely by the variance, *viz*

$$f_{\phi_p}(\varphi) = \frac{1}{\sqrt{2\pi}\sigma_{\phi_p}} e^{-\varphi^2/2\sigma_{\phi_p}^2} \quad (2.1-9)$$

¹ The GPS L2 frequency is 1227.6 MHz.

² The GPS L1 frequency is 1575.42 MHz.

³ The L2 P-Code is 3dB lower in power than the L1 P-Code. Refer to Section 2.2.

Unlike the Rayleigh or Rician fading models, the Nakagami-m model is not linked to the phase distribution through analytical expressions (ie. the Nakagami-m PDF for amplitude and Gaussian PDF for phase cannot be derived from an underlying signal model). Consequently, little is known of the joint statistics of amplitude and phase scintillations, although measurements suggest that they are negatively correlated with a correlation coefficient of approximately -0.6 [34]. However, it is the correlation between the amplitude and the rate of change of phase that is important in the study of tracking loop behaviour. Again, little is known of this correlation, although it is likely that the deep fades associated with large values of S_4 will be accompanied by rapid changes in the carrier phase [76], [33]. This is expected to put tracking loops under more stress than would be anticipated if amplitude and phase scintillations were considered to be independent.

2.1.4. Wide Band Scintillation Model

The Wide Band ionospheric scintillation MODel (WBMOD [82]) is a global model of ionospheric scintillation activity that enables users to predict the levels of scintillation activity at a given time and location. The parameters provided by WBMOD include the spectral index of phase, p , the spectral strength of phase, \mathbf{T} , occurrence statistics and the amplitude and phase scintillation indices, S_4 and σ_{ϕ_p} respectively. WBMOD consists of two parts; (i) a collection of empirically derived models of the global distribution and characteristics of ionospheric irregularities, and (ii) a power law phase screen propagation model which allows the strength of scintillation activity to be calculated in a user defined system. The propagation model assumes a spectral index of 2.5 at equatorial latitudes, and calculates \mathbf{T} from a series of eight parameters provided by the irregularity model (based on Equation (2.1-2)). These parameters include the in-situ spectral slope, $q = p - 1$, the height integrated irregularity strength, $C_k L$, the in-situ drift velocity of the irregularities, v_d , the phase screen height, three parameters describing the geometry and orientation of the irregularities, and the outer scale size, l_o . The only external inputs required by WBMOD are the carrier frequency, the satellite and receiver locations, local time and date, and solar and geomagnetic activity levels. In addition, the user must decide between two types of output, namely (i) the percentage of time that a specified level of scintillation activity is exceeded, or (ii) the level of scintillation activity associated with a given percentile of occurrence.

An example of the output provided by WBMOD is given in Figure 2.1-4. The scintillation indices σ_{ϕ_p} and S_4 are provided in the top panel, the spectral strength, T , is in the centre panel and the spectral index, p , is in the lower panel. All plots are a function of latitude at a longitude of 120°E and are at the 70th percentile (ie. the activity is expected to be stronger than the specified level for only 30% of the time). This example represents a period of high solar activity during the evening hours when the levels of scintillation activity are expected to be at their greatest. The two humps at approximately 25°N and 5°S correspond to the crests of the Northern and Southern equatorial anomaly (at this longitude, the magnetic equator is roughly 10° North of the geographic equator). Notice that when amplitude scintillations, and therefore S_4 , are small, phase scintillations, and therefore σ_{ϕ} and T , are also likely to be small.

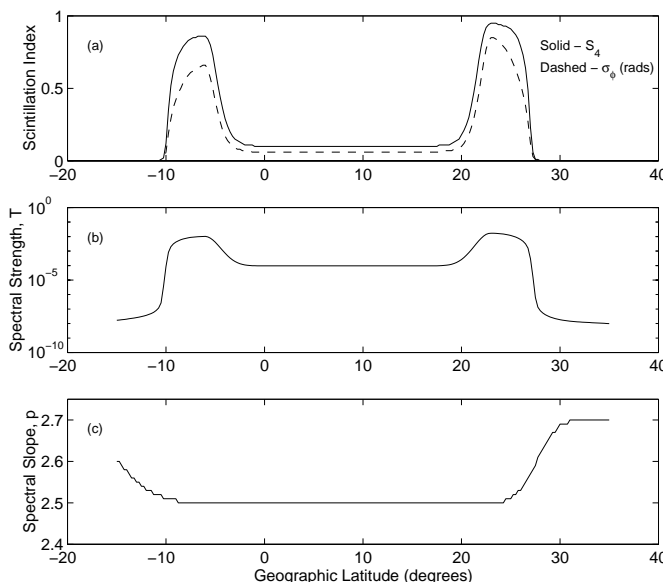


Figure 2.1-4: An example of the scintillation indices produced by WBMOD (April 10, 21:00 hrs local time, longitude 120°E, 70th percentile, L2 frequency, R12=150, $K_p=2$, Phase stability 10s).

In subsequent chapters, the various statistical parameters produced by WBMOD will be used to determine the performance of GPS receivers in a scintillation environment. By combining these results with the occurrence statistics provided by WBMOD, predictions can be made about the likely performance of a receiver at a given time and location.

2.1.5. Phase screen model

A simple model, based on Fresnel-Kirchoff diffraction theory, which demonstrates the effects of a thin phase screen on a vertically propagating plane wave is given in Appendix A. This model assumes that the plasma density irregularities are concentrated

within a thin layer or phase screen at a height that is typical of the F2-layer peak height (approximately 400km). The resulting patterns of amplitude and phase variations on the ground are then derived from the phase screen using simple diffraction theory. This model provides an insight into the types of irregularities that are likely to produce scintillations at L-band, as well as the characteristics of the resulting signals. It also allows simulated scintillation data to be created for the tracking loop simulator described in Appendix B.

2.1.5.1. Deterministic phase screen

In this section, the results obtained by modelling the irregularity layer as a series of discrete Gaussian shaped lenses is discussed. At GPS frequencies, irregularities with scale sizes of the order of the Fresnel zone radius¹ or smaller are likely to produce the most significant scintillation events. Larger irregularities produce very little amplitude variation and only gradual phase variation, unless the density gradients are extremely large. Very small irregularities (tens of metres or less) produce quite complex diffraction patterns, but at an intensity which is too low to have a significant effect on GPS.

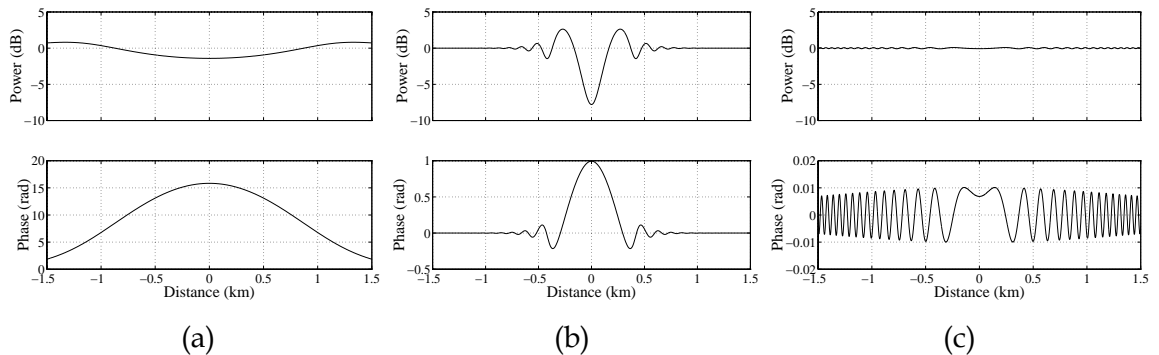


Figure 2.1-5: Modelled diffraction patterns based on a thin screen diffraction model and an isolated Gaussian shaped irregularity (see Appendix A). Scale sizes of the irregularities are (a) 1km, (b) 100m, and (c) 10m. The irregularities were centred at a height of 400km with a peak density variation of 500% over the background.

In Figure 2.1-5, three examples are given of the diffraction patterns produced by an isolated Gaussian shaped irregularity using the model described in Appendix A. From this figure, it is apparent that the 100m irregularity, which is approximately one third the size of the first Fresnel zone radius, produces the most significant amplitude variations

¹ The Fresnel zone radius is approximately equal to 276m at the GPS L1 frequency and 312m at the GPS L2 frequency, assuming an irregularity height of 400km.

(centre panel). Panel (a) shows the effects of a very large irregularity (1km) and panel (c) a very small irregularity (10m). Both of these will have much less of an impact on GPS receivers than the 100m irregularity. In addition, the high frequency phase variations associated with diffraction tend to be more pronounced when the irregularity size is of the order of the Fresnel zone radius. For much larger irregularities, the phase variations merely follows the in-situ density profile. Smaller irregularities produce prolific high frequency phase variations but at a level that is unlikely to affect GPS. In general, because the Fresnel zone radius at L-band frequencies is quite small, large density gradients are required in order to produce significant scintillation effects. This tends to restrict scintillation activity to the equatorial anomaly and polar regions where large density gradients are known to exist.

2.1.5.2. Random phase screen

Although the effects of isolated irregularities on transitionospheric signals has been reported in the literature (eg [42]), in general irregularities occur in large numbers with a range of sizes and densities (the spectrum of irregularity densities measured in-situ using rockets has a power-law form). By providing a more realistic in-situ density profile for the irregularity layer, the phase screen diffraction model will produce time series amplitude and phase scintillation data which has more realistic statistics (Appendix A). In Figure 2.1-6, a realisation of a random density layer with a Gaussian PDF and an in-situ spectral slope¹ of 2 has been used in place of the deterministic phase screen from the previous section. The wavenumber power spectrum of the vertically integrated density profile is given in panel (a) along with a straight line representing a spectral slope of -2 (on a log-log scale). The low frequency cutoff at a wavenumber of approximately $-31 \text{ dBmetres}^{-1}$ is produced by assuming an outer scale size, l_o , of 1.3km for the irregularities. The power spectra of the resulting phase and amplitude scintillations (panels (b) and (c) respectively) also have a spectral slope of 2. However, the amplitude scintillations display a low frequency cutoff, k_c ², at a wavenumber that corresponds to the Fresnel zone radius (approximately $-26 \text{ dBmetres}^{-1}$ for an irregularity height of 400km). The phase scintillation spectrum also shows evidence of Fresnel oscillations beginning at a wavenumber of about $-26 \text{ dBmetres}^{-1}$. These appear as a series of nulls in the power spectrum.

¹ For the integrated density profile.

² $k_c = f_c/v_e = 1/\sqrt{2}z_F$ from Equation (2.1-3).

The measured PDF's of both the amplitude and phase are also consistent with the models given in Section 2.1.3 (ie. Gaussian for phase and Nakagami-m for amplitude - panels (d) and (e) respectively). The smooth curves overlying both of these plots are the theoretical distribution functions obtained from the PDF expressions given in Section 2.1.3.

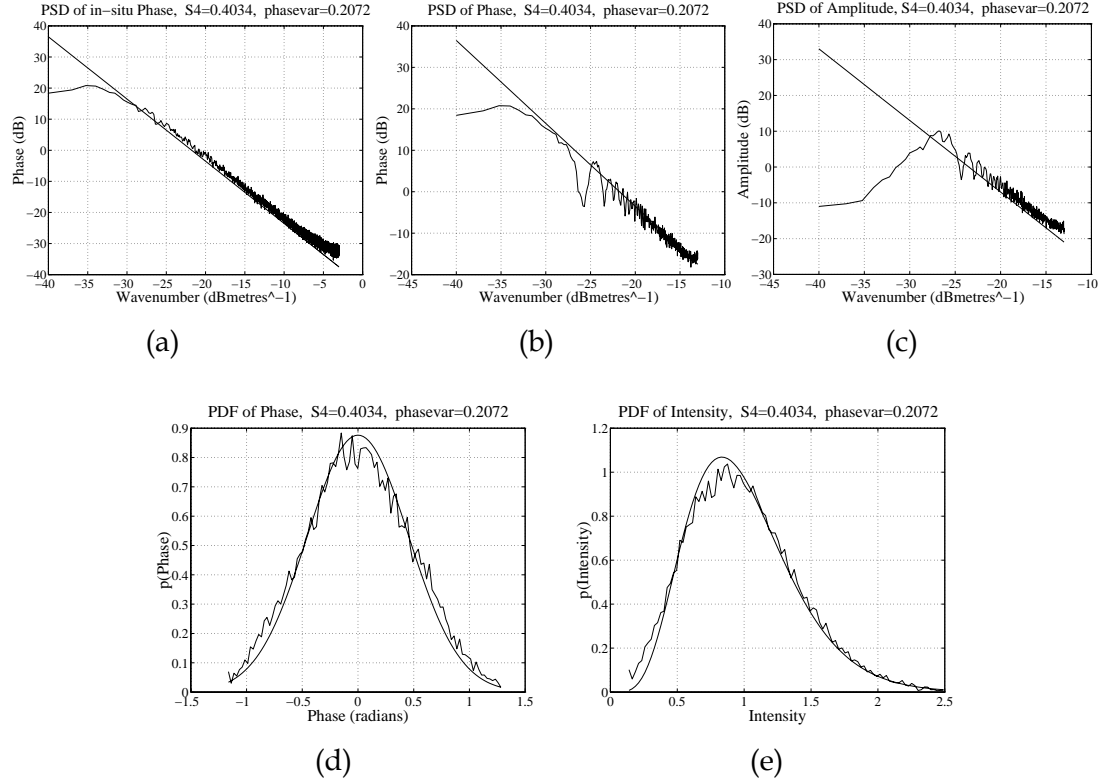


Figure 2.1-6: Scintillation statistics produced by a random, Gaussian distributed density layer with an in-situ spectral slope for the integrated density of 2. Shown are the in-situ spectrum (a), the phase scintillation power spectrum (b), the amplitude scintillation power spectrum (c), the phase PDF (d) and the Intensity PDF (e).

2.1.6. Summary

In this section, the morphology and statistical characteristics of scintillations were discussed. It was revealed that scintillations are generally restricted to specific times and locations and that these can be predicted using models such as the Wide Band Scintillation model. Based on studies of transitionospheric scintillation data, it was decided that scintillations can be modelled as a stochastic process in which the amplitude follows a Nakagami-m distribution and the phase follows a zero-mean Gaussian distribution. Furthermore, both the amplitude and phase can be assumed to have a power-law power spectral density with a low frequency cutoff for the amplitude. A technique for generating scintillation time series for simulation studies was also discussed. This

technique is based on a thin phase screen model for the irregularity layer and produces scintillation statistics that are consistent with the stochastic model described above. Details of the phase screen model are given in Appendix A.

2.2. Global Positioning System

GPS is a satellite based radio navigation system that provides accurate position, velocity and time information globally and continuously under all weather conditions. Although GPS is owned and operated by the US Department of Defense (DoD) and was developed primarily for defence applications, it is now used widely in both the defence and civilian communities in most countries. A convenient way of describing the GPS system is to divide it into the following three segments:

- (i) The Space Segment,
- (ii) The Control Segment, and
- (iii) The User Segment (the GPS receivers).

The Space Segment consists of 24 GPS satellites arranged in 6 orbital planes each of which are inclined at 55° to the equator. The coverage provided by the GPS constellation ensures that at least 4 satellites are visible at any time, anywhere on the Earth. As will be shown later, this is an important requirement to ensure accurate three-dimensional positioning by a receiver. The Control Segment consists of four monitor stations and four ground antennas which are distributed around the Earth, and a master control station located in Colorado Springs. The purpose of the Control Segment is to ensure that the Space Segment is operating within specification, and to provide adjustments where necessary. Communication between the Control Segment and the GPS satellites is via an S-band uplink from one of the four ground station antennas. The User Segment consists of GPS receivers, both military and civilian, and the associated infrastructure such as differential stations.

2.2.1. Principles of GPS positioning

GPS receivers estimate three-dimensional position by solving four independent time delay range measurement equations to four satellites in view. These equations can be represented as follows:

$$\rho_i = |[x_{Si}, y_{Si}, z_{Si}] - [x_R, y_R, z_R]| + c\Delta t \quad \text{for } i=1 \text{ to } 4, \quad (2.2-1)$$

$$= R_i + c\Delta t$$

where $[x_{Si}, y_{Si}, z_{Si}]$ is the 3 dimensional position vector of satellite i with respect to the centre of the Earth, $[x_R, y_R, z_R]$ is the position vector of the GPS receiver, c is the speed of light, Δt is the receiver clock offset from the satellite system time ($c\Delta t$ is usually referred to as the *receiver clock bias term*), R_i is the true range to satellite i , and ρ_i is referred to as the *Pseudorange* to satellite i (assumed here to be error free). The four unknowns in the range measurement equations are the x , y and z components of the GPS receiver position vector (ie. the location of the receiver) and the receiver clock bias. The four pseudorange measurements are found by measuring the delay in the propagation of the GPS signal from four satellites to the receiver, and will usually be contaminated by a variety of error sources. The four satellite position vectors $[x_{Si}, y_{Si}, z_{Si}]$ are obtained from the satellite ephemeris information which is transmitted by each satellite as part of the GPS navigation message¹.

GPS pseudorange measurements are obtained by correlating the pseudorandom noise (PRN) ranging codes transmitted by each GPS satellite with a replica code generated within the receiver. The time delay, τ , which must be applied to the replica code in order to achieve a correlation peak is related to the pseudorange, ρ , by $\rho = c\tau$. A second estimate of the satellite range can be obtained by integrating the carrier phase rate measurements that are generated within the carrier tracking loops. However, although the resulting carrier phase range measurements are relatively noise free compared to the code measurements, they are subject to an unknown integer cycle ambiguity. Therefore, a combination of these two measurements is often used in order to derive low noise, unambiguous estimates of the satellite pseudorange.

The GPS signal is transmitted on two carrier frequencies, L1=1575.42 MHz and L2=1227.6 MHz, each of which are bi-phase modulated by PRN ranging codes and GPS navigation data. The PRN codes serve two purposes; (i) to create direct sequence spread spectrum signals with good multiple access rejection and interference immunity, and (ii) to enable the GPS receiver to measure satellite ranges by code correlation. Two PRN codes are provided for this purpose, the Precision code or P-Code at 10.23 Mbits/s which is modulated onto both GPS carriers, and the Coarse/Acquisition code or C/A-Code at

¹ The navigation message is a 50 bits per second data stream that is modulated onto each satellite carrier and includes information about the system time, clock correction factors, satellite health, and synchronisation information for the military codes.

1.023 Mbit/s which is modulated onto the L1 carrier only. The US DoD reserves the right to deny access to the higher accuracy available from the P-Code by encrypting it with a second code referred to as the W-Code¹. The resulting Y-Code is then only available to authorised users who are equipped with the appropriate code decryption keys. This process is known as Anti-spoofing (AS) and its principal function is to protect authorised users from deceptive jamming (spoofing) by hostile forces. Prior to 1 May 2000, the US DoD also deliberately degraded the accuracy available to unauthorised users by dithering the satellite clocks and introducing small errors into the satellite ephemeris information. This process was known as Selective Availability (SA) and again could only be removed by users who had access to the code decryption keys. Although SA errors are currently set to zero, it is nevertheless possible for the US DoD to resume SA in the future if the need arises. In GPS terminology, the more accurate P(Y)-Code service is referred to as the Precise Positioning Service (PPS), and the less accurate C/A-Code service is referred to as the Standard Positioning Service (SPS).

GPS pseudorange measurements are contaminated by a number of errors, including ephemeris errors, ionospheric delays, tropospheric delays, RF channel biases, multipath and thermal noise. Expressions for the code and carrier phase pseudorange measurements that include these errors are as follows:

$$\text{Code: } \rho = R + c\Delta t + d_{TROPO} + d_{IONO}(f) + b_S + b_R + n_{Tp} + n_{Mp}, \quad (2.2-2)$$

$$\text{Carrier: } \phi = R + c\Delta t + d_{TROPO} - d_{IONO}(f) + b_S + b_R + n_{T\phi} + n_{M\phi} + N\lambda, \quad (2.2-3)$$

where R is the true range to the satellite, $c\Delta t$ is the receiver clock bias, d_{TROPO} is the tropospheric delay error, d_{IONO} is the ionospheric delay error, b_S and b_R are the satellite and receiver inter-channel biases (hardware biases), n_T and n_M are the thermal noise and multipath errors, and $N\lambda$ is the cycle ambiguity in the carrier phase measurement. Now that SA has been turned off, the principal source of error is likely to be the ionospheric delay, d_{IONO} . Under quiescent ionospheric conditions, the ionospheric delay is proportional to the integrated electron density in the ionosphere (also called the Total Electron Content or TEC), and inversely proportional to the square of the carrier frequency, f (ie. $d_{IONO} = kTEC/f^2$, where k is a constant [27]). As TEC is the same on the two GPS carrier frequencies for a particular satellite to receiver link, a dual frequency

¹ The chipping rate of the W-Code is 20 times less than the chipping rate of the P-Code.

receiver is capable of measuring, and therefore removing, ionospheric delays from satellite range measurements. Consequently, authorised military users who are equipped with P(Y)-Code receivers, and therefore have access to both carrier frequencies, will have the capacity to eliminate ionospheric delays directly [81]. However, as the C/A-Code is only modulated onto the GPS L1 carrier at present, unauthorised users are unable to remove ionospheric delays in this way and must rely on a correction factor that is derived from a broadcast ionospheric model [51]. In the future, modulation of the L2 carrier by the C/A-Code and a possible second civil frequency (referred to as the L5 frequency) will dramatically change this situation for civil users.

2.2.2. GPS receiver tracking loops

Figure 2.2-1 is an illustration of a generic GPS receiver in which the code and carrier tracking loops are shown embedded between an RF front end stage¹ and a navigation processor. A typical GPS receiver contains many such tracking loop channels, each of which consists of a Costas phase locked loop (PLL)² for carrier tracking linked to a non-coherent delay locked loop (DLL) for code tracking (see for example [47] & [92]). In most receivers, the code loop is also Doppler aided by the carrier loop to improve its robustness to dynamics³.

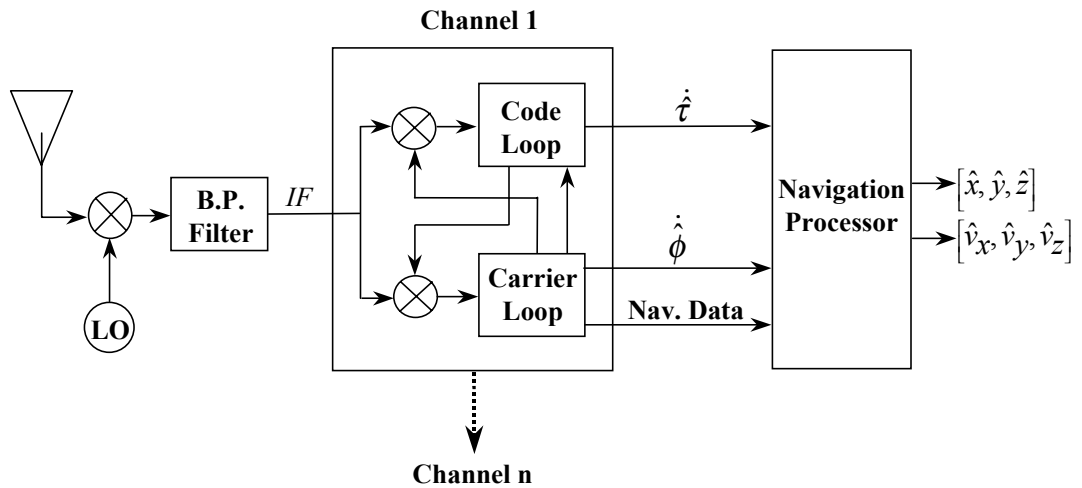


Figure 2.2-1: Architecture of a generic GPS receiver.

¹ The RF front end typically consists of an antenna, a low noise preamplifier, a down-conversion mixer and an image rejection filter.

² As 50Hz navigation data remains on the carrier after removal of the code, the carrier loop must be capable of tracking a suppressed carrier signal. Consequently, a Costas loop is used rather than an ordinary PLL.

³ Carrier aiding of the code loop removes virtually all of the line of sight dynamics from the code loop, allowing the code loop bandwidth to be significantly reduced.

In Figure 2.2-1, the mixer at the front of the code tracking loop is driven by a replica carrier from the carrier tracking loop and is responsible for down-converting the GPS intermediate frequency (IF) signal to a baseband IQ pair. The mixer at the front of the carrier tracking loop is driven by a replica code from the code tracking loop and is responsible for removing the satellite PRN code from the IF carrier. Consequently, under normal tracking conditions, the carrier loop receives an IF carrier which is modulated by the navigation data, and the code loop receives a PRN code which is modulo 2 added to the navigation data. Although other tracking techniques do exist (eg [44] & [71]), the Costas PLL/DLL combination is by far the most common for GPS.

Both the code and carrier tracking loops can be represented by the signal processing model illustrated in Figure 2.2-2. Here τ and ϕ represent the phases of the code and carrier components of the GPS signal at the input to the tracking loop, and $\hat{\tau}$ and $\hat{\phi}$ represent the phase estimates at the loop output. The loop contains two filters, a pre-detection filter $G(s)$ which reduces the levels of thermal noise prior to the phase discriminator, and a loop filter $F(s)$ which controls the order and bandwidth of the tracking loop. The phase discriminator is responsible for measuring the difference between the input phase and the loop phase estimate and is in general a non-linear device. The outputs of the tracking loop are Doppler estimates, $\dot{\tau}$ and $\dot{\phi}$, which are integrated in the Navigation Processor to produce the code and carrier range estimates. In addition, the navigation data is derived from the in-phase channel of the Costas loop at a point immediately after the pre-detection filter $G(s)$.

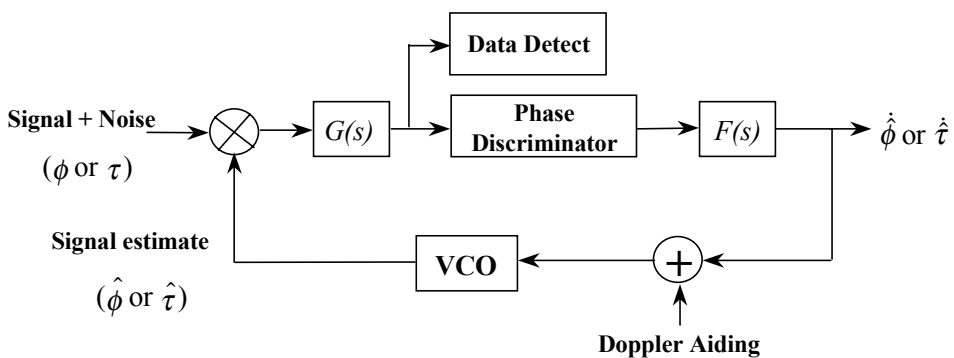


Figure 2.2-2: Signal processing model of a generic code or carrier tracking loop.

The function of the tracking loop is to provide estimates of the desired input phase process while rejecting unwanted phase noise. For GPS, the desired phase process is the Doppler introduced by satellite and receiver motion, while the phase noise is a combination of thermal noise, multipath, oscillator phase noise and ionospheric

scintillations. Important design objectives for the tracking loops are to minimise the phase noise on the Doppler estimates, and to minimise the tracking error between the input phase and the estimated phase processes (ie. $\tau_e = \tau - \hat{\tau}$ and $\phi_e = \phi - \hat{\phi}$). The second objective is associated with the ability of the loop to remain in phase lock and is probably the most important of the two under strong scintillation conditions.

2.3. A review of scintillation effects on GPS

To date there has been little detailed work done in the area of scintillation effects on GPS. The principal reason for this is that GPS was not declared to be fully operational until the end of 1994 [70], which is several years after the last solar maximum. Consequently, the effects of scintillations on a fully operational system are only now being observed. The majority of the work described in the GPS literature has either focused on the characteristics of the disturbed ionosphere or has dealt with the issue of GPS performance at a very qualitative level (see for example [2], [5], [9], [11], [14], [29], [53]& [98]). Other researchers have performed tests on GPS receivers using satellite signal simulators and either simulated or real scintillation data [12], [24], [63] & [94]. This work has shown that full code-correlation receivers are generally quite robust to moderate levels of scintillation activity, but that pseudorange noise and occasional loss-of-lock can occur if the scintillation activity becomes very strong. Nichols et al [66] correlated loss-of-lock events for a codeless receiver¹ with the scintillation statistics σ_ϕ and S_4 for a Northern Auroral region. Although this work has demonstrated that GPS receivers are indeed susceptible to the effects of scintillations, again it has not been accompanied by any detailed analytical studies. More recently, a number of researchers have begun to investigate the performance of GPS receiver tracking loops using phase locked loop simulations and simulated scintillation data. This has included simulation tests based on discrete irregularity structures [56], as well as those based on stochastic models of scintillations activity [41], [58] & [73]. Hegarty et al [41] used simulators for both the L1 code and carrier tracking loops tracking loops to determine the tracking errors as a function of S_4 and the quiescent C/N_o . His results suggest that very narrow bandwidth code loops are unlikely to be significantly affected by scintillations, but that carrier loops will suffer an increase in measurement noise and a loss of continuous carrier lock. He also found that codeless receivers will be significantly affected by scintillations and will even lose lock in

¹ For a description of codeless receivers, see Chapter 5.

the presence of quite mild scintillation activity. The principal advantage of using the simulation approaches outlined in [41], [56], [58] & [73] is that they overcome the problems associated with attempting to mathematically analyse the inherently non-linear code and carrier tracking loops. However, these approaches also fail to provide any deep insight into the problem and do not reveal the links that may exist between the scintillation statistical parameters and the receiver performance parameters.

Despite a lack of detailed research in the navigation community, a considerable amount of work has been done in the communications field on the effects of multipath fading on various types of communications systems, including Direct Sequence Spread Spectrum systems (see for example [30], [46] & [48]). However, most of this work has focused on the calculation of error rates in the transmitted message rather than the performance of the code and carrier tracking loops. For GPS, the probability of losing lock on the GPS signal and the magnitude of the measurement errors in the tracking loops is considered to be of far greater importance than errors in the navigation message. This is partly because of the large amount of diversity associated with the navigation message (diversity in both space and time), and partly because measurement errors in the tracking loops tend to be of more importance for a navigation system such as GPS than they are for a communications system. In addition, the majority of the communications literature deals with the more common Rayleigh and Rician fading models rather than the Nakagami-m model [64] which has been found to be more suitable under amplitude scintillation conditions [7], [34] & [101]. This is mainly because the Rayleigh and Rician fading models have traditionally been used to describe multipath effects, but also because they contain information about the joint statistics of amplitude and phase and so provide a more complete description of the fading statistics (the Nakagami-m distribution for amplitude and the Gaussian distribution for phase cannot be derived from an underlying signal model). Nevertheless, a few researchers in the communications field have looked at the effects of Nakagami-m fading on communications systems, and have identified ionospheric scintillations as a possible source of Nakagami-m fading (see for example [25], [26], [32], [61], [62], [65] & [102]). However, the work in this area has again focused on the calculation of error rates in the transmitted message rather than the performance of the code and carrier tracking loops. Indeed, in all of these cases, it has been assumed that the carrier is perfectly synchronised to the receiver local oscillator (ie. it is assumed that the carrier phase error, ϕ_e , is zero). Consequently, one of the principal objectives of the work described in this thesis was to derive expressions for the performance of the code and carrier tracking loops, navigation data demodulation and acquisition in terms of the

parameters of the scintillation model outlined in Section 2.1.3 and in [34], [35], [76], [77] & [101].

2.3.1. Carrier tracking loops

Under normal (quiescent) conditions, the tracking loop model of Figure 2.2-2 can be linearised by assuming that the phase tracking errors are small. This enables the non-linear discriminator element to be ignored which significantly simplifies the analysis. All text books on phase-locked loop theory discuss this approach and use it to obtain many of the measures which define loop performance (see for example [15], [36] & [43]). However, when the phase errors are large, either as a result of large amounts of direct phase noise, electromagnetic interference or amplitude fading, the linear model approximation may be significantly violated and the loop runs the risk of losing lock. Under these highly non-linear conditions, the behaviour of a phase locked loop is not well understood. Indeed, the only closed form analytical expressions that exist to define loop performance under these conditions are the probability density function of the phase errors (also called the "Tikhonov density function" and discussed in [97]), and the mean time to cycle slip (see for example [43]). Although these expressions have only been derived for a standard first order phase-locked loop that is subject to additive, white thermal noise, Lindsey and Charles [59] have shown that they are also a reasonable approximation for higher order loops and for non-white noise under certain conditions. In addition, Holmes [43] gives equivalent forms for these expressions that apply to an I.Q Costas phase locked loop. In a number of communications papers (eg [30], [46], [48]), the Tikhonov density function is used to determine the effects of imperfect carrier synchronisation on the bit error rates in a communications system that is subject to multipath fading. Also, Weber [100] has looked in detail at the effect of Rayleigh, Rician and Log-normal fading on a standard phase-locked loop, but again has only applied his results to the calculation of error rates in the received data. However, none of these researchers have looked at the effects of Nakagami-m fading on the performance of a phase locked loop. Also, none have looked at the probability of losing lock on the received signal, nor at the errors introduced into the code and carrier phase estimates. This is mainly because the code and carrier phase estimates provide information about the range to a satellite and so are of far less importance to a communications system than they are to a navigation system such as GPS. In addition, none of these papers have looked at the effects of a post-detection AGC on the susceptibility of the tracking loop to amplitude scintillations, nor the effects of relative motion between the transmitter and the receiver. Van Dierendonck [92] discusses the need for a post-detection AGC or a normalised discriminator such as Atan(Q/I) in

order to control the bandwidth of the tracking loop when the signal strength is unknown. Without such control, the instantaneous loop bandwidth may change significantly during periods of strong amplitude fading resulting in tracking difficulties, particularly under dynamic conditions. The behaviour of the AGC in the presence of amplitude scintillations will depend very much on its time constant. If the time constant of the AGC is short in relation to the correlation time of the amplitude, or the discriminator is normalised, the amplitude fluctuations are likely to be tracked quite accurately by the carrier loop, provided that the amplitude fading is not too deep (if the amplitude fade is very deep, the AGC will be limited by thermal noise). Under these conditions, the amplitude scintillations will be decoupled from the effects of phase scintillations and will merely act as a scaling factor for the receiver thermal noise. However, if the AGC time constant is long, it will be unable to accurately track the amplitude fluctuations and both the loop bandwidth and the damping factor will vary with time. Consequently, the amplitude will be strongly coupled to the effects of phase scintillations through the loop transfer function. Under these conditions, Weber [100] assumes that the bandwidth of the amplitude scintillations is narrow in relation to the loop noise bandwidth and derives an expression for the phase error variance as a function of the amplitude. The average variance is then obtained from this conditional variance using the Nakagami-m PDF.

Consequently, the objective of this part of the research was to derive expressions for the performance of the carrier tracking loops in terms of the scintillation parameters T , p , S_4 and σ_ϕ from Section 2.1.3, and to investigate the impact of different AGC regimes on carrier loop performance. The two principal performance measures to come out of this work were the variance of the phase tracking error and the variance of the loop phase estimate. The first of these is useful for determining the probability of losing carrier lock, the second is important for determining errors in carrier phase DGPS as well as errors in the estimation of velocity. Carrier loop tracking thresholds were then derived as a function of the two principal scintillation indices, T and S_4 , and compared with predictions obtained from the scintillation model WBMOD [82]. The dependence of these indices on both the satellite elevation angle and the satellite and receiver velocities was also examined.

Another significant component of this research was an investigation into the relationship between the fade depth and duration and the probability of a cycle slip for a carrier loop subject to a single fade with a simple rectangular profile. This problem is tackled using

both analytical techniques and simulations based on the carrier loop simulator from Appendix B. Kintner et al [50] also considers this issue using measured scintillation data and a real GPS receiver located in the equatorial region. His analysis shows that an increase in fade duration, possibly as a result of satellite and receiver motion, can cause a receiver channel to lose lock provided that the fade depth is near or below the tracking threshold of the carrier loop. He also indicates that when the velocity of the ionospheric pierce point matches the drift velocity, v_d , a situation referred to as *velocity resonance* can occur in which the fade duration becomes extremely long and greatly increases the probability of losing lock.

2.3.2. Code tracking loops

A delay locked-loop operates in essentially the same way as a phase-locked loop. The two main differences lie in the discriminator algorithm and in the need to generate a replica code for the code correlators. As the GPS carrier wavelength is more than a thousand times shorter than the length of a code chip, the effects of phase scintillations on the code loop can be ignored. However, the effects of amplitude scintillations on a code loop are essentially the same as their effects on a carrier loop and can be dealt with in much the same way. Probably the main difference in performance between the two loops is associated with the much narrower bandwidth of the code loop and the presence of post-detection integration within discriminator (see for example [47]). Although the principal reason for these differences is to reduce thermal noise errors in the code loop, a second effect will be to reduce the impact of amplitude scintillations, particularly if the fade duration is short in relation to the loop time constant. Indeed, using simulations Hegarty et al [41] found that the effects of amplitude scintillations on a very narrow bandwidth (0.1 Hz) delay locked loop were negligible. However, using a real GPS receiver, Coco et al [24] observed that strong amplitude scintillations could increase the pseudorange RMS as well as introducing large pseudorange spikes. Therefore, the key objective of this part of the work was to derive variance measures for the delay-locked loop which take into account the effects of post-detection integration, and to then relate these to the accuracy with which the code pseudorange can be measured. In order to achieve this using analytical techniques, assumptions must be made about the bandwidth of the code loop in relation to the correlation time of the amplitude scintillations.

A second objective of this work was to demonstrate that the distortion of the GPS ranging codes produced by frequency selective scintillation effects is likely to be negligible at GPS

frequencies. The work done by Bogusch et al. [16] & [17] on the effects of ionospheric disturbances on the performance of code correlators demonstrates that the irregularities must be extremely dense (such as those produced by a high altitude nuclear blast) and the code bandwidth must be relatively wide before significant code distortion can occur. At GPS frequencies, the distortion of the GPS codes is expected to be negligible under naturally occurring ionospheric conditions, even for the wider bandwidth P-Code.

2.3.3. Codeless and Semi-Codeless receivers

It is generally accepted that scintillations will have the most profound effect on codeless and semi-codeless tracking loops. This is based on studies of real GPS receivers exposed to scintillation effects (see for example [57], [66], [67] & [98]) and a number of more theoretical studies (eg. [41] & [93]). The reasons for this are that the tracking loops of codeless and semi-codeless receivers generally have both a significantly reduced SNR and a very narrow loop bandwidth. As a result, receivers of this sort may frequently revert to L1 only tracking under strong scintillation conditions. This is unlikely to have a very significant effect on the positional accuracy of a receiver (assuming SA is the dominant source of error), but will compromise a receiver's ability to measure ionospheric TEC. Consequently, it is only likely to be of importance for receivers that form part of a WAAS network and are therefore required to monitor TEC. However, with the introduction of a second civil frequency in the near future (referred to as the L5 frequency), it is unlikely that this problem will persist much beyond the current solar maximum.

The objective of this part of the work, therefore, was to develop analytical expressions that define the performance of codeless and semi-codeless receivers in terms of the scintillation parameters given in Section 2.1.3. The result of this analysis were then compared with measurements obtained from a semi-codeless GPS receiver co-located with an ionospheric scintillation monitoring receiver in an area known to experience scintillation effects.

2.3.4. Navigation data

A number of researchers in the communications field have looked at the effects of Nakagami-m fading on the error rate in communications systems. Wojnar [102] obtained an expression for the average bit error probability for a non-selective Nakagami-m fading channel based on an expression for the conditional bit error probability which applies to both coherent and non-coherent PSK and FSK. This result was based on earlier work by

Nesenbergs [65], Esposito [32], and Barrow [6]. Miyagaki [61] tackled the problem of non-selective Nakagami-m fading on coherent M-ary PSK, while Crepeau [25] & [26] considered the cases of frequency hopped non-coherent binary FSK, non-coherent M-ary FSK and differentially coherent binary PSK. In addition, Eng [31] analysed the problem of frequency-selective Nakagami-m fading on Direct Sequence CDMA and derived expressions for the bit error rate of a RAKE receiver. However, none of this work has included the effects of carrier loop phase tracking errors, and in particular the impact of direct phase noise from sources such as phase scintillations. Consequently, the objective of this part of the work was to determine the effects of Nakagami-m amplitude fading and carrier loop tracking errors from phase scintillations and thermal noise on the demodulation performance of the navigation data. This was done using an approach similar to those described in the cited papers, but with the Tikhonov density function used to account for the effects of imperfect carrier synchronisation.

2.3.5. Acquisition

McDonough & Whalen [60] (pages 262-265) use the Rayleigh PDF for the signal amplitude to find an average probability of detection for an envelope detector under multipath fading conditions. The approach used here is to use the Nakagami-m PDF and a square-law detector (see for example [43], [60], [72], [74] & [84]) that incorporates post-detection integration in order to derive a similar average probability of detection. This requires both the amplitude and phase variations of the scintillations to be slow in relation to the integration period of the detector. This condition that is likely to be met under normal scintillation conditions and for typical integration periods.

The false alarm probability of an acquisition detector is generally considered to be independent of the signal level once the design parameters of the detector are fixed (ie. the pre and post-detection integration periods and the detection threshold). However, correlation sidelobes produced by the GPS C/A-Codes can significantly increase the false alarm probability if they are not accounted for when the design parameters of the detector are chosen [92]. As amplitude scintillations lead to occasional enhancements in the signal strength, the impact of correlation sidelobes can be even greater. This effect has been examined using the Nakagami-m PDF to account for these enhancements, as well as the PDF of the sidelobe levels (based on a cumulative distribution function reported by Spilker [87]) to determine an average false alarm probability.

The impact of a reduced probability of detection on the mean time to acquire has also been investigated for a simple single-dwell, serial search strategy of the sort described in [72] & [84]. The effects of both short and long amplitude correlation times have been addressed, although a number of simplifying approximations have been made in order to arrive at a closed form analytical expression.

2.3.6. Optimum tracking of the carrier phase

As shown by Van Trees [95] & Brown & Hwang [19], the optimum filter for tracking a signal that is corrupted by additive thermal noise can often be mapped into an equivalent phase-locked loop structure, provided that the transfer functions of the two have the same general form. This allows the optimum bandwidth, loop order and damping factor of the carrier loop to be obtained through a procedure that is independent of phase-locked loop theory. By applying this approach to the case where a signal is corrupted by amplitude and phase scintillations, the optimum phase locked loop structure for a minimum probability of losing lock is obtained as a function of the scintillation parameters from Section 2.1.3. This approach has also been extended to the case where dynamics are present, although the resulting optimum loop transfer function cannot always be mapped into an equivalent phase locked loop structure. In a similar way, the optimum causal and non-causal post-loop filters for minimum carrier phase range errors were obtained.

2.3.7. Scintillation effects on navigation

As scintillations cannot be eliminated by pre-processing prior to the tracking loops¹, the most straightforward mitigation strategy involves simply avoiding the times and locations for which scintillation activity is most likely to be a problem. Scintillation models such as WBMOD [82] provide predictions of the occurrence and severity of scintillation activity and are therefore very useful for planning operations in areas that may be affected by scintillations. Other models such as the Scintillation Network Decision Aid or SCINDA, [21] & [38], collect scintillation data from multiple receiver sites and process the data using models of plume formation, evolution and destruction to forecast scintillation activity (the SCINDA model reverts to WBMOD in the absence of current

¹ For electromagnetic interference, techniques such as adaptive filtering and adaptive null steering antennas can be used to reduce the effects of interference prior to the tracking loops without the need to modify the receiver hardware.

scintillation measurements). By linking the analytical performance measures described in the previous sections with the scintillation statistics generated by WBMOD or SCINDA, predictions can be made about the likely performance of a receiver at a given time and location. It can be shown ([76] & [77]) that the principal amplitude and phase scintillation parameters, S_4 and T , are directly proportional to a third parameter, referred to as the *height integrated irregularity strength* or $C_k L$, which is a measure of the strength of scintillation activity (see Equation (2.1-2)). In WBMOD, the distribution of $\text{Log}(C_k L)$ in equatorial regions is modelled as the sum of three Gaussians, each of which have different means and variances (see for example [13] & [82]). Therefore, as many of the receiver performance measures are functions of S_4 and T , they are amenable to averaging using this distribution function. Consequently, using WBMOD the performance of a single satellite-receiver link can be predicted for a given time and location, either in terms of a percentile or as an average based on the distribution function of $C_k L$.

Ordinarily, in the absence of scintillations, the navigational accuracy of a GPS receiver is found by estimating the single link error (referred to as the User Equivalent Range Error or UERE) and translating this error into equivalent position and time errors using satellite geometry factors (the Dilution Of Precision or DOP factors: see for example Kaplan [47] pp. 261-269). The DOP factors assume that the range errors are the same on each satellite link and are uncorrelated between the individual links. However, when the effects of scintillations are included, WBMOD provides additional information from which the tracking status and range errors on each satellite link can be obtained independently. The problem then arises as to how these individual link predictions can be combined in order to determine the likely impact on navigational accuracy. In this section, it is shown that the joint statistics of the scintillation indices S_4 and T on the individual satellite-receiver links are required in order to solve this problem. However, as yet there are no models or data available from which this information can be derived. Nevertheless, in [57] data obtained from a receiver located in an active scintillation environment was analysed to show that the probability of losing lock simultaneously on multiple satellite links is extremely small. Further analysis of this data is required in order to determine the required statistics and the factors on which they depend.

2.4. Summary

In this chapter, an overview of the morphology and statistical characteristics of scintillations was given. It was revealed that scintillations can be modelled as a stochastic process in which the amplitude follows a Nakagami-m distribution and the phase follows a zero-mean Gaussian distribution. Furthermore, both the amplitude and phase can be assumed to have a power-law power spectral density with a low frequency cutoff for the amplitude. The scintillation model WBMOD was also described and its potential for predicting the statistics of various key scintillation parameters was explained. These statistics link WBMOD to the stochastic scintillation model as they define the distribution functions and spectral characteristics of the scintillations. A second scintillation model based on diffraction from a thin phase changing screen was also described. The primary purpose of this model was to generate scintillation time series for the simulation tests carried out in subsequent chapters.

The second part of this chapter provided an overview of the GPS system, including a brief description of the architecture of the front end of a GPS receiver and the operation of the receiver tracking loops. This was then followed by a literature review and an overview of each chapter in the thesis. The main point to come out of this review was that although various researchers have conducted simulation studies and measurement campaigns aimed at quantifying the effects of scintillations on GPS, there has been very little detailed analytical work done in the area. Consequently, the main thrust of this thesis is to link the various statistics associated with the stochastic scintillation model outlined above to measures of the tracking and acquisition performance of a GPS receiver.

Chapter 3

Carrier tracking loops

This chapter examines the effects of scintillations on carrier tracking loops. As carrier loops are generally the weakest link in a receiver channel, significantly more effort has been devoted to this chapter than to the following chapter on code tracking loops. A brief outline of each section in this chapter is given below:

- In Section 3.1, a signal processing model of the carrier tracking loop is given. This model is used throughout the thesis and is based on a Costas suppressed carrier tracking loop.
- In Section 3.2, the effects of phase scintillations on a Costas carrier loop is investigated. Phase scintillation effects include an increase in carrier tracking errors and an increase in carrier phase range errors. The first of these is associated with the ability of the carrier loop to remain in phase lock, the second is associated with errors in carrier phase differential GPS. The latter is dealt with in greater detail in Section 3.6 where the decorrelation with distance of the phase scintillation error is examined.
- In Section 3.3, the impact of amplitude scintillations on a Costas carrier loop is investigated. This is done for an I.Q discriminator that is normalised by a post-detection AGC. Because the joint statistics of amplitude and phase scintillations are unknown at this stage, it was decided to initially treat their effects separately, and to then deal with their combined effects by assuming independence. The potential problems associated with this assumption are highlighted.
- In Section 3.4, a rule of thumb tracking threshold for the Costas loop is defined in terms of the amplitude and phase scintillation indices, T and S_4 , and the loop bandwidth. This threshold is then compared with WBMOD predictions of T and S_4 obtained for a stationary receiver located in a region of high scintillation activity. The effects of satellite elevation angle and both satellite and receiver velocity on the scintillation indices, and therefore on the probability of exceeding the tracking thresholds, are examined using WBMOD data and the scintillation model from Section 2.1.3.

- In Section 3.5, both analytical techniques and simulations are used to determine the relationships between the depth and duration of a simple rectangular fade and the probability of a carrier cycle slip. The intention is to show that short duration fades have very little impact on the tracking loop performance, irrespective of the fade depth.
- Finally, in Section 3.7 the effects of scintillations on a Frequency Locked Loop (FLL) are examined. FLL's are used as a primary means of carrier tracking in some receivers, but more often as a fall-back strategy when phase locked loop operation is no longer possible. In this section, the susceptibilities of FLL's and PLL's to scintillations are compared.

3.1. Carrier loop model

Figure 3.1-1 is a representation of a generic Costas carrier phase tracking loop. A brief description of the operation of the Costas loop is given below.

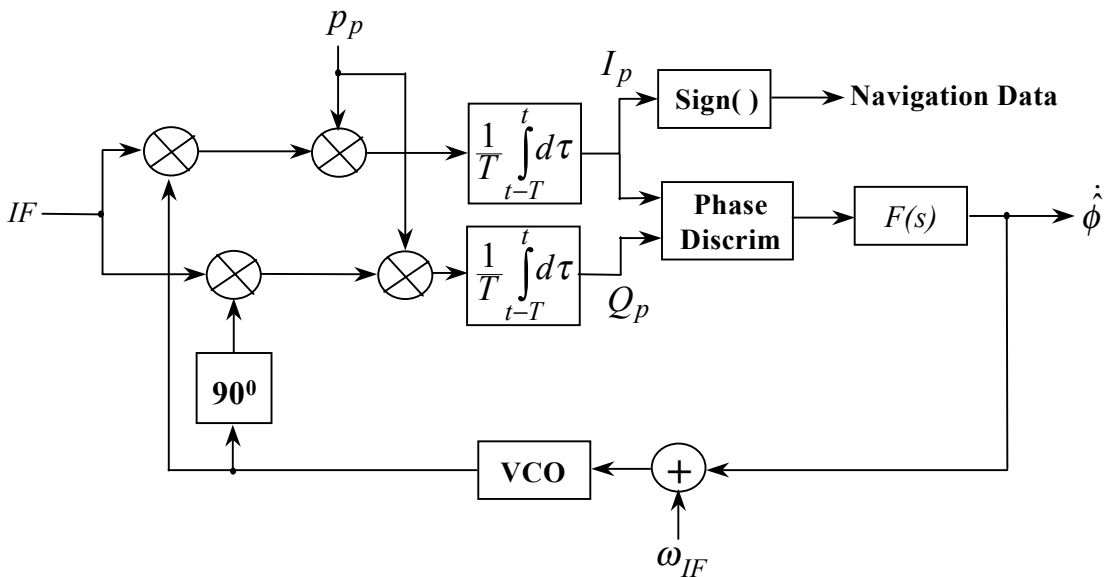


Figure 3.1-1: Model of a generic Costas phase locked loop.

The Costas carrier loop generates in-phase (I) and quadrature (Q) signals by mixing the GPS IF with I and Q reference signals produced by a voltage controlled oscillator (VCO). The PRN ranging code is then removed from the I and Q signals by mixing with an in-phase replica code, p_p , that is generated within the code tracking loop (see Chapter 4). This causes the energy of the GPS signal to be collapsed into the bandwidth of the navigation data which is 100Hz between nulls. The resulting I and Q signals are then

filtered by a pair of pre-detection integrate and dump filters¹ before being passed into the Costas loop discriminator. The function of the discriminator is to measure the phase error between the IF carrier and the VCO reference while simultaneously removing navigation data from the carrier. A list of the most common discriminator types along with their corresponding phase error functions is given in Table 3.1-1.

Discriminator	Discriminator Output
$\text{sign}(I).Q$	$\tilde{A} \sin(\phi_e)$
$I.Q$	$0.5\tilde{A}^2 \sin(2\phi_e)$
Q/I	$\tan(\phi_e)$
$\text{Atan2}(Q,I), \text{Atan}(Q/I)$	ϕ_e

Table 3.1-1: Common Costas loop discriminator functions. \tilde{A} is the filtered signal amplitude and ϕ_e is the phase error. Atan2(y,x) is the four quadrant arctangent function (ie. $-\pi \leq \text{Atan2}(y,x) \leq \pi$).

From the discriminator, the phase errors are passed through a loop filter, $F(s)$, and then on to the VCO. The loop filter controls the order and bandwidth of the tracking loop and must be adjusted according to the expected dynamics and noise conditions in order to maintain optimum tracking performance (ie. minimum phase tracking error). The filtered phase errors force the frequency of the loop VCO to be shifted in a direction that reduces tracking errors in subsequent phase measurements. In this way, the VCO tracks both the frequency and the phase of the IF carrier. Estimates of the line-of-sight Doppler and the ambiguous phase range (the integrated Doppler) are obtained directly from the filtered phase errors by applying appropriate scaling factors.

In the analysis that follows, the effects of scintillations are modelled as a modulation of the complex GPS signal². Based on this model, the IF signal can be represented by

¹ The integrate and dump filters are synchronised to the navigation data and have integration periods less than or equal to the length of a navigation data bit. Without synchronisation, the SNR of the filtered I & Q signals would be significantly degraded by changes in the sign of the navigation data.

² The modulation is of the form $A(t)\exp(-j\phi_p(t))$, where $A(t)$ and $\phi_p(t)$ are the amplitude and phase scintillation processes respectively.

$$IF(t) = A(t)p(t - \tau(t))d(t - \tau(t))\sin(\omega_{IF}t + \phi(t)) + n(t) \quad (3.1-1)$$

where:

$A(t)$ is the signal amplitude,

$p(t - \tau(t))$ is the satellite PRN code³,

$d(t - \tau(t))$ is the satellite navigation message³,

$\tau(t)$ is the code delay,

ω_{IF} is the IF carrier frequency,

$\phi(t) = \phi_d(t) + \phi_p(t) + \phi_o(t)$ is the phase of the GPS carrier,

$\phi_d(t)$ represents the effects of satellite and platform dynamics,

$\phi_p(t)$ represents the effects of phase scintillations,

$\phi_o(t)$ represents other effects such as VCO phase noise,

$n(t) = n_c(t)\cos(\omega_{IF}t) + n_s(t)\sin(\omega_{IF}t)$ is stationary, zero-mean, narrowband Gaussian thermal noise with a power spectral density of N_o W/Hz within the IF band, and

$n_c(t)$ and $n_s(t)$ are stationary, zero-mean, Gaussian noise processes which are independent and identically distributed (IID).

The IF signal is mixed with I and Q reference signals from the VCO and a prompt code, $p_p = p(t - \hat{\tau}(t))$, from the code tracking loop to produce a pair of baseband I and Q signals. The mixing process also generates double frequency terms centred on $2\omega_{IF}$, but these are eliminated by the pre-detection integrate and dump filters in the following stage. If it is assumed that the pre-detection filters are synchronised to the navigation data, and the phase error, ϕ_e , is relatively constant over the integration period, then after filtering the I and Q signals will become⁴

$$\begin{aligned} I_P &= \tilde{A}d(t - \tau)\cos(\phi_e) + n_{IP}, \\ Q_P &= \tilde{A}d(t - \tau)\sin(\phi_e) + n_{QP} \end{aligned} \quad (3.1-2)$$

where $\phi_e = \phi(t) - \hat{\phi}(t)$ is the carrier phase tracking error⁵, $\hat{\phi}(t)$ is the loop's estimate of the

³ Both the PRN ranging codes and the navigation data are represented by a ± 1 bit sequence.

⁴ The VCO signal is assumed to be of the form $2\sin(\omega_{IF}t + \hat{\phi}(t))$.

⁵ In this Chapter, the terms “phase error”, “carrier phase error” and “carrier phase tracking error” are used interchangeably.

carrier phase, $\tau = \tau(t)$, $\tilde{A} = \frac{1}{T} \int_{t-T}^t A(u)du$ is a filtered version of the signal amplitude, T is

the integration period of the pre-detection filters, and n_{IP} and n_{QP} are uncorrelated, baseband Gaussian noise processes with $\sigma_{n_{IP}}^2 = \sigma_{n_{QP}}^2 = N_o/T$. This step assumes that the replica prompt code is perfectly aligned with the satellite code and is therefore removed completely from the carrier (ie $\hat{\tau} = \tau$). The filtered I and Q signals are then processed in the Costas loop discriminator to produce the phase error estimates given in Table 3.1-1. In all cases, the discriminator algorithm eliminates the navigation data from the phase error estimates allowing the loop bandwidth to be reduced to a few Hz.

The Costas loop can be represented in an equivalent form in which the mixers and pre-detection filters are replaced by an adder, and the phase discriminator is replaced by the appropriate phase error function. An example of this baseband model for the I.Q discriminator is given in Figure 3.1-2. The $1/g$ factor represents gain control from an AGC.

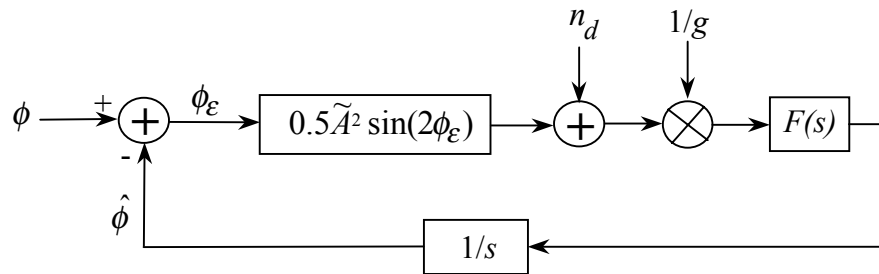


Figure 3.1-2: Non-linear baseband model of an I.Q Costas phase locked loop.

For small phase errors, the approximation $0.5\sin(2\phi_e) \approx \phi_e$ can be used to produce the linear baseband model shown in Figure 3.1-3. Similar approximations can be made for the other three discriminator types from Table 3.1-1.

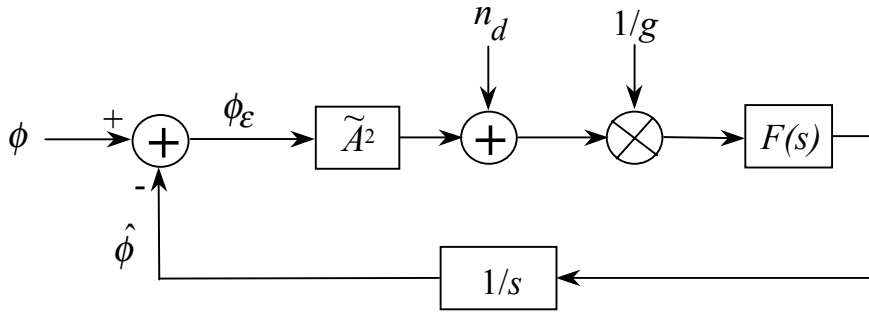


Figure 3.1-3: Linear baseband model of an I.Q Costas phase locked loop.

The noise term n_d represents the effects of additive thermal noise translated to the discriminator output, and includes products between the I and Q noise terms and the I and Q signal terms which are created within the discriminator. For the I.Q discriminator, n_d is given by (from Equation (3.1-2))

$$n_d = \tilde{A}d(t-\tau)[\cos(\phi_\varepsilon)n_{QP} + \sin(\phi_\varepsilon)n_{IP}] + n_{QP}n_{IP} \quad (3.1-3)$$

The gain control shown in these figures is typically provided by a post-detection AGC and is necessary to ensure that tracking loops based on un-normalised discriminators such as $I.Q$ and $\text{sign}(I).Q$ operate within their design parameters [92]. Without such control, the bandwidth and damping factor of the loops would be strongly affected by the signal amplitude, \tilde{A} . AGC's of this sort can either be applied after the discriminator (as shown in these diagrams) or at the IF stage prior to the tracking loop. In either case, their effect on the tracking loop will be the same. For an $I.Q$ discriminator, the AGC gain factor, g , is given by $I_P^2 + Q_P^2 \approx \tilde{A}^2$. If it is assumed that the discriminator is normalised (eg. $\text{Atan}(Q/I)$), or the AGC is capable of accurately tracking the signal amplitude, the closed loop transfer function of the Costas loop is given by (see for example [36])

$$H(s) = \frac{\hat{\Phi}(s)}{\Phi(s)} = \frac{F(s)}{s + F(s)} \quad (3.1-4)$$

where $\Phi(s)$ and $\hat{\Phi}(s)$ are the Laplace transforms of $\phi(t)$ and $\hat{\phi}(t)$ respectively. Typical loop transfer functions and their corresponding noise equivalent bandwidth's⁶ for the three loop orders are given in Table 3.1-2 (assuming active loop filters). As shown in

⁶ The single-sided noise equivalent bandwidth is given by $B_n = \frac{1}{2} \int_{-\infty}^{\infty} |H(f)|^2 df$.

Figure 3.1-4, the closed loop transfer function can be used to simplify the linear baseband model of the Costas loop.

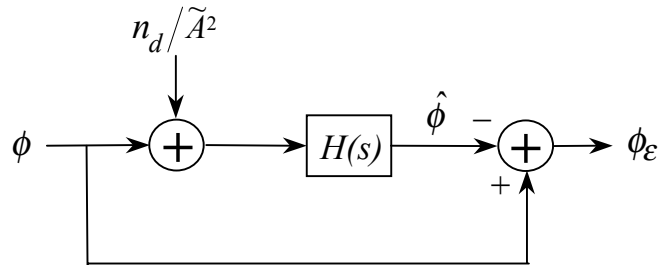


Figure 3.1-4: Closed loop transfer function model of a phase locked loop

	1st Order Loop	2nd Order Loop	3rd Order Loop
$F(s)$	ω_n	$2\zeta\omega_n + \omega_n^2/s$	$2\omega_n + 2\omega_n^2/s + \omega_n^3/s^2$
$H(s)$	$\frac{\omega_n}{s + \omega_n}$	$\frac{2\zeta\omega_n s + \omega_n^2}{s^2 + 2\zeta\omega_n s + \omega_n^2}$	$\frac{2\omega_n s^2 + 2\omega_n^2 s + \omega_n^3}{s^3 + 2\omega_n s^2 + 2\omega_n^2 s + \omega_n^3}$
B_n	$\omega_n/4$	$\frac{\omega_n}{2} \left(\zeta + \frac{1}{4\zeta} \right)$	$\omega_n/1.2$

Table 3.1-2: Open and closed loop transfer functions and single-sided noise bandwidth's for a phase locked loop. ω_n is the loop natural frequency and ζ is the damping factor for a second order loop.

The three loop transfer functions represent the optimum Wiener filters for tracking a phase step (1st order), a frequency step (2nd order with $\zeta = 1/\sqrt{2}$) and a frequency ramp (3rd order). These optimum filters were derived by Jaffe and Rechtin [45] based on a minimisation of the mean-square loop phase error in the presence of dynamics and noise. The derivation of an optimum Wiener filter in the presence of scintillations and dynamics will be discussed in Chapter 8.

3.2. The impact of phase scintillations on carrier phase tracking loops

In this section, the variance of the phase tracking errors and the variance of the phase range errors will be derived for a phase locked loop in the presence of phase scintillations and thermal noise. The variance of the phase tracking errors will be used to determine a threshold value for the spectral strength of phase scintillations beyond which loss-of-lock is likely to occur. The variance of the phase range errors will be used in Section 3.6 to investigate the effects of phase scintillations on carrier phase DGPS.

3.2.1. Phase tracking errors and thresholds

The mean-square carrier phase tracking error resulting from direct phase noise and thermal noise for the linearised carrier phase tracking loop is given by (based on Figure 3.1-4)

$$E\{\phi_e^2\} = \int_{-\infty}^{\infty} [|1 - H(f)|^2 S_\phi(f) + |H(f)|^2 S_{n'_d}(f)] df \quad (3.2-1)$$

where $1 - H(f)$ is the transfer function of the phase errors, $S_\phi(f)$ is the power spectral density (PSD) of the input phase process and $S_{n'_d}(f)$ is the PSD of the normalised thermal noise term, $n'_d = n_d / \tilde{A}^2$. The input phase process can be represented by (from Equation (3.1-1))

$$\phi(t) = \phi_d(t) + \phi_p(t) + \phi_o(t) \quad (3.2-2)$$

where $\phi_d(t)$, $\phi_p(t)$ and $\phi_o(t)$ represent the contributions from satellite and platform dynamics, ionospheric phase scintillations and other phase noise sources respectively. The autocorrelation function of $\phi(t)$ is therefore

$$\begin{aligned} R_{\phi\phi}(t_1, t_2) &= E\{\phi(t_1)\phi(t_2)\} \\ &= E\{[\phi_d(t_1) + \phi_p(t_1) + \phi_o(t_1)] * [\phi_d(t_2) + \phi_p(t_2) + \phi_o(t_2)]\} \\ &= R_{\phi_d\phi_d}(t_1, t_2) + R_{\phi_p\phi_p}(\tau) + R_{\phi_o\phi_o}(\tau) + \text{cross - correlation terms} \end{aligned} \quad (3.2-3)$$

where t_1 and t_2 are two instants in time and $\tau = t_2 - t_1$. In this analysis, it is assumed that $\phi_p(t)$ and $\phi_o(t)$ are stationary, zero-mean, Gaussian random signals, and that $\phi_d(t)$ may be deterministic or random, but is generally not zero-mean. It is also assumed that $\phi_d(t)$, $\phi_p(t)$ and $\phi_o(t)$ are independent as they are produced by entirely different physical processes. Consequently, the cross-correlation terms in Equation (3.2-3) are all zero. The corresponding PSD of $\phi(t)$ is thus

$$S_\phi(f) = S_{\phi_d}(f) + S_{\phi_p}(f) + S_{\phi_o}(f) \quad (3.2-4)$$

where $S_{\phi_d}(f) = E\{|\Phi_d(f)|^2\}$ is the PSD of the dynamics component (see Appendix E), $S_{\phi_p}(f)$ is the PSD of ionospheric phase scintillations (Equation (2.1-1)), and $S_{\phi_o}(f)$ is the PSD of the other phase noise sources. In the analysis that follows, it is assumed that thermal noise and ionospheric phase scintillations are the principal sources of phase noise, and that amplitude scintillations are not present (ie. $\tilde{A} = A$ where A is the unperturbed signal amplitude). Under these conditions, the mean-square phase tracking error reduces to

$$\begin{aligned} \sigma_{\phi_e}^2 &= \int_{-\infty}^{\infty} [|1 - H(f)|^2 S_{\phi_p}(f) + |H(f)|^2 S_{n'_d}(f)] df \\ &= \sigma_{\phi_{ep}}^2 + \sigma_{\phi_T}^2 \end{aligned} \quad (3.2-5)$$

where $\sigma_{\phi_{ep}}^2$ and $\sigma_{\phi_T}^2$ are the phase scintillation and thermal noise components of the tracking error variance, and $E\{\phi_e^2\}$ is equal to the phase error variance, $\sigma_{\phi_e}^2$, as both phase scintillations and thermal noise terms are zero-mean. Equation (3.2-5) can be simplified by making the following substitutions

$$\sigma_{\phi_T}^2 = \frac{B_n}{C/N_o} \left[1 + \frac{1}{2TC/N_o} \right], \text{ from Equation (D-19), Appendix D}$$

$$S_{\phi_p}(f) = \frac{T}{(f_o^2 + f^2)^{p/2}}, \text{ from Equation (2.1-1), and}$$

$$|1 - H(f)|^2 = \frac{f^{2k}}{f^{2k} + f_n^{2k}}, \text{ from Table 3.1-2 with } s = j2\pi f$$

where k is the loop order (1, 2 or 3), $f_n = \omega_n/2\pi$ is the loop natural frequency in Hertz, f_o is the outer scale size frequency, and a damping factor of $1/\sqrt{2}$ has been assumed for second order loops. The phase scintillation component of the tracking error variance is

$$\sigma_{\phi_{ep}}^2 = \int_{-\infty}^{\infty} \frac{f^{2k}}{(f^{2k} + f_n^{2k})} \cdot \frac{\mathbf{T}}{(f_o^2 + f^2)^{p/2}} df \quad (3.2-6)$$

Unfortunately, it is difficult to obtain a closed form solution to this equation. However, for $p < 2k$ and f_o much smaller than f_n , the following approximation can be made

$$\frac{f^{2k}}{(f^{2k} + f_n^{2k})} \cdot \frac{\mathbf{T}}{(f_o^2 + f^2)^{p/2}} \approx \frac{\mathbf{T}|f|^{2k-p}}{(f^{2k} + f_n^{2k})} \quad (3.2-7)$$

This is based on the observation that the phase error transfer function, $1 - H(f)$, is a high-pass filter, and so the low frequency components of the phase scintillation power spectrum will have a negligible effect on the phase errors. Therefore, letting $f_o = 0$ will not significantly affect the phase error variance. As f_o is usually very much smaller than f_n , this approximation will be accurate under the following conditions (based on $p < 2k$)

$$1^{\text{st}} \text{ order loop: } p < 2$$

$$2^{\text{nd}} \text{ order loop: } p < 4$$

$$3^{\text{rd}} \text{ order loop: } p < 6$$

As the carrier tracking loop in a GPS receiver is usually 3rd order (unaided) or 2nd order (aided), and p is in the range 1 to 4 (typically 2.5 at equatorial latitudes), this approximation is considered to be quite accurate under most circumstances. Equation (3.2-6) then becomes (using Spiegel's table of integrals [86], Equation 15.20)

$$\begin{aligned} \sigma_{\phi_{ep}}^2 &\approx \int_{-\infty}^{\infty} \frac{\mathbf{T}|f|^{2k-p}}{(f^{2k} + f_n^{2k})} df, \quad p < 2k \\ &\approx \frac{\pi \mathbf{T}}{kf_n^{p-1} \sin((p-1)\pi/2k)}, \quad 1 < p < 2k \end{aligned} \quad (3.2-8)$$

From Appendix C, the linear model tracking threshold for an I.Q Costas loop is given by

$$\sigma_{\phi_e}^2 \Big|_{Th} = \left(\frac{\pi}{12} \right)^2 \text{ radians}^2 \quad (3.2-9)$$

By equating the total phase error variance from Equation (3.2-5) with the linear model threshold given above, the following expression can be obtained for the threshold spectral strength

$$T|_{Th} = \left[\sigma_{\phi_e}^2 |_{Th} - \sigma_{\phi_T}^2 \right] \frac{k f_n^{p-1} \sin((p-1)\pi/2k)}{\pi} \quad (3.2-10)$$

In Figure 3.2-1, $T|_{Th}$ is plotted as a function of the spectral index, p , and the loop noise bandwidth, B_n , for both a second and third order carrier tracking loop under the specified threshold condition ($C/N_o = 41.5\text{dBHz}^7$ and $T=20\text{ms}$ are assumed). The relationships between the loop noise bandwidth and the loop natural frequency, f_n , for the two loop orders are given in Table 3.1-2.

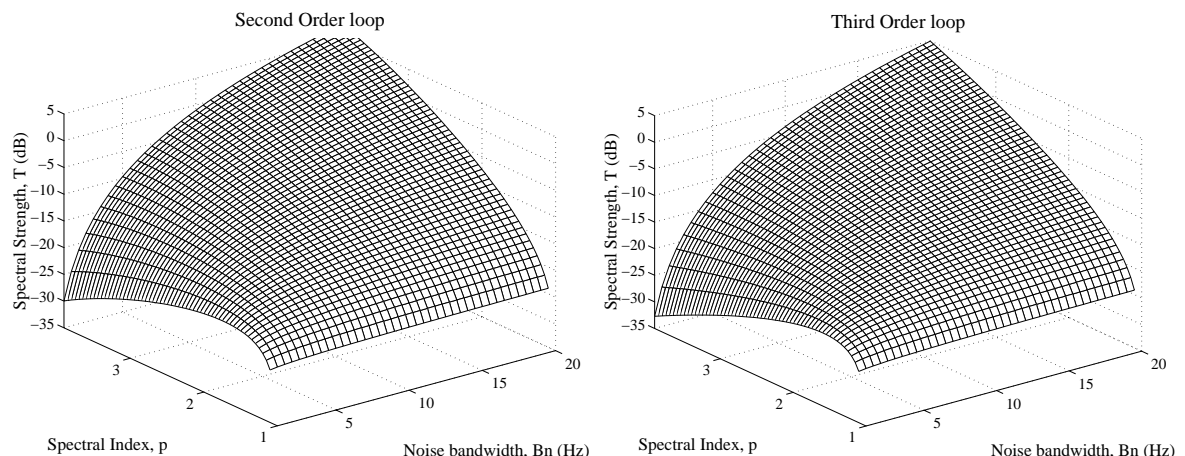


Figure 3.2-1: The threshold spectral strength, $T|_{Th}$, as a function of the spectral index, p , and the loop noise bandwidth, B_n , for a second order loop (left panel) and a third order loop (right panel). $C/N_o = 41.5\text{dBHz}$ and $T = 20\text{ms}$.

Figure 3.2-2 shows a cross-section through each of the plots in Figure 3.2-1 for $p=2.5$ (a typical equatorial value). By comparing these results with Figure 2.1-4 which was obtained using the WBMOD scintillation model, it is clear that in the region of the equatorial anomaly, it is possible for the spectral strength to exceed the specified tracking threshold and cause the carrier loop to lose lock. It is also clear that the loop noise

⁷ Throughout this thesis, $C/N_o = 41.5\text{dBHz}$ will frequently be used. This is based on a nominal GPS signal level of -160dBW [81] and a system noise temperature, T_S , of 512K . Thus $C/N_o = -160 - 10\log_{10}(kT_S) = 41.5$ where k is Boltzman's constant.

bandwidth strongly influences a receiver's tolerance to phase scintillations and that narrow bandwidth receivers tend to be far more susceptible (this becomes more pronounced for larger values of p). Although it is not apparent from these plots, it can be seen from Equation (3.2-5) that when the carrier to noise density ratio is significantly reduced, a point will be reached at which the thermal noise term, $\sigma_{\phi T}^2$, dominates the variance expression. When this occurs, wider bandwidth receivers will tend to be more susceptible to loss-of-lock. This may occur when strong amplitude scintillations are present or when the receiver is being affected by electromagnetic interference or attenuation from foliage or other sources.

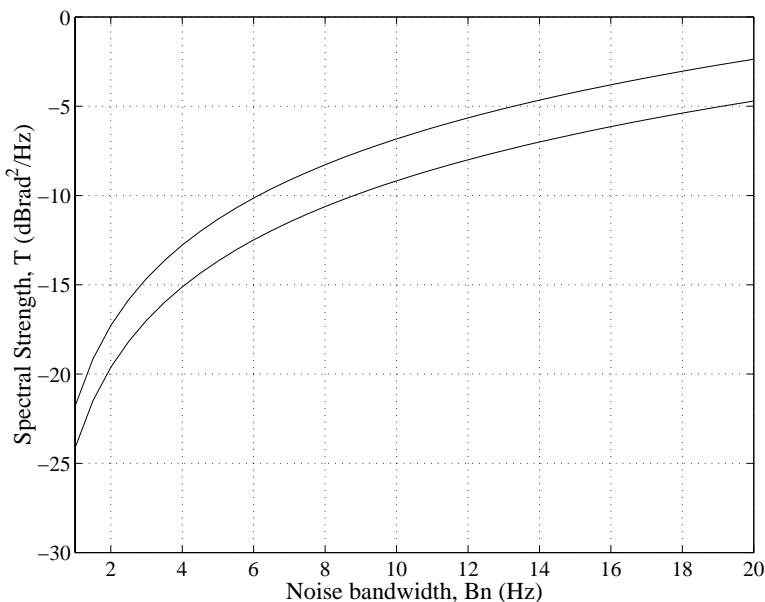


Figure 3.2-2: The threshold spectral strength, $T|_{Th}$, as a function of the loop noise bandwidth B_n for a second order loop (upper curve) and a third order loop (lower curve). $p = 2.5$, $C/N_o = 41.5 \text{ dBHz}$ and $T = 20 \text{ ms}$.

As INS⁸ aided receivers tend to adopt a very narrow tracking loop bandwidth, this result suggests that aided receivers will be more susceptible to phase scintillations than unaided receivers, although their tolerance to amplitude scintillations and interference will be better. This situation will become even worse if a receiver is in a state of open carrier loop aiding⁹, as it will no longer be able to track the high power, low frequency components of

⁸ INS - Inertial Navigation System.

⁹ With open carrier loop aiding, the VCO frequency is controlled by an INS. This technique is usually used as a weak signal hold-on strategy under conditions of strong interference.

the phase scintillations. However, INS aiding should also allow a receiver to recover more quickly from a state of loss-of-lock when the scintillation activity eventually passes.

A third observation that can be made from these plots is that in general, second order loops have a higher tolerance to phase scintillations than third order loops (by approximately 2 to 3 dB for $p=2.5$). In Chapter 8, it will be shown that the optimum loop order for minimum phase error is either first order or second order, depending on p , but is never third order.

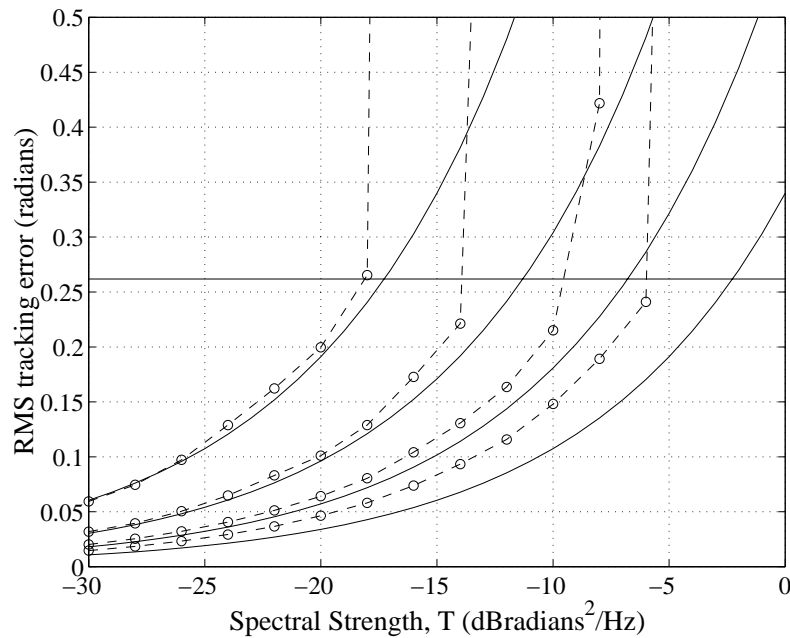


Figure 3.2-3: A comparison between the RMS phase scintillation error obtained from simulations (dotted lines) with those obtained from theory (solid line) for a second order Costas phase locked loop with $p = 2.5$, $f_o = 0.05\text{Hz}$, $T = 20\text{ms}$ and no thermal noise. The five different lines represent 2Hz, 5Hz, 10Hz and 20Hz loop noise bandwidths respectively (upper to lower curves).

In order to verify Equation (3.2-8), a number of simulations were conducted using the tracking loop simulator from Appendix B and simulated phase scintillation data from the model given in Appendix A. In Figure 3.2-3, the RMS phase scintillation error, $\sigma_{\phi_{ep}}$, obtained from both simulations (dotted lines and circles) and theory (solid lines) is plotted as a function of the Spectral Strength, T , for a range of loop noise bandwidths. These results show that the linear model is relatively accurate when the phase error variance is below the tracking loop threshold (given by the solid horizontal line above 0.25 radians). However, when T is increased to a point beyond the tracking threshold, the simulations fail to provide a clearly defined cutoff between tracking and loss of lock.

Rather, the frequency of cycle slips increases until the system is effectively no longer tracking (the sudden increases in the RMS error near the tracking threshold are the result of uncorrected cycle slips in the data).

In Figure 3.2-4, the mean time between cycle slips obtained from simulations is plotted as a function of T and B_n for a second order loop with $p = 2.5$. The solid line marked with a 200 represents an average of 200 seconds between cycle slips. The other solid line represents an average of 10 seconds between cycle slips. Also shown as a dotted line is the threshold based on the linear loop model from Figure 3.2-2 (the upper curve). These results suggest that the linear model threshold is quite conservative and represents a situation in which the loop is suffering from frequent cycle slips rather than a complete loss of lock.

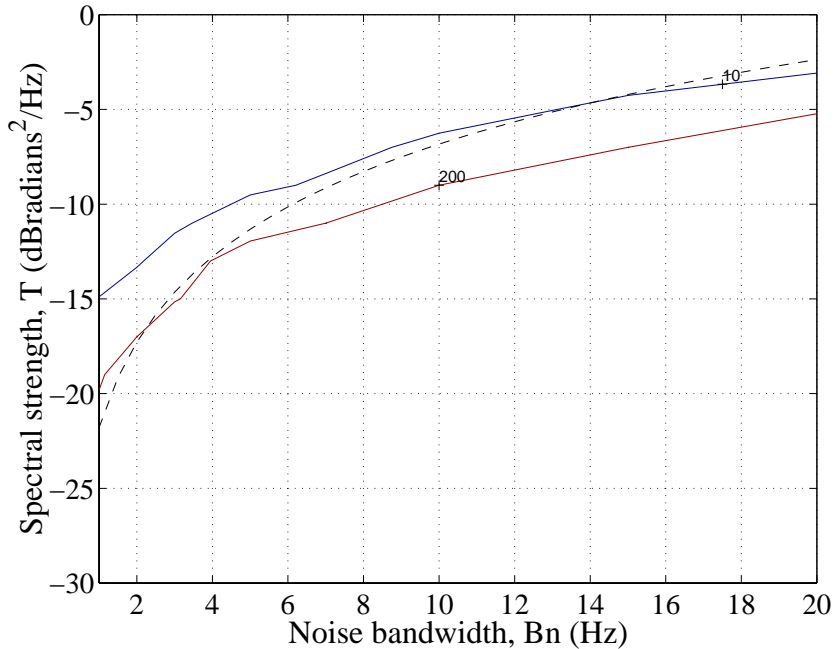


Figure 3.2-4: Mean time between cycle slips (in seconds) for a second order Costas phase locked loop in the presence of phase scintillations with $p = 2.5$, $f_o = 0.05\text{Hz}$, $C/N_o = 41.5\text{dBHz}$ and $T=20\text{ms}$. The dashed curve represents the theoretical threshold from Figure 3.2-2 (upper curve).

Finally, it is clear from Figure 3.2-3 that the accuracy of Equation (3.2-8) is reduced as the loop noise bandwidth increases. This is primarily a result of pre-detection filtering and will be discussed further in the next section.

3.2.2. The effects of pre-detection filtering on phase errors

In the analysis so far, it has been assumed that the pre-detection filters have a negligible effect on the phase errors. This assumption is based on the observation that the majority of the energy in the phase error power spectrum is within the 50Hz noise bandwidth¹⁰ of the pre-detection filters. However, for wide bandwidth receivers it unclear whether this approximation is valid. In the analysis that follows, the transfer function of the tracking loop is modified to include the effects of the pre-detection filtering. The results of this analysis are then compared with the simulations obtained from the previous section over a range of loop bandwidths.

To account for the effects of filtering, Equation (3.1-2) can be modified as follows

$$\begin{aligned} I_p &= \tilde{A}d(t-\tau) \frac{1}{T} \int_{t-T}^t \cos(\phi_e(u)).du + n_{IP}, \\ Q_p &= \tilde{A}d(t-\tau) \frac{1}{T} \int_{t-T}^t \sin(\phi_e(u)).du + n_{QP} \end{aligned} \quad (3.2-11)$$

where I_p and Q_p are the prompt I and Q signals after the pre-detection filters. This result also assumes that the amplitude is approximately constant over the T second period of the pre-detection filters. As will be shown in Section 3.3, this is a reasonable approximation under most circumstances. If it is assumed that ϕ_e is small (ie. $\sin(\phi_e) \approx \phi_e$ and $\cos(\phi_e) \approx 1$)¹¹, then to a first approximation, I_p and Q_p can be simplified as follows

$$\begin{aligned} I_p &= \tilde{A}d(t-\tau) + n_{IP}, \\ Q_p &= \tilde{A}d(t-\tau) \frac{1}{T} \int_{t-T}^t \phi_e(u).du + n_{QP} \\ &= \tilde{A}d(t-\tau)[\phi_e(t) \otimes g(t)] + n_{QP} \end{aligned} \quad (3.2-12)$$

where $g(t) = \frac{1}{T} \text{rect}\left(\frac{t - T/2}{T}\right)$ is the impulse response of the pre-detection filters, and \otimes represents the convolution integral.

The output of the I.Q discriminator is then

¹⁰ The double-sided noise bandwidth of a T second integrate and dump filter is $1/T$ Hz (= 50Hz for $T = 20\text{ms}$).

¹¹ These approximations are based on the first terms in the Taylor series expansions of $\sin(\)$ and $\cos(\)$.

$$I_p.Q_p = \tilde{A}^2[\phi_e(t) \otimes g(t)] + n_d \quad (3.2-13)$$

If the transfer function of the pre-detection filters is denoted by $G(f)$, the cascade of the pre-detection filters and the loop filter can be approximated by $G(f)F(f)$. The closed loop transfer function is therefore

$$H(f) = \frac{G(f).F(f)}{j2\pi f + G(f).F(f)} \quad (3.2-14)$$

and the transfer function of the phase errors is given by

$$1 - H(f) = \frac{j2\pi f}{j2\pi f + G(f).F(f)} \quad (3.2-15)$$

where $G(f) = \text{sinc}(fT)\exp(-j\pi fT)$ (Holmes, [43] pp. 423)¹². This new transfer function can be substituted into the expression for the phase error variance to account for the effects of pre-detection filtering. For a second order Costas loop, this gives

$$\begin{aligned} \sigma_{\phi_e}^2 &= \int_{-\infty}^{\infty} |1 - H(f)|^2 S_{\phi_p}(f) df + \sigma_{\phi_T}^2 \\ &\approx T \int_{-\infty}^{\infty} |1 - H(f)|^2 |f|^{-p} df + \sigma_{\phi_T}^2 \end{aligned} \quad (3.2-16)$$

where

$$|1 - H(f)|^2 = \frac{f_N^4}{\text{sinc}(fT)^2 [1 + 2f_N^2] - 2f_N^2 \text{sinc}(fT) [\cos(\pi fT) + \sqrt{2}f_N \sin(\pi fT)] + f_N^4} \quad (3.2-17)$$

and $f_N = f/f_n$. In Figure 3.2-5, the RMS phase scintillation error obtained from this modified transfer function is plotted as a function of T for a range of loop noise bandwidths. Also shown are the simulation results from Figure 3.2-3. It is clear from this figure that the simulations now match the theory much more closely, particularly for the wider loop bandwidths.

¹² $G(f)$ consists of two factors, (i) a $\text{sinc}(fT)$ attenuation factor, and (ii) an $\exp(-j\pi fT)$ phase shift factor associated with the filter delay. Of the two, the phase shift factor has by far the greatest impact on ϕ_e .

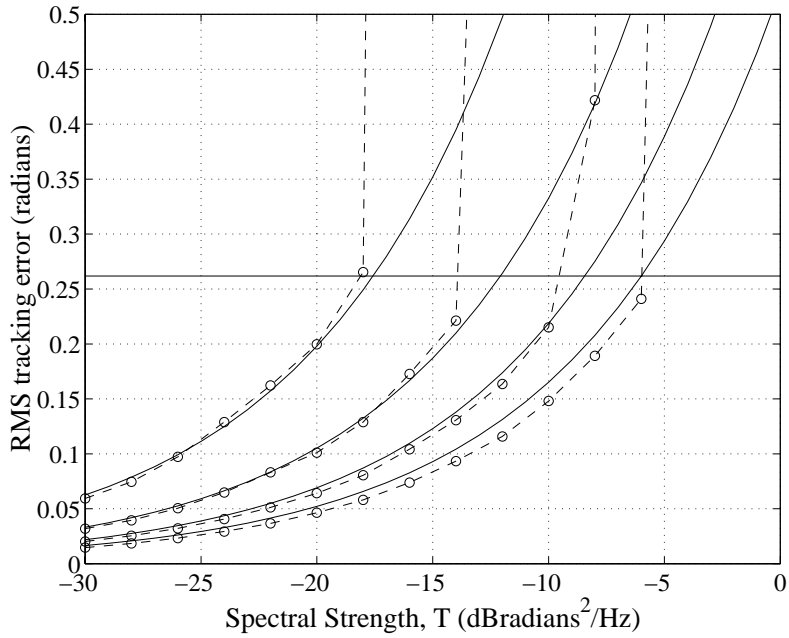


Figure 3.2-5: The effects of pre-detection filtering on the RMS phase scintillation error for a second order Costas loop with $p = 2.5$, $f_o = 0.05\text{Hz}$, $T = 20\text{ms}$ and no thermal noise. The five different lines represent 2Hz, 5Hz, 10Hz and 20Hz loop noise bandwidths respectively (upper to lower curves). The dashed lines represent the results of simulations from the previous section.

3.2.3. Carrier phase range errors

Another quantity of interest in the study of GPS receiver performance is the error in the estimate of range obtained from the carrier phase, $\phi_{er}(t) = \phi_d(t) - \hat{\phi}(t)$ (referred to here as the carrier phase range error). The carrier phase range error reflects the second function of the carrier phase tracking loop which is to provide estimates of the satellite and receiver dynamics (represented by $\phi_d(t)$) while rejecting unwanted phase noise from other sources. Consequently, $\phi_{er}(t)$ represents the error in the loop's estimate of $\phi_d(t)$ and is of interest to systems that make use of carrier phase range measurements such as carrier phase DGPS, or require precise velocity information. The mean-square value of the carrier phase range error is given by

$$E\{\phi_{er}^2\} = \int_{-\infty}^{\infty} [|1 - H(f)|^2 S_{\phi_d}(f) + |H(f)|^2 [S_{\phi_p}(f) + S_{\phi_o}(f) + S_{n'_d}(f)]] df. \quad (3.2-18)$$

The contribution to the carrier phase range error from phase scintillations is simply the carrier loop's estimate of the phase scintillation process, $\phi_p(t)$. This is given by

$\hat{\phi}_p(t) = h(t) \otimes \phi_p(t)$, where $h(t)$ is the impulse response of the loop filter and \otimes is the convolution integral. The variance of $\hat{\phi}_p(t)$ is therefore

$$\sigma_{\hat{\phi}_p}^2 = \int_{-\infty}^{\infty} |H(f)|^2 S_{\phi_p}(f) df. \quad (3.2-19)$$

By making the following substitutions

$$S_{\phi_p}(f) = \frac{T}{(f_o^2 + f^2)^{p/2}}, \text{ from Equation (2.1-1), and}$$

$$|H(f)|^2 = \frac{f_n^{2k}}{f^{2k} + f_n^{2k}} [1 + 2(k-1)(f/f_n)^{2(k-1)}], \text{ from Table 3.1-2}$$

the variance of the carrier phase range error resulting from phase scintillations becomes

$$\sigma_{\hat{\phi}_p}^2 = \int_{-\infty}^{\infty} \frac{f_n^{2k}}{(f^{2k} + f_n^{2k})} [1 + 2(k-1)(f/f_n)^{2(k-1)}] \times \frac{T}{(f_o^2 + f^2)^{p/2}} df. \quad (3.2-20)$$

A closed form solution to this integral is again difficult to obtain. However, as the carrier tracking loop is essentially a low pass filter for the carrier phase, the low frequency components of the phase scintillation power spectrum will provide the greatest contribution to $\sigma_{\hat{\phi}_p}^2$. Therefore, the outer scale size parameter, f_o , will have a significant effect on $\sigma_{\hat{\phi}_p}^2$ and must be carefully modelled in order to produce accurate results (ie. it cannot be set to zero as before). In Figure 3.2-6, $\sigma_{\hat{\phi}_p}^2$ is plotted as a function of the loop noise bandwidth for a second order Costas phase locked loop and for three values of f_o (this is based on a numerical solution to Equation (3.2-20)). It is clear from these plots that $\sigma_{\hat{\phi}_p}^2$ is very sensitive to f_o , but relatively insensitive to the noise bandwidth. This is because the majority of the energy in the phase scintillation power spectrum is well below the lowest noise bandwidth for typical values of f_o and p . The slightly higher values at very low noise bandwidth's are the result of a hump in the transfer function of the second order loop near $f = f_n$.

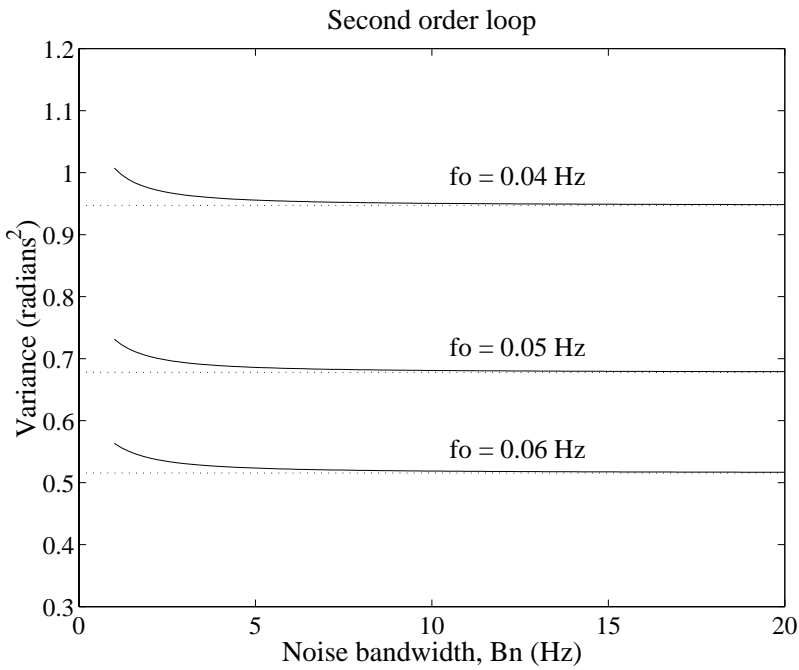


Figure 3.2-6: The variance of the carrier phase range error, $\sigma_{\phi_p}^2$, as a function of the loop noise bandwidth for a second order Costas phase locked loop in the presence of phase scintillations. $p = 2.5$, $T = -25$ dB radians²/Hz, and $f_o = 0.05$ Hz.

These results suggest that a reasonable approximation for $\sigma_{\phi_p}^2$ can be obtained by ignoring the loop transfer function. This implies that for all sensible values of the loop noise bandwidth, the majority of the phase scintillation energy is tracked by the carrier loop. Equation (3.2-20) can therefore be approximated by

$$\sigma_{\phi_p}^2 \approx \int_{-\infty}^{\infty} \frac{T}{(f_o^2 + f^2)^{p/2}} df. \quad (3.2-21)$$

From a table of integrals (eg Gradshteyn [37], Equation 3.241-4), this can be reduced to

$$\sigma_{\phi_p}^2 = \frac{T\sqrt{\pi}\Gamma((p-1)/2)f_o^{1-p}}{\Gamma(p/2)}. \quad (3.2-22)$$

The results obtained from this approximation are given in Figure 3.2-6 as a series of horizontal dotted lines. It is clear from these plots that the error in this approximation is quite small for B_n greater than a few Hertz.

The carrier phase range error is generally only of concern to users who require precise carrier phase range measurements for carrier phase DGPS. For such applications, the

distance over which the phase errors become decorrelated is of interest. This is discussed further in Section 3.6.

3.2.4. Doppler errors

Carrier Doppler measurements are used for the precise determination of velocity in GPS. The error introduced into these measurements by phase scintillations is given by

$$\omega_{ep}(t) = \frac{d\hat{\phi}_p(t)}{dt} \quad \text{radians/s} \quad (3.2-23)$$

where $\hat{\phi}_p(t)$ is the carrier loop's estimate of the phase scintillation process. The variance of the Doppler error is thus

$$\begin{aligned} \sigma_{\omega_{ep}}^2 &= \int_{-\infty}^{\infty} S_{\omega_{ep}}(f) df \\ &= \int_{-\infty}^{\infty} (2\pi f)^2 S_{\hat{\phi}_p}(f) df \\ &= \int_{-\infty}^{\infty} (2\pi f)^2 |H(f)|^2 S_{\phi_p}(f) df \quad (\text{radians/s})^2 \end{aligned} \quad (3.2-24)$$

where $S_{\omega_{ep}}(f)$ and $S_{\hat{\phi}_p}(f)$ are the power spectral densities of the Doppler errors and the phase estimate errors from phase scintillations respectively. It is clear from this equation that the Doppler errors are a filtered version of the phase scintillations, where the filter transfer function is given by $j2\pi f H(f)$. As this is a high pass filter (at least for second and third order carrier loops), the approximation $S_{\phi_p}(f) = T|f|^{-p}$ can once again be used to obtain the following expression (based on Equation (3.2-20))

$$\sigma_{\omega_{ep}}^2 \approx \int_{-\infty}^{\infty} (2\pi f)^2 \frac{f_n^{2k}}{(f^{2k} + f_n^{2k})} \left[1 + 2(k-1)(f/f_n)^{2(k-1)} \right] \times T|f|^{-p} df, \quad k > 1 \quad (3.2-25)$$

This can be solved using a table of integrals (eg. Spiegel [86], Equation 15.20) to give the following result

$$\sigma_{\omega_{ep}}^2 \approx \frac{4T\pi^3 f_n^{3-p}}{k} \left[\frac{1}{\sin([3-p]\pi/2k)} + \frac{2(k-1)}{\sin([p-1]\pi/2k)} \right], \quad 1 < p < 3 \quad (3.2-26)$$

In Figure 3.2-7, $\sigma_{\omega_{ep}}^2$ is plotted as a function of the loop noise bandwidth, B_n , for $p=2.5$ and $T=-25$ dBadians 2 /Hz.

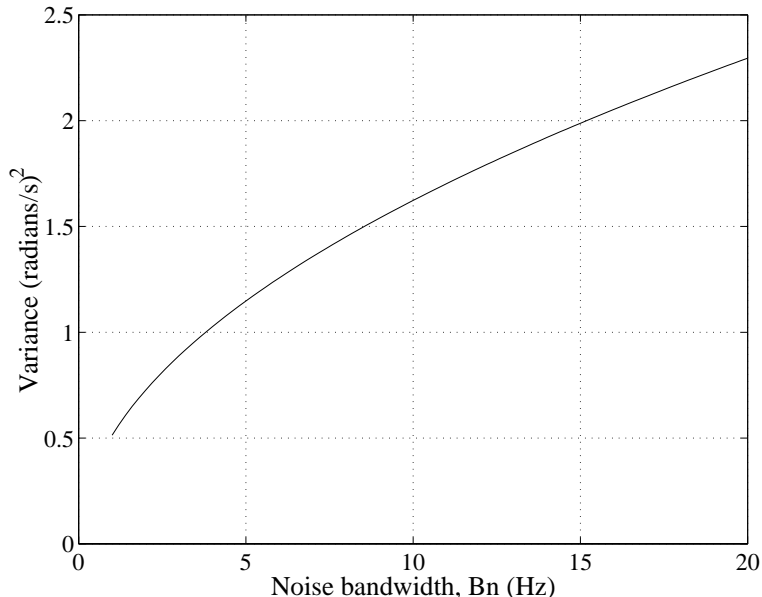


Figure 3.2-7: Variance of the Doppler error as a function of the loop noise bandwidth for a second order Costas phase locked loop in the presence of phase scintillations. $p = 2.5$, $T = -25$ dBadians 2 /Hz.

It is clear from this figure that as the loop noise bandwidth increases, the Doppler errors increase, unlike the phase estimate errors which remain approximately constant. This is because a wider bandwidth receiver will allow more of the high frequency components of the phase scintillation energy to be present on the carrier loop phase estimates (high frequency phase fluctuations contribute more to the Doppler errors than low frequency fluctuations). The results given in Figure 3.2-7 can be converted into equivalent velocity errors by multiplying by the factor $(c/\omega_T)^2$, where c is the speed of light and ω_T is the angular frequency of the GPS carrier (either $2\pi*L1$, or $2\pi*L2$). For the spectral strength value specified in Figure 3.2-7, the variance of the velocity errors is only of the order of a few tens of (cm/s) 2 which is probably negligible for all but a few precision applications.

3.2.5. Summary

In this section, the effects of phase scintillations on a Costas carrier tracking loop was examined. An expression was derived for the variance of the carrier phase tracking error in terms of the bandwidth and order of the tracking loop and the spectral strength and

spectral index of phase scintillations. By assigning a tracking threshold to this expression, the conditions under which a Costas loop would be expected to lose carrier lock were determined. In general, it was found that the susceptibility of a carrier loop to phase scintillations increased as the loop bandwidth decreased. Also, the effects of phase scintillations became worse as the spectral strength and the spectral index increased (ie. as the amount of high frequency phase scintillation energy increased).

Expressions were also obtained for the variance of the phase range errors. Essentially, these are errors in the carrier loop's estimate of the satellite-to-receiver range and are mainly of interest for carrier phase differential GPS. It was found that phase range errors are predominantly affected by the ionospheric outer scale size as well as the spectral strength and spectral index of phase scintillations, but show very little dependence on the loop bandwidth. The outer scale size parameter is a function of the large scale structure of the ionosphere. As this is not accurately modelled by WBMOD, nor by any of the other scintillation models known to the author, the evaluation of the phase range error was considered to be beyond the scope of this thesis.

3.3. The impact of amplitude scintillations on carrier phase tracking loops

In the previous section, the linear loop model was used to obtain a simple closed form expression for the variance of the carrier phase tracking error for a Costas loop in the presence of phase scintillations and thermal noise. This expression was then compared with the linear model threshold derived in Appendix C to determine the strength of phase scintillation activity required to force the Costas loop to lose lock. An assumption inherent in this analysis was that the carrier to noise density ratio of the GPS signal was relatively large, implying that the GPS signal was unaffected by amplitude scintillations. In this section, the effects of amplitude scintillations on the carrier phase errors will be examined using both the linear loop model and a non-linear approach. Variance measures will be derived as a function of the amplitude scintillation index, S_4 , and the loop noise bandwidth for an I.Q Costas loop. However, as these measures tend to be a poor indicator of loss-of-lock, an alternative approach will be used in the next section to determine suitable tracking thresholds for the Costas loop when both amplitude and phase scintillations are present together.

A complicating factor associated with the analysis of amplitude scintillations is that, if large enough, they have the capacity to significantly alter the transfer function of the tracking loop. This causes the effects of amplitude and phase scintillations to be coupled so that the two must be considered together when deriving a single variance measure. Unfortunately, this requires a knowledge of the joint statistics of amplitude and phase which, at this stage, is unknown for scintillations (refer to the end of Section 2.1.3). This problem can be circumvented to some extent by assuming that the discriminator is normalised (eg. Q/I or $\text{Atan}(Q/I)$), or that a post-detection AGC is present (for $I.Q$ or $\text{sign}(I)Q$ discriminators). In doing so, the effects of amplitude scintillations are translated to the thermal noise term allowing the two effects to be dealt with separately (phase scintillations and thermal noise are associated with entirely different physical processes and are therefore independent). In the analysis that follows, the effects of different AGC time constants will also be examined.

3.3.1. Background

As shown by Weber [100], if the bandwidth of the amplitude is relatively small compared to the loop noise bandwidth, the PDF of the phase errors for a first order phase locked loop is given by the Tikhonov density function. For the first order Costas phase locked loop, this is (Equation (C-6) and [43])

$$f_\vartheta(\varphi) = \frac{\exp(\rho_e \cos(2\varphi))}{\pi I_o(\rho_e)}, \quad |\varphi| \leq \frac{\pi}{2} \quad (3.3-1)$$

where $\vartheta = [\phi_e \bmod \pi]$ is the phase error reduced modulo π , ρ_e is the effective loop signal to noise ratio (SNR), and I_o is the modified Bessel function of the first kind of order zero. Although an equivalent expression has not yet been found for higher order loops, Lindsey and Charles [59] have verified experimentally that the distribution of phase errors for a second order loop is very close to the Tikhonov density function. As shown by Viterbi [97], Lindsey and Charles [59] and Holmes [43] (for the Costas loop), a good approximation to the effective loop SNR is the reciprocal of the variance obtained from the linear model, *viz*

$$\rho_e = \frac{1}{4\sigma_{\phi_e}^2} \quad (3.3-2)$$

where, from Equation (3.2-5)

$$\begin{aligned} \sigma_{\phi_e}^2 &= \int_{-\infty}^{\infty} [1 - H(f)^2 S_{\phi_p}(f) + |H(f)|^2 S_{n_d}(f)] df \\ &= \sigma_{\phi_{ep}}^2 + \sigma_{\phi_T}^2 \end{aligned} \quad (3.3-3)$$

and $\sigma_{\phi_{ep}}^2$ and $\sigma_{\phi_T}^2$ are the contributions to the tracking error variance from phase scintillations and thermal noise respectively (other phase noise sources have been ignored). For reasonably slow amplitude fluctuations, the transfer function of the tracking loop, $H(f)$, will be a function of the signal amplitude, \tilde{A} , and the post detection AGC gain factor, g (which is also a function of \tilde{A}). If \tilde{A} and g are assumed to vary slowly with time, then over a time period, τ , for which \tilde{A} and g are approximately constant, the I.Q Costas loop can be characterised by the following expression (see Figure 3.1-3)

$$\begin{aligned}\Phi_{\varepsilon\tau}(f) &= \Phi_\tau(f) - \hat{\Phi}_\tau(f) \\ &= \Phi_\tau(f) - [\tilde{A}^2 \Phi_{\varepsilon\tau}(f) + N_{d\tau}(f)] \frac{F(f)}{j2\pi f \cdot g}\end{aligned}\quad (3.3-4)$$

where $\Phi_\tau(f)$, $\hat{\Phi}_\tau(f)$, $\Phi_{\varepsilon\tau}(f)$ and $N_{d\tau}(f)$ are the Fourier Transforms of the random processes $\phi(t)$, $\hat{\phi}(t)$, $\phi_\varepsilon(t)$ and $n_d(t)$ which have been truncated to zero outside of the time interval 0 to τ seconds. Rearranging this expression gives

$$\Phi_{\varepsilon\tau}(f) = \frac{j2\pi f}{j2\pi f + (\tilde{A}^2/g)F(f)} \cdot \Phi_\tau(f) - \frac{(\tilde{A}^2/g)F(f)}{j2\pi f + (\tilde{A}^2/g)F(f)} \cdot \frac{N_{d\tau}(f)}{\tilde{A}^2} \quad (3.3-5)$$

If it is assumed that $E\{\Phi_\tau(f)N_{d\tau}(f)^*\} = 0$ (as $n_d(t)$ is both zero-mean and independent of $\phi(t)$), the expectation of the power spectral density of $\phi_\varepsilon(t)$ is given by

$$E\left\{\frac{1}{\tau}|\Phi_{\varepsilon\tau}(f)|^2\right\} = \left|1 - H'(f, \tilde{A})\right|^2 E\left\{\frac{1}{\tau}|\Phi_\tau(f)|^2\right\} + \left|H'(f, \tilde{A})\right|^2 E\left\{\frac{1}{\tau}\left|\frac{N_{d\tau}(f)}{\tilde{A}^2}\right|^2\right\} \quad (3.3-6)$$

where $H'(f, \tilde{A}) = \frac{(\tilde{A}^2/g)F(f)}{j2\pi f + (\tilde{A}^2/g)F(f)}$ is the modified loop transfer function. In the limit as $\tau \rightarrow \infty$, this becomes

$$S_{\phi_\varepsilon}(f, \tilde{A}) = \left|1 - H'(f, \tilde{A})\right|^2 S_\phi(f) + \left|H'(f, \tilde{A})\right|^2 \frac{S_{n_d}(f)}{\tilde{A}^4} \quad (3.3-7)$$

Consequently, as a function of the signal amplitude, the phase error variance based on the linear model is given by

$$\begin{aligned}\sigma_{\phi_\varepsilon}^2(\tilde{A}) &= \int_{-\infty}^{\infty} S_{\phi_\varepsilon}(f, \tilde{A}) df \\ &= \int_{-\infty}^{\infty} \left[\left|1 - H'(f, \tilde{A})\right|^2 S_{\phi_p}(f) + \left|H'(f, \tilde{A})\right|^2 \frac{S_{n_d}(f)}{\tilde{A}^4} \right] df \\ &= \sigma_{\phi_{ep}}^2(\tilde{A}) + \sigma_{\phi_T}^2(\tilde{A})\end{aligned}\quad (3.3-8)$$

This expression is useful for determining both an average phase error variance and a “rule of thumb” tracking threshold and will be discussed further in the next section.

3.3.2. Phase errors from the linear model

3.3.2.1. Amplitude scintillations only

If, for the moment, the effects of phase scintillations are ignored, the linear model variance becomes (from Equation (3.3-8))

$$\sigma_{\phi_T}^2(\tilde{A}) = \int_{-\infty}^{\infty} |H'(f, \tilde{A})|^2 \frac{S_{n_d}(f)}{\tilde{A}^4} df \quad (3.3-9)$$

This represents the contribution to both the tracking error variance and the variance of the phase range errors from amplitude scintillations and thermal noise. Equation (D-14) from Appendix D can be used to reduce the above expression to

$$\begin{aligned} \sigma_{\phi_T}^2(\tilde{A}) &= 2TB_n(\tilde{A}) \frac{\sigma_{n_d}^2(\tilde{A})}{\tilde{A}^4} \\ &= 2TB_n(\tilde{A}) \sigma_{n'_d}^2(\tilde{A}) \end{aligned} \quad (3.3-10)$$

where $B_n(\tilde{A})$ is the single-sided noise equivalent bandwidth of the tracking loop as a function of the amplitude, $n'_d = n_d/\tilde{A}^2$, and T is the integration period of the pre-detection filters. Again, based on Equation (D-18) from Appendix D, the discriminator noise variance $\sigma_{n'_d}^2(\tilde{A})$ can be expanded to give (for an I.Q Costas loop)

$$\begin{aligned} \sigma_{\phi_T}^2(\tilde{A}) &= 2TB_n(\tilde{A}) \times \frac{N_o}{T\tilde{A}^2} \left[1 + \frac{N_o}{T\tilde{A}^2} \right] \\ &= \frac{B_n(\tilde{A})}{C/N_o} \left[\frac{1}{\tilde{A}_N^2} + \frac{1}{2TC/N_o \tilde{A}_N^4} \right] \end{aligned} \quad (3.3-11)$$

where $C/N_o = \mathbf{A}^2/2N_o$, \mathbf{A} is the nominal (unperturbed) signal amplitude, and $\tilde{A}_N = \tilde{A}/\mathbf{A}$ is a normalised signal amplitude. The single-sided noise bandwidth is given by

$$\begin{aligned} B_n(\tilde{A}) &= \frac{1}{2} \int_{-\infty}^{\infty} |H'(f, \tilde{A})|^2 df \\ &= \frac{1}{2} \int_{-\infty}^{\infty} \left| \frac{(\tilde{A}^2/g)F(f)}{j2\pi f + (\tilde{A}^2/g)F(f)} \right|^2 df \\ &= \frac{1}{2} \int_{-\infty}^{\infty} \left| \frac{(\tilde{A}_N^2/g_N)F(f)}{j2\pi f + (\tilde{A}_N^2/g_N)F(f)} \right|^2 df \end{aligned} \quad (3.3-12)$$

where $g_N = g/\mathbf{A}^2$ is a normalised AGC gain factor. For first and second order loops, the noise equivalent bandwidths become (from Table 3.1-2)

1. First order:

$$B_n(\tilde{A}) = \left(\frac{\tilde{A}_N^2}{g_N} \right) \frac{\omega_n}{4} = \left(\frac{\tilde{A}_N^2}{g_N} \right) \bar{B}_n, \text{ where } \bar{B}_n \text{ is the design loop noise bandwidth.}$$

2. Second order:

$$B_n(\tilde{A}) = \frac{\omega_n}{2} \left[\left(\frac{\tilde{A}_N^2}{g_N} \right) \zeta + \frac{1}{4\zeta} \right], \text{ where } \zeta \text{ is the damping factor.}$$

To be consistent with the non-linear analysis that will be presented in the next section, only first order loops will be considered. Substituting the above expression for $B_n(\tilde{A})$ for a first order loop into Equation (3.3-11) gives

$$\sigma_{\phi_T}^2(\tilde{A}) = \frac{\bar{B}_n}{C/N_o} \left[\frac{1}{g_N} + \frac{1}{2TC/N_o \tilde{A}_N^2 g_N} \right] \quad (3.3-13)$$

For the I.Q Costas loop, the AGC gain factor will be of the form

$$\begin{aligned} g &= \frac{1}{k} \sum_{i=1}^k [I_{Pi}^2 + Q_{Pi}^2] \\ &= \frac{1}{k} \sum_{i=1}^k [\tilde{A}_i^2 + 2\tilde{A}_i d(t_i - \tau) (n_{IPi} \cos(\phi_e) + n_{QPi} \sin(\phi_e)) + n_{IPi}^2 + n_{QPi}^2] \\ &= \frac{1}{k} \sum_{i=1}^k \tilde{A}_i^2 + \varepsilon_g \end{aligned} \quad (3.3-14)$$

where I_{Pi} and Q_{Pi} are given by Equation (3.1-2), and ε_g is the error in the AGC gain. The k samples in Equation (3.3-14) represent the outputs from the pre-detection filters over the previous kT seconds. Three different models are considered for the AGC. These are:

1. An ideal AGC for which $g = \tilde{A}^2$. This assumes that $k=1$ and $\varepsilon_g = 0$.
2. A fast AGC for which $g = \tilde{A}^2 + E\{\varepsilon_g\}$. In this case, k is assumed to be small enough to allow the AGC to accurately track the signal amplitude, but large enough to average the effects of thermal noise.
3. A very slow (or non-existent) AGC for which $g = \mathbf{A}^2 + E\{\varepsilon_g\}$.

From Equation (3.3-14), the expectation of the error in the AGC gain factor is given by

$$\begin{aligned}
E\{\epsilon_g\} &= E\left\{\frac{1}{k} \sum_{i=1}^k [2\tilde{A}_i d(t_i - \tau)(n_{IPi} \cos(\phi_e) + n_{QPi} \sin(\phi_e)) + n_{IPi}^2 + n_{QPi}^2]\right\} \\
&= \frac{1}{k} \sum_{i=1}^k [E\{n_{IPi}^2\} + E\{n_{QPi}^2\}] \\
&= \frac{2N_o}{T} \quad (\text{from Equation (D-7), Appendix D})
\end{aligned} \tag{3.3-15}$$

Consequently, after normalising, the three AGC gain factors become

1. Ideal: $g_N = \tilde{A}_N^2$.
2. Fast: $g_N = \tilde{A}_N^2 + \frac{1}{TC/N_o}$
3. Slow: $g_N = 1 + \frac{1}{TC/N_o}$

$$\text{where } \frac{E\{\epsilon_g\}}{\mathbf{A}^2} = \frac{1}{TC/N_o}.$$

We now substitute the above expressions for g_N into Equation (3.3-13) to derive expressions for the contributions to the tracking error variance from thermal noise and amplitude scintillations.

Case 1: Ideal AGC

For the ideal AGC model, Equation (3.3-13) becomes

$$\sigma_{\phi_T}^2(\tilde{A}_N) = \frac{\bar{B}_n}{C/N_o} \left[\frac{1}{\tilde{A}_N^2} + \frac{1}{2TC/N_o \tilde{A}_N^4} \right] \tag{3.3-17}$$

and the average phase error variance is given by

$$\begin{aligned}
\sigma_{\phi_T}^2 &= \int_0^\infty \sigma_{\phi_T}^2(A_N) f_{\tilde{A}_N}(A_N) dA_N \\
&= \frac{\bar{B}_n}{C/N_o} \left[E\left\{\frac{1}{\tilde{A}_N^2}\right\} + \frac{1}{2TC/N_o} E\left\{\frac{1}{\tilde{A}_N^4}\right\} \right], \quad \text{radians}^2
\end{aligned} \tag{3.3-18}$$

where $f_{\tilde{A}_N}(A_N)$ is the PDF of the normalised signal amplitude \tilde{A}_N . For slow amplitude fluctuations, $f_{\tilde{A}_N}(A_N)$ is assumed to follow the Nakagami-m distribution with $\langle \tilde{A}_N^2 \rangle = 1$.

The two expectation terms in Equation (3.3-18) can be simplified as follows

$$\begin{aligned} E\left\{\frac{1}{\tilde{A}_N^2}\right\} &= \int_0^\infty \frac{1}{A_N^2} f_{\tilde{A}_N}(A_N) dA_N \\ &= \int_0^\infty \frac{1}{A_N^2} \cdot \frac{2m^m A_N^{2m-1}}{\Gamma(m)} \exp(-mA_N^2) dA_N \\ &= \frac{2m^m}{\Gamma(m)} \int_0^\infty A_N^{2m-3} \exp(-mA_N^2) dA_N \end{aligned} \quad (3.3-19)$$

From a table of integrals (eg. Spiegel [86], Equation 15.77), this becomes

$$\begin{aligned} E\left\{\frac{1}{\tilde{A}_N^2}\right\} &= \frac{2m^m}{\Gamma(m)} \left(\frac{\Gamma(m-1)}{2m^{m-1}} \right) \quad m > 1 \\ &= \frac{m}{m-1} \\ &= \frac{1}{1-S_4^2}, \quad S_4 < 1 \end{aligned} \quad (3.3-20)$$

Also,

$$\begin{aligned} E\left\{\frac{1}{\tilde{A}_N^4}\right\} &= \int_0^\infty \frac{1}{A_N^4} f_{\tilde{A}_N}(A_N) dA_N \\ &= \frac{m^2}{m^2 - 3m + 2}, \quad m > 2 \\ &= \frac{1}{1-3S_4^2+2S_4^4}, \quad S_4 < 1/\sqrt{2} \end{aligned} \quad (3.3-21)$$

Therefore, for an ideal AGC the phase error variance can be expressed as

$$\sigma_{\phi_T}^2 = \frac{B_n}{C/N_o} \left[\frac{1}{(1-S_4^2)} + \frac{1}{2TC/N_o(1-3S_4^2+2S_4^4)} \right], \quad \text{radians}^2 \quad (3.3-22)$$

This expression is only valid for $S_4 < 1/\sqrt{2}$. For $S_4 = 1/\sqrt{2}$ it becomes infinite and for $S_4 > 1/\sqrt{2}$ it becomes negative implying that the loop is likely to lose lock (at least for this AGC model). In Figure 3.3-1, the phase error variance is plotted as a function of S_4 for $C/N_o = 44$ dBHz (typical of a strong satellite signal), and $C/N_o = 30$ dBHz (a very weak

satellite signal). It is clear from these plots that as S_4 approaches $1/\sqrt{2}$, the phase error variance increases very rapidly. Indeed, the rather conservative tracking threshold of $(\pi/12)^2$ radians² derived in Appendix C is only surpassed when S_4 is larger than about 0.7, even for the weak signal case. $S_4 > 0.7$ represents quite strong scintillation activity, and would only be expected to occur in equatorial regions during the evening hours and under solar maximum conditions. Consequently, at other times and locations, the effects of amplitude scintillations on the carrier phase errors is likely to be negligible.

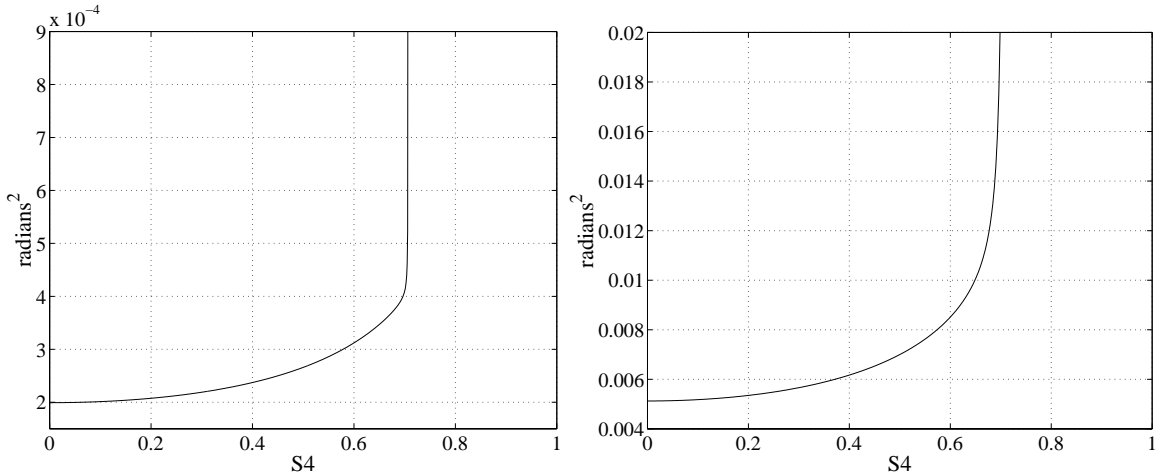


Figure 3.3-1: Phase error variance as a function of S_4 for a first order I.Q Costas loop with an ideal AGC. Parameter values are $T = 20\text{ms}$, $B_n = 5\text{Hz}$, $C/N_o = 44 \text{ dBHz}$ (left panel), and $C/N_o = 30 \text{ dBHz}$ (right panel).

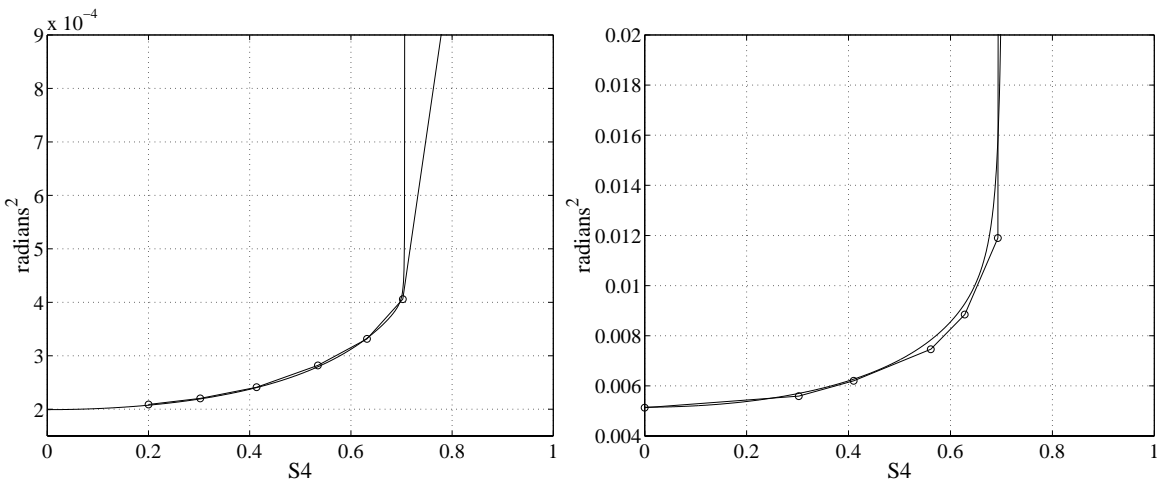


Figure 3.3-2: Phase error variance as a function of S_4 from simulations for a first order I.Q Costas loop with an ideal AGC (the circles denote simulation results). The unmarked curve represents the theoretical results from Equation (3.3-22). Parameter values are $T = 20\text{ms}$, $B_n = 5\text{Hz}$, $C/N_o = 44 \text{ dBHz}$ (left panel), and $C/N_o = 30 \text{ dBHz}$ (right panel).

In order to verify Equation (3.3-22), a number of simulations were conducted using simulated amplitude scintillation data and the tracking loop simulator from Appendix B with an ideal AGC (ie. $g = \tilde{A}^2$). In Figure 3.3-2, phase error variance values obtained from simulations are plotted against S_4 for the two values of C/N_o used in Figure 3.3-1¹. It is clear from these plots that the simulations are in good agreement with the theory, particularly for values of S_4 less than $1/\sqrt{2}$. For larger values of S_4 , the occurrence of frequent cycle slips complicates the process of estimating the variance. Nevertheless, the simulation results do confirm that amplitude scintillations are of little concern unless S_4 exceeds $1/\sqrt{2}$.

Case 2: Fast AGC

For the fast AGC model, the phase error variance of a first order Costas phase locked loop is given by (from Equations (3.3-13) and (3.3-16))

$$\sigma_{\phi_T}^2(\tilde{A}_N) = \frac{\bar{B}_n}{C/N_o} \left[\frac{1}{[\tilde{A}_N^2 + 1/[TC/N_o]]} + \frac{1}{2TC/N_o \tilde{A}_N^2 [\tilde{A}_N^2 + 1/[TC/N_o]]} \right] \quad (3.3-23)$$

Again, the Nakagami-m PDF can be used to find the average phase error variance as follows

$$\begin{aligned} \sigma_{\phi_T}^2 &= \int_0^\infty \sigma_{\phi_T}^2(A_N) f_{\tilde{A}_N}(A_N) dA_N \\ &= \frac{\bar{B}_n}{C/N_o} \left[E\left\{ \frac{1}{[\tilde{A}_N^2 + 1/[TC/N_o]]} \right\} + \frac{1}{2TC/N_o} E\left\{ \frac{1}{\tilde{A}_N^2 [\tilde{A}_N^2 + 1/[TC/N_o]]} \right\} \right], \quad \text{radians} \end{aligned} \quad (3.3-24)$$

where

$$E\left\{ \frac{1}{[\tilde{A}_N^2 + 1/[TC/N_o]]} \right\} = \int_0^\infty \frac{1}{[A_N^2 + 1/[TC/N_o]]} f_{\tilde{A}_N}(A_N) dA_N = X_1, \quad \text{and} \quad (3.3-25)$$

$$E\left\{ \frac{1}{\tilde{A}_N^2 [\tilde{A}_N^2 + 1/[TC/N_o]]} \right\} = \int_0^\infty \frac{1}{A_N^2 [A_N^2 + 1/[TC/N_o]]} f_{\tilde{A}_N}(A_N) dA_N = X_2$$

¹ The simulation results are represented by the small circles in Figure 3.3-2.

If we let $I_N = A_N^2$, the first integral becomes

$$\begin{aligned} X_1 &= \int_0^\infty \frac{1}{[I_N + 1/(TC/N_o)]} \cdot f_{I_N}(I_N) dI_N \\ &= \frac{m^m}{\Gamma(m)} \int_0^\infty I_N^{m-1} \cdot \exp(-mI_N) dI_N \end{aligned} \quad (3.3-26)$$

From a table of integrals (Gradshteyn [37], Equation 3.383-10), we have

$$\int_0^\infty \frac{x^{\nu-1} \cdot \exp(-\mu x)}{x + \beta} dx = \beta^{\nu-1} \cdot \exp(\beta\mu) \cdot \Gamma(\nu) \cdot \Gamma(1-\nu, \beta\mu) \quad (3.3-27)$$

where $|\arg(\beta)| < \pi$, $\operatorname{Re}(\mu) > 0$, $\operatorname{Re}(\nu) > 0$ ² and $\Gamma(a, b) = \int_b^\infty \exp(-t) * t^{a-1} dt$ is the incomplete

gamma function. X_1 then becomes

$$X_1 = m^m (1/[TC/N_o])^{m-1} \cdot \exp(m/[TC/N_o]) \cdot \Gamma(1-m, m/[TC/N_o]) \quad (3.3-28)$$

and X_2 becomes

$$X_2 = \frac{m^m}{m-1} (1/[TC/N_o])^{m-2} \cdot \exp(m/[TC/N_o]) \cdot \Gamma(2-m, m/[TC/N_o]) \quad (3.3-29)$$

Substituting these two expressions back into Equation (3.3-24) gives

$$\sigma_{\phi T}^2 = \frac{\bar{B}_n \cdot m^m \exp(m/[TC/N_o])}{C/N_o (TC/N_o)^{m-1}} \left[\Gamma(1-m, m/[TC/N_o]) + \frac{\Gamma(2-m, m/[TC/N_o])}{2(m-1)} \right] \quad (3.3-30)$$

Equation (3.3-30) has been used to evaluate the phase error variance as a function of S_4 for $C/N_o = 44$ dBHz and $C/N_o = 30$ dBHz. This is shown in Figure 3.3-3 along with the results of a series of simulations based on an AGC with $k=10$ (the ideal AGC curves from Figure 3.3-1 are also included for comparison). The simulations show quite good agreement with the theory when S_4 is less than about 0.9, but tend to produce much smaller values when S_4 is very large. This is probably the result of a failure to account for the non-linear behaviour of the tracking loop in Equation (3.3-30). It was also observed in simulations that for large values of S_4 , cycle slips would only occur when the amplitude scintillation rate was significantly reduced. This is because the probability of a cycle slip

² For both X_1 and X_2 , these conditions are met for all values of m .

depends not only on the fade depth, but also on the fade duration (see Section 3.5). Consequently, when the amplitude scintillation rate is reduced, the fade durations increase and the probability of a cycle slip increases. This suggests that loss-of-lock may only occur when the amplitude scintillation rate is quite small, even when the strength of scintillation activity is very large.

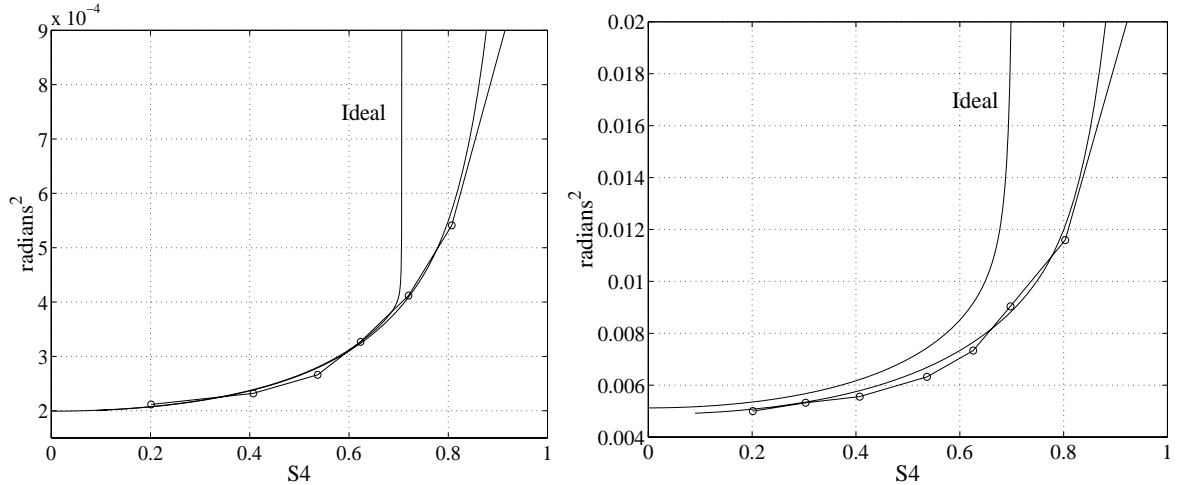


Figure 3.3-3: Phase error variance as a function of S_4 for a first order I.Q Costas loop with a fast AGC ($k=10$). Parameter values are $T = 20\text{ms}$, $B_n = 5\text{Hz}$, $C/N_o = 44 \text{ dBHz}$ (left panel), and $C/N_o = 30 \text{ dBHz}$ (right panel). The circles denote simulation results.

Case 3: Slow AGC

For a very slow (or non-existent) AGC, the AGC gain factor is a constant. The phase error variance is then (from Equations (3.3-13) and (3.3-16))

$$\sigma_{\phi_T}^2(\tilde{A}_N) = \frac{\bar{B}_n}{C/N_o} \left[\frac{1}{[1+1/[TC/N_o]]} + \frac{1}{2TC/N_o \tilde{A}_N^2 [1+1/[TC/N_o]]} \right] \quad (3.3-31)$$

and the average variance is given by

$$\begin{aligned} \sigma_{\phi_T}^2 &= \int_0^\infty \sigma_{\phi_T}^2(A_N) f_{\tilde{A}_N}(A_N) dA_N \\ &= \frac{\bar{B}_n}{C/N_o} \left[\frac{1}{[1+1/[TC/N_o]]} + \frac{1}{2TC/N_o [1+1/[TC/N_o]] (1 - S_4^2)} \right], \quad \text{radians}^2 \end{aligned} \quad (3.3-32)$$

Variance values obtained from Equation (3.3-32) are plotted in Figure 3.3-4 for $C/N_o = 44 \text{ dBHz}$ and $C/N_o = 30 \text{ dBHz}$ (the ideal AGC curves from Figure 3.3-1 have again been included for comparison). These plots suggest that in the absence of an input phase process, the phase error variance is only affected by amplitude scintillations when S_4 is

very close to 1. The simulations results, which have also been included in Figure 3.3-4, confirm this result.

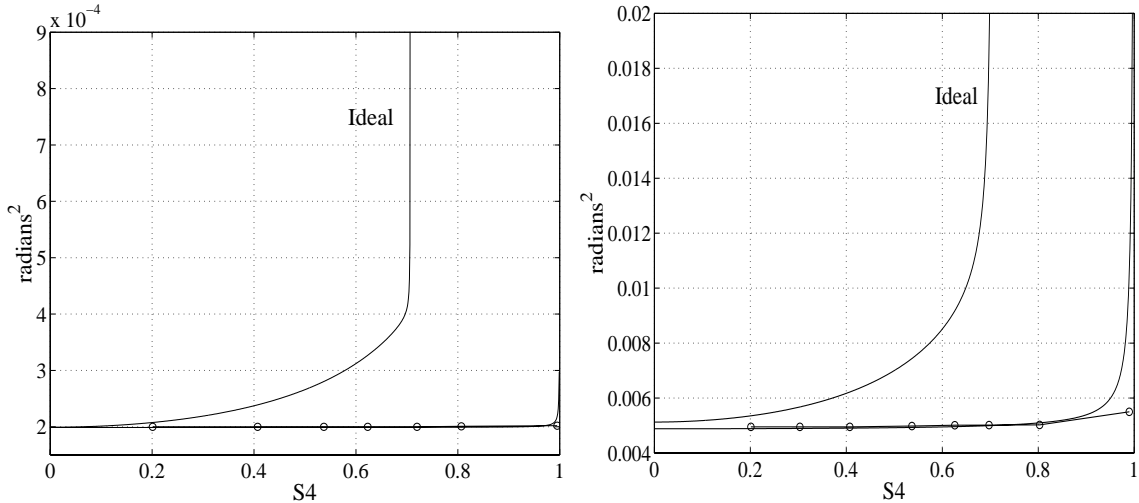


Figure 3.3-4: Phase error variance as a function of S_4 for a first order I.Q Costas loop with a slow AGC. Parameter values are $T = 20\text{ms}$, $B_n = 5\text{Hz}$, $C/N_o = 44 \text{ dBHz}$ (left panel), and $C/N_o = 30 \text{ dBHz}$ (right panel). The circles denote simulation results.

Although these results appear to suggest that a slow AGC is the best choice to overcome the effects of amplitude scintillations (compare Figure 3.3-3 with Figure 3.3-4), as will be shown in the next section, a slow AGC will also significantly increase the tracking errors associated with phase scintillations and dynamics. Consequently, in an overall system sense, a slow AGC may not necessarily perform any better than a fast AGC (a similar argument can be used when comparing non-ideal AGC models with the ideal AGC model).

It is clear from Equation (3.3-13) that when $\tilde{A}_N = 0$ (ie. in the absence of a signal), the phase error variance becomes infinite for all three AGC models. This occurs because a first order tracking loop becomes an integrator for the white noise process $n_d(t).\omega_n/g$

when the amplitude is zero (ie. the phase error will be given by $\phi_e(t) = \int_{-\infty}^t n_d(t).\omega_n/g dt$

(from Figure 3.1-3 with $\tilde{A} = 0$). Consequently, $\phi_e(t)$ will become a Random Walk process (non-stationary) with a mean of zero and a variance that is proportional to the time t (see for example Van Trees [96]). Therefore, on occasions when the amplitude approaches zero (this occurs more often when S_4 is very large), the phase error variance will increase with

time and without bound until loss-of-lock occurs. However, if the amplitude recovers before the loop reaches the point of losing lock, the feedback mechanism in the loop will be restored and the phase error variance will return to much lower levels. Clearly then, the duration of the deep amplitude fades will strongly influence both the phase error variance and the probability of a cycle slip. Consequently, for large values of S_4 , very slow amplitude scintillations are likely to produce a much larger average variance than faster scintillations, even when the bandwidths of the two scintillations are much less than the loop bandwidth. For this reason, the variance corresponding to $S_4 \approx 1$ was found to be highly dependent on the amplitude scintillation rate. The relationship between the duration of a deep amplitude fade and the probability of a cycle slip will be examined in more detail in Section 3.5 using a simple rectangular model for the fade profile.

3.3.2.2. Amplitude and phase scintillations

From Equation (3.3-8), the phase scintillation component of the phase error variance is given by

$$\sigma_{\phi_{ep}}^2(\tilde{A}) = \int_{-\infty}^{\infty} |1 - H'(f, \tilde{A})|^2 S_{\phi_p}(f) df \quad (3.3-33)$$

where $S_{\phi_p}(f) = \frac{T}{(f_o^2 + f^2)^{p/2}}$ (Equation (2.1-1)), and $1 - H'(f, \tilde{A}) = \frac{j2\pi f}{j2\pi f + (\tilde{A}_N^2/g_N)F(f)}$

(Equation (3.3-5)). Consequently, the open loop transfer function of the I.Q Costas loop, $F(f)$, is scaled by a factor $\alpha = \tilde{A}_N^2/g_N$. For an ideal AGC (ie. $g_N = \tilde{A}_N^2 \Rightarrow \alpha = 1$), $\sigma_{\phi_{ep}}^2(\tilde{A})$ ceases to be a function of the signal amplitude and the effects of amplitude and phase scintillations can be treated separately (ie. the results presented in Section 3.2 will apply without modification). For a non-ideal AGC ($\alpha \neq 1$), both the loop bandwidth and the damping factor will be influenced by the amplitude. From Table 3.1-2, it is clear that for a first order loop, both the loop natural frequency, ω_n , and the loop bandwidth, B_n , will be scaled by a factor α . For a second order loop, ω_n and the damping factor, ζ , will both be scaled by a factor $\sqrt{\alpha}$, while the bandwidth will become equal to $\frac{\omega_n}{2} \left[\alpha\zeta + \frac{1}{4\zeta} \right]$.

Consequently, if α is reduced by amplitude fading³, both the bandwidth and damping

³ For both of the non-ideal AGC models, a reduction in \tilde{A}_N will cause a reduction in α .

factors of the two loops will be reduced. This effect will be far more pronounced for a slow AGC for which α can become very small during periods of deep fading.

For a second order loop with a damping factor of $1/\sqrt{2}$, Equation (3.3-33) reduces to

$$\sigma_{\phi_{ep}}^2(\tilde{A}) = \int_{-\infty}^{\infty} \frac{f^4}{(\alpha f_n^2 - f^2)^2 + 2(\alpha f_n f)^2} \cdot \frac{T}{(f_o^2 + f^2)^{p/2}} df \quad (3.3-34)$$

This is plotted in Figure 3.3-5 as a function of the fading intensity, $20\log_{10}(\tilde{A}_N)$, for both the fast and slow AGC models. Also shown are a pair of horizontal dotted lines which represent the linear model tracking threshold given by Equation (3.2-9).

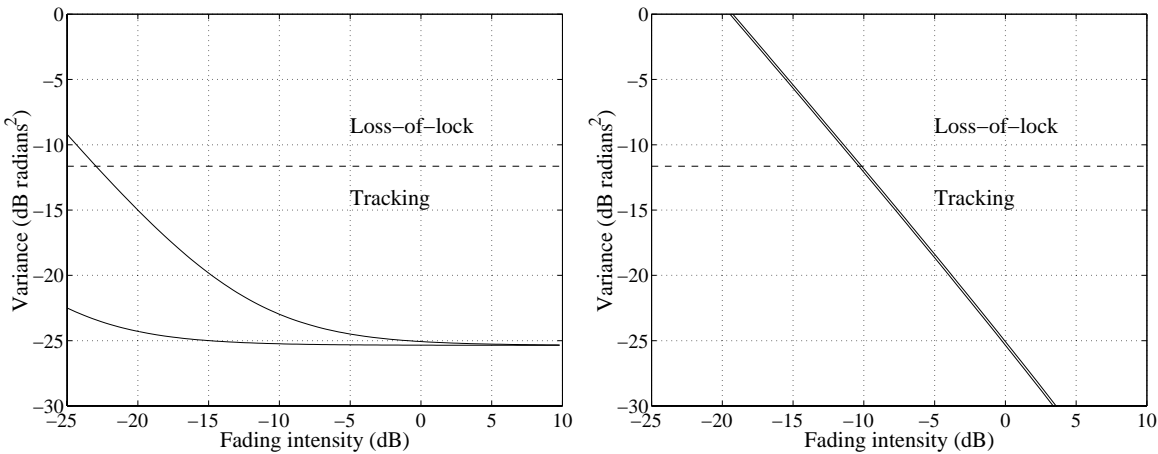


Figure 3.3-5: $\sigma_{\phi_{ep}}^2(\tilde{A})$ as a function of the fading intensity for a first order I.Q Costas loop with a fast AGC (left panel) and a slow AGC (right panel). Parameter values are $T = 20ms$, $B_n = 5Hz$, $C/N_o = 44 dBHz$ (lower curve), $C/N_o = 30 dBHz$ (upper curve), $T = -25 dBradians^2/Hz$, $p=2.5$, $f_o = 0 Hz$.

It is clear from this figure that when the AGC is unable to track the signal amplitude (the right panel), the phase errors produced by phase scintillations become very large. Essentially, the deep fades associated with large values of S_4 cause the instantaneous bandwidth of the tracking loop to become narrow, resulting in large phase tracking errors. A similar effect occurs for the fast AGC model when C/N_o is small (upper curve in the left panel). Note that the expected value of Equation (3.3-34) could have been found

by averaging $\sigma_{\phi_{ep}}^2(\tilde{A})$ using the Nakagami-m PDF (ie. $\bar{\sigma}_{\phi_{ep}}^2 = \int_0^{\infty} \sigma_{\phi_{ep}}^2(A) f_{\tilde{A}}(A) dA$).

However, as $\bar{\sigma}_{\phi_{ep}}^2$ provides no information about carrier phase range errors and very little information about the probability of losing lock, this was not done.

The results given in Figure 3.3-5 are based on the assumption that the amplitude and phase are independent of one another. In particular, they assume that the rate of change of phase (embodied in the parameter T) is independent of the amplitude. If this assumption is invalid, and the rate of change of phase tends to increase as the amplitude decreases, then the actual variance will be larger than is predicted by Equation (3.3-33)

(ie. Equation (3.3-33) may take on the form $\sigma_{\phi_{ep}}^2(\tilde{A}) = \int_{-\infty}^{\infty} |1 - H'(f, \tilde{A})|^2 S_{\phi_p}(f, \tilde{A}) df$ where

$S_{\phi_p}(f, \tilde{A}) = T(\tilde{A}) (f_o^2 + f^2)^{-p/2}$). An analysis of simulated scintillation data based on the model given in Appendix A suggests that the rate of change of phase is highly correlated with the fade depth. However, as this model is based on a greatly simplified view of the real world, these results should be treated with some caution. As yet, there have been no equivalent studies on real scintillation data to test the validity of this observation [33].

The phase range errors produced by phase scintillations, $\sigma_{\hat{\phi}_p}^2$ (see Equation (3.2-19)), will be affected in a similar way by amplitude scintillations. As a function of the signal amplitude, the variance of the phase range errors is given by

$$\sigma_{\hat{\phi}_p}^2(\tilde{A}) = \int_{-\infty}^{\infty} |H'(f, \tilde{A})|^2 S_{\phi_p}(f) df \quad (3.3-35)$$

and the average variance is

$$\sigma_{\hat{\phi}_p}^2 = \int_0^{\infty} \sigma_{\hat{\phi}_p}^2(A_N) f_{\tilde{A}_N}(A_N) dA_N \quad (3.3-36)$$

where $f_{\tilde{A}_N}(A_N)$ is the Nakagami-m PDF. As discussed at the beginning of Section 3.2.3, the variance of the phase range errors tends to be affected more by the outer scale size parameter, f_o , and less by the loop bandwidth. However, if deep fading results in very narrow loop bandwidth's, this situation may change, depending on the value of f_o . For a second order loop with a damping factor of $1/\sqrt{2}$, Equation (3.3-35) reduces to

$$\sigma_{\hat{\phi}_p}^2(\tilde{A}) = \int_{-\infty}^{\infty} \frac{2(f_n f)^2 + f_n^4}{(f_n^2 - f^2/\alpha)^2 + 2(f_n f)^2} \cdot \frac{T}{(f_o^2 + f^2)^{p/2}} df \quad (3.3-37)$$

The average variance for a second order loop, $\sigma_{\hat{\phi}_p}^2$, is plotted in Figure 3.3-6 for both the slow and fast AGC models (based on Equation's (3.3-36) and (3.3-37)). It is clear from this figure that the effects of amplitude scintillations on the phase range errors resulting from phase scintillations is quite small, even for the slow AGC model and for small values of C/N_o .

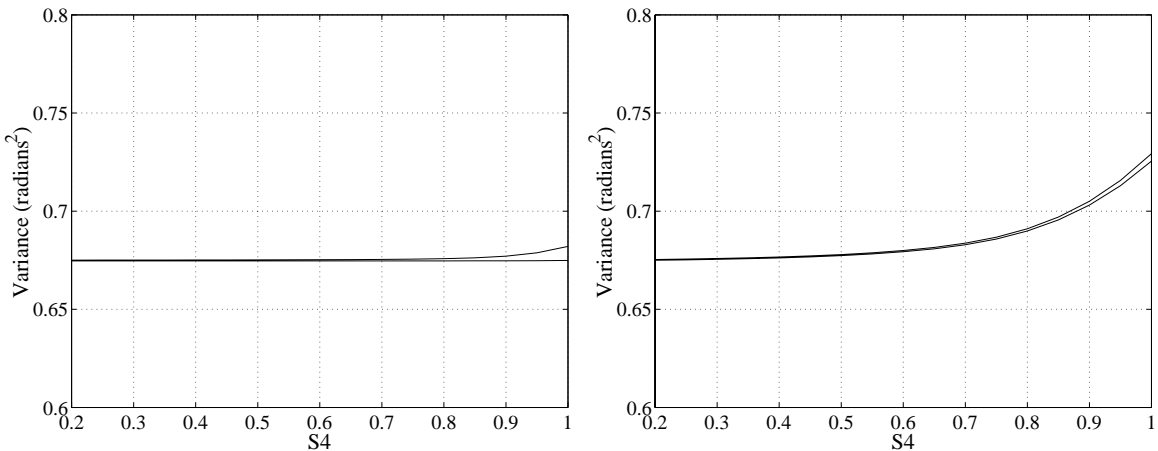


Figure 3.3-6: $\sigma_{\hat{\phi}_p}^2$ as a function of S_4 for a first order I.Q Costas loop with a fast AGC (left panel) and a very slow AGC (right panel). Parameter values are $T = 20ms$, $B_n = 5Hz$, $C/N_o = 44 dBHz$ (lower curves), $C/N_o = 30 dBHz$ (upper curves), $T = -25 dBradians^2/Hz$, $p = 2.5$, $f_o = 0.05 Hz$.

3.3.2.3. Amplitude scintillations and dynamics

The effects of a changing loop bandwidth are also observed when the loop is subject to dynamics, particularly when the order of the dynamics⁴ exceeds the order of the tracking loop resulting in errors that are not zero-mean. Again, at times when the signal amplitude is heavily attenuated by scintillations, the instantaneous loop bandwidth will be small and the loop will become unresponsive to dynamics. If it is assumed that the bandwidth of the amplitude scintillations is narrow enough for the phase errors to settle at their steady state values, then using Table E.1 (Appendix E) it is possible to determine the steady state error as a function of the amplitude. For a second order loop in the presence of a constant acceleration, the steady state tracking error is given by (from Table E.1)

⁴ 1st order: Phase step, 2nd Order: Constant velocity, 3rd Order: Constant acceleration.

$$\phi_{eSS} = \frac{2\pi}{\lambda} * \frac{a_o}{\bar{\omega}_n^2} \text{ radians} \quad (3.3-38)$$

where a_o is the acceleration in m/s². Under amplitude scintillation conditions, the loop natural frequency becomes a function of the signal amplitude. For a second order loop this is given by (based on Equation (3.3-12))

$$\begin{aligned} \omega_n(\tilde{A}_N) &= \sqrt{\alpha \bar{\omega}_n} \\ &= \left(\frac{\tilde{A}_N}{\sqrt{g_N}} \right) \bar{\omega}_n \end{aligned} \quad (3.3-39)$$

where $\bar{\omega}_n$ is the nominal loop natural frequency. The steady state phase error is thus

$$\phi_{eSS}(\tilde{A}_N) = \frac{2\pi}{\lambda} * \frac{a_o}{\bar{\omega}_n^2} \left(\frac{g_N}{\tilde{A}_N^2} \right) \text{ radians} \quad (3.3-40)$$

An equivalent expression for a first order loop in the presence of a constant velocity, v_o , is

$$\phi_{eSS}(\tilde{A}_N) = \frac{2\pi}{\lambda} * \frac{v_o}{\bar{\omega}_n} \left(\frac{g_N}{\tilde{A}_N^2} \right) \text{ radians} \quad (3.3-41)$$

Consequently, the steady state errors for the first and second order loops are scaled by the same factor, $1/\alpha$. The biases represented by Equation's (3.3-40) and (3.3-41) affect the tracking thresholds for the phase error variance. From Equation (C-3) (Appendix C), a new tracking threshold can be obtained based on the steady state error, *viz*

$$\sigma_{\phi_e}^2 |_{Th} (\tilde{A}_N) = \frac{1}{9} \left[\frac{\pi}{4} - \phi_{eSS}(\tilde{A}_N) \right]^2 \text{ radians}^2 \quad (3.3-42)$$

Therefore, in the presence of dynamics, amplitude fading may result in both an increase in $\sigma_{\phi_e}^2$ and a decrease in the threshold, $\sigma_{\phi_e}^2 |_{Th}$. Together, these two effects will result in an increase in the probability of losing lock.

3.3.2.4. Additional comments

For an ideal AGC, or for a fast AGC for which C/N_o is large and S_4 is less than $1/\sqrt{2}$, the effects of amplitude scintillations are decoupled from the loop transfer function and from the effects of phase scintillations. As the AGC normalised noise term, n'_d , is zero-mean and uncorrelated between successive T second epochs, the phase error variance resulting

from thermal noise is given by (from Equation (D-14))

$$\sigma_{\phi_T}^2 = 2TB_n \sigma_{n'_d}^2$$

where (from Equation (D-28))

$$\sigma_{n'_d}^2 = \frac{1}{2TC/N_o} \left[E \left\{ \frac{\tilde{A}_N^2}{g_N^2} \right\} + \frac{1}{2TC/N_o} E \left\{ \frac{1}{g_N^2} \right\} \right]$$

If we assume that $g_N \approx \tilde{A}_N^2$ and \tilde{A}_N is Nakagami-m distributed, this becomes

$$\begin{aligned} \sigma_{n'_d}^2 &= \frac{1}{2TC/N_o} \left[E \left\{ \frac{1}{\tilde{A}_N^2} \right\} + \frac{1}{2TC/N_o} E \left\{ \frac{1}{\tilde{A}_N^4} \right\} \right] \\ &= \frac{1}{2TC/N_o} \left[\frac{1}{1-S_4^2} + \frac{1}{2TC/N_o (1-3S_4^2+2S_4^4)} \right]. \end{aligned}$$

The phase error variance is thus

$$\sigma_{\phi_T}^2 = \frac{B_n}{C/N_o} \left[\frac{1}{(1-S_4^2)} + \frac{1}{2TC/N_o (1-3S_4^2+2S_4^4)} \right]$$

which is the same as Equation (3.3-22). However, this result has been obtained without assuming that the bandwidth of the amplitude scintillations is narrow in relation to the loop noise bandwidth. It only requires that the amplitude bandwidth be narrower than the pre-detection filter bandwidth, $1/T$, that C/N_o is relatively large, and that S_4 is less than $1/\sqrt{2}$. As this result is based on Equation (D-14), it is also independent of the loop order.

3.3.3. Phase errors from the non-linear model

In the previous section, Equation (3.3-8) was used to determine an average phase error variance based on the linear loop model. In this section, the Tikhonov PDF for the reduced phase error (Equation (3.3-1)) will be used to determine an equivalent non-linear model variance.

Consider the following conditional form of the Tikhonov PDF

$$f_{\vartheta}(\varphi|\tilde{A}) = \frac{\exp(\rho_e(\tilde{A})\cos(2\varphi))}{\pi I_o(\rho_e(\tilde{A}))}, \quad |\varphi| \leq \frac{\pi}{2} \quad (3.3-43)$$

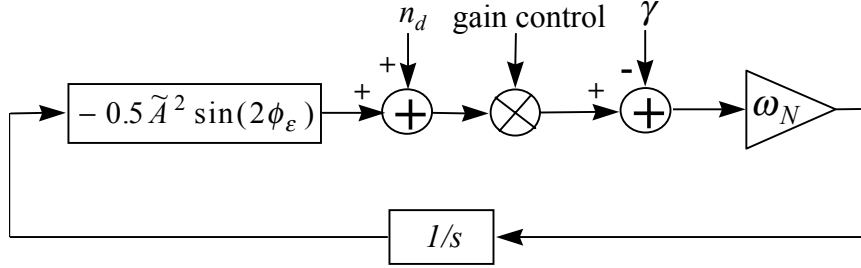
where $\rho_e(\tilde{A}) = \frac{1}{4\sigma_{\phi_e}^2(\tilde{A})}$ and $\sigma_{\phi_e}^2(\tilde{A})$ is given by Equation (3.3-8)⁵. The conditional

Tikhonov PDF can then be used to obtain an expression for the tracking error variance that is equivalent to Equation (3.3-8), but based on a non-linear model of the tracking loop, *viz*

$$\sigma_{\vartheta}^2(\tilde{A}) = \int_{-\pi/2}^{\pi/2} \varphi^2 f_{\vartheta}(\varphi|\tilde{A}) d\varphi \quad (3.3-44)$$

Although this non-linear approach provides a more accurate variance measure than the linear model, it does have a number of limitations. These are; i) the Tikhonov PDF strictly only applies to a first order phase locked loop (although Lindsey and Charles [59] have verified experimentally that the PDF of a second order loop is very similar), ii) it does not take into account the effects of satellite and receiver dynamics, and iii) the approximation of setting ρ_e equal to the reciprocal of the linear model variance (Equation (3.3-2)) is only accurate for reasonably high SNR's (Weber [100], Lindsey and Charles [59] and Viterbi [97]). This last restriction implies that the effects of phase scintillations can only be included if S_4 is assumed to be relatively small. However, as shown by Van Trees [96], if the loop is first order and the spectral index is equal to 2, the phase noise associated with scintillations can be considered to be equivalent to additional white thermal noise at the input. This is illustrated in Figure 3.3-7 where the input phase process, $\phi_p(t)$, associated with phase scintillations has been translated back through the VCO and loop filter to

produce a term $\gamma = \frac{1}{\omega_N} \frac{d\phi_p(t)}{dt}$ at the discriminator output.



⁵ This expression will also be used in Section 6 to determine the bit error rate in the navigation data in the presence of scintillations.

Figure 3.3-7: An equivalent non-linear model of a first order Costas phase locked loop with phase scintillations translated back through the VCO and loop filter to the discriminator output.

If it is assumed that $S_{\phi_p}(f) = T f^{-2}$ (ie. f_o is assumed to be small and $p = 2$), the power spectral density of γ is given by

$$\begin{aligned} S_\gamma(f) &= \frac{(2\pi f)^2}{\omega_N} S_{\phi_p}(f) \\ &= \frac{(2\pi)^2 T}{\omega_N} \end{aligned} \quad (3.3-45)$$

where $(2\pi)^2 T / \omega_N$ is a constant. Consequently, for a first order loop with $p = 2$, γ is white and can be treated as if it were produced by additive white thermal noise. Therefore, under these conditions it is quite reasonable to use the non-linear model to describe the phase errors, even when S_4 is quite large.

An average non-linear model variance can be found by applying the Nakagami-m PDF, $f_{\tilde{A}}(A)$, to the variance given by Equation (3.3-44). Thus

$$\sigma_\vartheta^2 = \int_0^\infty \sigma_\vartheta^2(A) f_{\tilde{A}}(A) dA \quad (3.3-46)$$

Theoretically, all of the linear model analysis given earlier (apart from the Doppler analysis) could be repeated using the equations given above in order to obtain equivalent non-linear model results. If only amplitude scintillations and thermal noise are considered, Equation (3.3-46) represents both the average tracking error variance and the average phase range variance from the non-linear model (ie. σ_ϑ^2 becomes the non-linear equivalent of $\sigma_{\phi_T}^2$ ⁶). In Figure 3.3-8, σ_ϑ^2 is compared with both $\sigma_{\phi_T}^2$ and the results of simulations for the fast AGC model (from Figure 3.3-3). It is clear from this figure that the two models give very similar results until S_4 is quite large, at which point the non-linear model variance begins to fall below the linear model variance.

⁶ This is used in Section 3.6 to account for the effects of amplitude scintillations and thermal noise on carrier phase DGPS systems.

Notice that because the Tikhonov PDF approaches a uniform distribution when the linear model phase error variance is very large (ie. $f_\vartheta(\varphi|\tilde{A}) = 1/\pi$, $|\varphi| \leq \frac{\pi}{2}$), the largest possible

value of σ_ϑ^2 that can be produced by this model is $\int_{-\pi/2}^{\pi/2} \varphi^2 / \pi \cdot d\varphi \approx 0.82 \text{ radians}^2$ ($\sim 7.5 \text{ cm}^2$)

at GPS L1). Consequently, even for very low values of C/N_o and for $S_4 = 1$, σ_ϑ^2 will never exceed this level (indeed, loss-of-lock is likely to occur well before this point).

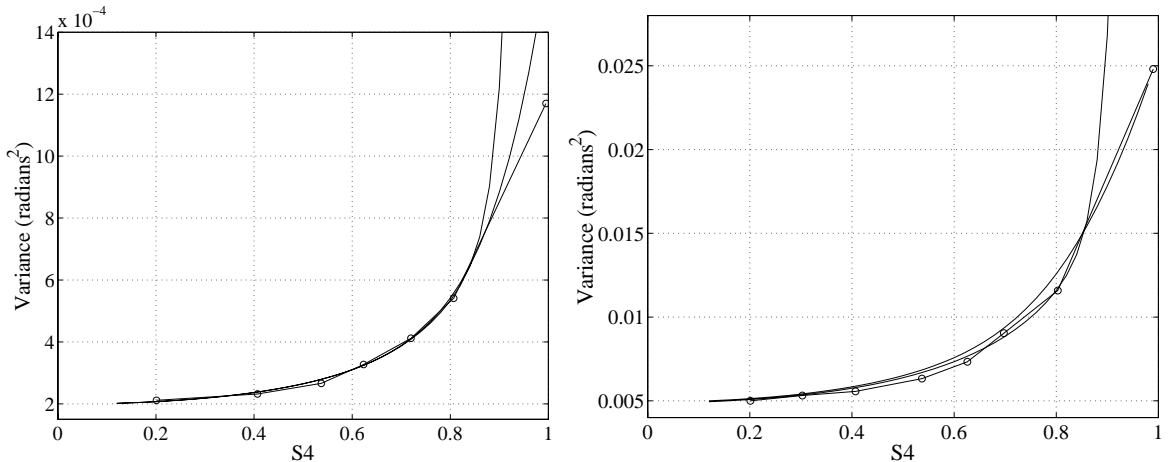


Figure 3.3-8: σ_ϑ^2 (lower curves) and $\sigma_{\phi_T}^2$ (upper curves) as a function of S_4 for a first order I.Q Costas loop with a fast AGC. Parameter values are $T = 20\text{ms}$, $B_n = 5\text{Hz}$, $C/N_o = 44 \text{ dBHz}$ (left panel), and $C/N_o = 30 \text{ dBHz}$ (right panel). The circles denote simulation results.

3.3.4. The effects of pre-detection filtering on phase errors

In Equation (3.1-2), the amplitude following the pre-detection filters is given by

$$\tilde{A} = \frac{1}{T} \int_{t-T}^t A(u) du \quad (3.3-47)$$

where A is the unfiltered signal amplitude. In general, it has been assumed that \tilde{A} is Nakagami-m distributed and approximately equal to A . This is based on the observation that the bandwidth of the pre-detection filters, $1/T$, is usually much greater than the bandwidth of the amplitude scintillations, which is typically less than a few hertz (see Appendix G). In this section, the validity of this assumption will be examined.

The power spectral density of the filtered signal amplitude, \tilde{A} , is given by

$$S_{\tilde{A}}(f) = |G(f)|^2 S_A(f) \quad (3.3-48)$$

where $G(f) = \text{sinc}(fT)\exp(-j\pi fT)$ is the transfer function of the pre-detection filters, and $S_A(f)$ is the power spectral density of the unfiltered signal amplitude. In Figure 3.3-9, both $S_A(f)$ and $S_{\tilde{A}}(f)$ are given for $f_c = 1\text{Hz}$ and $p=2.5$ ($S_A(f)=1$ is assumed for $f < f_c$). It is clear from this figure that the impact of the pre-detection filters on amplitude scintillations is insignificant for fluctuation frequencies less than about 10Hz. Consequently, for typical values of f_c (of the order of 1Hz or less), the impact of the pre-detection filters on the total amplitude variance is likely to be quite small (ie. very little scintillation energy lies above 10Hz for typical values of p and f_c). However, this may not be true under high velocity conditions when f_c may be quite large on certain satellite-receiver links.

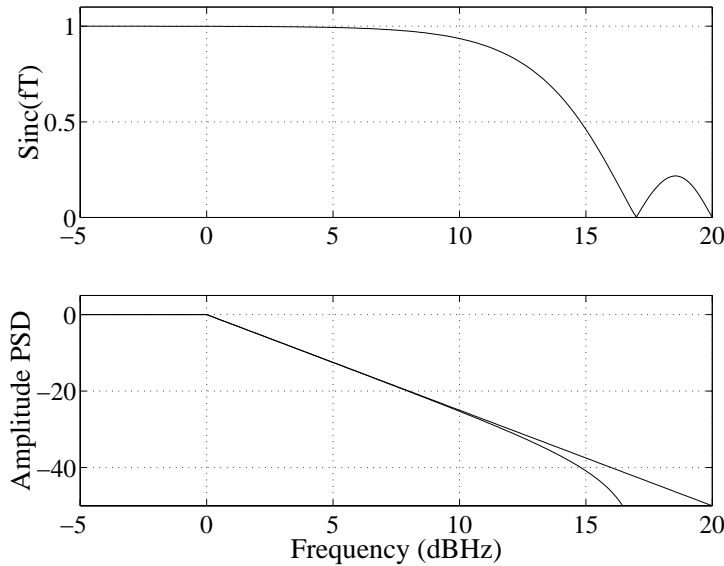


Figure 3.3-9: The impact of a 20ms pre-detection filter on the power spectral density of amplitude scintillations. The upper panel represents the magnitude of the filter transfer function. The lower panel represents the power spectral densities of amplitude for $p=2.5$ and $f_c = 1\text{Hz}$ (in the lower panel, the upper and lower curves represent the unfiltered and filtered amplitudes respectively).

Unfortunately, the power spectral density does not provide a complete picture of the effects of pre-detection filtering on the amplitude. Using simulated scintillation data obtained from the model described in Appendix A, it appears that the very deep fades that cause the greatest loop stress are often quite short in duration. Consequently, the pre-detection filters are likely to have a greater impact on deep amplitude fades than on

shallower fades. In Figure 3.3-10, a scatter plot of the fade depth after filtering versus the fade depth before filtering is given for a 40s segment of simulated scintillation data for which $f_c = 1\text{Hz}$, $p = 2.5$, and $S_4 \approx 0.75$. Also given are equivalent average plots for $f_c = 0.5\text{Hz}$, 1Hz and 2Hz based on approximately 20min of scintillation data. It is clear from these plots that on average, the pre-detection filters significantly attenuate the very deep fades. It is also clear that for larger values of f_c (and so shorter average fade durations), the effects of filtering become even more apparent. Indeed, it appears that the average fade depth after filtering tends to plateau at different fade depths depending on the value of f_c . Consequently, for very large values of f_c it is possible that pre-detection filtering on its own may significantly reduce the effects of amplitude scintillations within the tracking loop. However, as f_c is usually much less than about 1Hz for a stationary receiver (often considerably so – see Appendix G), this effect can probably be ignored for stationary receivers.

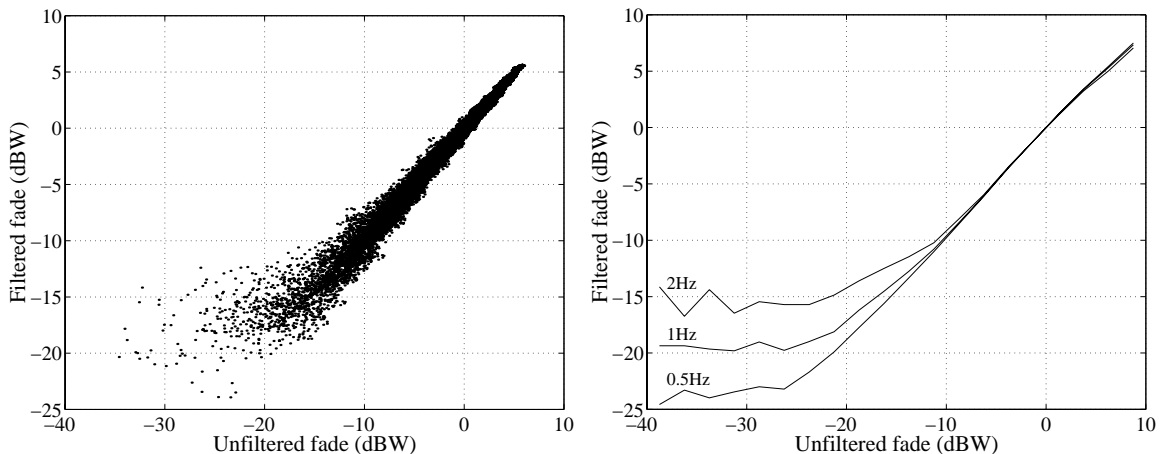


Figure 3.3-10: Scatter plot of the fade depth after filtering versus the fade depth before filtering for a 40s segment of simulated scintillation data with $f_c = 1\text{Hz}$, $p = 2.5$, and $S_4 \approx 0.75$ (left panel). Equivalent average plots for $f_c = 0.5\text{Hz}$, 1Hz and 2Hz based on approximately 20min of simulated scintillation data (right panel). Fade depths are shown relative to a normalised quiescent signal level of 0dBW.

3.3.5. Summary

In this section, the effects of amplitude scintillations on a Costas carrier tracking loop was examined. In order to approach this problem using analytical techniques, it was decided to assume that the discriminator algorithm was I.Q, normalised by a post-detection AGC.

As other discriminator types⁷ are not as amenable to direct analysis as the I.Q discriminator, a simulation approach would be required in order to assess their susceptibilities. This was considered to be beyond the scope of this thesis.

In Section 3.3.2, expressions were derived for the variance of the thermal noise errors for an I.Q Costas phase locked loop in the presence of amplitude scintillations. Three different AGC cases were considered; (i) an ideal AGC that provided a perfect estimate of the GPS signal strength, (ii) a fast AGC with a time constant much shorter than the duration of a typical amplitude fade, and (iii) a very slow AGC. It was shown that the effects of amplitude scintillations on the phase error variance is negligible, unless the amplitude scintillation index, S_4 , is very large. It was also shown that for non-ideal AGC's, the bandwidth of the tracking loop may fluctuate with the amplitude. If phase scintillations and Doppler errors are also present, this could result in a significant increase in carrier tracking errors (ie. phase scintillation errors may become larger during deep fades as a result of a momentary reduction in the loop bandwidth). Finally, it was observed that thermal noise errors, and therefore amplitude scintillation effects, increase with the loop bandwidth. This is the reverse of the situation observed for phase scintillations.

The analysis carried out in Section 3.3.2 was based on a linearised model of the Costas carrier loop. In Section 3.3.3, the thermal noise variance was re-calculated using the Tikhonov PDF, which is based on a non-linear model of a 1st order Costas loop. It was found that significant variations between the linear model (based on a fast AGC) and the non-linear model only occurred for very large values of S_4 . However, as shown in the next section, it is highly likely that loss-of-lock or frequent cycle slips will occur under these conditions anyway.

⁷ For example, the arctangent or decision-directed discriminators.

3.4. Carrier loop tracking thresholds

The principal objective of this section is to determine the strength of scintillation activity required to force the Costas loop to lose lock. However, as discussed in Appendix C, it is difficult, if not impossible, to precisely define a point at which a phase locked loop will transition to a state of loss-of-lock¹. Usually, a threshold is defined beyond which the linear model approximations are significantly violated. Although this does not guarantee that the loop will lose lock, it does suggest that the probability of frequent cycle slips and perhaps loss of lock will become very high.

In Section 3.3.3, it was shown that the average variance measures for the linear and non-linear loop models, σ_ϑ^2 and $\sigma_{\phi_e}^2$ respectively, diverged when S_4 was very large. Although this implies that the linear model approximations are being violated, it does not indicate how frequently this is occurring. For example, a very deep fade for a short duration may produce the same average linear model variance as a shallower fade for a longer duration (or a series of shallower fades for shorter durations). Consequently, a comparison between the average phase error variance measures is not considered to be a good measure of loss-of-lock.

In this section, the Nakagami-m PDF is used to determine the percentage of time that the amplitude falls below the tracking threshold for the linear loop model. This is then used as a basis for deciding whether loss-of-lock is likely to occur in the tracking loop. Inherent in this approach is the assumption that the bandwidth of the amplitude scintillations is narrow in relation to the carrier loop bandwidth. This ensures that fade durations below the tracking threshold are sufficiently long to produce carrier cycle slips and loss-of-lock (the impact of a reduced fade duration on loop behaviour is discussed in Section 3.5). The justification for this assumption is that for a power law PSD, the majority of the amplitude scintillation energy is near the cut-off frequency, f_c , which is typically much less than the loop bandwidth, B_n (see Appendix G). Although this condition is likely to be met for a stationary or slowly moving receiver, it is not guaranteed under high dynamic conditions. Under such conditions, the effects of amplitude scintillations may be

¹ Loss-of-lock is defined as the point at which the VCO frequency drifts away from the IF frequency and the phase errors (reduced modulo π) become uniformly distributed.

significantly suppressed on certain links, particularly for narrow bandwidth tracking loops (again, see Section 3.5 for more details).

From Equation (3.3-8), the variance of the phase tracking error resulting from scintillations and thermal noise is given by

$$\sigma_{\phi_e}^2(\tilde{A}) = \sigma_{\phi_{ep}}^2(\tilde{A}) + \sigma_{\phi_T}^2(\tilde{A})$$

where $\sigma_{\phi_{ep}}^2(\tilde{A})$ represents the contribution from phase scintillations (Equation (3.3-33)) and $\sigma_{\phi_T}^2(\tilde{A})$ represents the contribution from thermal noise (Equation (3.3-11)). By equating $\sigma_{\phi_e}^2(\tilde{A})$ with the linear model tracking threshold, $\sigma_{\phi_e}^2|_{T_h}$ (Equation (C-3), Appendix C), a threshold amplitude, \tilde{A}_{Th} , can be obtained below which the tracking loop would be expected to lose lock, *viz*

$$\sigma_{\phi_e}^2(\tilde{A}_{Th}) = \sigma_{\phi_e}^2|_{T_h} \quad (3.4-1)$$

Unfortunately, a closed form expression for \tilde{A}_{Th} is difficult to obtain for the non-ideal AGC models. However, for the ideal AGC model, $\sigma_{\phi_{ep}}^2(\tilde{A})$ ceases to be a function of the signal amplitude and is given by Equation (3.2-8). Consequently, the threshold variance for thermal noise only becomes $\sigma_{\phi_T}^2|_{T_h} = \sigma_{\phi_e}^2|_{T_h} - \sigma_{\phi_{ep}}^2$. By rearranging the standard expression for the variance of the phase tracking error for an I.Q Costas PLL (Equation (D-19), Appendix D), the signal amplitude corresponding to this new threshold can be obtained as follows

$$\tilde{A}_{Th} = A \sqrt{\frac{[1 + \sqrt{1 + \beta}]}{\beta T C/N_o}} \quad (3.4-2)$$

where $\beta = \frac{2\sigma_{\phi_T}^2|_{T_h}}{TB_n}$, A is the nominal (unperturbed) signal amplitude, and C/N_o is the nominal carrier to noise density ratio. In Figure 3.4-1, the normalised threshold amplitude, (\tilde{A}_{Th}/A) , is plotted as a function of the spectral strength, T , for both the ideal AGC model (solid line) and the non-ideal AGC model (dotted line). It is clear from these plots that the two models return approximately the same value of \tilde{A}_{Th}/A . It is also apparent that for the specified loop bandwidth (5Hz), the carrier loop will lose lock when

the spectral strength exceeds about -11 dBradians²/Hz, even in the absence of amplitude fading.

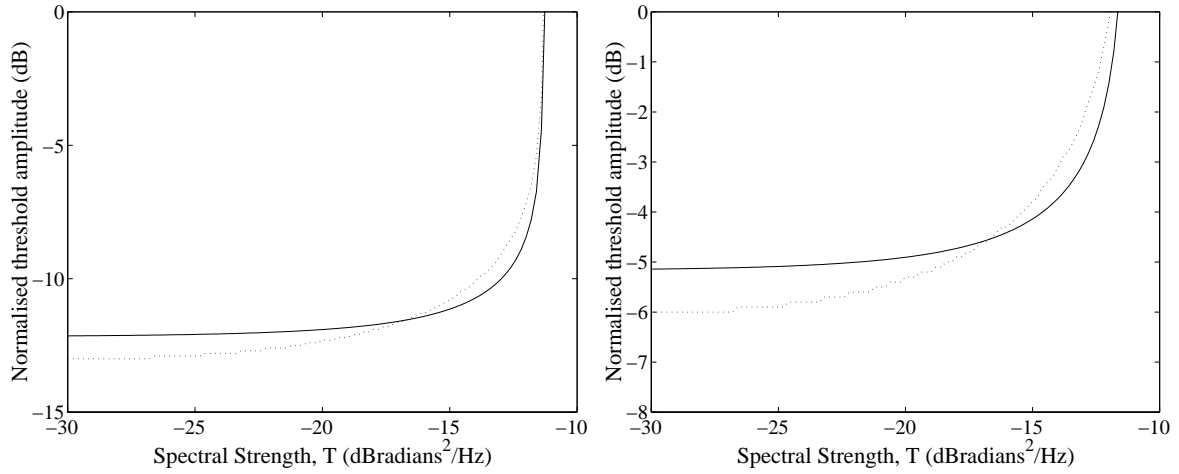


Figure 3.4-1: The normalised threshold amplitude, $\tilde{A}_{Th}/\mathbf{A}$, as a function of the phase scintillation spectral strength, T , for both the ideal AGC model (dotted line) and the fast AGC model (solid line). Parameter values are $T = 20ms$, $B_n = 5Hz$, $p = 2.5$, $f_o = 0.05Hz$, $C/N_o = 44 dBHz$ (left panel), and $C/N_o = 30 dBHz$ (right panel).

Using the Nakagamai-m PDF, the probability that the amplitude will drop below the threshold \tilde{A}_{Th} (thus resulting in cycle slips or loss-of-lock) can be found as follows

$$P_L = \int_0^{\tilde{A}_{Th}} f_{\tilde{A}}(\mathbf{A}) d\mathbf{A} \\ = \frac{2m^m}{\Gamma(m) \cdot \langle \tilde{A}^2 \rangle^m} \int_0^{\tilde{A}_{Th}} \mathbf{A}^{2m-1} e^{-m \cdot \mathbf{A}^2 / \langle \tilde{A}^2 \rangle} d\mathbf{A} \quad (3.4-3)$$

In Figure 3.4-2, the probability of losing carrier lock is plotted as a function of S_4 and B_n for $C/N_o = 41.5 dBHz$ under the assumption that phase scintillations are not present and the AGC is ideal (ie. $\sigma_{\phi_{ep}}^2 = 0$ is assumed). This figure clearly shows that the probability of losing lock in the presence of amplitude scintillations increases as the loop bandwidth increases. However, even for a very wide bandwidth receiver at $S_4=1$, this probability is still quite small for the specified nominal signal level. If the duration of the amplitude fading is relatively short, this may only result in an occasional cycle slip rather than a complete loss of signal lock. Indeed, for an inertially aided receiver for which the loop bandwidth is likely to be very narrow (less than a few Hertz), the effects of amplitude

scintillations may be negligible (particularly since an inertial aiding unit will usually assist the receiver to recover lock once the fading has passed).

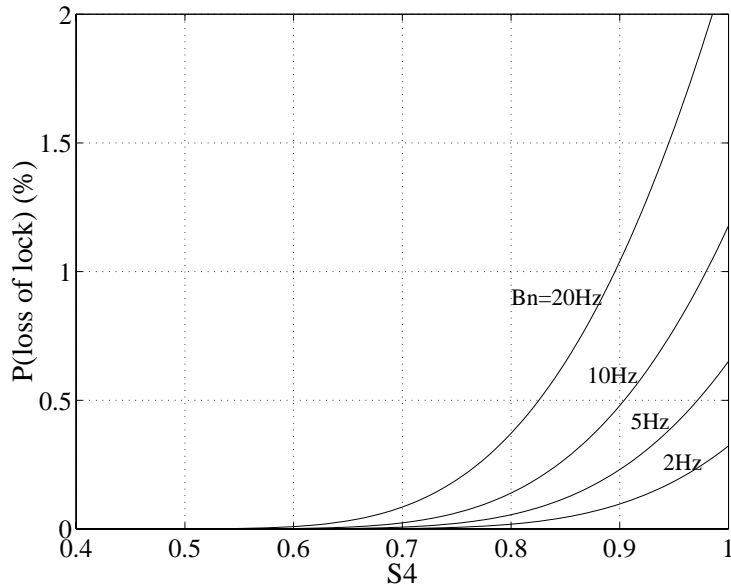


Figure 3.4-2: The probability of losing lock for a 2nd order Costas PLL as a function of S_4 and B_n .

Parameter values are $C/N_o = 41.5 \text{ dBHz}$ and $\sigma_{\phi_{ep}}^2 = 0$.

Although, Equation (3.4-3) does not provide a clearly defined threshold for S_4 above which loss of lock will occur, based on simulations it has been found that a threshold of 1% is quite a good choice, particularly for 2nd and 3rd order loops (for 1st order loops, the frequency of cycle slips merely increases with S_4 with no clearly defined threshold). Using this somewhat conservative threshold, it is still clear that amplitude scintillations alone are unlikely to significantly affect GPS receivers, unless the activity is very severe and the bandwidth of the tracking loop is quite wide. However, as will be shown later, this does not necessarily apply to codeless and semi-codeless receivers for which the SNR is significantly reduced.

In Figure 3.4-3, the tolerance of a receiver to scintillations is plotted as a function of T and S_4 using the approach outlined above. It is clear from this plot that as the loop bandwidth increases the tolerance to phase scintillation increases while the tolerance to amplitude scintillation decreases. Indeed, using Wiener filter analysis it is possible to find an optimum loop bandwidth and order that minimises the phase tracking error, and therefore the probability of losing lock, for any combination of T and S_4 (See Chapter 8).

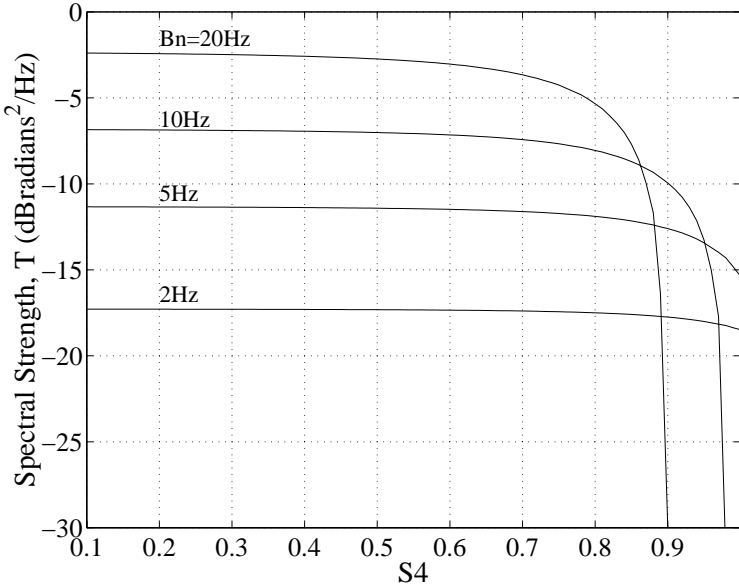


Figure 3.4-3: Tracking threshold as a function of T , S_4 , and B_n . Parameter values are $C/N_o = 41.5 \text{ dBHz}$ and $p = 2.5$.

Figure 3.4-3 is based on the underlying assumption that the spectral strength of phase scintillations, T , is independent of the amplitude, A (note that this does not imply that T is independent of S_4). With reference to Section 3.3.2.2, if T can be expressed as a function of A , then $\sigma_{\phi_{ep}}$ will become a function of A and the derivation of \tilde{A}_{Th} will become more complicated.

3.4.1. Optimum loop bandwidths

The optimum loop bandwidth for a minimum probability of losing lock is found by minimising Equation (3.4-3). As the amplitude PDF must always be positive, this can be achieved by minimising the threshold amplitude, \tilde{A}_{Th} , from Equation (3.4-2). The first derivative of \tilde{A}_{Th} with respect to B_n is given by

$$\frac{\partial \tilde{A}_{Th}}{\partial B_n} = \frac{A}{2\sqrt{\beta T C/N_o} [1+\sqrt{1+\beta}]} \left[\frac{1}{2\sqrt{1+\beta}} - \frac{[1+\sqrt{1+\beta}]}{\beta} \right] \frac{\partial \beta}{\partial B_n} \quad (3.4-4)$$

where β is a function of B_n . For the ideal AGC model, β can be expressed in the following form (from Equations (3.4-2) and (3.2-8))

$$\beta = \frac{2 \left[\sigma_{\phi_e}^2 |_{Th} - \alpha \mathbf{T} B_n^{(1-p)} \right]}{TB_n} \quad (3.4-5)$$

where $\alpha = \frac{\pi}{k \sin([p-1]\pi/2k)} \left(\frac{2\pi}{\xi} \right)^{p-1}$ and $\xi = \frac{\omega_n}{B_n}$ is a constant for a given loop order. The only real, non-trivial roots to Equation (3.4-4) are found by solving $\frac{\partial \beta}{\partial B_n} = 0$ to give

$$B_n|_{opt} = \left[\frac{p\alpha\mathbf{T}}{\sigma_{\phi_e}^2 |_{Th}} \right]^{\frac{1}{(p-1)}} \quad (3.4-6)$$

Equation (3.4-6) represents the bandwidth that minimises \tilde{A}_{Th} , and therefore the probability of losing lock, for a given phase scintillation spectral strength, \mathbf{T} . In Figure 3.4-4, the optimum bandwidth is plotted as a function of \mathbf{T} for a phase scintillation spectral index, p , of 2.5. The corresponding phase error variance due to phase scintillations is given by $\sigma_{\phi_{ep}}^2 = \frac{\sigma_{\phi_e}^2 |_{Th}}{p}$ which is very close to the threshold variance, $\sigma_{\phi_e}^2 |_{Th}$, particularly for p close to unity. This implies that the optimisation process attempts to keep the bandwidth as small as possible (and thus the phase scintillation error as large as possible) in order to minimise \tilde{A}_{Th} .

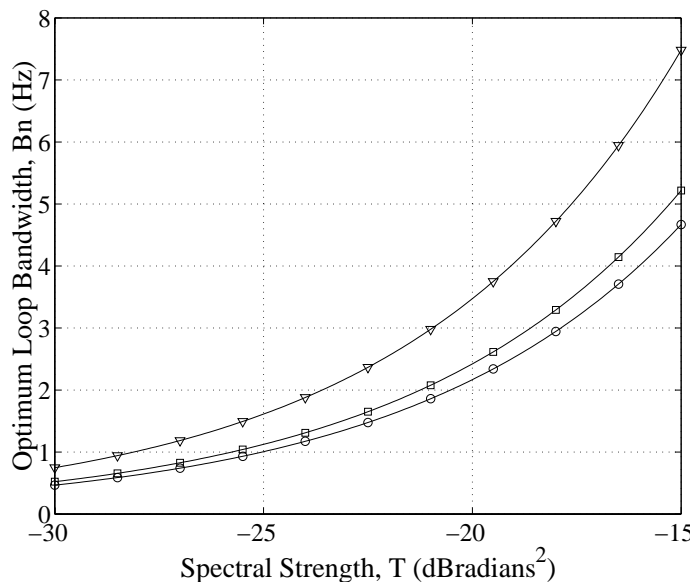


Figure 3.4-4: Threshold loop noise bandwidth as a function of the phase scintillation spectral strength, \mathbf{T} , for the three loop orders (\circ : 1st order, \square : 2nd order, ∇ : 3rd order loops).

3.4.2. WBMOD predictions of T and S₄

By combining Equations (2.1-6) (the weak scatter formula for S₄) and (2.1-7) (the strong scatter approximation), it is possible to obtain a relatively simple expression which links T and S₄ through the various geometrical factors discussed in Section 2.1.3, *viz*

$$T = -\frac{\ln(1 - S_4^2)}{\gamma} \quad (3.4-7)$$

where $\gamma \propto \frac{F z_F^{(p-1)}}{G v_e^{(p-1)}}$ is a factor that depends mainly on the satellite-receiver geometry

and the orientation and elongation of the ionospheric irregularities. The logarithm of Equation (3.4-7) is thus

$$T_{dB} = 10 \log_{10} \left(\ln \left(\frac{1}{1 - S_4^2} \right) \right) - \gamma_{dB} \quad (3.4-8)$$

Consequently, for a given geometry factor, γ_{dB} , the locus of possible values of T and S₄ is a single line (at least for the scintillation model discussed in Section 2.1). From WBMOD, it appears that for a stationary GPS receiver, γ_{dB} is usually greater than about 20dB in equatorial regions above a 5° elevation angle. Therefore, T and S₄ values will normally lie below the line obtained from Equation (3.4-8) by letting $\gamma_{dB} = 20$ dB. This is illustrated in Figure 3.4-5 where the line obtained from Equation (3.4-8) with $\gamma_{dB} = 20$ dB is plotted along with a series of dots representing the T and S₄ values for each visible satellite at 64 locations near to the equatorial anomaly. Also shown in Figure 3.4-5 are the threshold curves from Figure 3.4-3.

The T and S₄ values in this figure were obtained from WBMOD under the following conditions, which represents strong scintillation activity:

- An area of 60 × 60 degrees centred on 10°N and 120°E.
- A sunspot number of 150 (ie. high solar activity).
- A magnetic activity index, K_p of 5.6.
- The September Equinox.
- 12:00 hrs GMT (~20:00 hrs local time at 120°E).
- 2 hours duration from 12:00 hours GMT.
- A 5° elevation mask angle (elevation angle cutoff).
- The 90th percentile of scintillation activity.

Very similar results were obtained at other times and at other equatorial locations.

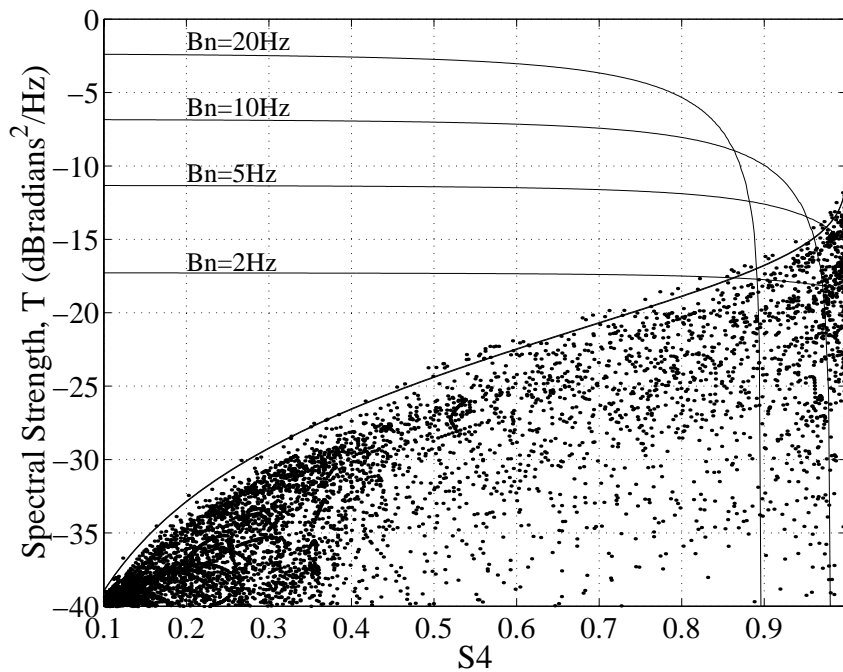


Figure 3.4-5: T and S_4 values obtained from WBMOD for a period of high solar activity plotted over the tracking thresholds from Figure 3.4-3. $C/N_o = 41.5$ dBHz is assumed.

This result suggests that a stationary receiver is probably more likely to lose lock from amplitude scintillations than from phase scintillations, except when the bandwidth is very narrow (ie. for medium to wide bandwidths, it is unlikely that the threshold will be exceeded unless S_4 is very large). However, an increase in the effective scan velocity, v_e , perhaps due to receiver motion, will reduce γ and force the locus in Figure 3.4-5 to move upwards. As a result, phase scintillations will have more of an effect on loop performance, as will the choice of the loop bandwidth. However, the optimum bandwidth for minimum tracking error will still be quite different for each satellite link as a result of the different geometries and signal levels on each link.

3.4.3. Velocity and elevation angle effects

3.4.3.1. Elevation angle effects

From the equations given in Section 2.1.3, it appears likely that the geometry factors for T and S_4 will be larger at low elevation angles as a result of a larger ionospheric pierce point velocity due to satellite motion, v_s , and a larger Fresnel zone radius, z_F ,

respectively. This is demonstrated in Figure 3.4-6 which was obtained using WBMOD data under the same conditions as Figure 3.4-5.

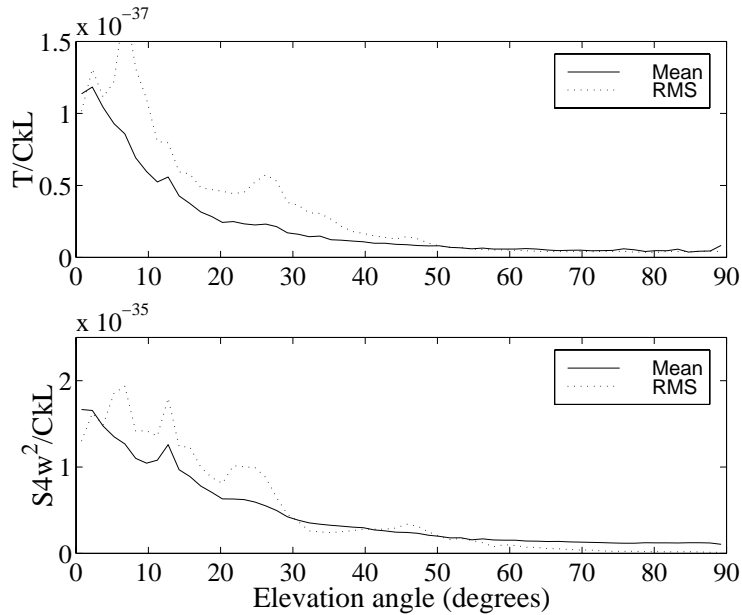


Figure 3.4-6: The mean and RMS of the geometry factors for T (upper panel) and S_{4w} (lower panel) obtained from WBMOD for a period of high solar activity.

The two geometry factors used in Figure 3.4-6 were obtained by dividing T (Equation (2.1-2)) and S_4 obtained from the weak scintillation model (Equation (2.1-6)) by the height integrated irregularity strength parameter, $C_k L$, viz

$$\frac{T}{C_k L} = K_1 * G v_e^{(p-1)} \sec(\theta) \quad (3.4-9)$$

$$\frac{S_{4w}^2}{C_k L} = K_2 * F z_F^{(p-1)} \sec(\theta) \quad (3.4-10)$$

where, from Equation (2.1-7), $S_{4w}^2 = -\ln(1 - S_4^2)$ and K_1 and K_2 are factors that are independent of the geometry.

For the phase geometry factor, the principal contribution to the elevation angle dependence originates from the effective scan velocity, v_e , and from the $\sec(\theta)$ term. As the elevation angle decreases, the ionospheric pierce point velocity due to satellite

motion, v_s , increases which in general leads to an increase in v_e (see Figure 3.4-7)². A more thorough discussion of the effects of velocity on v_e is given in the next section and in Appendix F.

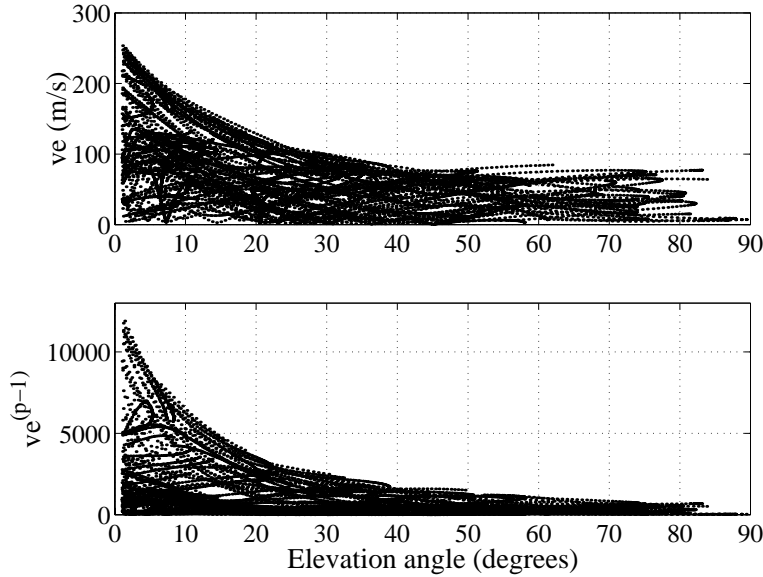


Figure 3.4-7: Effective scan velocity, v_e , as a function of the satellite elevation angle for a stationary receiver. The elevation angle dependence is largely due to satellite motion and the individual curves represent different satellite trajectories. $p = 2.5$.

For the amplitude geometry factor, the Fresnel zone radius, z_F , and the $\sec(\theta)$ terms provide the greatest contribution to the elevation angle dependence. z_F can be approximated by $z'_F \sqrt{\sec(\theta)}$ where $z'_F = \sqrt{h_i \lambda}$ is the Fresnel zone radius of a vertically propagating plane wave. Therefore, the majority of the elevation angle dependence for S_{4w} can be accounted for through a single $\sec(\theta)^{(p+1)/2}$ term. For highly elongated irregularities, the Fresnel filter factor, F , tends to be mainly a function of p , and therefore shows very little dependence on the elevation angle [78].

It is also anticipated that at low elevation angles, the carrier to noise density ratio of the GPS signal will be reduced. This is a result of a combination of additional atmospheric absorption, a greater distance to the satellites, and satellite and receiver antenna gain

² The actual effect on v_e will depend on the vector sum of v_s and the drift velocity, v_d , and on the orientation and elongation of the irregularities. v_e can be quite small if the vector sum of v_s and v_d is either very small or approximately aligned to the principal irregularity axis [76].

pattern effects. From Equation (3.4-2), it is clear that a reduction in C/N_o will lead to an increase in the threshold amplitude, \tilde{A}_{Th} , which in turn will increase the probability of losing lock. Consequently, the threshold curves of Figure 3.4-5 will be shifted to the left, and the loop will become even more susceptible to the effects of amplitude scintillations.

Consequently, through a combination of a reduced C/N_o and larger geometry factors, satellite links that penetrate the peak of the equatorial anomaly at low elevation angles are likely to be significantly more stressed than high elevation angle links. Notice that this is not guaranteed to occur on all links as there are large variations in the geometry factors between the individual links (ie. the RMS values of the geometry factors for both T and S_4 are also large – see Figure 3.4-6).

3.4.3.2. Satellite and receiver velocity

In the presence of receiver dynamics, two effects will alter a receiver's tolerance to scintillations. These are:

- (i) the additional stresses imposed directly upon the tracking loops by dynamics, and
- (ii) the change in the scintillation rate caused by motion of the receiver through the interference patterns.

The stresses introduced into the carrier tracking loop by dynamics may be accounted for if the characteristics of the dynamics are known. If a steady state phase error, ϕ_{eSS} , is produced by a constant dynamic process, then a modified tracking threshold of the form

$$\sigma_{\phi_e}^2 \Big|_{Th2} = \left[\frac{\pi}{12} - \frac{\phi_{eSS}}{3} \right]^2 \text{ radians}^2 \text{ can be obtained from Equations (C-3) and (E-7) and used}$$

in place of Equation (3.4-1). The effects of transient errors may be accounted for by adding an extra term to the tracking error variance to account for the *Total Transient Distortion*, ε_T^2 (Equation (E-11)). This results in another modified tracking threshold of the form

$$\sigma_{\phi_e}^2 \Big|_{Th3} = \left[\frac{\pi}{12} \right]^2 - \varepsilon_T^2. \text{ If amplitude scintillations influence the transfer function of a}$$

tracking loop, both the steady state and transient errors produced by dynamics will change. Indeed, during deep fades, the instantaneous bandwidth of the tracking loop may be reduced, resulting in an increase in both ϕ_{eSS} and ε_T^2 during those times.

The second effect of dynamics is related more directly to scintillations and can be accounted for by adjusting the spectral strength parameter, T , and the Fresnel cutoff

frequency, f_c . As shown in Equation (2.1-2), T can be related to the effective scan velocity, v_e , through the expression $T = Bv_e^{p-1}$, where B is a constant for a given set of ionospheric conditions and satellite-receiver geometry. The effective scan velocity is a function of the ionospheric drift velocity, v_d , the ionospheric pierce point velocity, v_I (consisting of the satellite component, v_s , and the receiver component, v_r), and the geometry and orientation of the irregularities. At equatorial latitudes, v_d is typically of the order of 50 to 200 m/s in an Easterly direction and is accounted for in WBMOD through a drift velocity model. For an ionospheric height of 350km, v_s is typically between about 60 and 500 m/s depending on the elevation and azimuth angles of the GPS satellites (Appendix F). In Figure 3.4-8, v_s is plotted as a function of the elevation angle over a 24-hour period for a receiver located at 10°N and 120°E. It is clear from this figure that v_s shows a strong dependence on the satellite elevation angle, being much larger at low elevation angles. It is also apparent that despite the effects of Earth's rotation, the East-West component of v_s is usually in an Easterly direction for all satellites (ie. v_y is usually positive). Consequently, the East-West component of v_s is in the same direction as the drift velocity, v_d , which tends to reduce v_e somewhat (ie. the ionospheric pierce point scans across the plasma density contours at a reduced rate as a result of satellite motion).

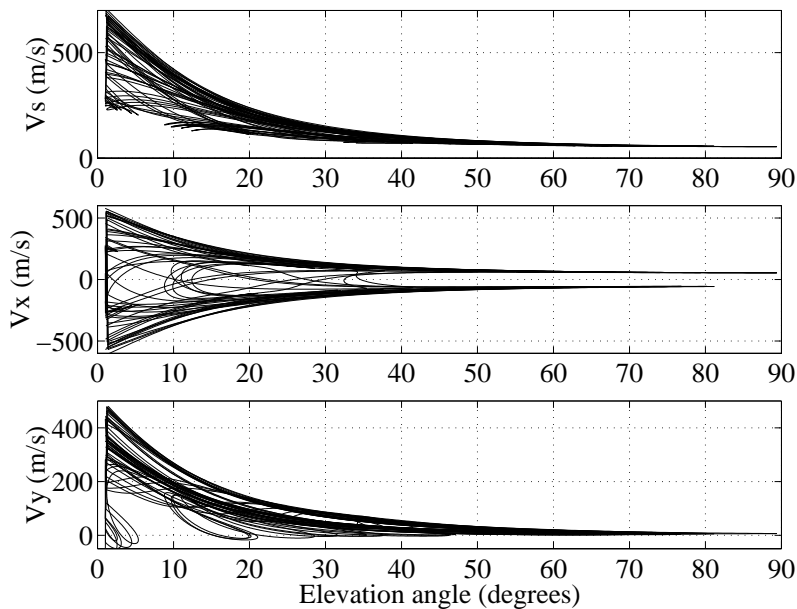


Figure 3.4-8: Ionospheric pierce point velocity due to satellite motion (upper panel), North velocity component, v_x , (middle panel) and East velocity component, v_y , (lower panel) for a GPS receiver located at 10°N and 120°E. The ionospheric height is assumed to be 350km. $v_s^2 = v_x^2 + v_y^2$.

The pierce point velocity due to receiver motion, v_r , is a function of the receiver velocity and the elevation and azimuth angles of the satellite (Appendix F). In Figure 3.4-9, v_r is plotted as a function of the satellite elevation angle and the direction of motion of the receiver in relation to the satellite azimuth angle³ (v_r is plotted as a percentage of the receiver velocity, v_R). In this figure, it is assumed that the receiver is moving in a horizontal plane with velocity v_R and at a height that is small in relation to the mean ionospheric height (ie. level aircraft flight will meet this requirement). It is clear from this figure that v_r is approximately equal to the receiver velocity, except at moderate to low elevation angles, and when the receiver motion has a large component that is aligned with the satellite azimuth angle. Although WBMOD allows only one end of a link to be in motion (usually the satellite end), it is possible to account for receiver motion by translating v_r to the satellite end and determining an equivalent satellite velocity⁴.

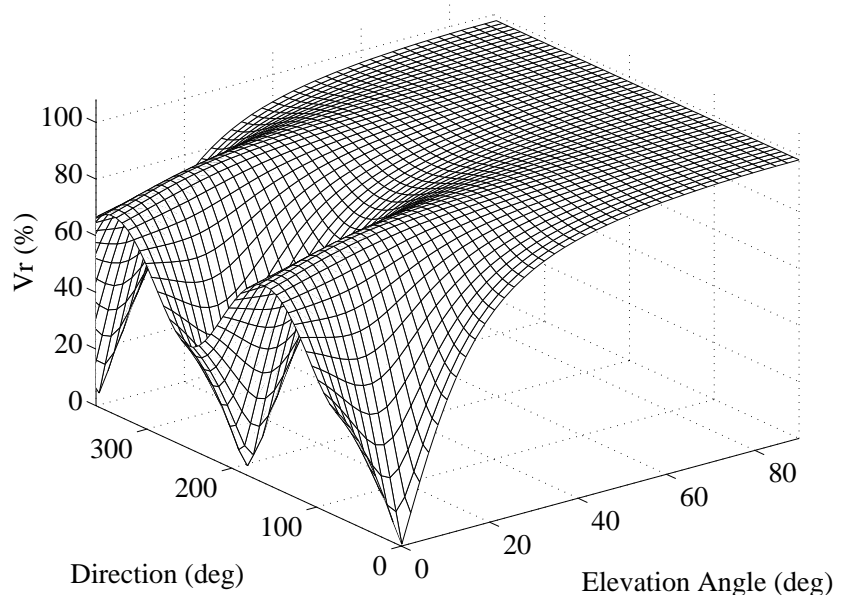


Figure 3.4-9: Ionospheric pierce point speed as a percentage of the receiver speed and as a function of the satellite elevation angle and the direction of motion. The ionospheric height is assumed to be 350km.

From the foregoing discussion, it is clear that the speed with which the satellite propagation path cuts across the plasma density contours is given approximately by

³ 0° represents motion of the receiver towards the satellite.

⁴ If v'_s is the pierce point velocity due to the modified satellite motion, then $v'_s = v_s + v_r$ where v_s is the unmodified satellite pierce point velocity. This approach is discussed further in Appendix F.

$|v_d - (v_s + v_r)|$, where v_d , v_s , and v_r are two-dimensional velocity vectors in a horizontal plane at the mean ionospheric height. For isotropic irregularities, this result is also the effective scan velocity, v_e . However, as the irregularities are in general highly anisotropic, the degree of anisotropy and the orientation of the irregularities must all be taken into account in order to determine v_e .

In general, very high receiver velocities are likely to lead to an increase in v_e , although not on all satellite links. On average, this will lead to an increase in the spectral strength, T , with a consequent increase in the probability of losing lock due to phase scintillations. With reference to Figure 3.4-5, this effect will be manifested as an upward shift in the curve that represents the likely combinations of T and S_4 . If this shift is sufficiently large (say 10dB or so), it may cause narrow bandwidth receivers to become much more susceptible to scintillations than wide bandwidth receivers. Although the amplitude scintillation strength, S_4 , is not influenced by v_e , the Fresnel cutoff frequency, f_c , increases with v_e (Equation (2.1-3)). Consequently, the duration of the deep fading events that lead to loss of lock in a receiver will be reduced. This will be an advantage for narrow bandwidth receivers for which the time constant of the tracking loops may exceed the duration of the deep fading event (see Section 3.5). Although this effect is not accounted for in the threshold curves of Figure 3.4-5, for very high receiver velocities, it is likely that loss of lock will mainly occur as a result of phase scintillations (ie. the effects of amplitude scintillations can be ignored on many of the links).

3.4.4. Summary

Expressions were derived for the probability of losing lock, P_L , as a function of both the tracking loop parameters and the scintillation statistics. It was shown that in general, amplitude and phase scintillation activity must be at a high level before loss of carrier lock will occur. It was also shown that as the carrier loop bandwidth increases, the susceptibility to amplitude scintillations increases, but the susceptibility to phase scintillations decreases. Consequently, for a given set of signal and scintillation conditions, an optimum bandwidth exists which minimises the probability of losing lock.

Predictions of the amplitude and phase scintillation indices, S_4 and T , based on the scintillation model WBMOD suggest that even during times of severe scintillation activity (ie. during high solar activity, at equinox and near the equator), the majority of a

receiver's channels will remain in lock. This is despite a relatively conservative threshold being chosen for P_L and a large percentile for the WBMOD predictions. However, this result assumes that the receiver is stationary, uses full code correlation tracking loops and is not subject to any other sources of loop stress.

The relationship between the geometry of the propagation path and the strength of scintillation activity was investigated. The intention was to determine under what conditions a satellite-receiver link would be subject to the greatest scintillation stresses, and therefore when it would be most likely to lose lock. The two geometry factors examined in this section were the elevation angle of the propagation path and its velocity through the ionosphere. It was found that in general, for a given level of ionospheric disturbance (embodied in the parameter $C_K L$; the height integrated irregularity strength), both S_4 and T tended to be larger at low elevation angles. Consequently, propagation paths that penetrate highly disturbed regions of the ionosphere at low elevation angles will have the greatest probability of losing lock. It was also found that an increase in the effective scan velocity of the propagation path through the irregularity layer, v_e , will result in an increase in the phase scintillation index, T , and therefore an increase in the susceptibility of narrow bandwidth tracking loop to scintillations. v_e is a function of satellite motion, receiver motion, ionospheric drift and the irregularity geometry. The effects of both satellite and receiver motion on v_e were examined and a technique for incorporating receiver motion into the WBMOD model was discussed. Although the dependence of v_e on the various geometry and velocity factors is quite complex, it can be said that in general under very high velocity conditions, v_e is likely to increase on most satellite-receiver links which will increase the probability of losing lock, particularly for narrow bandwidth tracking loops.

3.5. The impact of fade depth and duration on cycle slips

The results given in Sections 3.3 and 3.4 do not explicitly take into account the amplitude scintillation rate. In these sections, it was assumed that if the amplitude scintillation bandwidth was much less than the carrier loop bandwidth⁵, the carrier loop would lose lock once the amplitude had fallen below the tracking threshold, A_{Th} . However, if the deep fades occur with very short durations, this assumption may become invalid. This may occur in the presence of high velocity dynamics, particularly if a receiver is aided by an Inertial Navigation System (INS) and can therefore adopt a very narrow tracking loop bandwidth. In this section, the relationship between fade depth and duration and the probability of a cycle slip is investigated for a simple rectangular fade. Although the issue of loss-of-lock is not dealt with directly in this analysis, it can be assumed that if the probability of a cycle slip becomes very large, the carrier loop has a much greater chance of losing lock.

From Holmes [43], the mean time to cycle slip for a 1st order I.Q Costas phase locked loop is given by

$$\bar{T} = \frac{\pi^2}{2B_n} \rho_e I_o^2(\rho_e) \quad (3.5-1)$$

where B_n is the loop noise bandwidth, $\rho_e = 1/4\sigma_{\phi T}^2$ is the effective loop SNR (the thermal noise variance, $\sigma_{\phi T}^2$, is obtained from the linear loop model), and $I_o()$ is the modified Bessel function of the first kind of order zero. Based on simulations ([43] page 199), it has been found that an approximate mean time to cycle slip for a 2nd order loop can be obtained from Equation (3.5-1) by increasing $\sigma_{\phi T}^2$ by 1dB. Viterbi [97] has shown that the cycle slipping rate is the inverse of the mean time to cycle slip for a 1st order loop, and approximately so for a 2nd order loop. As the slipping process is approximately Poisson distributed ([43], page 95), the probability of slipping in τ seconds from a state of zero error is given by

⁵ A justification for this assumption is given in Appendix G using data obtained from WBMOD for a stationary receiver at an equatorial location.

$$\begin{aligned}
P_{CS} &= 1 - \exp(-\tau/\bar{T}) \\
&= 1 - \exp\left(-\frac{2\tau B_n}{\pi^2 \rho_e I_o^2(\rho_e)}\right)
\end{aligned} \tag{3.5-2}$$

If τ is taken as the duration of the fade, and ρ_e is calculated for a given fade depth and loop bandwidth⁶, then the probability that one or more cycle slips will occur over the duration of the fade will be given by this expression.

Equation (3.5-2) implies that for an infinitely deep fade (ie. $\rho_e = 0$), the probability of a cycle slip is one, irrespective of the fade duration, τ . However, Viterbi's equation is modelled on an ideal I.Q discriminator for which the discriminator noise term, n_d , becomes infinite when $\rho_e = 0$. For a real tracking loop, the characteristics of the discriminator will tend to override this effect and prevent P_{CS} from becoming large when the fade duration is very short. Indeed, for an arctangent discriminator, there is a minimum fade duration below which the probability of a cycle slip is zero, irrespective of the fade depth. In the analysis that follows, a correction to Equation (3.5-2) is derived for the case of an infinitely deep fade. The probability of a cycle slip is then given as a function of fade depth and duration for two representative loop bandwidths and compared with the results obtained from simulations. The impact of loop order and dynamics is also discussed.

For an infinitely deep fade (ie. $\tilde{A} = 0$), the phase locked loop behaves as if it was an open loop. With reference to Figure 3.1-2, when $\tilde{A} = 0$ the phase locked loop takes on the following form

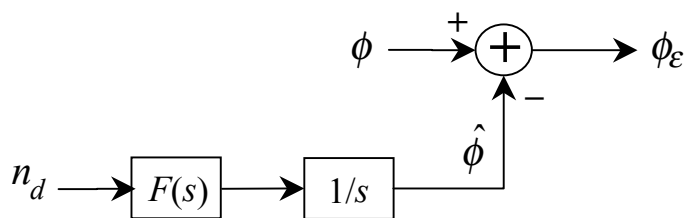


Figure 3.5-1: Model of a phase locked loop for zero signal amplitude.

⁶ Note $C/N_o|_{\text{Faded}} = C/N_o|_{\text{Unfaded}} - F$ where F is the fade depth in decibels.

where n_d is the discriminator noise term which is zero-mean but is generally not Gaussian. n_d can be found by applying the discriminator algorithms given in Table 3.1-1 to the prompt I and Q signals from the pre-detection filters. In the absence of a GPS signal, the I and Q signals have the following form (from Equation (3.1-2))

$$\begin{aligned} I_P &= n_{IP} \\ Q_P &= n_{QP} \end{aligned} \quad (3.5-3)$$

where n_{IP} and n_{QP} are zero-mean, Gaussian and IID. For the arctangent discriminators, n_d is given by

$$n_d = \text{Atan}\left(\frac{n_{QP}}{n_{IP}}\right) \text{ or } \text{Atan2}(n_{QP}, n_{IP})^7 \quad (3.5-4)$$

From studies of narrowband Gaussian noise processes (see for example [39] pages 294 onwards), it is known that the arctangent of the ratio of two zero-mean, Gaussian, IID random variables has a uniform PDF. Consequently, the PDF of n_d is also uniform and can be represented by

$$f_{n_d}(n_d) = \frac{1}{2\sqrt{3}\sigma_{n_d}} \text{rect}\left(\frac{n_d}{2\sqrt{3}\sigma_{n_d}}\right) \quad (3.5-5)$$

where σ_{n_d} is the standard deviation of n_d and is equal to $\pi/2\sqrt{3}$ for the Atan discriminator, and $\pi/\sqrt{3}$ for the Atan2 discriminator.

For the normalised I.Q discriminator, the PDF is considerably more difficult to determine. However, using numerical techniques it has been found that $\sigma_{n_d} = 1/2\sqrt{2}$ ⁸.

⁷ Atan2(y, x) is the four quadrant arctangent function.

⁸ This is found by evaluating $\int_{-\infty}^{\infty} \int_{-\infty}^{\infty} n_d^2 f_{n_{IP}, n_{QP}}(n_{IP}, n_{QP}) dn_{IP} dn_{QP}$ where $f_{n_{IP}, n_{QP}}(n_{IP}, n_{QP})$ is a bivariate Gaussian PDF and $n_d = n_{IP}n_{QP}/(\sqrt{n_{IP}^2 + n_{QP}^2})$.

3.5.1. 1st Order loops

For a 1st order phase locked loop, the phase error γ seconds after the start of an infinitely deep fade is given by

$$\begin{aligned}\phi_e(t_o, t) &= \phi(t) - \hat{\phi}(t_o, t) \\ &= \phi(t) - \left[\int_{t_o}^t n_d(u) \omega_n du + \hat{\phi}(t_o) \right] \quad \text{for } t \geq t_o\end{aligned}\tag{3.5-6}$$

where $F(s) = \omega_n$ is the transfer function of the loop filter, t_o is the time at which the fade begins, $t = t_o + \gamma$, and $\hat{\phi}(t_o)$ is the loop phase estimate at time t_o . If it is assumed that $\phi(t) - \hat{\phi}(t_o) = 0$ (ie. the input phase process, $\phi(t)$, is constant and the initial phase error, $\phi_e(t_o)$, is zero), then

$$\phi_e(t_o, t) = \int_{t_o}^t n_d(u) \omega_n du \quad \text{for } t \geq t_o\tag{3.5-7}$$

Therefore, $\phi_e(t_o, t)$ is a random walk (or Brownian motion) process which begins from zero at time $t = t_o$. As $\phi_e(t_o, t)$ is zero-mean, its variance is given by

$$\begin{aligned}\sigma_{\phi_e}^2(\gamma) &= E\{\phi_e(t_o, t)^2\} \\ &= E\left\{ \int_{t_o}^t n_d(u) \omega_n du \int_{t_o}^t n_d(v) \omega_n dv \right\} \\ &= \omega_n^2 \int_{t_o}^t \int_{t_o}^t E\{n_d(u)n_d(v)\} du dv \\ &= \omega_n^2 \int_{t_o}^t \int_{t_o}^t \sigma_{n_d}^2 \text{rect}\left(\frac{u-v}{T}\right) du dv \\ &= \omega_n^2 \sigma_{n_d}^2 T \gamma\end{aligned}\tag{3.5-8}$$

Consequently, for a 1st order loop the variance of the phase error increases linearly with the fade duration, γ . If the magnitude of the phase error exceeds the threshold of the discriminator, $\phi_e|_T$ ⁹, a cycle slip will occur when the signal level eventually returns to normal. Consequently, even for an infinitely deep fade, the probability of a cycle slip will

⁹ $\phi_e|_T = \pi/2$ for an I.Q or Atan discriminator, and π for an Atan2 discriminator.

be quite small if the total fade duration, τ , is very small. This is particularly true if the loop bandwidth, which is proportional to ω_n , is also very small.

As the loop is effectively open circuit during an infinitely deep fade, the concept of a cycle slip becomes meaningless during this time. A cycle slip will only occur if the magnitude of the phase error exceeds $\phi_e|_T$ when the signal level returns to normal (or at least becomes large enough for the loop to re-lock). Nevertheless, by comparing the phase errors for an infinitely deep fade with $\phi_e|_T$, it is possible to determine an upper limit on the probability of a cycle slip for different fade durations. This assumes that $\sigma_{\phi_e}^2(\gamma)$ is at a maximum value when the fade is infinitely deep.

The Random Walk described by Equation (3.5-7) is essentially a first order Markoff process for which the PDF of ϕ_e at time t_k depend only on the value of ϕ_e at time t_{k-1} . The time separation between consecutive samples in this model (ie. $t_k - t_{k-1}$) is given by the hold period, T , of the integrate and dump pre-detection filters. Consequently, the joint PDF of the sequence of phase errors, $[\phi_{e_k}, \phi_{e_{k-1}}, \dots, \phi_{e_0}]$ is given by

$$f_{\phi_{e_k}, \dots, \phi_{e_0}}(\phi_{e_k}, \dots, \phi_{e_0}) = f_{\phi_{e_0}}(\phi_{e_0}) \prod_{i=1}^k f_{\phi_{e_i} | \phi_{e_{i-1}}}(\phi_{e_i} | \phi_{e_{i-1}}) \quad (3.5-9)$$

where $f_{\phi_{e_i} | \phi_{e_{i-1}}}(\phi_{e_i} | \phi_{e_{i-1}})$ is the conditional PDF of ϕ_{e_i} given $\phi_{e_{i-1}}$ and ϕ_{e_0} is the phase error immediately after the start of the fade. For the Atan and Atan2 discriminators, this is given by ¹⁰

$$f_{\phi_{e_i} | \phi_{e_{i-1}}}(\phi_{e_i} | \phi_{e_{i-1}}) = \frac{1}{2\sqrt{3}\sigma_{n_d}\omega_n T} \text{rect}\left(\frac{\phi_{e_i} - \phi_{e_{i-1}}}{2\sqrt{3}\sigma_{n_d}\omega_n T}\right) \quad (3.5-10)$$

which is based on the following discrete version of Equation (3.5-7)

$$\begin{aligned} \phi_{e_i} &= \sum_{j=1}^i n_{d_j} \omega_n T \\ &= \phi_{e_{i-1}} + n_{d_i} \omega_n T \end{aligned} \quad (3.5-11)$$

¹⁰ An equivalent expression for the normalised I.Q discriminator has not been found.

The probability that the magnitude of the phase error exceeds the threshold, $\phi_\varepsilon|_T$, at any time during the fade is therefore

$$\begin{aligned}
P(\max(|\phi_{\varepsilon_k}|, |\phi_{\varepsilon_{k-1}}|, \dots, |\phi_{\varepsilon_0}|) \geq \phi_\varepsilon|_T) &= 1 - \int_{-\phi_\varepsilon|_T}^{\phi_\varepsilon|_T} \dots \int_{-\phi_\varepsilon|_T}^{\phi_\varepsilon|_T} f_{\phi_{\varepsilon_0}}(\phi_{\varepsilon_0}) \prod_{i=1}^k f_{\phi_{\varepsilon_i}|\phi_{\varepsilon_{i-1}}}(\phi_{\varepsilon_i}|\phi_{\varepsilon_{i-1}}) d\phi_{\varepsilon_k} \dots d\phi_{\varepsilon_0} \\
&= 1 - \frac{1}{(2\sqrt{3}\sigma_{n_d}\omega_n T)^k} \int_{-\phi_\varepsilon|_T}^{\phi_\varepsilon|_T} \dots \int_{-\phi_\varepsilon|_T}^{\phi_\varepsilon|_T} \prod_{i=1}^k \text{rect}\left(\frac{\phi_{\varepsilon_i} - \phi_{\varepsilon_{i-1}}}{2\sqrt{3}\sigma_{n_d}\omega_n T}\right) d\phi_{\varepsilon_k} \dots d\phi_{\varepsilon_0}
\end{aligned} \tag{3.5-12}$$

Although this has not been solved in closed form, it has been evaluated using Matlab™ for a range of fade durations¹¹ and found to correspond very closely with the results of simulations.

One of the implications of this result is that for an Atan discriminator, it is impossible for the phase error to exceed $\phi_\varepsilon|_T$ and produce cycle slips prior to a certain time which is a function of the loop bandwidth, irrespective of the fade depth (assuming that the link is not subject to any dynamics and the phase error is initially zero). The reason for this is that the discriminator noise term, n_d , is limited to $\pm\phi_\varepsilon|_T$ (Equation (3.5-5)), and so the maximum possible phase error at time kT is $kT\omega_n\phi_\varepsilon|_T$ radians. Consequently, a cycle slip cannot occur before $1/\omega_n$ seconds from the beginning of the fade. Indeed, if this is less than the pre-detection integration period, T , the pre-detection filters will play a significant role in limiting the effects of the fade (see Section 3.5.3).

In Figure 3.5-2 and Figure 3.5-3, the probability of a cycle slip, P_{CS} , is plotted as a function of the fade depth and duration based on Equation (3.5-2) and the correction for an infinitely deep fade given by Equation (3.5-12). Thus if P_{CS1} and P_{CS2} represent the cycle slip probabilities from Equations (3.5-2) and (3.5-12) respectively, the corrected curves are given by $\min(P_{CS1}, P_{CS2})$.

¹¹ The total fade duration, τ , is assumed to be kT seconds.

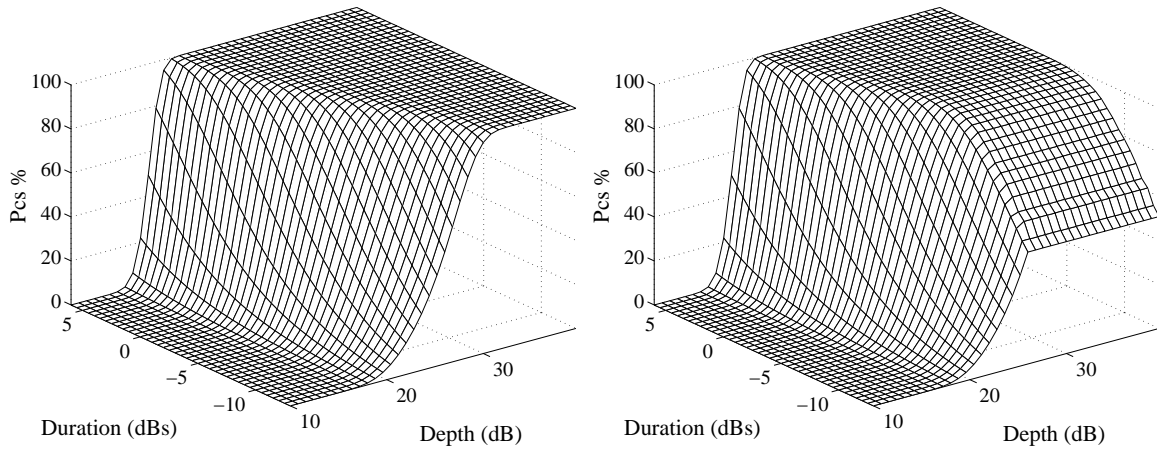


Figure 3.5-2: Probability of a cycle slip as a function of the fade depth and duration for a 1st order Costas carrier tracking loop based on theory. The left panel represents an ideal I.Q discriminator from Equation (3.5-2). The right panel incorporates the correction based on an infinitely deep fade for an Atan discriminator. Parameter values are $B_n = 15\text{Hz}$, $T=20\text{ms}$, $C/N_o = 40\text{dBi}$.

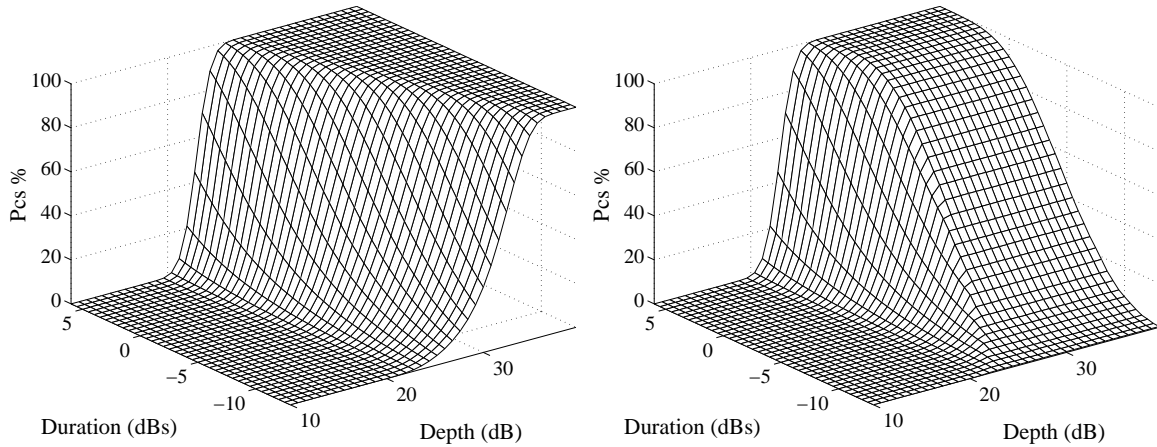


Figure 3.5-3: Probability of a cycle slip as a function of the fade depth and duration for a 1st order Costas carrier tracking loop based on theory. The left panel represents an ideal I.Q discriminator from Equation (3.5-2). The right panel incorporates the correction based on an infinitely deep fade for an Atan discriminator. Parameter values are $B_n = 5\text{Hz}$, $T=20\text{ms}$, $C/N_o = 40\text{dBi}$.

The following observations can be made from these figures:

- For long duration fades (seconds to hundreds of seconds), P_{CS} increases sharply when the fade depth approaches the theoretical tracking threshold given by Equation (3.4-2) (16.2 dB for the 15Hz bandwidth tracking loop and 20.3 dB for the 5Hz bandwidth tracking loop for $C/N_o = 40\text{dBi}$). However, as the fade duration decreases, increasingly larger fade depths are required for the same value of P_{CS} .

- Narrow bandwidth tracking loops have a much greater resistance to fades than wide bandwidth loops.
- The correction for an Atan discriminator based on an infinitely deep fade greatly reduces P_{CS} for short duration fades, particularly for the narrow bandwidth tracking loops.
- Although Equation (3.5-2) strictly only applies to an ideal I.Q discriminator, the correction associated with Equation (3.5-12) should provide an upper limit on P_{CS} for an Atan discriminator (as σ_{n_d} will be a maximum when the fade is infinitely deep).

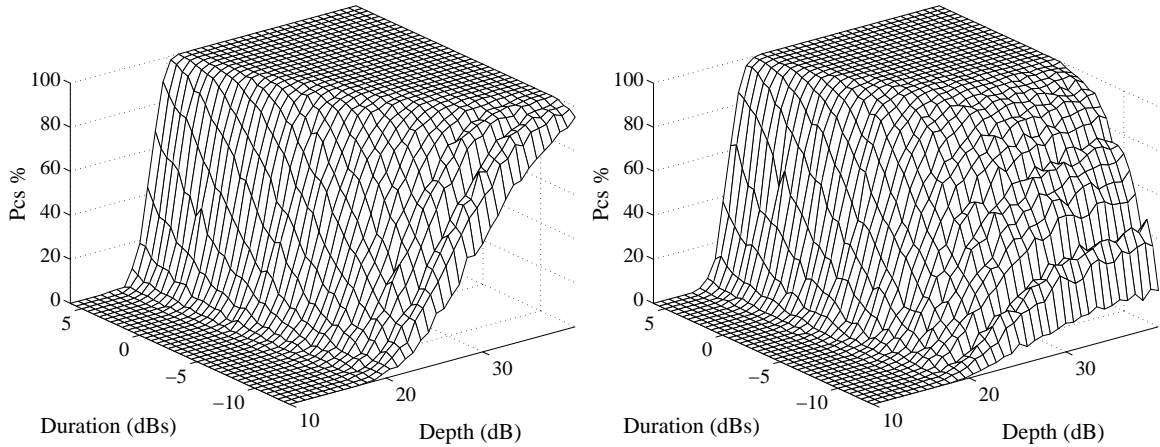


Figure 3.5-4: Probability of a cycle slip as a function of the fade depth and duration for a 1st order Costas carrier tracking loop based on simulations. The left panel represents an ideal I.Q discriminator. The right panel represents an Atan(Q/I) discriminator. Parameter values are $B_n = 15\text{Hz}$, $T=20\text{ms}$, $C/N_o = 40\text{dBHz}$.

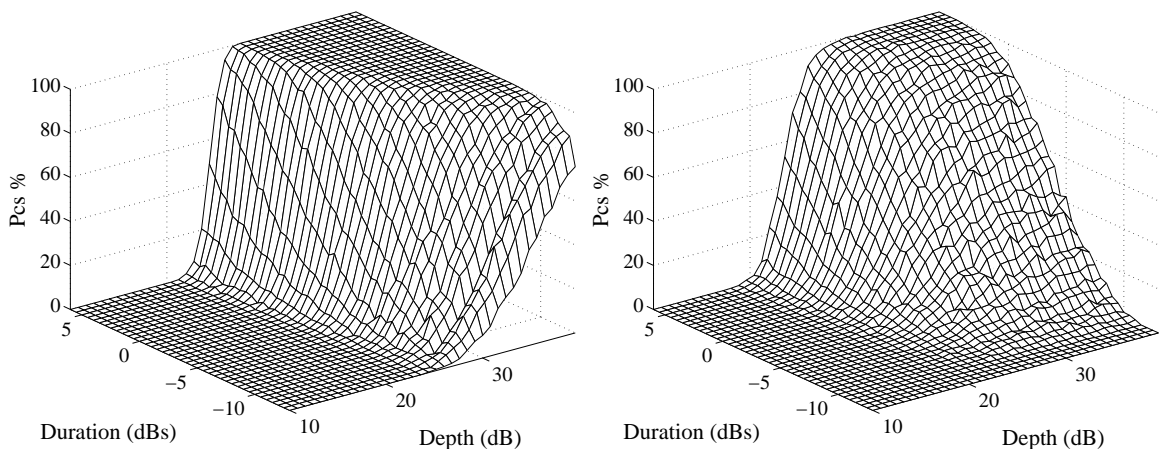


Figure 3.5-5: Probability of a cycle slip as a function of the fade depth and duration for a 1st order Costas carrier tracking loop based on simulations. The left panel represents an ideal I.Q discriminator. The right panel represents an Atan(Q/I) discriminator. Parameter values are $B_n = 5\text{Hz}$, $T=20\text{ms}$, $C/N_o = 40\text{dBHz}$.

In Figure 3.5-4 and Figure 3.5-5, the probability of a cycle slip is plotted as a function of fade depth and duration for both an ideal I.Q discriminator and an Atan(Q/I) discriminator based on simulations¹². It is clear from these plots that the simulations match the theory from Figure 3.5-2 and Figure 3.5-3 quite closely.

The following observations can be made from these figures:

- For the ideal I.Q discriminator, the theory appears to break down for very short duration fades (ie. less than about 0.1s or so). This may be the result of a failure to correctly account for the effects of pre-detection filtering in Equation (3.5-2). This will be discussed further in Section 3.5.3.
- For the Atan(Q/I) discriminator, Equation (3.5-2) appears to provide a good fit for longer duration fades, and the correction for infinitely deep fades appears to provide a reasonably good fit for short duration fades.

Simulations were also performed for 1st order Costas loops based on both normalised I.Q and Atan2(Q,I) discriminators. The results of these tests are given in Figure 3.5-6 for a 15Hz bandwidth tracking loop (this can be compared with the right panels of Figure 3.5-2 and Figure 3.5-4).

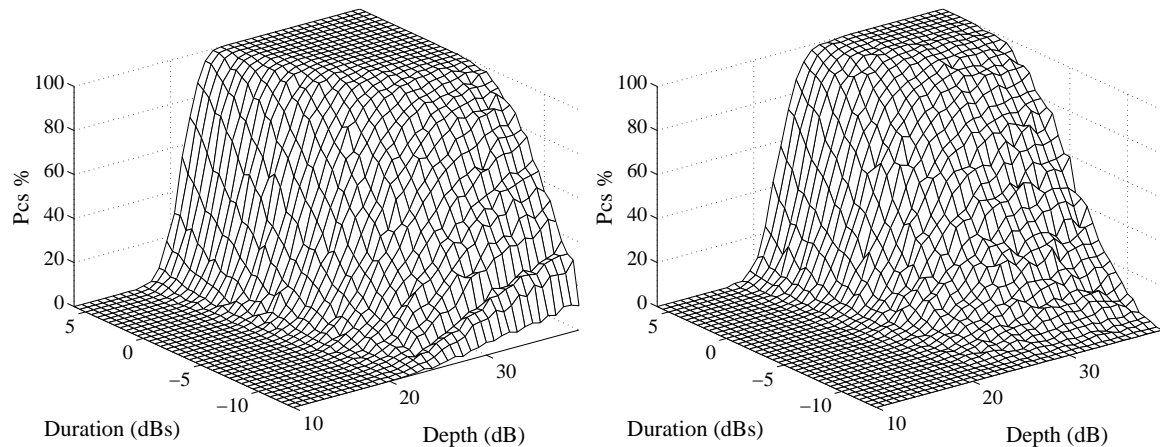


Figure 3.5-6: Probability of a cycle slip as a function of fade depth and duration for a 1st order Costas carrier tracking loop based on simulations. The left panel represents an Atan2(Q,I) discriminator. The right panel represents a normalised I.Q discriminator. Parameter values are $B_n = 15\text{Hz}$, $T=20\text{ms}$, $C/N_o = 40\text{dBHz}$.

¹² Several hundred simulations were performed for each combination of fade depth and duration.

In both cases, it is clear that the sharp upward trend in P_{CS} occurs at a greater fade depth than is predicted by the theory. For the Atan2 discriminator, the reason for this is that the discriminator threshold, $\phi_e|_T$, is twice as large as the corresponding threshold for an I.Q or Atan discriminator (ie. π compared with $\pi/2$ radians). Consequently, an Atan2 discriminator is capable of tolerating twice as much thermal noise as the other two discriminators before the non-linear region is encountered. However, for infinitely deep fades (not shown), it was found that the tracking loop based on an Atan2 discriminator followed the Random Walk theory very closely (ie. P_{CS} for the Atan2 and Atan tracking loops converged for infinitely deep fades). However, for the normalised I.Q discriminator, a tradeoff is occurring between thermal noise errors, and thus P_{CS} , and the ability of the loop to track dynamics under deep fading conditions. Consequently, although the normalised I.Q tracking loop appears to perform better at low signal levels (ie. P_{CS} is generally less), its ability to respond to dynamics tends to be worse. As this analysis assumes that the link is not subject to any dynamics, this tradeoff is not apparent in these results. In addition, because the statistics are not known for a normalised I.Q discriminator, the Random Walk model cannot be used to define P_{CS} under extremely deep fades.

3.5.1.1. Constant velocity

So far, this analysis has only considered 1st order loops that are not subject to any line of sight dynamics. One of the reasons for this is that the Fokker-Planck non-linear stochastic differential equation which defines loop performance (see Appendix C) has only been solved for a 1st order loop which is driven by thermal noise. When a 1st order loop is subject to a constant velocity, the phase tracking error will no longer be zero-mean (see Appendix E) and the probability of a cycle slip will be different. However, if the velocity, and thus ϕ_{eSS} , is relatively small, the impact on P_{CS} should not be very great. For an infinitely deep fade, the phase error will consist of a combination of a Random Walk due to thermal noise, and a linearly increasing phase error resulting from the dynamics (ie. the loop will be an open circuit and will no longer be capable of tracking the input phase process, $\phi(t)$, during the fade). For a constant velocity of v radians/s, the input phase process γ seconds after the start of an infinitely deep fade is given by (from Equation (3.5-6))

$$\phi_e(t_o, t) = vt - \left[\int_{t_o}^t n_d(u) \omega_n du + \hat{\phi}(t_o) \right] \quad \text{for } t \geq t_o \quad (3.5-13)$$

If it is assumed that $\hat{\phi}(t_o) = vt_o - \phi_{eSS}$, where ϕ_{eSS} is the steady state tracking error, then

$$\begin{aligned} \phi_e(t_o, t) &= v\gamma + \phi_{eSS} - \int_{t_o}^t n_d(u) \omega_n du \quad \text{for } t \geq t_o \\ &= \phi_{eSS} + \int_{t_o}^t [v - n_d(u) \omega_n] du \quad \text{for } t \geq t_o \end{aligned} \quad (3.5-14)$$

An equivalent discrete form of this expression is

$$\begin{aligned} \phi_{e_i} &= \phi_{eSS} + \sum_{j=1}^i [vT - n_{d_j} \omega_n T] \\ &= [\phi_{e_{i-1}} + vT] - n_{d_i} \omega_n T \end{aligned} \quad (3.5-15)$$

Consequently, for Atan and Atan2 discriminators, the PDF of ϕ_{e_i} given $\phi_{e_{i-1}}$ is now

$$f_{\phi_{e_i} | \phi_{e_{i-1}}}(\phi_{e_i} | \phi_{e_{i-1}}) = \frac{1}{2\sqrt{3}\sigma_{n_d} \omega_n T} \text{rect}\left(\frac{\phi_{e_i} - [\phi_{e_{i-1}} + vT]}{2\sqrt{3}\sigma_{n_d} \omega_n T}\right) \quad (3.5-16)$$

which is the rectangle function centred on $\phi_{e_{i-1}} + vT$. An equivalent form of Equation (3.5-12) can then be used to determine a new upper limit on the probability of a cycle slip. Clearly, this new upper limit will depend heavily on the magnitude of the velocity. For sustained higher order dynamics (eg. a constant acceleration), the 1st order loop will quickly lose lock, even in the absence of scintillation activity.

3.5.2. 2nd Order loops

For a 2nd order Costas loop, the loop filter takes on the form illustrated in Figure 3.5-7. Under steady state conditions, the output of the integrator in the upper path provides an estimate of the line of sight velocity (\hat{v} in radians/s) which is then combined with the phase error estimate provided by the lower path. The resulting filtered phase error is then passed to the VCO which is represented by the second integrator block. The velocity estimate, \hat{v} , provided by the loop filter enables the second order loop to track a constant velocity with zero steady state error (see Appendix E).

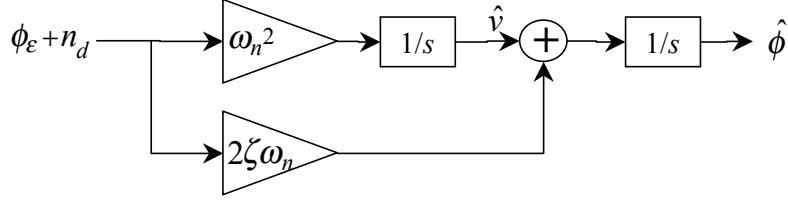


Figure 3.5-7: Loop filter for a 2nd order phase locked loop. ζ is the damping factor.

In the absence of dynamics, it has been shown that the expression for P_{CS} given in Equation (3.5-2) is a good approximation, provided that σ_{ϕ_T} is reduced by 1dB (Viterbi [97]). However, under infinitely deep fading conditions, the loop filter is once again driven only by the discriminator noise term, n_d , which tends to create both a Random Walk process (from the lower path), and an integrated Random Walk process (from the upper path). If velocity is present, the integrated Random Walk component will begin from an initial value of \hat{v} radians/s. The phase error γ seconds after the onset of an infinitely deep fade is therefore

$$\phi_e(t_o, t) = vt - \left[\int_{t_o}^t \left[2\zeta n_d(u) \omega_n + \omega_n^2 \int_{t_o}^u n_d(w) dw + \hat{v} \right] du + \hat{v} t_o \right] \quad \text{for } t \geq t_o \quad (3.5-17)$$

If it is assumed that $\hat{v} = v$ and the initial phase error is zero, this reduces to

$$\begin{aligned} \phi_e(t_o, t) &= \int_{t_o}^t \left[2\zeta n_d(u) \omega_n + \omega_n^2 \int_{t_o}^u n_d(w) dw \right] du \quad \text{for } t \geq t_o \\ &= \int_{t_o}^t 2\zeta n_d(u) \omega_n du + \omega_n^2 \int_{t_o}^t \int_{t_o}^u n_d(w) dw du \quad \text{for } t \geq t_o \end{aligned} \quad (3.5-18)$$

In discrete form, this is given by

$$\begin{aligned} \phi_{e_i} &= \sum_{j=1}^i 2\zeta n_{d_j} \omega_n T + \omega_n^2 \sum_{j=1}^i \sum_{m=1}^j n_{d_m} T^2 \\ &= \sum_{j=1}^i n_{d_j} \omega_n T [2\zeta + \omega_n T(i-j+1)] \\ &= \phi_{e_{i-1}} + \omega_n T \left[2\zeta n_{d_i} + \sum_{j=1}^i n_{d_j} \omega_n T \right] \end{aligned} \quad (3.5-19)$$

Equation (3.5-19) implies that for a 2nd order loop, the phase error is not a first order Markoff process. Consequently, the result given in Equation (3.5-12) cannot be used to

evaluate the probability of a cycle slip. However, it is clear from the additional $[2\zeta + \omega_n T(i - j + 1)]$ factor in Equation (3.5-19) that the phase error will grow much more rapidly for a 2nd order loop, particularly if the fade duration is quite long (ie. if the time index, i , is large). Nevertheless, using simulations it has been found that P_{CS} for a 2nd order loop is only slightly greater than P_{CS} for a 1st order loop and tends to follow the theory for a 1st order loop quite closely. In Figure 3.5-8, P_{CS} is plotted as a function of fade depth and duration for a 2nd order loop which is based on an Atan(Q/I) discriminator.

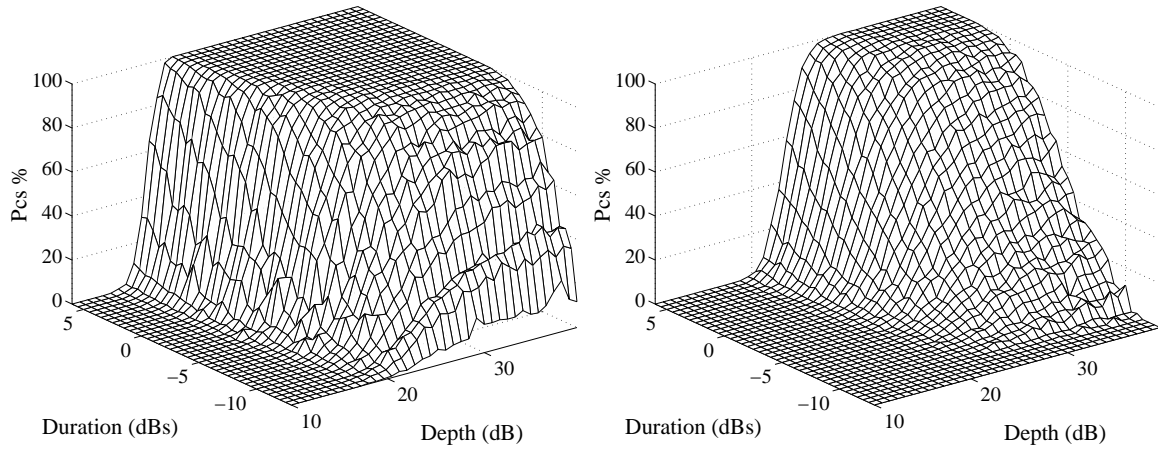


Figure 3.5-8: Probability of a cycle slip as a function of fade depth and duration for a 2nd order Atan(Q/I) Costas carrier tracking loop based on simulations. The left panel represents a 15Hz bandwidth tracking loop. The right panel represents a 5Hz bandwidth tracking loops. Parameter values are $T=20ms$, $C/N_o = 40dB$.

3.5.2.1. Constant acceleration

In the presence of a constant acceleration, the phase error for a 2nd order loop has a non-zero mean, ϕ_{ESS} , which is a function of the magnitude of the acceleration and the loop bandwidth (see Appendix E). The phase tracking error is given by

$$\phi_e(t_o, t) = \frac{at^2}{2} - \left[\int_{t_o}^t \left[2\zeta n_d(u) \omega_n + \omega_n^2 \int_{t_o}^u n_d(w) dw + \hat{v} \right] du + \hat{\phi}(t_o) \right] \quad \text{for } t \geq t_o \quad (3.5-20)$$

where $\hat{\phi}(t_o) = \frac{at_o^2}{2} - \phi_{ESS}$ and $\hat{v} = at_o$. The error component associated with the dynamics is given by

$$\begin{aligned} & \frac{at^2}{2} - \left[\int_{t_0}^t at_o du + \frac{at_o^2}{2} - \phi_{eSS} \right] \\ &= \frac{a\gamma^2}{2} + \phi_{eSS} \end{aligned} \quad (3.5-21)$$

Consequently, the total phase error is given by the Random Walk of Equation (3.5-18) added to the quadratic error term given above. For sustained higher order dynamics or very large accelerations, the 2nd order loop would be expected to lose lock irrespective of the presence of scintillations.

A similar approach can be applied to the analysis of 3rd order loops in the presence of sustained velocity, acceleration and jerk.

3.5.3. Pre-detection filters

In the previous two sections it has been shown that very narrow fades have a negligible impact on tracking loop performance, irrespective of their depth. A second factor which comes into play for very narrow fades is the effect of the pre-detection filters. From Equation (3.1-2), the I and Q signals at the output of the pre-detection filters is given by

$$\begin{aligned} I_P &= \tilde{A}d(t-\tau)\cos(\phi_e) + n_{IP}, \\ Q_P &= \tilde{A}d(t-\tau)\sin(\phi_e) + n_{QP} \end{aligned} \quad (3.5-22)$$

where \tilde{A} is a filtered version of the received GPS signal amplitude. For a rectangular fade of depth $10\log_{10}(1-\beta)$ dB and duration d seconds, the unfiltered amplitude is given by

$$A(t) = 1 - \beta \text{rect}\left(\frac{t}{d}\right) \quad (3.5-23)$$

and the filtered amplitude is

$$\tilde{A}(t) = 1 - \frac{\beta}{T} \int_{t-T}^t \text{rect}\left(\frac{u}{d}\right) du \quad (3.5-24)$$

In Figure 3.5-9, $\tilde{A}(t)$ is plotted as a function of time for a range of infinitely deep fades (ie. $\beta=1$) with varying durations. It is clear from this figure that for fades less than T seconds, the pre-detection filters will heavily suppress the fade. Also, as the sample time of the

sample and hold circuits is uncorrelated with the fade times, the filtered signal amplitude is effectively based on a random sampling of these waveforms (at a sample rate of T s).

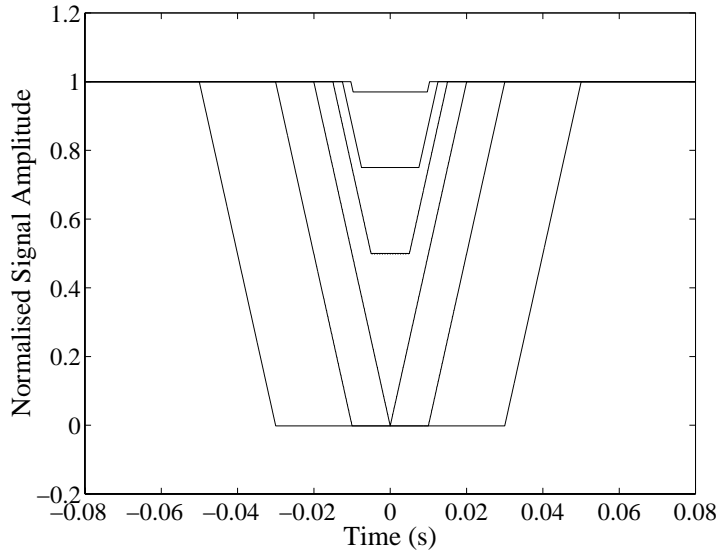


Figure 3.5-9: The filtered signal amplitude as a function of time for a range of infinitely deep fades with varying durations ($4T$, $2T$, T , $T/2$, $T/4$ and $T/32$ seconds).

3.5.4. Summary

In this section, the impact of fade depth and duration on the probability of a carrier cycle slip was examined. It was shown that the probability of a cycle slip can become extremely small if the fade duration is sufficiently short, irrespective of the fade depth. It was also shown that this behaviour becomes more pronounced as the bandwidth of the tracking loop is reduced. By assuming an infinitely deep fade and taking account of the characteristics of the discriminator, it was possible to develop a crude correction to the standard expression for the probability of a cycle slip which took account of this effect. Through the use of simulations, it was shown that this correction used in conjunction with the standard expression produced a relatively accurate measure of the probability of a cycle slip. The effects of line-of-sight velocity, acceleration, higher loop orders and pre-detection filtering was also examined.

3.6. Scintillation effects on carrier phase differential GPS

Carrier phase differential GPS techniques can be used to calculate the relative locations of GPS receivers separated by hundreds of kilometres to centimetre level accuracy in real time. As scintillations affect both the amplitude and phase of the incoming signals, it is reasonable to assume that they will impact on the accuracy of the phase range measurements made by carrier phase DGPS (CPDGPS) receivers. One of the most important processes involved in CPDGPS is the resolution of the integer cycle ambiguities in the carrier phase measurements. This involves forming a number of carrier phase observables including the single difference observable $\Delta\phi_{iab}$ (the difference in the carrier phase measurements to satellite i from two receivers, a and b), and the double difference observable $\nabla\Delta\phi_{ijab}$ (the difference in the single difference observables between two satellites, i and j). Errors in these measurements will increase the time taken for a receiver to resolve the cycle ambiguities and therefore the time required to obtain an accurate carrier phase measurement. This is likely to be of greatest concern to systems that attempt to resolve ambiguities on the fly from moving platforms.

In this section, the effects of amplitude and phase scintillations on the single difference phase observable, $\Delta\phi$, will be examined. If we assume that the ionospheric irregularities are infinitely long, field aligned, rod like structures [16], then the scintillation patterns on the ground will show negligible variation in a North-South direction. If the East-West velocity of the patterns is given by v_p m/s (a function of v_e), then for a pair of receivers separated by S metres in an East-West direction, the component of the single difference phase observable that is associated with phase scintillations and thermal noise is given by

$$\Delta\phi = [\hat{\phi}_{p1}(t) + n_1(t)] - [\hat{\phi}_{p2}(t) + n_2(t)] \quad (3.6-1)$$

where,

$\hat{\phi}_{p1}(t) = h_1(t) \otimes \phi_p(t)$ is the component of the carrier loop phase estimate produced by phase scintillations at site #1 (\otimes denotes the convolution integral),

$\hat{\phi}_{p2}(t) = h_2(t) \otimes \phi_p(t - \gamma)$ is the component of the carrier loop phase estimate produced by phase scintillations at site #2,

$h_1(t)$ and $h_2(t)$ are the impulse responses of the two carrier tracking loops,
 $\phi_p(t)$ is the phase scintillation time series at site #1,
 $\gamma = S/v_p$ is the time taken for the scintillation pattern to traverse the distance between the two sites (moving from site #1 to site #2), and
 $n_1(t)$ and $n_2(t)$ are associated with thermal noise and amplitude scintillations at the two sites.

Although the amplitude scintillations may be correlated between the two sites, it is quite straightforward to show that $n_1(t)$ and $n_2(t)$ are uncorrelated with each other and with $\hat{\phi}_p(t)$, irrespective of the baseline length. As $\Delta\phi$ is zero-mean in the presence of phase scintillations and thermal noise, its variance is given by

$$\begin{aligned}\sigma_{\Delta\phi}^2 &= E\{\Delta\phi^2\} \\ &= \sigma_{\hat{\phi}_{p1}}^2 + \sigma_{\hat{\phi}_{p2}}^2 - 2E\{\hat{\phi}_{p1}(t) * \hat{\phi}_{p2}(t)\} + \sigma_{n_1}^2 + \sigma_{n_2}^2\end{aligned}\quad (3.6-2)$$

where $\sigma_{\hat{\phi}_{p1}}^2$ and $\sigma_{\hat{\phi}_{p2}}^2$ are the variances of the phase estimates associated with phase scintillations, and $\sigma_{n_1}^2$ and $\sigma_{n_2}^2$ are the thermal noise variances (given by $\sigma_{\phi_T}^2$ or σ_ϑ^2 from Section's 3.3.2 or 3.3.3). If we assume that the majority of the phase scintillation energy is within the bandwidth's of the two carrier loops, then $\hat{\phi}_{p1}(t) \approx \phi_p(t)$ and $\hat{\phi}_{p2}(t) \approx \phi_p(t - \gamma)$. The variance of the single difference phase observable then becomes

$$\sigma_{\Delta\phi}^2 = 2[\sigma_{\phi_p}^2 - R_{\phi_p\phi_p}(\gamma)] + \sigma_{n_1}^2 + \sigma_{n_2}^2 \quad (3.6-3)$$

where $\sigma_{\phi_p}^2 \approx \int_{-\infty}^{\infty} S_{\phi_p}(f) df = \frac{T\sqrt{\pi}\Gamma((p-1)/2)f_o^{1-p}}{\Gamma(p/2)}$ from Section 3.2.3, Equation (3.2-22), and

$$\begin{aligned}R_{\phi_p\phi_p}(\gamma) &= E\{\phi_p(t)\phi_p(t - \gamma)\} \\ &= \int_{-\infty}^{\infty} S_{\phi_p}(f) \cos(2\pi f \gamma) df\end{aligned}\quad (3.6-4)$$

is the autocorrelation function of $\phi_p(t)$. The following simplification can be made using a table of integrals (eg. Gradshteyn [37], Equation 3.771-2)

$$R_{\phi_p\phi_p}(\gamma) = \frac{2T\sqrt{\pi}K_q(2\pi f_o \gamma)}{\Gamma(p/2)} \left(\frac{\pi \gamma}{f_o} \right)^q \quad (3.6-5)$$

where $q = (p-1)/2$, $\Gamma(x)$ is the Gamma function, T is the spectral strength, and $K_y(x)$ is the Bessel function of imaginary argument. In Figure 3.6-1, the RMS difference in carrier phase between two GPS receivers is plotted as a function of the baseline length in an East-West direction in the presence of phase scintillations (the five curves represent different outer scale size parameters, f_o). These curves assume that the two receivers will be subject to the same phase scintillation spatial patterns, but with a delay that is a function of the baseline length, S , and the pattern velocity, v_p . In this figure, the effects of thermal noise and amplitude scintillations have been ignored as they will be independent of the baseline length (ie. it has been assumed that σ_{n1}^2 and σ_{n2}^2 are both zero). This figure shows that although the single difference error depends on the outer scale size parameter, f_o , in general the baseline length must be less than a few hundred metres in order to significantly reduce the impact of phase scintillations.

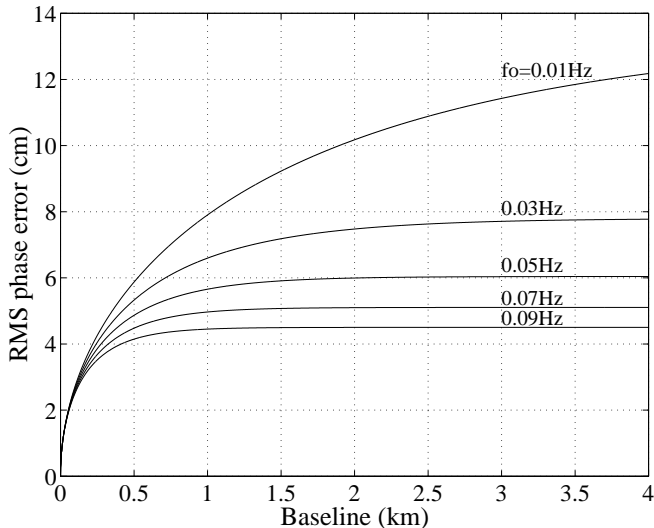


Figure 3.6-1: $\sigma_{\Delta\phi}$ as a function of f_o and the baseline length in the presence of scintillations. Parameter values are $T = -15$ dBadians $^2/\text{Hz}$, $p = 2$, $v_p = 150\text{m/s}$, and $f = L1$.

This analysis assumes that the irregularities are infinitely long, field-aligned, rod like structures. Under this model, the component of $\sigma_{\Delta\phi}^2$ which is produced by phase scintillations is dependent only on the East-West component of the baseline length. For a pair of receivers placed at two arbitrary locations, the variance of the single difference observable can be obtained from the previous expression, but with γ replaced by $S|\sin(\alpha)|/v_p$, where α is the azimuth of the baseline. If it is assumed that the irregularities are not field aligned, then the decorrelation with distance will be much less dependent on

the direction of the baseline and the direction of velocity of the patterns (indeed, for vertical propagation it will be independent).

In Figure 3.6-2, the RMS phase error from thermal noise and amplitude scintillations (σ_ϑ , Section 3.3.3) is plotted as a function of S_4 for a range of loop bandwidths. This result is based on the fast AGC model and the Tikhonov PDF for the modulo π reduced phase error, ϑ . By comparing this with Figure 3.6-1, it is apparent that the contribution to the phase estimate error from thermal noise and amplitude scintillations, $\sqrt{\sigma_{n1}^2 + \sigma_{n2}^2}$, is quite small compared to the contribution from phase scintillations, even over relatively short baselines, quite small values of f_o and large values of S_4 .

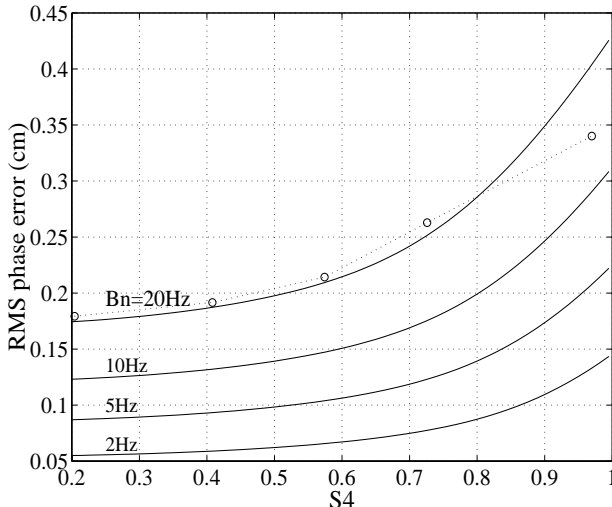


Figure 3.6-2: The RMS phase error (modulo π) as a function of S_4 and the loop bandwidth. Parameter values are $C/N_0 = 38\text{dBHz}$, $T = 0$, and $f = L1$. Simulation results are also shown for $B_n = 20\text{Hz}$ (the dotted line).

Using WBMOD, it is theoretically possible to determine $\sigma_{\Delta\phi}$ for each of the satellites in a receiver's field of view. However, the accuracy of the results will depend on the accuracy with which the parameters T , p , f_o and v_e are modelled in WBMOD. Although the models for T , p and v_e are quite sophisticated, the model for f_o is rather crude. Consequently, at this stage WBMOD is not considered to be a very effective tool for predicting the effects of scintillations on CPDGPS.

3.7. Carrier frequency tracking loops

Frequency locked loops (FLLs) or Automatic Frequency Control loops (AFCs) track the frequency of the GPS carrier and are normally used during times when the carrier phase is difficult to track or during acquisition¹. Indeed, many receivers use FLL assisted PLL's and will automatically transition to FLL operation when phase locked loop tracking is no longer possible [99]. The FLL discriminator estimates the carrier frequency by measuring the change in the carrier phase over a finite interval of time, Δt . As these frequency estimates will in general be sensitive to changes in the sign of the navigation data, they are usually obtained within the period of a data bit². The general form of an FLL is very similar to that of a PLL (compare Figure 3.7-1 with Figure 3.1-1). The principal differences lie in the discriminator algorithm (see Table 3.7-1) and in the additional integrator prior to the loop VCO (the loop filter, $F(s)$, is identical to the phase locked loop filter from Table 3.1-2).

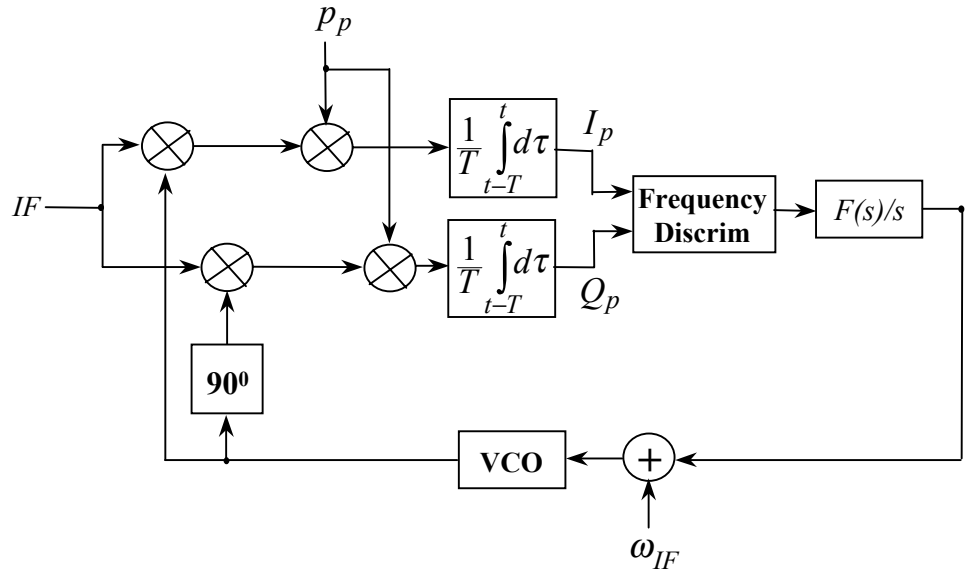


Figure 3.7-1: Representation of a generic frequency locked loop.

For small frequency errors (ie. $\phi_{\epsilon_2} - \phi_{\epsilon_1}$ is small compared to 1 radian, where $\phi_{\epsilon_i} = \phi_{\epsilon}(t_i)$), the output of each discriminator is proportional to $d\phi_{\epsilon}/dt$. Under this condition, the

¹ However, some receivers such as the Miniature Airborne GPS Receiver or MAGR only track the carrier frequency.

² This is not true of decision directed and Atan2 discriminators.

linear equivalent circuit of an FLL has a similar form to the linear equivalent circuit of a PLL (see Figure 3.7-2).

Discriminator	Discriminator output
$\frac{\beta}{\Delta t}$	$\frac{\tilde{A}^2 \sin(\phi_{\varepsilon_2} - \phi_{\varepsilon_1})}{\Delta t}$
$\frac{\beta \text{sign}(\alpha)}{\Delta t}$	$\frac{\tilde{A}^2 \sin(\phi_{\varepsilon_2} - \phi_{\varepsilon_1})}{\Delta t}$
$\frac{\text{Atan}(Q_{P_2}/I_{P_2}) - \text{Atan}(Q_{P_1}/I_{P_1})}{\Delta t}$	$\frac{\phi_{\varepsilon_2} - \phi_{\varepsilon_1}}{\Delta t}$
$\frac{\text{Atan2}(\beta, \alpha)}{\Delta t}$	$\frac{\phi_{\varepsilon_2} - \phi_{\varepsilon_1}}{\Delta t}$

Table 3.7-1: Typical frequency locked loop discriminators. \tilde{A} is the filtered signal amplitude, $\alpha = I_{P_1}I_{P_2} + Q_{P_1}Q_{P_2}$, $\beta = I_{P_1}Q_{P_2} - I_{P_2}Q_{P_1}$, $\Delta t = t_2 - t_1 \leq 10 \text{ ms}$, I_{P_1} and Q_{P_1} are the I and Q signals at time t_1 , and I_{P_2} and Q_{P_2} are the I and Q signals at time t_2 .

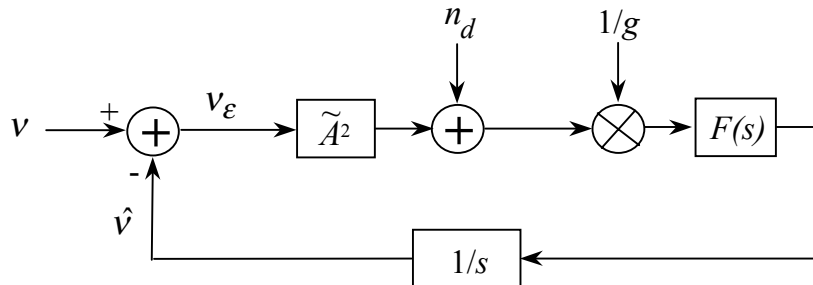


Figure 3.7-2: Linear equivalent model of a frequency locked loop (for either of the first two discriminator types).

The transfer functions and noise bandwidths of a frequency locked loop are the same as those given in Section 3.1 for a phase locked loop. The mean-square frequency error is also very similar to the mean-square carrier phase error and is given by

$$E\{v_e^2\} = \int_{-\infty}^{\infty} [|1 - H(f)|^2 S_v(f) + |H(f)|^2 S_{n_d}(f)] df \quad (3.7-1)$$

where f is the fluctuation frequency of the carrier frequency v , $S_{n_d}(f)$ is the power spectral density of frequency errors associated with thermal noise, and $S_v(f)$ is the

power spectral density of input frequency processes such as dynamics and phase scintillations.

3.7.1. The impact of phase scintillations on frequency tracking loops

The power spectral density of the input frequency process is given by

$$\begin{aligned} S_v(f) &= E\{v(f)v(f)^*\} \\ &= E\{(j2\pi f)\Phi(f).(-j2\pi f)\Phi(f)^*\} \\ &= (2\pi f)^2 \cdot S_\phi(f) \end{aligned} \quad (3.7-2)$$

where $S_\phi(f)$ is the power spectral density of the input phase process. For phase scintillations, $S_\phi(f) = S_{\phi_p}(f) = \frac{\mathbf{T}}{(f_o^2 + f^2)^{p/2}}$. As the frequency errors resulting from phase scintillations are zero-mean, the mean-square frequency error is

$$\begin{aligned} \sigma_{v_{ep}}^2 &= \int_{-\infty}^{\infty} |1 - H(f)|^2 (2\pi f)^2 S_{\phi_p}(f) df \\ &= \int_{-\infty}^{\infty} \frac{f^{2k}}{(f^{2k} + f_n^{2k})} \frac{\mathbf{T}(2\pi f)^2}{(f_o^2 + f^2)^{p/2}} df \\ &\approx (2\pi)^2 \mathbf{T} \int_{-\infty}^{\infty} \frac{|f|^{2k+2-p}}{(f^{2k} + f_n^{2k})} df, \quad p < 2k+2 \end{aligned} \quad (3.7-3)$$

For $3 < p < 2k+2$ this becomes

$$\sigma_{v_{ep}}^2 \approx \frac{(2\pi)^3 \mathbf{T}}{2k f_n^{p-3} \sin([p-3]\pi/2k)} \quad (3.7-4)$$

For $p < 3$ the integral in Equation (3.7-3) is infinite.

Equation (3.7-3) implies that there is no limit to the rate of phase fluctuation that can be detected by the FLL discriminator. Consequently, very low level but high frequency phase fluctuations can introduce significant frequency jitter. Under these circumstances, the frequency error is given by

$$\begin{aligned}
v_\epsilon &= v - \hat{v} \\
&= \frac{d\phi}{dt} - \frac{d\hat{\phi}}{dt} \\
&= \frac{d\phi_\epsilon}{dt}
\end{aligned} \tag{3.7-5}$$

where $\phi_\epsilon = \phi - \hat{\phi}$. However, as the incoming phase process, ϕ , is only sampled every T seconds, what is actually detected by the discriminator is

$$\begin{aligned}
v_\epsilon &= \frac{\phi_2 - \phi_1}{T} - \frac{\hat{\phi}_2 - \hat{\phi}_1}{T} \\
&= \frac{\phi_{\epsilon 2} - \phi_{\epsilon 1}}{T}
\end{aligned} \tag{3.7-6}$$

where ϕ_i and $\phi_{\epsilon i}$ imply $\phi(t_i)$ and $\phi_\epsilon(t_i)$ respectively, and $t_2 - t_1 = T$. Consequently, the power spectral density of the incoming phase process will be limited to $1/2T$ Hz. Although aliasing will cause the power spectral density to fold back on itself for frequencies beyond $1/2T$ Hz, we can approximate the effect of sampling by limiting the integral in Equation (3.7-3) to $\mp 1/2T$ Hz. By ignoring spectral foldover in this way, the resulting variance will be slightly less than the actual value. However, the error should not be too large as the power spectral density falls off according to a power-law relationship.

The variance obtained by limiting the power spectral density to $1/2T$ Hz is useful for determining the tracking state of the FLL. From [47] and [99], the tracking threshold of an FLL is defined as the point at which the 3σ frequency jitter from all sources equals $\pi/2$ radians in one T second period. Therefore, it is given by

$$\sigma_{v_\epsilon}^2 \Big|_{Th} = \left(\frac{\pi}{6T} \right)^2 \text{ (radians/s)}^2 \tag{3.7-7}$$

Consequently, for the FLL to remain in lock, the following condition must be met

$$\begin{aligned}
E\{v_\epsilon^2\} &< \sigma_{v_\epsilon}^2 \Big|_{Th}, \text{ or} \\
E\{[\phi_{\epsilon 2} - \phi_{\epsilon 1}]^2\} &< \left(\frac{\pi}{6} \right)^2, \text{ radians}^2
\end{aligned} \tag{3.7-8}$$

The threshold spectral strength for phase scintillations is therefore (from Equation (3.7-3))

$$T|_{Th} = \frac{\left[\sigma_{v\epsilon}^2 |_{Th} - \sigma_{vT}^2 \right]}{(2\pi)^2 \int_{-1/2T}^{1/2T} \frac{|f|^{2k+2-p}}{(f^{2k} + f_n^{2k})} df}, \quad p < 2k + 2 \quad (3.7-9)$$

where σ_{vT}^2 is the thermal noise component of the frequency error (see Appendix D, Equation (D-21)). In Figure 3.7-3, the difference in the threshold spectral strengths between a frequency locked loop and a phase locked loop are plotted as a function of the spectral index and the loop noise bandwidth (Equation (3.2-10) is used for the phase locked loop threshold). It is clear from this figure that the frequency locked loop is in general less susceptible to phase scintillations than the phase locked loop (ie. the difference in thresholds is positive for all values of p and B_n). This is particularly true for narrow bandwidth tracking loops and large values of p .

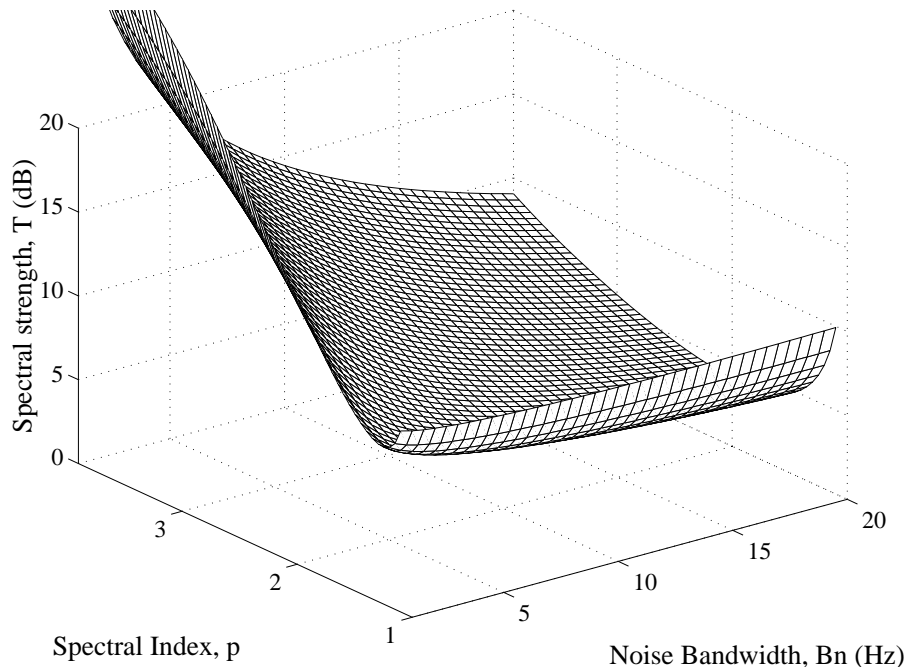


Figure 3.7-3: The difference between the threshold spectral strength of a frequency locked loop and the threshold spectral strength of a Costas phase locked loop. Parameter values are $C/N_o = 41.5 \text{ dBHz}$, $T = 20 \text{ ms}$, and $k = 2$ (ie. second order loops).

3.7.2. The impact of amplitude scintillations on frequency tracking loops

From Equation (D-21) in Appendix D, the thermal noise variance in an FLL is given by

$$\sigma_{v_\epsilon}^2 \Big| = \frac{4F_3B_n}{T^2 C/N_o} \left[1 + \frac{1}{TC/N_o} \right] \text{ (radians/s)}^2$$

where $F_3 = 1$ for high C/N_o and 2 for low C/N_o (near the tracking threshold). By making use of the following relationship

$$C/N_o|_{Th} = \frac{\tilde{A}_{Th}^2}{\mathbf{A}^2} \times C/N_o \quad (3.7-10)$$

where $C/N_o|_{Th}$ is the threshold carrier to noise density ratio, \tilde{A}_{Th} is the threshold amplitude, and \mathbf{A} is the quiescent or unperturbed signal amplitude, the following expression can be obtained for \tilde{A}_{Th}

$$\tilde{A}_{Th} = \mathbf{A} \sqrt{\frac{1 + \sqrt{1 + 2\alpha}}{\alpha T C/N_o}} \quad (3.7-11)$$

where $\alpha = \frac{T\sigma_{vT}^2|_{Th}}{2F_3B_n}$, $\sigma_{vT}^2|_{Th} = \sigma_{v_\epsilon}^2|_{Th} - \sigma_{v_{ep}}^2$ is the threshold variance due to thermal noise alone, $\sigma_{v_\epsilon}^2|_{Th}$ is given by Equation (3.7-7), and $\sigma_{v_{ep}}^2$ is the contribution to the tracking error variance from phase scintillations (Equation (3.7-3)).

Equation (3.7-11) can be compared with the equivalent expression for a PLL which is (from Equation (3.4-2))

$$\tilde{A}_{Th} = \mathbf{A} \sqrt{\frac{1 + \sqrt{1 + \beta}}{\beta T C/N_o}} \quad (3.7-12)$$

where $\beta = \frac{2\sigma_{\phi T}^2|_{Th}}{TB_n}$, $\sigma_{\phi T}^2|_{Th} = \sigma_{\phi_\epsilon}^2|_{Th} - \sigma_{\phi_{ep}}^2$ is the threshold variance due to thermal noise alone, $\sigma_{\phi_\epsilon}^2|_{Th} = (\pi/12)^2$ (Equation (3.2-9)), and $\sigma_{\phi_{ep}}^2$ is the contribution to the tracking error variance from phase scintillations (Equation (3.2-8)).

Consequently, if T and C/N_o are the same for each loop, the ratio of the two threshold amplitude values is given by

$$\frac{\tilde{A}_{Th}|_{FLL}}{\tilde{A}_{Th}|_{PLL}} = \sqrt{\frac{[1 + \sqrt{1 + 2\alpha}]\beta}{[1 + \sqrt{1 + \beta}]\alpha}} \quad (3.7-13)$$

If the effects of phase scintillations are ignored (ie. $\sigma_{v_{ep}}^2 = \sigma_{\phi_{ep}}^2 = 0$), and $F_3 = 2$ is assumed (ie. near the tracking threshold), Equation (3.7-13) reduces to $\sqrt{2}$. Consequently, the threshold signal power is 3dB higher for an FLL assuming that T is the same for both loops. As a result, FLL's will be marginally more susceptible to amplitude scintillations than PLL's.

These results suggest that in general, FLL's are more robust to scintillations than PLL's. Also, because FLL's are much less susceptible to phase scintillations, the optimum bandwidth of an FLL should be less than the optimum bandwidth of a PLL.

3.8. Conclusions

The analysis carried out in this chapter suggests that in general, the carrier tracking loops of full code correlation GPS receivers are quite robust to scintillations, even when the levels of scintillation activity are quite high. It was shown that as the carrier loop bandwidth increases, the susceptibility to amplitude scintillations increases, while the susceptibility to phase scintillations decreases. Consequently, an optimum bandwidth exists for minimum probability of losing lock which depends on the relative contributions of amplitude and phase scintillation activity, as well as the quiescent signal level and the presence of dynamics.

For a given level of ionospheric disturbance, the geometry of the propagation path affects the ratio of amplitude to phase scintillation activity as well as the absolute levels of scintillation activity. Therefore, geometry will affect both the optimum bandwidth of a tracking loop and its overall susceptibility to scintillations (for this reason, the optimum bandwidths will be different for each channel in a receiver). It was found that propagation paths that penetrate highly disturbed regions of the ionosphere at low elevation angles generally experienced higher levels of amplitude and phase scintillation

activity. It was also found that an increase in the effective scan velocity of the propagation path through the irregularity layer resulted in an increase in the phase scintillation spectral strength, and therefore an increase in the susceptibility of narrow bandwidth tracking loops to scintillations. Although the dependence of the scan velocity on the geometry and the receiver velocity is quite complex, it can be said that in general, under very high velocity conditions, the scan velocity is likely to increase on most propagation paths, thus increasing the probability of losing lock.

Carrier tracking loops are generally very robust to signal fades of short duration, particularly if the bandwidth of the tracking loop is narrow. Indeed, for fades with a sufficiently short duration, the probability of a cycle slip can approach zero, irrespective of the fade depth. However, the precise effect on a tracking loop will depend on the discriminator algorithm, the quiescent signal level, and the presence of other factors such as dynamics.

RMS carrier phase errors of several centimetres can be introduced into satellite range measurements as a result of scintillations. Generally, these errors will become decorrelated over distances of a few kilometres, depending upon the magnitude of the ionospheric outer scale size parameter, f_o , and the geometry of the baseline. This may have a significant impact on carrier phase DGPS observations made in equatorial regions during solar maximum, particularly for baselines of a kilometre or more.

Frequency locked loops are more robust to phase scintillations but slightly less robust to amplitude scintillations than phase locked loops for the same loop bandwidth and pre-detection integration period. Therefore, receivers that make use of frequency locked loops, either as a primary means of carrier tracking or as a fall-back strategy to phase locked loops, are likely to be more tolerant to scintillations than receivers that employ only phase locked loops.

Many of the results presented in this chapter are based on the assumption that the phase scintillation spectral strength, T , is uncorrelated with the amplitude (ie. the rate of change and strength of phase scintillations are uncorrelated with the amplitude). If T is negatively correlated to the amplitude (ie. T increases when the amplitude decreases), then the combined effects of amplitude and phase scintillations on carrier tracking loops may be greater than is suggested by these results.

Chapter 4

Code tracking loops

This chapter examines the effects of scintillations on code tracking loops. In Section 4.1, a signal processing model of a code tracking loop is given which is based on a generic non-coherent delay locked loop with a normalised Early-Late power discriminator. In Section 4.2, it is shown that the effects of phase scintillations on a code tracking loop are negligible and can therefore be ignored. In section 4.3, the impact of amplitude scintillations on the range measurement accuracy of a code loop is examined. It is shown that unless the levels of amplitude scintillation activity are very large (ie. S_4 close to unity), the additional thermal noise associated with amplitude scintillations is on average quite low, although occasional noise spikes may occur when the amplitude undergoes very deep fades. Finally, in Section 4.4 it is shown that because GPS signals are narrowband, it is expected that frequency selective scintillation effects will produce negligible distortion of the PRN codes.

4.1. Code loop model

Figure 4.1-1 is a representation of a generic, non-coherent delay locked loop (DLL). The function of the DLL is to track the GPS PRN codes and to provide estimates of the code delay from which pseudorange measurements can be obtained. The DLL mixes the baseband I and Q signals from the carrier tracking loop with an early code, p_E , a prompt code, p_P , and a late code, p_L which are produced by a PRN code generator and a 3 bit shift register¹. The resulting early, prompt and late I and Q signals are then filtered by a bank of pre-detection filters and passed into the DLL discriminator. The function of the discriminator is to determine the difference in code phase between the received GPS

¹ The shift register spacing is typically $\frac{1}{2}$ code chips

signal and the replica signal represented by the prompt code, p_P . A list of the most common discriminator types and their delay error functions is given in Table 4.1-1.

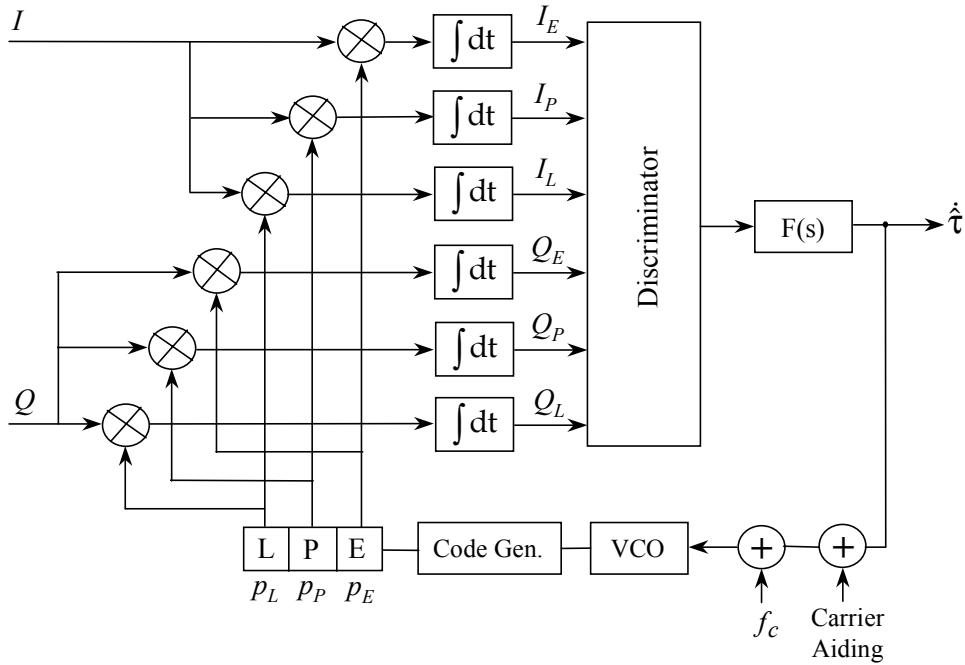


Figure 4.1-1: Representation of a generic delay locked loop.

Discriminator algorithm	Discriminator name	Delay error function
$\sum(I_E - I_L)I_P + \sum(Q_E - Q_L)Q_P$	Dot product	$\alpha(R_E - R_L)R_P$
$\sum(I_E^2 + Q_E^2) - \sum(I_L^2 + Q_L^2)$	Early-Late power	$\alpha(R_E^2 - R_L^2)$
$\sum\sqrt{I_E^2 + Q_E^2} - \sum\sqrt{I_L^2 + Q_L^2}$	Early-Late envelope	$\beta(R_E - R_L)$

Table 4.1-1: Common delay locked loop discriminators. α and β are functions of the signal amplitude ($\alpha = \tilde{A}^2$, $\beta = \tilde{A}$), $R(\tau)$ is the autocorrelation function of the PRN code, $R_E = R(\tau_e + T_c/2)$, $R_L = R(\tau_e - T_c/2)$, $R_P = R(\tau_e)$, $\tau_e = \tau - \hat{\tau}$ is the delay error and T_c is the code chip width.

The discriminator errors given in Table 4.1-1 are a function of the autocorrelation function of the PRN code which is given by

$$\begin{aligned}
 R(\tau) &= \frac{1}{T_p} \int_{-T_p/2}^{T_p/2} p(t + \tau) \cdot p(t) dt \\
 &= \begin{cases} 1 - \frac{|\tau|}{T_c}, & |\tau| \leq T_c \\ 0, & |\tau| > T_c \end{cases} \quad (4.1-1)
 \end{aligned}$$

where T_c is the code chip width (approximately 1μs for the C/A-Code and 100ns for the P-Code), and T_p is the code period (1ms for the C/A-Code and 7 days for the P-Code). Although the period of the P-Code is extremely long, its autocorrelation function can be well approximated over relatively short code segments. The delay error function of an Early-Late power discriminator is illustrated in Figure 4.1-2.

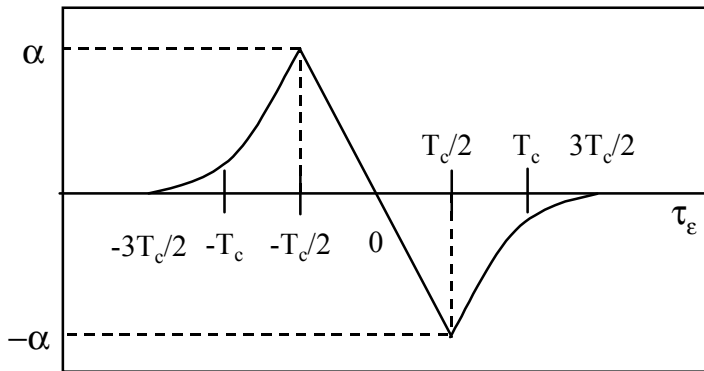


Figure 4.1-2: Delay error function of an Early-Late power discriminator.

It is clear from this figure that for delay errors in the range $-T_c/2 \leq \tau_e \leq T_c/2$, the delay error function is a straight line given by $-2\alpha\tau_e/T_c$. Errors larger than this will eventually cause the code loop to lose lock (ie. the code phase estimate will drift away from the true code phase). From the discriminator, the code error estimates are passed through a code loop filter, $F(s)$, and then on to the code VCO. The frequency of the code VCO, and therefore the code chipping rate, is then adjusted in a direction that minimises subsequent delay errors (this is a very similar process to the one that occurs in a phase locked loop). In addition, a carrier aiding signal from the carrier loop is used to remove the majority of the Doppler induced code phase error allowing the use of a much narrower loop bandwidth and a lower loop order (typically 1st order).

An analysis of the code loop which tackles the issue of scintillation induced amplitude variations is given below.

The early, prompt and late codes from the code generator are mixed with the baseband I and Q signals to give (from Equation 3.1-1)

$$\begin{aligned}
I'_E &= A(t)p(t-\tau)p(t-\hat{\tau}+T_c/2)d(t-\tau)\cos(\phi_e) + n'_{IE} \\
Q'_E &= A(t)p(t-\tau)p(t-\hat{\tau}+T_c/2)d(t-\tau)\sin(\phi_e) + n'_{QE} \\
I'_P &= A(t)p(t-\tau)p(t-\hat{\tau})d(t-\tau)\cos(\phi_e) + n'_{IP} \\
Q'_P &= A(t)p(t-\tau)p(t-\hat{\tau})d(t-\tau)\sin(\phi_e) + n'_{QP} \\
I'_L &= A(t)p(t-\tau)p(t-\hat{\tau}-T_c/2)d(t-\tau)\cos(\phi_e) + n'_{IL} \\
Q'_L &= A(t)p(t-\tau)p(t-\hat{\tau}-T_c/2)d(t-\tau)\sin(\phi_e) + n'_{QL}
\end{aligned} \tag{4.1-2}$$

where the superscript ' indicates that the signals are at a point immediately prior to the pre-detection filters. If it is again assumed that the pre-detection filters are synchronised to the navigation data, and that the carrier phase errors are relatively constant over the integration period, T , then the I and Q signals will become (only I_E is shown)

$$I_E = d(t-\tau)\cos(\phi_e) \frac{1}{T} \int_{t-T}^t A(u)p(u-\tau)p(u-\hat{\tau}+T_c/2).du + n_{IE} \tag{4.1-3}$$

where $\sigma_{n_{IE}}^2 = N_o/T$. If the integral in Equation (4.1-3) is divided into L equal parts in which $A(u)$ is approximately constant, we have

$$I_E = d(t-\tau)\cos(\phi_e) \frac{1}{T} \sum_{j=1}^L \left[\int_{t-jT/L}^{t-(j-1)T/L} A_j p(u-\tau)p(u-\hat{\tau}+T_c/2).du \right] + n_{IE} \tag{4.1-4}$$

where A_j represents the constant amplitude value at each T/L second interval. By removing A_j from the integral and letting $L = 20$ (giving $T/L = 1\text{ms}$ which is the period of the C/A-Code, assuming $T=20\text{ ms}$), the integral in Equation (4.1-4) becomes the autocorrelation function of the code². Thus,

$$\begin{aligned}
I_E &= d(t-\tau)\cos(\phi_e) \frac{1}{L} \sum_{j=1}^L A_j \left[\frac{L}{T} \int_{t-jT/L}^{t-(j-1)T/L} p(u-\tau)p(u-\hat{\tau}+T_c/2).du \right] + n_{IE} \\
&= d(t-\tau)\cos(\phi_e) R(\tau_e + T_c/2) \frac{1}{L} \sum_{j=1}^L A_j + n_{IE}
\end{aligned} \tag{4.1-5}$$

² This is also an accurate approximation for the P-Code even though its period is much greater than 1ms.

The amplitude summation term can then be replaced with the filtered amplitude \tilde{A} giving (for all six signals)

$$\begin{aligned}
 I_E &= \tilde{A}d(t-\tau)R(\tau_e + T_c/2)\cos(\phi_e) + n_{IE} \\
 Q_E &= \tilde{A}d(t-\tau)R(\tau_e + T_c/2)\sin(\phi_e) + n_{QE} \\
 I_P &= \tilde{A}d(t-\tau)R(\tau_e)\cos(\phi_e) + n_{IP} \\
 Q_P &= \tilde{A}d(t-\tau)R(\tau_e)\sin(\phi_e) + n_{QP} \\
 I_L &= \tilde{A}d(t-\tau)R(\tau_e - T_c/2)\cos(\phi_e) + n_{IL} \\
 Q_L &= \tilde{A}d(t-\tau)R(\tau_e - T_c/2)\sin(\phi_e) + n_{QL}
 \end{aligned} \tag{4.1-6}$$

Notice that the prompt I and Q signals contain an $R(\tau_e)$ factor. This was ignored in the analysis given in Chapter 3 as τ_e was assumed to be zero (ie. perfect code tracking). The statistics of the various thermal noise terms, n_{IE}, n_{QE}, \dots etc, are examined in Appendix D.

This approximation assumes that the majority of the power in the amplitude scintillation power spectrum is at frequencies below 1 kHz (ie less than L/T Hz). This is considered to be quite an accurate approximation as the low frequency cutoff in the amplitude scintillation power spectrum is typically less than a few Hertz, even at very high platform velocities³. Therefore, for a spectral index, p , of 2.5⁴ and a low frequency cutoff, f_c , of 1 Hz, the power spectrum of amplitude at 1 kHz will be approximately 75dB below the cutoff value.

The filtered I and Q signals ($I_E, Q_E, I_P, Q_P, I_L, Q_L$) are processed in the code loop discriminator to produce code delay errors of the form given in Table 4.1-1. In all cases, the navigation data and carrier phase error terms will be eliminated by this process. Consequently, the code loop is referred to as non-coherent (ie. it does not require the carrier phase to remain in lock).

If it is assumed that the summations in the code loop discriminator are over m successive periods of the integrate and dump filter (ie. Tm seconds in total), the coefficients of the delay error function for the three un-normalised discriminators are

³ Scintillation frequencies are determined by the relative velocity between the spatial diffraction patterns and the receiver. At high relative velocities, the spectrum is translated to higher frequencies.

⁴ A spectral index of 2.5 is typical of equatorial scintillation activity.

$$\alpha_i = \sum_{j=i-m+1}^i \tilde{A}_j^2 \quad \text{and} \quad \beta_i = \sum_{j=i-m+1}^i \tilde{A}_j \quad (4.1-7)$$

where $\tilde{A}_j = \int_{(j-1)T}^{jT} A(u) du$ are the amplitude values after filtering. This assumes that τ_e is relatively constant over the time interval Tm (a reasonable assumption if the loop is expected to track the delay).

The code loop can be represented in an equivalent linear form in which the mixers and pre-detection filters are replaced by an adder, and the discriminator is replaced by the appropriate delay error function. For an Early-Late power discriminator, this representation is given in Figure 4.1-3.

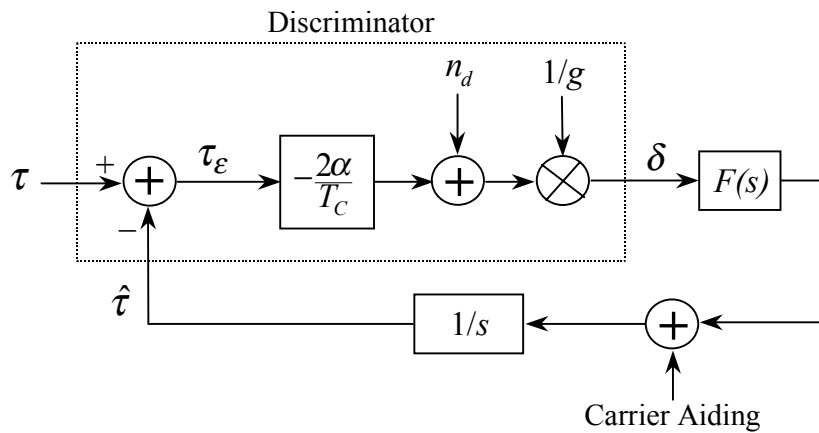


Figure 4.1-3: Linear model of a delay locked loop with an Early-Late power discriminator.

In this form, the delay errors are assumed to be in the linear range, $-T_c/2 \leq \tau_e \leq T_c/2$ (for a $1/2$ chip spacing between the Early, Prompt and Late codes). Consequently, the loop is assumed to be in lock. In Figure 4.1-3, n_d is the thermal noise translated to the discriminator output and includes cross-terms between the input thermal noise term and the I and Q signals. An expression for n_d for the Early-Late power discriminator is given in Section 4.3.

The delay on the received GPS PRN code, τ , can be represented in the following way

$$\tau = T + \tau_d + \tau_p + \tau_o \quad (4.1-8)$$

where T represents the constant contributions to the code delay (including the mean satellite to receiver range, satellite and receive clock biases, benign ionospheric delays, benign tropospheric delays and hardware channel biases), τ_d represents the effects of satellite and platform motion, τ_p represents the effects of ionospheric phase scintillations on the code, and τ_o represents other delay noise effects (eg tropospheric scintillations and VCO oscillator jitter etc.).

For a normalised discriminator, the transfer function of the DLL is given by

$$H(s) = \frac{\hat{T}(s)}{T(s)} = \frac{F(s)}{s + F(s)} \quad (4.1-9)$$

The transfer functions and noise bandwidth's of the delay locked loop are the same as those defined for the phase locked loop in Table 3.1-2, although the loop order is usually no greater than 2 because of carrier aiding.

4.2. The impact of phase scintillations on code tracking loops

The mean-square delay tracking error resulting from code delay noise and thermal noise for the linearised code tracking loop is given by

$$E\{\tau_e^2\} = \int_{-\infty}^{\infty} \left[|1 - H(f)|^2 S_\tau(f) + |H(f)|^2 S_{n_d}(f) \right] df \quad (4.2-1)$$

where $S_\tau(f)$ is the PSD of the input delay process and $S_{n_d}(f)$ is the PSD of the thermal noise, n_d . If it is assumed that the carrier phase advance and code group delay are equal in magnitude under scintillations conditions (as they are under quiescent ionospheric conditions, Davies [27]), the code delay can be related to the carrier phase advance by

$$\tau_p(t) = -\phi_p(t) \frac{f_p}{2\pi f_L}, \quad \text{chips} \quad (4.2-2)$$

where $\phi_p(t)$ is the component of the carrier phase associated with phase scintillations (in radians), f_L is the L-band carrier frequency (L1 = 1575.42 MHz, L2 = 1227.6 MHz) and f_p is the PRN code chipping rate (C/A-Code: 1.023 Mchips/s, P-Code: 10.23 Mchips/s).

One of the undesirable consequences of carrier aiding of the code loop is that the code error resulting from ionospheric effects is doubled. This occurs because at L-band frequencies, the carrier phase is advanced and the code phase is delayed by equal amounts (Davies [27]). Consequently, in the presence of carrier aiding, the component of the code delay associated with phase scintillations becomes

$$\begin{aligned} \tau_p(t) &= -2 * \phi_p(t) \frac{f_p}{2\pi f_L} \\ &= -\xi \phi_p(t), \quad \text{chips} \end{aligned} \quad (4.2-3)$$

In Table 4.2-1, the scaling factor ξ is given for the four combinations of carrier frequency and code chipping rate which may be encountered in GPS.

ξ	C/A-Code	P-Code
L1	2.07×10^{-4}	2.07×10^{-3}
L2	2.65×10^{-4}	2.65×10^{-3}

Table 4.2-1: Scaling factor, ξ , as a function of carrier frequency and code type.

The PSD of the ionospheric delay process is given by

$$\begin{aligned}
S_{\tau_p}(f) &= E\left\{F(\tau_p(t)) * F(\tau_p(t))^*\right\} \\
&= E\left[\xi^2 F(\phi_p(t)) * F(\phi_p(t))^*\right] \\
&= \xi^2 S_{\phi_p}(f) \text{ chips}^2/\text{Hz}
\end{aligned} \tag{4.2-4}$$

where $F()$ denotes the Fourier Transform. Consequently, the variance of the delay error resulting from phase scintillations (in chips²) is ξ^2 times smaller than the corresponding phase error variance for the carrier loop (in radians²) for the same loop order and bandwidth. Therefore, as the thermal noise errors on the code and carrier loops are of a comparable size, it is reasonable to expect that phase scintillations will have a negligible effect on the delay errors (ie. they will be swamped by the effects of thermal noise).

The effects of phase scintillations on the code pseudorange measurements may, however, be significant, particularly if f_o is very small. The variance of the code pseudorange error is given by

$$\begin{aligned}
\sigma_{\hat{\tau}_p}^2 &= \int_{-\infty}^{\infty} |H(f)|^2 S_{\tau}(f) df \\
&= \xi^2 \sigma_{\hat{\phi}_p}^2, \text{ chips}^2 \\
&= (T_c \xi)^2 \sigma_{\hat{\phi}_p}^2, \text{ m}^2
\end{aligned} \tag{4.2-5}$$

Where $\sigma_{\hat{\phi}_p}^2$ is the variance of the carrier phase range error due to phase scintillations, and T_c is the code chip width in metres. The low frequency components of the phase scintillation power spectrum provide the greatest contribution to $\sigma_{\hat{\tau}_p}^2$ (ie. $\sigma_{\hat{\tau}_p}^2$ is very sensitive to f_o). However, as these are associated more with the background ionosphere than with scintillations, it can be argued that phase scintillations will probably have a negligible effect on the pseudorange.

4.3. The impact of amplitude scintillations on code tracking loops

In this section, an expression is derived for the delay error variance of a delay locked loop in the presence of amplitude scintillations and thermal noise. To simplify the analysis, other sources of noise including phase scintillations, dynamics and oscillator phase noise etc. have been ignored. It is also assumed that code distortion caused by frequency selective scintillation effects is negligible at GPS frequencies because of the narrow bandwidth of the GPS PRN codes (see Section 4.4).

The discriminator used in this analysis is an Early-Late power discriminator which is normalised by a post-detection AGC (see Table 4.1-1). The AGC ensures that the principal effect of amplitude scintillations is to scale the thermal noise component of the tracking error rather than altering the loop transfer function. The output of a normalised Early-Late power discriminator is given by (see Table 4.1-1).

$$\delta = \frac{1}{g.k} \sum_{i=1}^k \left[(I_{E_i}^2 + Q_{E_i}^2) - (I_{L_i}^2 + Q_{L_i}^2) \right] \quad (4.3-1)$$

where k represents the number of T second epochs over which data is averaged in the discriminator, I_{E_i} , Q_{E_i} , I_{L_i} and Q_{L_i} represent the early and late I and Q signals from the pre-detection filters (see Equation (4.1-6)), and g is the output of a post-detection AGC. This expression is based on the assumption that the discriminator is operating within the linear region (ie. $-T_c/2 \leq \tau_e \leq T_c/2$). The AGC output can be approximated by (assuming that τ_e is small)

$$\begin{aligned} g &= \frac{1}{k} \sum_{i=1}^k [I_{P_i}^2 + Q_{P_i}^2] \\ &= \frac{1}{k} \sum_{i=1}^k \left[\tilde{A}_i^2 R_p^2 + 2\tilde{A}_i d(t_i - \tau) R_p (n_{IP_i} \cos(\phi_e) + n_{QP_i} \sin(\phi_e)) + n_{IP_i}^2 + n_{QP_i}^2 \right] \\ &\approx \frac{1}{k} \sum_{i=1}^k \tilde{A}_i^2 + \varepsilon_g \end{aligned} \quad (4.3-2)$$

where $R_p = R(\tau_e)$ is the cross-correlation function of the prompt code with the satellite code and is approximately equal to one for small values of τ_e , and ε_g is the thermal noise component of the AGC gain factor.

The expression for the discriminator output can be expanded to give

$$\delta = \frac{1}{g \cdot k} \sum_{i=1}^k \left[\tilde{A}_i^2 \left(R_E^2 - R_L^2 \right) + 2 \tilde{A}_i d(t_i - \tau) \left(R_E n_{E_i} - R_L n_{L_i} \right) + n_{IE_i}^2 + n_{QE_i}^2 - n_{IL_i}^2 - n_{QL_i}^2 \right] \quad (4.3-3)$$

where $R_E = R(\tau_\epsilon + T_c/2)$ and $R_L = R(\tau_\epsilon - T_c/2)$ are the cross-correlation functions of the early and late codes with the satellite code (assuming a $\frac{1}{2}$ chip correlator spacing), τ_ϵ is the true delay error, and $n_{E_i} = n_{IE_i} \cos(\phi_\epsilon) + n_{QE_i} \sin(\phi_\epsilon)$ and $n_{L_i} = n_{IL_i} \cos(\phi_\epsilon) + n_{QL_i} \sin(\phi_\epsilon)$ are zero-mean, white, Gaussian random variables. The first term in the discriminator expression (Equation (4.3-3)) is proportional to the delay error and is given by

$$\begin{aligned} & \frac{1}{g \cdot k} \sum_{i=1}^k \tilde{A}_i^2 \left(R_E^2 - R_L^2 \right) \\ &= \left(R_E^2 - R_L^2 \right) \left(\frac{1}{k} \sum_{i=1}^k \frac{\tilde{A}_i^2}{g} \right) \\ &\approx R_E^2 - R_L^2 \quad \text{for } \epsilon_g \approx 0 \\ &= \gamma \tau_\epsilon \end{aligned} \quad (4.3-4)$$

where γ is the slope of the discriminator delay error function. For delay errors in the region $-T_c/2 \leq \tau_\epsilon \leq T_c/2$, the discriminator slope is

$$\gamma = -\frac{2}{T_c} \quad (4.3-5)$$

where T_c is the code chip width. The remaining terms in Equation (4.3-3) represent the effects of thermal noise and amplitude scintillations and are given by

$$n_{dN} = \frac{n_d}{g} = \frac{1}{g \cdot k} \sum_{i=1}^k \left[2 \tilde{A}_i d(t_i - \tau) \left(R_E n_{E_i} - R_L n_{L_i} \right) + n_{IE_i}^2 + n_{QE_i}^2 - n_{IL_i}^2 - n_{QL_i}^2 \right] \quad (4.3-6)$$

where n_d is the equivalent thermal noise term for an un-normalised discriminator. As n_{IE_i} , n_{QE_i} , n_{IL_i} , and n_{QL_i} are zero-mean random variables which are independent⁵ and identically distributed (IID) and independent of \tilde{A}_i and g ⁶, the thermal noise term, n_{dN} , must also be zero-mean. The variance of n_{dN} is therefore given by

⁵ For a $\frac{1}{2}$ chip correlator spacing, n_{IE_i} , n_{QE_i} , n_{IL_i} , and n_{QL_i} are all independent (see Appendix D).

⁶ g is a function of \tilde{A}_i , n_{IP_i} and n_{QP_i} which are all independent of n_{IE_i} , n_{QE_i} , n_{IL_i} , and n_{QL_i} for a $\frac{1}{2}$ chip correlator spacing.

$$\begin{aligned}
\sigma_{n_{dN}}^2 &= E\left\{ n_{dN}^2 \right\} \\
&= E\left\{ \frac{1}{(g.k)^2} \left[\sum_{i=1}^k \sum_{j=1}^k 2\tilde{A}_i d(t_i - \tau) (R_E n_{E_i} - R_L n_{L_i}) * 2\tilde{A}_j d(t_j - \tau) (R_E n_{E_j} - R_L n_{L_j}) + \right. \right. \\
&\quad 2 \sum_{i=1}^k \sum_{j=1}^k 2\tilde{A}_i d(t_i - \tau) (R_E n_{E_i} - R_L n_{L_i}) * (n_{IE_j}^2 + n_{QE_j}^2 - n_{IL_j}^2 - n_{QL_j}^2) + \\
&\quad \left. \left. \sum_{i=1}^k \sum_{j=1}^k (n_{IE_i}^2 + n_{QE_i}^2 - n_{IL_i}^2 - n_{QL_i}^2) * (n_{IE_j}^2 + n_{QE_j}^2 - n_{IL_j}^2 - n_{QL_j}^2) \right] \right\} \tag{4.3-7}
\end{aligned}$$

Again, as the four thermal noise terms are zero-mean and IID, the expectation of the second term in the variance expression is zero, and both the first and third terms are zero when $i \neq j$. Squaring also eliminates the navigation data from the first term (ie. $d(t_i - \tau)^2 = 1$). The variance expression therefore reduces to

$$\begin{aligned}
\sigma_{n_{dN}}^2 &= E\left\{ \frac{1}{(g.k)^2} \sum_{i=1}^k \left[4\tilde{A}_i^2 (R_E n_{E_i} - R_L n_{L_i})^2 + (n_{IE_i}^2 + n_{QE_i}^2 - n_{IL_i}^2 - n_{QL_i}^2)^2 \right] \right\} \\
&= \frac{1}{k^2} \sum_{i=1}^k \left[4E\left\{ \frac{\tilde{A}_i^2}{g^2} \right\} E\left\{ (R_E n_{E_i} - R_L n_{L_i})^2 \right\} + E\left\{ \frac{1}{g^2} \right\} E\left\{ (n_{IE_i}^2 + n_{QE_i}^2 - n_{IL_i}^2 - n_{QL_i}^2)^2 \right\} \right] \tag{4.3-8} \\
&= \frac{1}{k^2} \sum_{i=1}^k \left[4E\left\{ \frac{\tilde{A}_i^2}{g^2} \right\} (R_E^2 E\{n_{E_i}^2\} + R_L^2 E\{n_{L_i}^2\}) + E\left\{ \frac{1}{g^2} \right\} (4E\{n_{\alpha\beta_i}^4\} - 4[E\{n_{\alpha\beta_i}^2\}]^2) \right]
\end{aligned}$$

where α represents either I or Q, and β represents either E or L. From Equation (D-5) in Appendix D, the variance of $n_{\alpha\beta_i}$ is given by N_o/T where T is the pre-detection integration period. Also, as $n_{\alpha\beta_i}$ is a real, zero-mean, Gaussian random variable,

$E\{n_{\alpha\beta_i}^4\} = 3[E\{n_{\alpha\beta_i}^2\}]^2 = 3(N_o/T)^2$. In addition, the amplitude sequence is assumed to be stationary and so $E\{\tilde{A}_i^2\} = E\{\tilde{A}_j^2\} = E\{\tilde{A}^2\}$. Therefore, the variance reduces further to

$$\sigma_{n_{dN}}^2 = \frac{4N_o}{k.T} \left[(R_E^2 + R_L^2) E\left\{ \frac{\tilde{A}^2}{g^2} \right\} + 2 \frac{N_o}{T} E\left\{ \frac{1}{g^2} \right\} \right] \tag{4.3-9}$$

For a small delay error, the early and late autocorrelation functions, R_E and R_L , are approximately equal to $1/2$ giving

$$\sigma_{n_{dN}}^2 \approx \frac{2N_o}{k.T} \left[E\left\{ \frac{\tilde{A}^2}{g^2} \right\} + 4 \frac{N_o}{T} E\left\{ \frac{1}{g^2} \right\} \right] \tag{4.3-10}$$

The signal amplitude \tilde{A} and the AGC gain factor, g , can be normalised by dividing by the nominal (unperturbed) signal amplitude, \mathbf{A} , as follows

$$\tilde{A}_N = \frac{\tilde{A}}{\mathbf{A}}, \quad g_N = \frac{g}{\mathbf{A}^2} \quad (4.3-11)$$

By substituting $\tilde{A} = \mathbf{A} * \tilde{A}_N$, $g = \mathbf{A}^2 * g_N$ and $C/N_o = \mathbf{A}^2/2N_o$ into the variance expression, the following result is obtained

$$\sigma_{n_{dN}}^2 \approx \frac{1}{k.T C/N_o} \left[E \left\{ \frac{\tilde{A}_N^2}{g_N^2} \right\} + \frac{2}{T C/N_o} E \left\{ \frac{1}{g_N^2} \right\} \right] \quad (4.3-12)$$

The discriminator noise, $n_{dN}(t)$, consists of a sequence of random variables that are maintained at constant for kT seconds, but are uncorrelated between successive kT second epochs. Therefore, based on the analysis given in Appendix D for the Costas loop, the power spectral density of n_{dN} is given by

$$S_{n_{dN}}(f) = \sigma_{n_{dN}}^2 kT \operatorname{sinc}^2(fkT) \quad (4.3-13)$$

and the variance of the delay error resulting from thermal noise becomes

$$\begin{aligned} \sigma_{\tau_T}^2 &= \frac{1}{\gamma^2} \int_{-\infty}^{\infty} |H(f)|^2 S_{n_{dN}}(f) df \\ &= \frac{\sigma_{n_{dN}}^2 kT}{\gamma^2} \int_{-\infty}^{\infty} |H(f)|^2 \operatorname{sinc}^2(fkT) df \end{aligned} \quad (4.3-14)$$

As the bandwidth of the closed loop transfer function, $H(f)$, must be smaller than the bandwidth of the $\operatorname{sinc}(fkT)$ function⁷, the $\operatorname{sinc}^2(fkT)$ term can be approximated by one, giving

$$\begin{aligned} \sigma_{\tau_T}^2 &\approx \frac{2\sigma_{n_{dN}}^2 kT}{\gamma^2} \left[\frac{1}{2} \int_{-\infty}^{\infty} |H(f)|^2 df \right] \\ &= \frac{2\sigma_{n_{dN}}^2 kTB_n}{\gamma^2} \end{aligned} \quad (4.3-15)$$

⁷ In order to correctly track the desired signal (in this case the code delay process), the bandwidth of the pre-detection filters must be greater than the design bandwidth of the tracking loop.

where $B_n = \frac{1}{2} \int_{-\infty}^{\infty} |H(f)|^2 df$ is the loop noise bandwidth and $\gamma = -2/T_c$ is the slope of the delay error function. Combining Equations (4.3-12) and (4.3-14) gives

$$\begin{aligned}\sigma_{\tau_T}^2 &= \frac{B_n T_c^2}{2C/N_o} \left[E\left\{ \frac{\tilde{A}_N^2}{g_N^2} \right\} + \frac{2}{TC/N_o} E\left\{ \frac{1}{g_N^2} \right\} \right] \quad m^2 \\ &= \frac{B_n}{2C/N_o} \left[E\left\{ \frac{\tilde{A}_N^2}{g_N^2} \right\} + \frac{2}{TC/N_o} E\left\{ \frac{1}{g_N^2} \right\} \right] \quad \text{chips}^2\end{aligned}\quad (4.3-16)$$

If it is assumed that there are no amplitude scintillations (ie. $\tilde{A}_N^2 = 1$ and $g_N \approx \tilde{A}_N^2 = 1$), the delay error variance expression reduces to the standard form for a delay locked loop (see Equation (D-20), Appendix D), *viz*

$$\sigma_{\tau_T}^2 = \frac{B_n}{2C/N_o} \left[1 + \frac{2}{TC/N_o} \right] \quad \text{chips}^2 \quad (4.3-17)$$

Discussion

As the code loop is usually aided by Doppler estimates from the carrier loop, its noise bandwidth can be made quite narrow in order to minimise the effects of thermal noise. Indeed, if external Doppler aiding is provided by an inertial measurement unit, the code loop bandwidth can be as small as 0.1Hz [47]. Under these conditions, the bandwidth of the discriminator errors can be reduced significantly by increasing the size of k (ie. summing more terms in the discriminator). This will also reduce the effects of amplitude scintillations by an amount which depends on both the sample rate of the discriminator ($1/kT$), and the bandwidth of the scintillations. To quantify this effect, it is first necessary to show that the signal intensity under amplitude scintillation conditions is chi-squared distributed with $2m$ degrees of freedom (ie. χ_{2m}^2 where $m = 1/S_4^2$).

The PDF of a chi-squared random variable, X , with $2m$ degrees of freedom is given by [74]

$$f_X(x) = \begin{cases} \frac{(x/2)^{m-1} \exp(-x/2)}{2\Gamma(m)}, & x > 0 \\ 0, & x \leq 0 \end{cases} \quad (4.3-18)$$

If we let $x = 2mI/\langle I \rangle$ where $I = \tilde{A}^2$ is the signal intensity at the output of the pre-detection filters, and $\langle I \rangle = \mathbf{A}^2$ is the average value of I , the PDF of I can be found from

$$f_I(I) = f_X(x(I)) \left| \frac{dx}{dI} \right| \quad (4.3-19)$$

where $x(I) = \frac{2mI}{\langle I \rangle}$ and $\frac{dx}{dI} = \frac{2m}{\langle I \rangle}$. This leads to the following expression for the PDF of the intensity

$$f_I(I) = \begin{cases} \frac{m^m \cdot I^{m-1}}{\Gamma(m) \langle I \rangle^m} \exp(-m \cdot I / \langle I \rangle), & I > 0 \\ 0, & I \leq 0 \end{cases} \quad (4.3-20)$$

which is the Nakagami-m PDF for intensity (this can be obtained from Equation (2.1-8) through a simple change of variables). If k successive values of the random variable X are summed, the number of degrees of freedom of the resulting random variable will be increased. The amount by which the number of degrees of freedom increases will depend on the summation period, kT , and the correlation time, T_{CT} , of X . In Haykin, page 246 [39], the correlation time of a zero-mean, wide-sense stationary random process, $Z(t)$, is the time taken for the autocorrelation function, $R_Z(\tau)$, to reduce to a small fraction of $R_Z(0)$ (say 1%). For a random process, $X(t)$, that is not zero-mean, the correlation time can be defined as the time taken for the autocovariance function, $K_X(\tau)$, to reduce to a small fraction of $K_X(0)$. Therefore, the correlation time, T_{CT} , can be defined by

$$K_X(T_{CT}) = \varepsilon \quad (4.3-21)$$

where $K_X(\tau) = R_X(\tau) - [E\{X(t)\}]^2$ is the autocovariance function of $X(t)$, and ε is a very small number. Consequently, T_{CT} defines the separation required between successive samples of $X(t)$ in order for those samples to be uncorrelated (ie. to have a zero correlation coefficient). If we make the following definition

$$\alpha = \begin{cases} 1, & T_{CT} \leq T \\ T/T_{CT}, & T < T_{CT} < kT \\ 1/k, & T_{CT} \geq kT \end{cases} \quad (4.3-22)$$

then a random variable given by $Y = \alpha \sum_{i=1}^k X_i$ is chi-squared distributed with $2mok$ effective degrees of freedom (ie. $Y \sim \chi^2_{2mok}$). Y can be related to the normalised AGC gain factor, g_N , in the following way

$$\begin{aligned}
Y &= \alpha \sum_{i=1}^k X_i \\
&= 2m\alpha k \left(\frac{1}{k} \sum_{i=1}^k I_{Ni} \right) \\
&\approx 2m\alpha k * g_N
\end{aligned} \tag{4.3-23}$$

where $I_{Ni} = I_i / \langle I \rangle$ is the normalised signal intensity. This expression only applies for moderately deep fades where the effects of thermal noise on the AGC gain factor can be ignored (ie. $\varepsilon_g \approx 0$). If we let $m' = m\alpha k$, then $Y = 2m' * g_N$ where $Y \sim \chi^2_{2m'}$. Therefore, g_N is also approximately Nakagami-m distributed but with $m = m'$. The increase in the number of degrees of freedom (and the consequent decrease in the apparent strength of scintillation activity) is unlikely to be very significant unless k is quite large and/or T_{CT} is quite small. Such a situation is most likely to occur when a GPS receiver is aided by an inertial measurement unit and can therefore adopt a very narrow loop bandwidth (ie. k is large), and when the GPS ray path is moving rapidly in relation to the irregularity layer (ie. T_{CT} is small). Both of these conditions may be encountered when a GPS receiver is operating within a jet aircraft.

4.3.1. Slow amplitude fluctuations

In Chapter 3, the impact of deep, slow fades on the transfer function of a 1st order Costas carrier tracking loop was accounted for by expressing the loop noise bandwidth as a function of the amplitude. This allowed the tracking error variance to be expressed as a function of amplitude, and from there an average variance could be obtained using the Nakagami-m PDF. An equivalent approach can also be used to analyse the DLL, although the results will only apply for very slow amplitude fluctuations because of the narrow bandwidth of most DLL's.

Using the approach outlined in Section 3.3 for the Costas carrier loop (see Equations (3.3-4) to (3.3-7)), the following expression can be obtained for the power spectral density of the delay errors as a function of the signal amplitude (assuming that the amplitude remains approximately constant for a time period which greatly exceeds the time constant of the tracking loop)

$$S_{\tau_e}(f, \tilde{A}) = |1 - H'(f, \tilde{A})|^2 S_\tau(f) + |H'(f, \tilde{A})|^2 \frac{S_{n_d}(f)}{\gamma^2 \tilde{A}^4} \quad (4.3-24)$$

The component of the delay error variance associated with thermal noise and amplitude scintillations is given by

$$\begin{aligned} \sigma_{\tau_T}^2(\tilde{A}) &= \frac{1}{\gamma^2} \int_{-\infty}^{\infty} |H'(f, \tilde{A})|^2 \frac{S_{n_d}(f)}{\tilde{A}^4} df \\ &= \frac{2kTB_n(\tilde{A})}{\gamma^2} \cdot \frac{\sigma_{n_d}^2(\tilde{A})}{\tilde{A}^4} \end{aligned} \quad (4.3-25)$$

where $\gamma = -2/T_c$. $\sigma_{n_d}^2(\tilde{A})$ represents the variance of the discriminator noise as a function of the amplitude (ie. conditioned on the random variable \tilde{A}) for an un-normalised discriminator. An expression for $\sigma_{n_d}^2(\tilde{A})$ can be obtained from Equation's (4.3-6) to (4.3-10) by letting $g=1$. This gives

$$\sigma_{n_d}^2(\tilde{A}) \approx \frac{2N_o}{kT} \left[\tilde{A}^2 + \frac{4N_o}{T} \right] \quad (4.3-26)$$

From Equation (3.3-12), the loop noise bandwidth of a 1st order loop is given by

$$B_n(\tilde{A}) = \left(\frac{\tilde{A}_N^2}{g_N} \right) \bar{B}_n \quad (4.3-27)$$

Inserting Equations (4.3-26) and (4.3-27) into (4.3-25) results in

$$\sigma_{\tau_T}^2(\tilde{A}) = \frac{\bar{B}_n}{2C/N_o} \left[\frac{1}{g_N} + \frac{2}{TC/N_o \cdot g_N \tilde{A}_N^2} \right] \text{ chips}^2 \quad (4.3-28)$$

The expected value of the delay error variance is therefore

$$\sigma_{\tau_T}^2 = \frac{\bar{B}_n}{2C/N_o} \left[E \left\{ \frac{1}{g_N} \right\} + \frac{2}{TC/N_o} E \left\{ \frac{1}{g_N \tilde{A}_N^2} \right\} \right] \quad (4.3-29)$$

The differences between Equations (4.3-16) and (4.3-29) will only become significant for large values of S_4 when the probability of a deep fade becomes sufficiently large. The simplifications applied to the fast AGC model (model #2) for the I.Q Costas loop can be applied to Equation (4.3-29) to obtain the following result (see Equation's (3.3-23) to (3.3-30))

$$\sigma_{\tau_T}^2 = \frac{\bar{B}_n m^m \exp(m/T C/N_o)}{2C/N_o (T C/N_o)^{m-1}} \left[\Gamma(1-m, m/T C/N_o) + \frac{2\Gamma(2-m, m/T C/N_o)}{(m-1)} \right] \quad (4.3-30)$$

where $\Gamma(a,b)$ is the Incomplete Gamma function (the integral from b to infinity), and

$g_N = \tilde{A}_N^2 + \frac{1}{T C/N_o}$ has been assumed (from Equation (3.3-16)). Equations (4.3-16) and

(4.3-30) are compared in Figure 4.3-1 over a range of typical code loop bandwidths for the C/A-Code and for $C/N_o = 38$ dBHz. Also included as a dotted line are the results of simulations for the case $B_n = 2$ Hz. This result assumes that the dynamics driving the input delay process is being tracked by the DLL with zero steady state error.

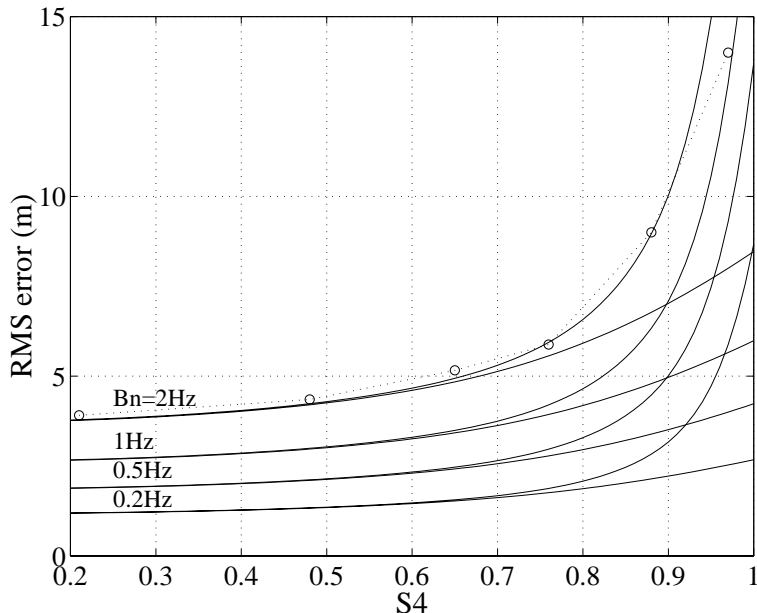


Figure 4.3-1: The delay error variance as a function of S_4 from Equation (4.3-16) (lower curves) and (4.3-30) (upper curves). The small circles and the dotted line represent the results of simulations for $B_n = 2$ Hz. Parameter values are $T=20\text{ms}$ and $C/N_o = 38\text{dBHz}$.

It is clear from this figure that the two models do not diverge significantly until the scintillation activity is moderately strong ($S_4 > 0.7$ or so), and that the RMS pseudorange error resulting from scintillations does not become excessive until the scintillation activity is very strong ($S_4 > 0.9$ say). However, this level of activity is likely to be close to, if not beyond, the tracking threshold of the carrier loop. Moreover, the effect is small when compared with the RMS error from the background ionosphere which tends to dominate the pseudorange error budget for a stand-alone SPS receiver. Nevertheless, for DGPS or

WADGPS users, the increase in thermal noise errors from amplitude scintillations may become a significant factor under strong scintillation conditions.

Nominal figures for the RMS thermal noise errors for a standard DLL are 1.5m for the C/A-Code, and 20cm for the L1 P(Y)-Code ([47] Chapter 7). However, modern receivers frequently achieve a significant reduction in these levels by smoothing the code measurements with carrier phase measurements obtained from the carrier loop. In the absence of significant multipath, this approach typically reduces RMS thermal noise errors to a few tenths of a metre. This approach will also reduce thermal noise errors in the presence of amplitude scintillations, provided that the carrier loop remain in lock and does not suffer from an excessive number of cycle slips. Although this condition is likely to be met under moderately strong scintillation conditions, as explained below, it may not hold under very strong scintillation conditions.

The RMS errors plotted in Figure 4.3-1 represent an ensemble average based on a distribution of GPS signal levels given by the Nakagami-m PDF. As it is assumed that scintillations are ergodic, these measures also represent the statistics of an individual realisation of the delay error process. In practice, a time sequence of delay errors obtained under amplitude scintillation conditions will contain a series of noise spikes, separated by several seconds or more, which represent momentary increases in the DLL tracking error resulting from deep fading events. These noise spikes, which become larger and more frequent as the strength of scintillation activity increases, tend to provide the largest contribution to the RMS error. Under strong scintillation conditions, it is likely that the carrier loop will either lose lock or suffer frequent cycle slip during these events which may preclude carrier smoothing during those times. Consequently, the impact of amplitude scintillations on the carrier smoothed code observable may be quite pronounced when the scintillation activity is strong.

The DLL analysis presented in this chapter parallels the linear model analysis for the PLL in that it is based on the premise that the delay errors are unbounded. However, from Figure 4.1-2 it is clear that for delay errors beyond $\pm T_C/2$ (for an E-L spacing of 1 chip), the discriminator delay error function will begin to return to zero. Indeed, when the delay errors exceed $\pm 3T_C/2$, the delay error function will become equal to zero and will remain at that level until the delay error approaches the period of the code sequence (1ms for the C/A-Code). This behaviour implies that if the magnitude of the delay error exceeds $T_C/2$, the feedback mechanism in the DLL will force the delay error beyond $3T_C/2$, at

which point the loop will lose lock. However, during these times, the reported delay error will be at a maximum when the true delay error is at $\pm T_C/2$, and will then become smaller as the true delay error increases beyond this point. Although this non-linear discriminator model differs significantly from the simple linear model used to obtain Equations (4.3-16) and (4.3-30), the differences are only significant when the delay errors become very large. From the linear model, it is clear that this will occur when the amplitude is heavily attenuated during deep fading events. Indeed, even if the PLL was to remain in lock during these events, the DLL may lose lock, and be unable to regain lock until the fade has passed and the loop has reverted to re-acquisition mode (the DLL cannot cycle slip and then regain lock in the same way as the PLL). In the case of the Costas PLL, the non-linear behaviour of the discriminator was accounted for by making use of the Tikhonov PDF for the modulo π reduced phase error. For the DLL, an equivalent non-linear PDF does not exist for the delay error. A crude approximation that has been applied to this problem has been to formulate the RMS error as a function of the amplitude using Equation (4.3-28), and to then restrict the errors to some upper limit based on a nominal tracking threshold for the DLL ($d/3$ code chips, where d is the correlator spacing [47]). As before, the RMS error is then found by averaging over all possible amplitude values using the Nakagami-m PDF. This procedure results in an RMS error curve which lies slightly above the curve obtained from Equation (4.3-16). This suggests that for moderately strong scintillation activity (ie. $S_4 > 0.7$ or so), the depth and frequency of the deep fading events which force delay errors beyond the tracking threshold is sufficiently large to significantly affect the average RMS delay error. Consequently, for large values of S_4 , the analytical expressions for the RMS delay error must be treated with some caution.

Nevertheless, based on simulations for which the cutoff frequency of the amplitude scintillation power spectrum, f_c , is much less than B_n , the RMS delay error appears to follow the upper curve given by Equation (4.3-30). For larger values of f_c , the RMS errors become smaller, particularly when S_4 is large.

4.4. Frequency-selective scintillation effects

In the analysis so far, it has been assumed that all frequency components in the GPS code spectrum undergo the same amplitude and phase variations at the receiver. This situation, which is also referred to as *frequency-flat* or *frequency-nonselective* fading (see for example [72], [75] or [88]), may produce fluctuations in the amplitude and delay of a code sequence, but will not result in any code pulse distortion. Consequently, tracking errors and pseudorange noise will be produced mainly by additive thermal noise, assuming that phase scintillations have a negligible effect.

However, if the bandwidth of the code is sufficiently large and/or the scintillation activity is sufficiently strong, variations will exist in the amplitude and phase of the scintillation waveforms across the code spectrum (ie. the frequency response of the propagation path will no longer be flat). If these variations are large enough, they will produce distortions in the code sequence which may affect the performance of the code loop discriminator. When a channel's frequency response exhibits statistical decorrelation across its bandwidth, it is said to be *frequency-selective*. The most common source of frequency-selective fading in a wireless communications system is multipath. In a multipath environment, the multipath reflectors introduce different delays and reflection coefficients relative to the direct path, and so the electrical lengths of each path will be a function of the frequency. Consequently, each frequency component in the signal spectrum will be subject to slightly different amplitude and phase variations at the receiver. From the model given in Appendix A, it is clear that this is very similar to scintillation effects, where the received signal is a composite of multiple rays scattered from different points on a phase screen, each of which are subject to different phase advances.

The parameter that characterises the degree of frequency selectivity of a propagation channel is the *coherence or correlation bandwidth*, B_{coh} . The coherence bandwidth determines the frequency separation for which the fading statistics of two frequency components are essentially uncorrelated. Therefore, if the bandwidth of the transmitted code sequence is much greater than B_{coh} , significant frequency-selective fading may occur leading to code pulse distortion. The coherence bandwidth is related to the RMS code delay jitter, σ_τ , by the following relationship (see for example [17], [55], [83] & [88])

$$B_{coh} = \frac{1}{2\pi\sigma_\tau} \text{ Hz} \quad (4.4-1)$$

Consequently, if $B_{code} > B_{coh}$ or $\sigma_\tau > \frac{1}{2\pi B_{code}}$, where B_{code} is the two-sided bandwidth of the code sequence, code pulse distortion may occur. For the GPS C/A-Code and P(Y)-Code, this becomes $\sigma_\tau > 23\text{m}$ ($B_{code} = 2.046 \text{ MHz}$) and $\sigma_\tau > 2.3\text{m}$ ($B_{code} = 20.46 \text{ MHz}$), respectively.

Unfortunately, there are few measurements of either the delay jitter or the coherence bandwidth for transitionospheric radio channels at GPS frequencies. However, in [79] Rino derives an expression for the single-point, two-frequency coherence function, $R(\delta f; f)$, of a transitionospheric radio channel that is subject to scintillations. $R(\delta f; f)$ is a measure of the correlation between the time varying transfer functions of the propagation channel at two frequencies, f_1 and f_2 ⁸, and can be used to determine the coherence bandwidth, *viz*

$$R(B_{coh}; f) = \mu \quad (4.4-2)$$

where B_{coh} is defined as the value of δf for which $R(\delta f; f)$ drops to some pre-defined value μ (see for example Steele, [88]). In [79], it is shown that for highly anisotropic (*rod-like*) irregularities, such as might be encountered at equatorial latitudes, $R(\delta f; f)$ can be expressed as a function $g(\cdot)$ of the form

$$R(\delta f; f) = g\left(H \times \left[\frac{\delta f}{f}\right]^{(p-1)/2}\right) \quad (4.4-3)$$

where H is a measure of the strength of scintillation activity (proportional to S_4^2 under weak scatter conditions, [79]), and p is the spectral index (the slope of the phase scintillation power spectrum). Therefore, for a given level of scintillation activity, H , the two-frequency coherence function and the channel coherence bandwidth will depend only on the ratio $\delta f/f$. Consequently, the following relationship will hold

$$\frac{B_{coh1}}{f_1} = \frac{B_{coh2}}{f_2} \quad (4.4-4)$$

⁸ $\delta f = |f_1 - f_2|$ and $f = (f_1 + f_2)/2$.

where B_{coh1} is the coherence bandwidth at frequency f_1 for a channel with a scintillation strength of H at f_1 , and B_{coh2} is the coherence bandwidth at f_2 for a channel with the same scintillation strength H at f_2 .

In [55], Knepp determines the channel coherence bandwidth at VHF frequencies (centred on 155.5 MHz) by isolating the component of the code delay spread due to scintillations and applying this to Equation (4.4-1). At these frequencies, it was found that the channel coherence bandwidth could be as low as 0.5 MHz under very disturbed scintillation conditions. Indeed, the measured S_4 values on a two-way propagation path were in excess of 2.25, implying a one-way S_4 slightly greater than one. This indicates strong Rayleigh fading with some focusing effects to drive S_4 above one. By applying these results to Equation (4.4-4), it can be shown that under very intense scintillation conditions, the channel coherence bandwidths at the two GPS carrier frequencies will be

$$B_{cohL1} = f_{L1} \times \frac{0.5}{155.5} = 5.1 \text{ MHz} \quad (4.4-5)$$

$$B_{cohL2} = f_{L2} \times \frac{0.5}{155.5} = 4.0 \text{ MHz}$$

Therefore, under very strong scintillation conditions, the P(Y)-Code may suffer from frequency-selective scintillation effects, and thus code pulse distortion, whereas the C/A-Code is unlikely to be affected. In addition, the L2 channel is likely to be affected more by frequency-selective scintillation effects than the L1 channel, partly because the coherence bandwidth at L2 is less for a given level of scintillation activity (as shown above), and partly because the scintillation activity is stronger at L2 for a given set of irregularity conditions.

In order to test whether frequency-selective scintillation effects will cause significant code pulse distortion, the phase screen model from Appendix A was used to generate amplitude and phase scintillation waveforms at a number of frequencies across the code spectrum (note that in all cases, the in-situ carrier phase perturbations were Gaussian distributed with a power-law power spectral density). Examples of these waveforms at the GPS L1 frequency and 10 MHz above L1 are given in Figure 4.4-1. It is clear that although the general shape of the waveforms are quite similar, the detailed structures are very different between these two frequencies. In particular, it appears that the differences are at their greatest when the amplitude fading is at a maximum.

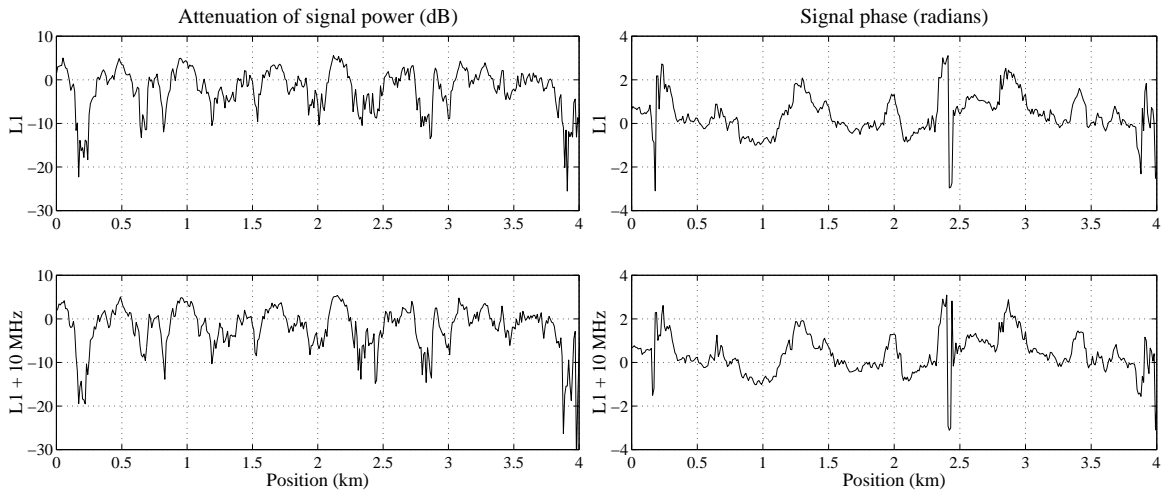


Figure 4.4-1: Amplitude and phase scintillation waveforms (left and right respectively) at the GPS L1 frequency (upper two panels) and 10 MHz above GPS L1 (lower two panels). The scintillation index S_4 is approximately equal to 0.8.

The amplitude and phase scintillation waveforms, $A(x, f)$ and $\phi_p(x, f)$, were then converted to a complex modulation for each frequency component, f , in the GPS code spectrum, *viz*

$$M(x, f) = A(x, f) \exp(j\phi_p(x, f)) \quad (4.4-6)$$

where x represents a position in the scintillation pattern (the East-West ground position in these examples). If $P(f)$ is the Fourier transform of an ideal pulse with a pulse-width equal to the GPS code chip-width, T_c , then the distorted code pulse, $p'(x, t)$, can be found by taking the inverse Fourier transform of the product of $M(x, f)$ and $P(f)$ as follows

$$p'(x, t) = \int_{-\infty}^{\infty} M(x, f) P(f) \exp(j2\pi ft) df \quad (4.4-7)$$

Examples of the effects of frequency selective scintillations on a single code pulse are given in Figure 4.4-2 to Figure 4.4-4. In these figures, it is assumed that the code pulse spectrum is limited to the first nulls of the $\text{sinc}(fT_c)$ power spectrum (ie.

$$p'(x, t) = \int_{-1/T_c}^{1/T_c} M(x, f) P(f) \exp(j2\pi ft) df , \text{ where } 1/T_c = 1.023 \text{ MHz for the C/A-Code and}$$

10.23 MHz for the P(Y)-Code). Figure 4.4-2 shows the full effect of scintillations on a P(Y)-Code pulse as a function of time and ground position, while Figures 4.4-3 and 4.4-4 represent the distorted waveforms that have been normalised by their respective peak

pulse values. Consequently, the last two figures provide a more accurate picture of the true distortion to the code pulse shape.

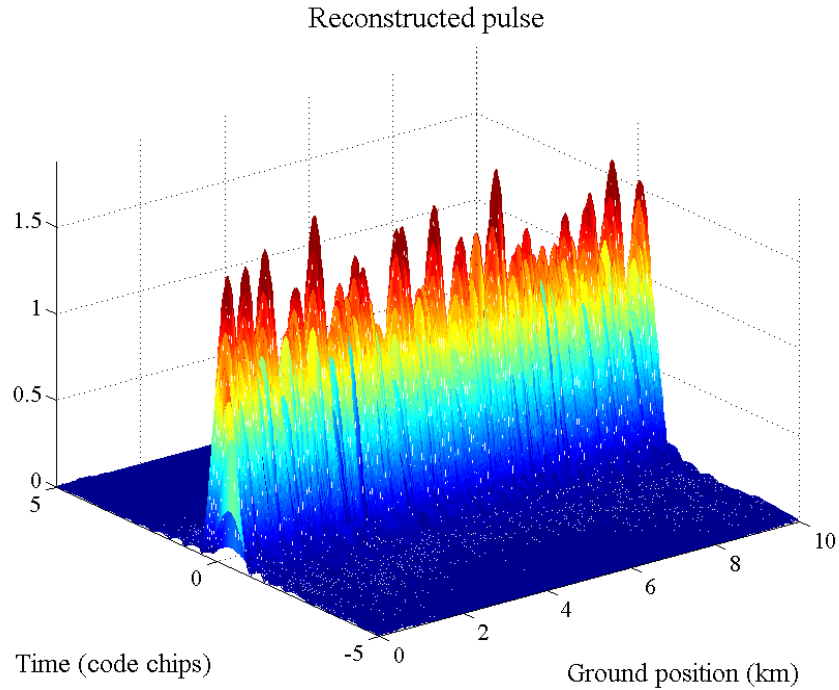


Figure 4.4-2: The impact of a single phase-changing screen with a power law in-situ density profile on 0.0978 μ s pulses that are bandlimited to ± 10.23 MHz (representative of a single P(Y)-Code chip).

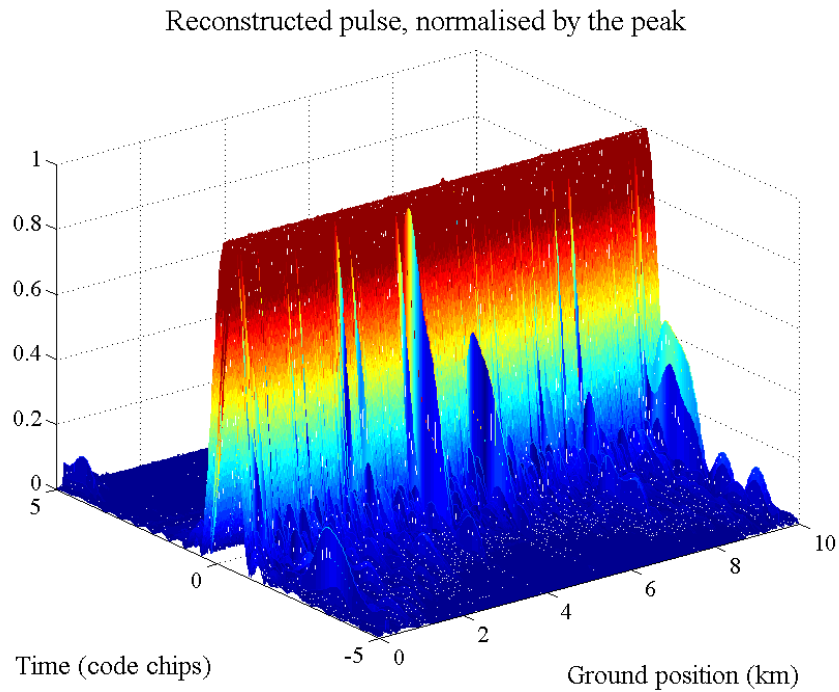


Figure 4.4-3: Figure 4.4-2 normalised by the peak pulse height.

Reconstructed pulse, normalised by the peak

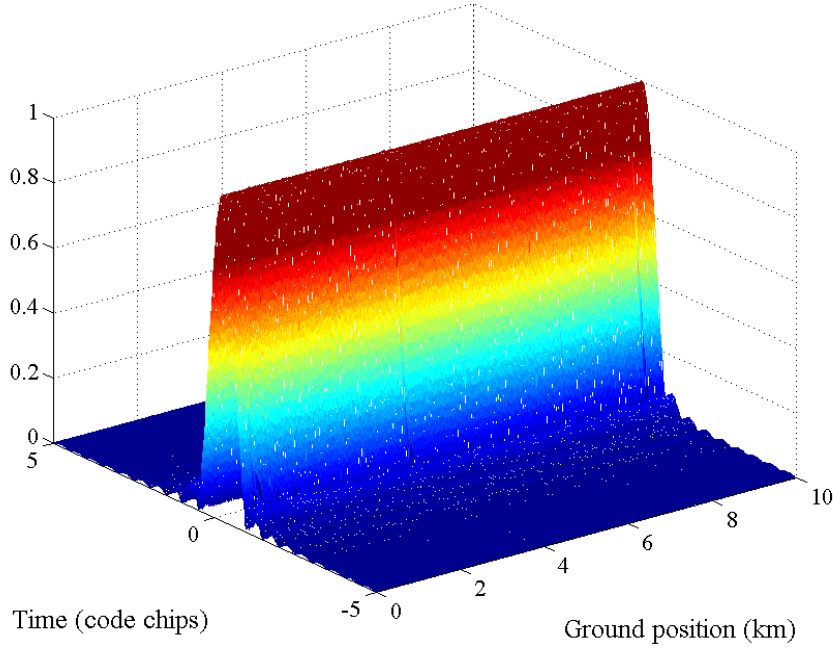


Figure 4.4-4: The impact of a single phase-changing screen with a power law in-situ density profile on $0.978 \mu\text{s}$ pulses that are bandlimited to $\pm 1.023 \text{ MHz}$ (representative of a single C/A-Code chip). In this example, the reconstructed pulses are normalised by their peak values.

By applying these pulses to a simple Early-Late gate error function, the error in the code loop discriminator can be found. The Early-Late gate error function is given by the following expression

$$\varepsilon(x, \tau_e) = \frac{1}{T_c} \left[\int_{-\infty}^{\infty} p'(x, t) p(t + \tau_e + T_c/2) dt - \int_{-\infty}^{\infty} p'(x, t) p(t + \tau_e - T_c/2) dt \right] \quad (4.4-8)$$

where τ_e is the code tracking error, $p(t + \tau_e + T_c/2)$ is a locally generated (ideal) early pulse, and $p(t + \tau_e - T_c/2)$ is a locally generated late pulse. This is equivalent to a normalised version of the Early-Late envelope discriminator from Table 4.1-1 (ie. $\varepsilon(x, \tau_e) = R_E(x) - R_L(x)$). In Figures 4.4-5 to 4.4-7, the Early-Late gate error function is plotted for the distorted code pulses from the previous figures. Figures 4.4-6 and 4.4-7 represent the error function normalised by their respective peak values to isolate the effects of code distortion from frequency-flat amplitude fading.

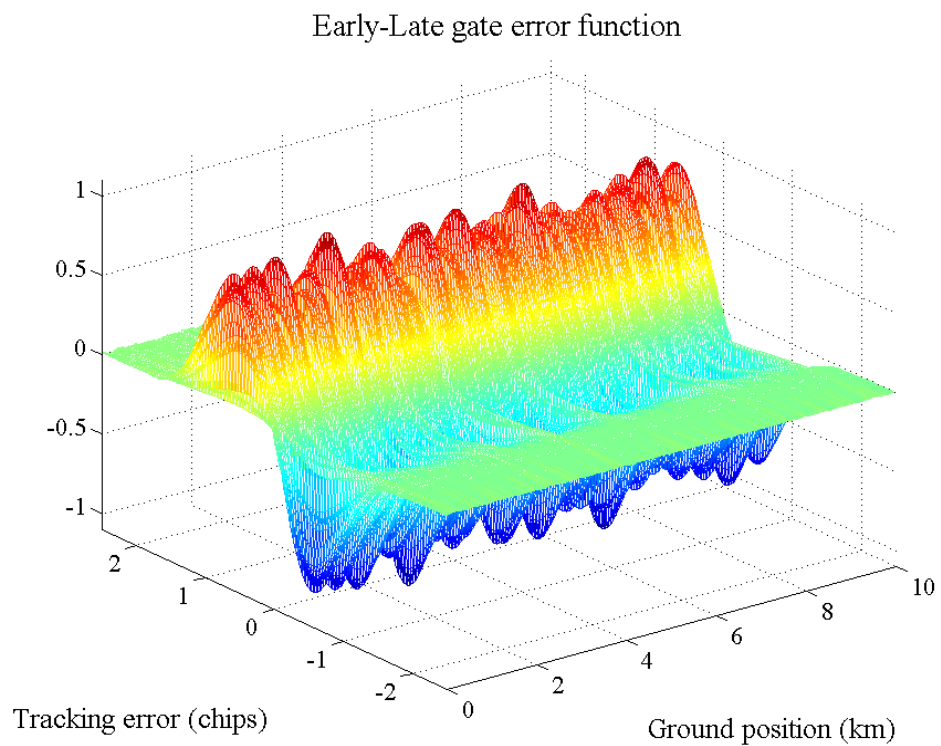


Figure 4.4-5: Early-Late gate error function for the bandlimited $0.0978 \mu\text{s}$ pulses.

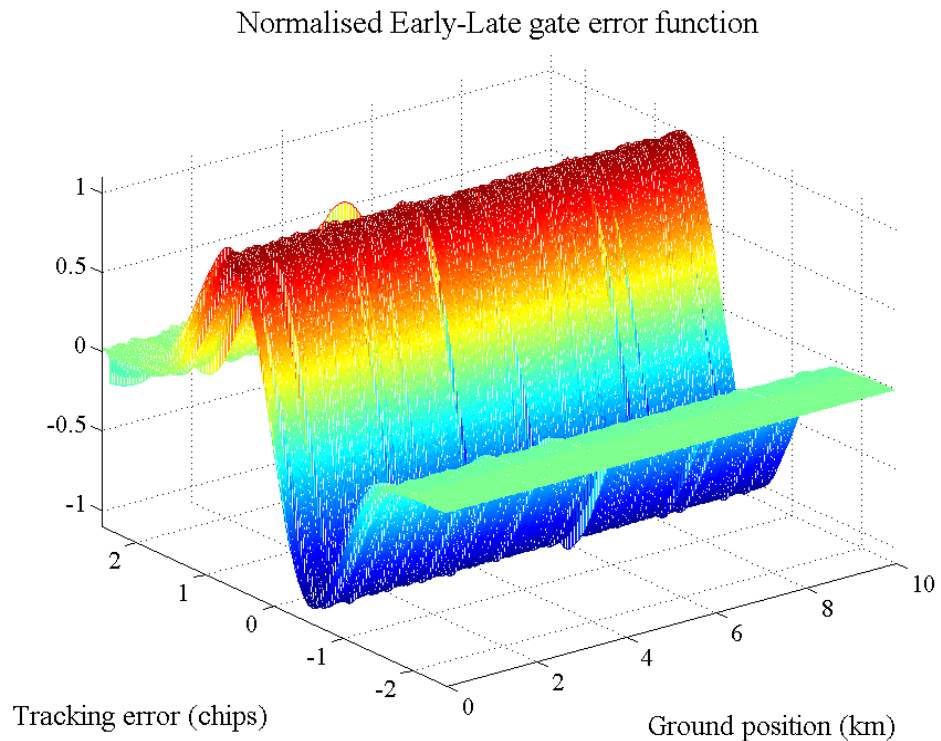


Figure 4.4-6: Figure 4.4-5 normalised by the peak discriminator error.

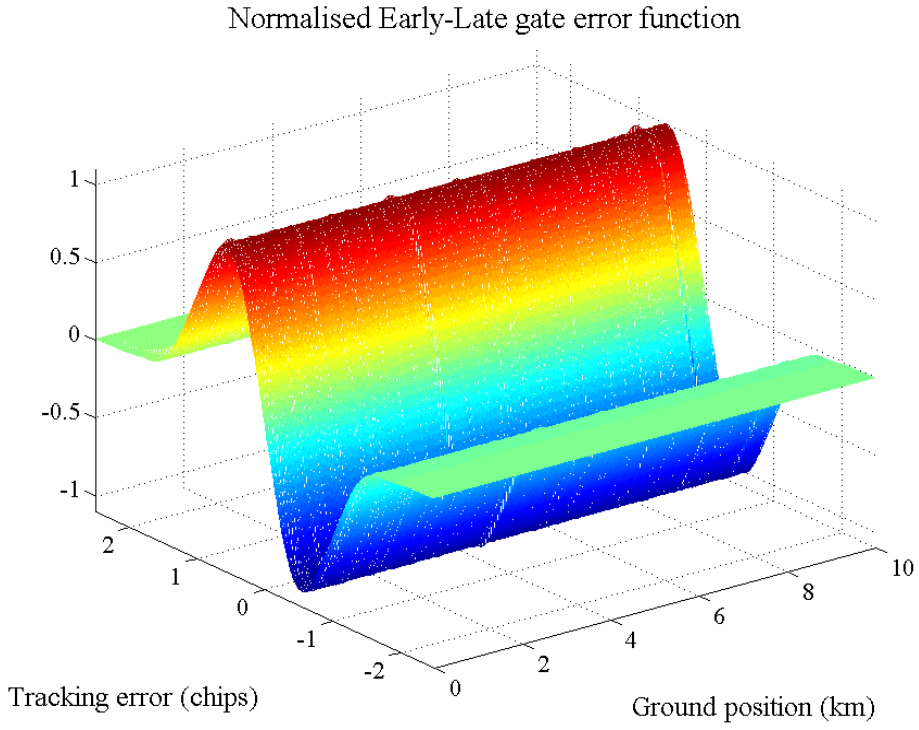


Figure 4.4-7: Early-Late gate error function normalised by the peak discriminator error for the $0.978 \mu\text{s}$ pulses.

From the results presented in these figures, it is clear that the effects of frequency-selective fading are much greater for the wider bandwidth P(Y)-Code than for the C/A-Code, as would be expected. However, it is also apparent that even under relatively strong scintillation conditions (ie. $S_4 \approx 0.8$), the distortions to the P(Y)-Code are only significant for relatively short periods of time. As will be shown next, these times are usually associated with deep amplitude fading.

In Figures 4.4-8 and 4.4-9 (left panels), the code delay errors are plotted as a function of the ground position, x , for $\tau_\epsilon = 0$. As $\tau_\epsilon = 0$ represents a situation in which the replica code is correctly aligned to the received code, the errors in these figures are associated entirely with distortions to the code pulse shape. It is clear from these figures that the discriminator errors associated with the P(Y)-Code (in chips) are much greater than those associated with the C/A-Code. It is also clear from the scatter plots on the right that significant tracking errors are usually associated with the time periods during which the amplitude is deeply faded. Consequently, when the scattered rays come close to complete cancellation on the ground (ie. during deep fading), the amplitude and phase response of the channel attains its greatest sensitivity to frequency. However, as the carrier tracking loops of a GPS receiver are likely to suffer from cycle slips and tracking problems during

these times, it is questionable whether these errors will be of practical importance in a real GPS receiver.

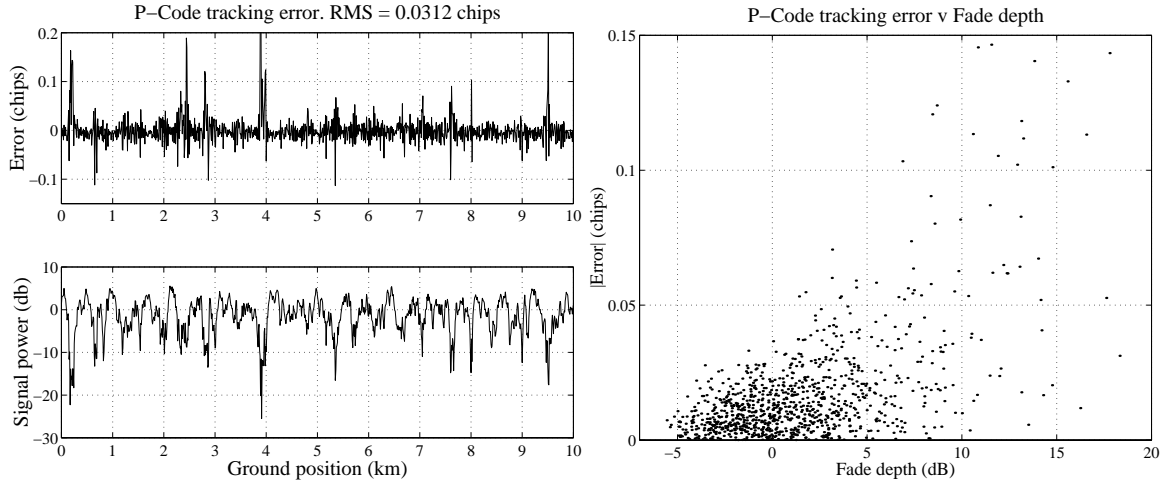


Figure 4.4-8: The delay errors (upper left panel) and amplitude scintillation waveform (lower left panel) as a function of ground position for the bandlimited $0.0978 \mu\text{s}$ pulses. The scatter plot on the right compares the delay errors to the fade depth.

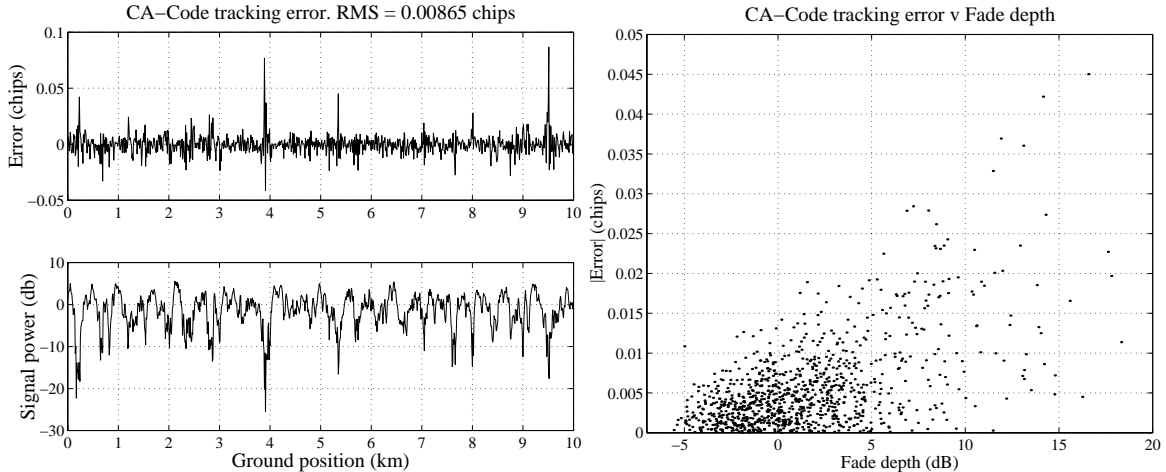


Figure 4.4-9: The delay errors (upper left panel) and amplitude scintillation waveform (lower left panel) as a function of ground position for the bandlimited $0.978 \mu\text{s}$ pulses. The scatter plot on the right compares the delay errors to the fade depth.

The procedures outlined above are very similar to those followed by Bogusch [16], [17] and Knepp [54] using their more sophisticated multiple phase screen model. However, their results suggest that the coherence bandwidth at L-band frequencies (2 GHz) could be as low as 0.25 MHz under very strong scintillation conditions [17]. Using Equation (4.4-4), this implies that $B_{cohL1} \approx 0.2 \text{ MHz}$, which is roughly 25 times smaller than the

value derived from the measurements in [55]. Although this result implies that code distortion could be quite severe under strong scintillation conditions (ie. $B_{cohL1} \ll B_{code}$), it was not clear in [17] whether significant distortion was only observed during periods of deep amplitude fading.

4.5. Conclusions

In this chapter, the effects of scintillations on code tracking loops was examined. It was found that phase scintillations have a negligible effect on code loops, and that the additional RMS thermal noise error associated with amplitude scintillations is only small, unless S_4 is close to unity. Nevertheless, under strong amplitude scintillation conditions, it is likely that error spikes will exist in the code pseudorange measurements during times when the amplitude is deeply faded. However, as the carrier loop is likely to be stressed to the point of losing lock during these times, this effect may not be regarded as important for most GPS users. It was also found that because of the very narrow bandwidth of GPS signals, frequency selective scintillation effects are unlikely to produce significant code distortion under naturally occurring ionospheric conditions, except possibly for the P(Y)-Code during times when the amplitude is deeply faded.

Chapter 5

Codeless and semi-codeless receivers

In this Chapter, the effects of scintillations on codeless and semi-codeless receivers¹ is examined. Because codeless tracking loops have a much lower signal to noise ratio than full code correlation tracking loops, their susceptibility to scintillations is expected to be far greater. In Section 5.1, the various codeless tracking techniques employed in non-military, dual frequency receivers are outlined. In Section 5.2, a theoretical analysis is given of the effects of amplitude and phase scintillations on codeless tracking loops. Essentially, the reduced signal to noise ratio of codeless tracking loops increases their susceptibility to amplitude scintillations, while their much narrower loop bandwidths increases their susceptibility to phase scintillations. Finally, in Section 5.3 the theoretical performance measures of semi-codeless tracking loops are compared with measurements taken from a semi-codeless receiver located in a region of high scintillation activity.

5.1. Codeless processing techniques

Codeless and Semi-codeless receivers obtain L2 code and carrier phase measurements without requiring access to the military Y-Code. These receivers are frequently used in WAAS and LAAS² systems and are therefore important for civilian applications such as air traffic control. The two most commonly used codeless techniques are *squaring* and *cross-correlation* [91]. Squaring removes both the navigation data and the Y-Code from the L2 signal and produces a carrier at twice the L2 frequency. However, this technique does not provide code phase information, and with such a high carrier frequency the process of resolving carrier cycle ambiguities can be difficult and time consuming. Cross-correlation is an improvement on the squaring technique that produces a carrier at the

¹ To improve the readability of this Chapter, the term “codeless” will frequently imply both codeless and semi-codeless tracking loops.

² WAAS: Wide Area Augmentation Systems, and LAAS: Local Area Augmentation Systems.

difference in frequency between L1 and L2 as well as a measure of the code delay difference between the two frequencies. The much lower frequency allows carrier cycle ambiguities to be resolved more rapidly, while the code delay difference provides an unambiguous measure of the ionospheric delay on each carrier.

Both techniques can be enhanced by employing *semi-codeless* processing prior to the codeless tracking loops. In a semi-codeless receiver, the P-Code (which is known *a priori*) is removed from the GPS signal to produce an L2 carrier which is modulated by the encryption code (also called the W-Code) and the navigation data. As the bandwidth of the encryption code is 20 times less than the P-Code bandwidth, the resulting signal can be filtered to reduce the noise power by up to 13dB [4]. Consequently, a semi-codeless receiver will have a 13dB advantage in signal to noise ratio (SNR) over a purely codeless receiver. Both techniques, however, suffer a considerable reduction in SNR over full code correlation P(Y)-Code tracking.

Another semi-codeless technique that is frequently used in Novatel™ receivers involves tracking the P-Code directly using a standard tracking loop, but with a pre-detection bandwidth that is equal to the W-Code bandwidth (500 kHz)³. Consequently, the W-Code is treated in essentially the same way as the navigation data in a full code correlation tracking loop. An advantage of this technique is that a true estimate of the L2 P-Code pseudorange is produced, although the associated thermal noise errors are at a greatly elevated level.

In order to cope with the reduced SNR, codeless receivers employ very narrow tracking loop bandwidths, typically much less than 1 Hz. To reduce the consequent dynamic stresses associated with satellite and receiver motion, codeless carrier tracking loops are aided by carrier phase error estimates provided by the more robust L1 C/A-Code carrier tracking loops. These estimates tend to reduce, but not eliminate, the phase scintillation errors on the codeless loops.

³ The pre-detection integration period, T , is therefore 2×10^{-6} s.

5.2. Theoretical analysis

Based partly on the above discussion, the various aspects of codeless tracking loops which determine their susceptibility to ionospheric scintillations can be summarised as follows:

1. The L2 signal power is approximately 6dB below the L1 C/A-Code signal power.
2. The SNR of codeless tracking loops is significantly less than the SNR of full code correlation tracking loops.
3. Both amplitude and phase scintillations are slightly stronger at the lower L2 frequency as a result of the inverse frequency scaling of scintillations.
4. L1 carrier aiding of the L2 codeless loop reduces the effects of phase scintillations.
5. Carrier aiding virtually eliminates dynamic stresses on the codeless loops allowing the tracking loop bandwidth of the carrier loop to be significantly reduced.

The first two factors can be accounted for by determining an equivalent C/N_o for the codeless tracking loops. This can then be used to determine a tracking threshold under amplitude scintillation conditions based on the variance expression for a standard phase locked loop.

The degradation in C/N_o for codeless and semi-codeless tracking loops is given by [91]

$$7.8 + 10\log_{10}(B_I) - C/N_o|_{C/A} dB \xrightarrow{10^{x/10}} \frac{6B_I}{C/N_o|_{C/A}} \quad (5.2-1)$$

where B_I is the pre-detection bandwidth (10MHz for a codeless loop, 500kHz for a semi-codeless loop), and $C/N_o|_{C/A}$ is the carrier to noise density ratio of the C/A-Code. The equivalent C/N_o is thus [91]

$$C/N_o|_{Eq} = \frac{(C/N_o|_{C/A})^2}{6B_I} \quad (5.2-2)$$

As both squaring and cross-correlation eliminates the navigation data from the GPS signal, a standard (non-Costas) phase locked loop can be used to track the resulting carrier. For a standard phase locked loop, the variance of the tracking error is given by the inverse of the loop SNR [73], *viz*

$$\begin{aligned}
\sigma_{\phi_e}^2 &= (\text{Loop SNR})^{-1} \\
&= \frac{B_n}{C/N_o|_{Eq}} \\
&= \frac{6B_n B_I}{(C/N_o|_{C/A})^2}
\end{aligned} \tag{5.2-3}$$

where B_n is the tracking loop bandwidth. If a variance threshold is chosen for σ_{ϕ_e} , threshold values of the signal amplitude can be found for both codeless and semi-codeless receivers as a function of B_n , B_I , and the nominal $C/N_o|_{C/A}$, *viz*

$$\tilde{A}_{Th} = \mathbf{A}_4 \sqrt{\frac{6B_n B_I}{(C/N_o|_{C/A} * \sigma_{\phi_T}|_{Th})^2}} \tag{5.2-4}$$

where \mathbf{A} is the nominal signal amplitude and $\sigma_{\phi_T}|_{Th}$ is the threshold RMS error once the effects of phase scintillations have been removed (see Section 3.4). As before, these threshold values can be used to determine the probability of losing lock as a function of S_4 (see Equation (3.4-3)).

The third factor (ie. the difference in the strength of scintillations at the L2 frequency) is automatically accounted for by using the L2 frequency as an input to the WBMOD scintillation model. In Section 2.1.3, it was stated that S_4 and σ_{ϕ_p} scale in the following way with the carrier frequency, ν

$$\begin{aligned}
S_4 &\propto \nu^{-(p+3)/4}, \text{ for low to moderate levels of scintillation activity} \\
&\approx 1 \quad , \text{ for strong scintillations} \\
\sigma_{\phi_p} &\propto \nu^{-1}
\end{aligned} \tag{5.2-5}$$

From Equations (2.1-1) and (2.1-4) it is also apparent that for a constant outer scale size parameter, f_o , T also scales with the carrier frequency as $T \propto \nu^{-2}$ (ie. $\sigma_{\phi_p}^2 \propto T$). Consequently, at the L2 frequency, S_4 is between 1 and 1.4 times larger than the corresponding L1 value, while T is approximately 1.65 times larger.

The fourth factor (ie. carrier aiding of the codeless loops) is accounted for by assuming that the majority of the phase scintillation energy is associated with refraction effects

which show a simple v^{-1} dependence with frequency. Consequently, scintillation induced phase variations on the L2 carrier, ϕ_{PL2} , can be related to the corresponding variations on the L1 carrier, ϕ_{PL1} , through⁴

$$\phi_{PL2} = \frac{v_{L1}}{v_{L2}} \phi_{PL1} \quad (5.2-6)$$

where $v_{L1} = 1575.42 \text{ MHz}$ and $v_{L2} = 1227.6 \text{ MHz}$. Aiding of the L2 carrier loop is primarily intended to eliminate Doppler errors associated with satellite and receiver motion. The Doppler correction term is given by

$$\frac{v_{L2}}{v_{L1}} \phi_{dL1} \quad (5.2-7)$$

where ϕ_{dL1} is the phase error associated with Doppler on the L1. The v_{L2}/v_{L1} factor in this expression is also applied to the phase scintillation errors on L1, ϕ_{PL1} , before they are removed from the L2 carrier loop. The residual phase scintillation error is thus [91]

$$\begin{aligned} \phi'_{PL2} &= \phi_{PL2} - \frac{v_{L2}}{v_{L1}} \phi_{PL1} \\ &= \phi_{PL2} \left[1 - \left(\frac{v_{L2}}{v_{L1}} \right)^2 \right] \\ &= 0.393 \phi_{PL2} \end{aligned} \quad (5.2-8)$$

Consequently, the phase scintillation spectral strength, T, obtained from models such as WBMOD at the L2 frequency must be scaled by a factor of 0.393^2 (-8.1dB) to account for the effects of carrier aiding.

The last factor (ie. a very narrow loop bandwidth) provides a considerable amount of resistance to the effects of amplitude scintillations. By implementing a narrow loop bandwidth, the codeless receiver reduces thermal noise errors on the phase estimates which in turn increases the SNR of the tracking loop. This helps to overcome some of the

⁴ It is worth noting that if diffraction effects were to predominate, this simple relationship would not necessarily apply. However, as the bandwidths of the codeless loops are very narrow, it is reasonable to assume that a large proportion of the energy in the carrier loop phase tracking errors is below the Fresnel cutoff frequency and so can be attributed mainly to the effects of refraction.

effects associated with the lower signal level at the L2 frequency and the reduced SNR of the codeless tracking loops. A second effect of a narrow loop bandwidth is that the duration of the deep fading events which lead to loss-of-lock may now be much less than the time constant of the tracking loop. For loop bandwidths as low as 0.1Hz, this could greatly improve a loop's tolerance to amplitude scintillations, particularly if the amplitude scintillation rate is increased by receiver motion. However, this effect will be offset somewhat by the greatly reduced amplitude threshold of codeless tracking loops. Figure 5.2-1 is an illustration of the impact of a reduced amplitude threshold on the fade duration using a short segment of simulated amplitude scintillation data obtained from the model in Appendix A. For deep fading events, the signal amplitude will be below the semi-codeless threshold for much longer periods of time, effectively resulting in a longer duration fade.

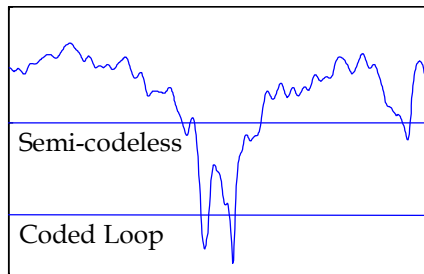


Figure 5.2-1: Illustration of the effect of a reduced amplitude threshold on the fade duration.

5.3. Threshold curves

In Figure 5.3-1, threshold curves are plotted for both codeless and semi-codeless receivers (both techniques) based on the following assumptions:

- The loop bandwidths are 0.1Hz.
- C/N_o for the C/A-Code tracking loop is 44dBHz (at 38dBHz, the codeless loop is already very close to losing lock for a loop bandwidth of 0.1Hz). Therefore, $C/N_o|_{Eq}$ is 10.2dBHz for the codeless loop, and 23.2dBHz for the semi-codeless loop.
- Carrier aiding of the codeless loops reduces T by 8.1dB.
- The amplitude scintillation bandwidth is narrow compared to the loop bandwidth. This assumption is necessary in the absence of a suitable approach to the problem of very narrow loop bandwidths and may result in an overestimation of the susceptibility of tracking loops to amplitude scintillations.

The threshold curve for the semi-codeless-2 technique (see caption of Figure 5.3-1) is simply found using the approach outlined in Section 3.4 with $T = 2 \times 10^{-6}$ s and the

Spectral strength, T , reduced by 8.1dB. Also shown as a dotted line is the curve obtained from Equation (3.4-8) with $\gamma_{dB} = 20$ dB (ie. the approximate upper limit on $[T, S_4]$ values for a stationary receiver obtained from WBMOD).

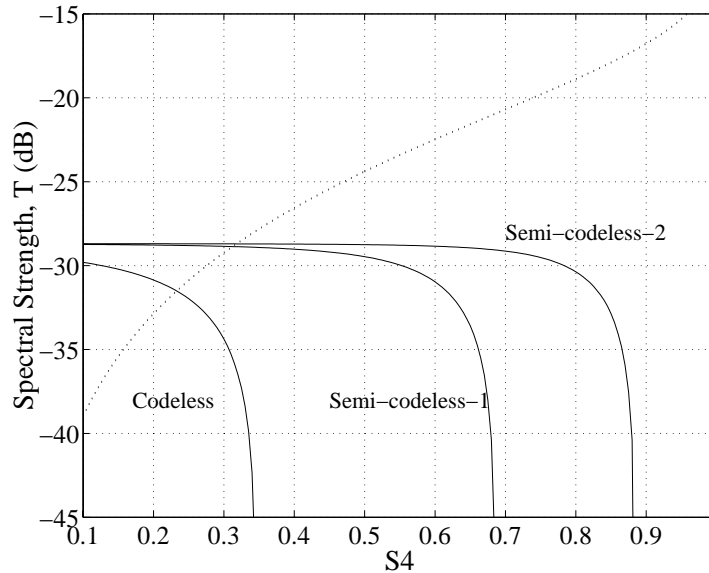


Figure 5.3-1: Tracking thresholds for both codeless and semi-codeless receivers as a function of the Spectral Strength, T , and the amplitude scintillation index, S_4 . A loop bandwidth of 0.1Hz has been assumed. Semi-codeless-1 refers to the process of removing the P-Code from the L2 carrier prior to codeless processing. Semi-codeless-2 refers to the technique of adopting a much wider pre-detection bandwidth in a Costas loop to accommodate the W-Code.

It is clear from this figure that because the various threshold curves lie well below the dotted line obtained from WBMOD, the probability of losing lock is likely to be reasonably high on links that are affected by scintillations. By comparing this with Figure 3.3-3, it is also clear that codeless and semi-codeless tracking loops are considerably more susceptible to scintillations than full code correlation tracking loops. The very narrow loop bandwidth increases their susceptibility to phase scintillations, despite a reduction in phase scintillation energy through aiding from the C/A-Code carrier loop. Similarly, the reduced SNR greatly increases their susceptibility to amplitude scintillations, despite a very narrow loop bandwidth.

5.4. Scintillation measurements

The objective of this section is to check the validity of the semi-codeless performance models derived in the previous sections using data obtained from co-located Novatel

Millennium™ and PAQ12™ Ionospheric Scintillation Monitoring (ISM) receivers. The Millennium™ uses full code correlation for the L1 C/A-Code and a semi-codeless tracking technique for the L2 Y-Code. The ISM receivers are high data rate L1 SPS receivers which are designed specifically to measure the scintillation indices S_4 and T [92]. Although data from the peak of the current solar cycle has not yet been processed, ISM data from the September 1998 and March 1999 equinoxes shows sufficient evidence of scintillation activity for an analysis to be performed.

5.4.1. Overview of scintillation data

The data used in this study was obtained from co-located Millennium™ and ISM receivers deployed at Parepare in Indonesia. Parepare is located at 4°S, 119.6°E, which places it beneath the crest of the southern anomaly in a region of potentially strong scintillation activity. The 12 month smoothed mean monthly sunspot number (SSN)⁵ for the March 1999 equinox was approximately 83.8, which represents a moderate level of solar activity. At the time of writing (November 2000), the measured SSN's for the September 1999, March 2000 and September 2000 equinoxes were 102.3, 119.8 and 128.7, respectively. In addition, it is predicted that the peak of the current solar cycle will occur in December 2000, and that it will take until late 2003 before the solar activity drops below the level measured in September 1998 (69.5). Consequently, over the coming few years it is expected that scintillation activity and its impact on GPS will continue, although mainly during the equinoctial months.

5.4.1.1. Novatel Millennium™ data

The Novatel Millennium™ provides an indication of the tracking state of the L1 and L2 code and carrier tracking loops as part of its standard output⁶. A second set of lock indicators obtained by comparing the reported code and carrier pseudorange measurements with the range calculated from the satellite ephemeris information was found to give virtually the same results. Consequently, for convenience it was decided that the tracking state indicator would be used in all subsequent analysis as an indicator of a loss of valid pseudorange data. In addition, a 10° elevation angle mask was chosen to

⁵ Sunspot numbers were obtained from the Australian Ionospheric Prediction Service (IPS) web site at "<http://www.ips.gov.au>".

⁶ Tracking state information is contained within the Novatel format RGEA/B data blocks [68].

avoid multipath effects and the possibility of satellite obscuration on low elevation angle links.

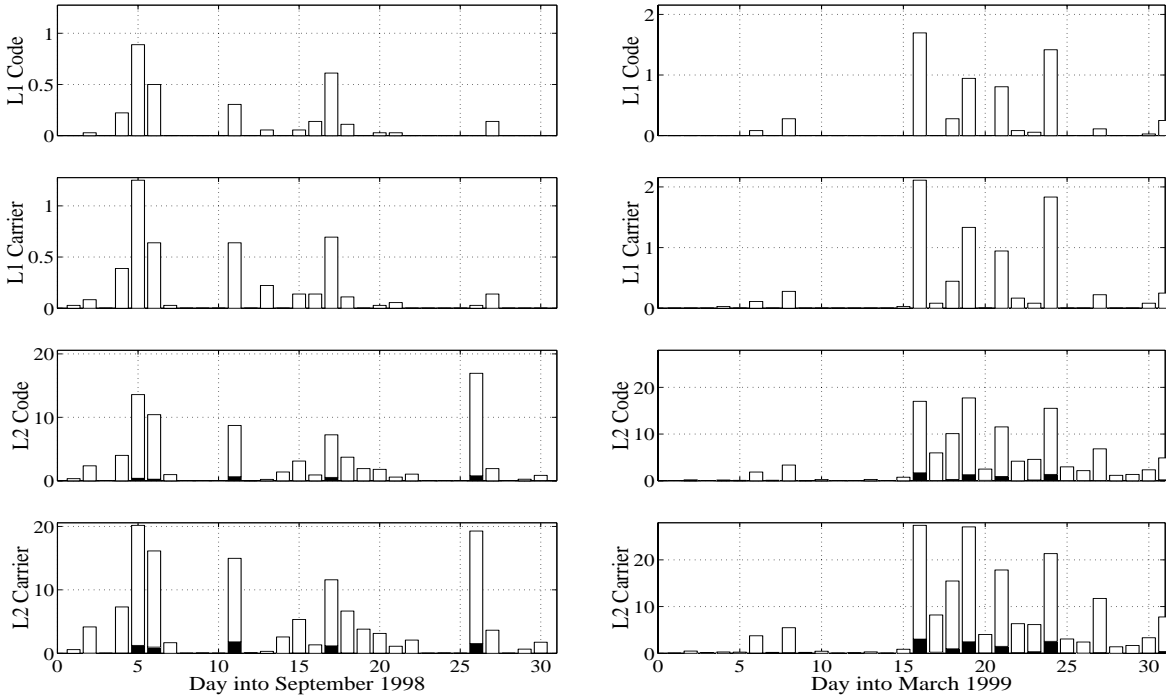


Figure 5.4-1: The percentage of time from 8:00pm to 10:00pm (local time) that the Novatel Millennium™ loses lock on one or more satellites at Parepare, Indonesia (left panel: September 1998 equinox, right panel: March 1999 equinox). The white bars represent the loss of one satellite. The solid bars represent the simultaneous loss of two or more satellites.

In Figure 5.4-1, the percentage of time between 8:00pm and 10:00pm (local time) that the Millennium™ loses lock on one or more satellites is plotted as a function of the day for both the September 1998 and March 1999 equinoxes. It is clear from this figure that the carrier loops lose lock slightly more often than the code loops (by a factor of about 1.5). This supports the assertion that in the absence of external Doppler aiding, the code loop loses lock soon after the carrier loop. It is also apparent that the semi-codeless L2 loops are considerably more susceptible to the effects of scintillations than the L1 loops. Indeed, on average the L2 carrier loop loses lock on one or more satellites about 30 times more often than the L1 carrier loop, although this factor varied significantly from day to day. It is also apparent that for the moderate levels of solar activity represented by these two months, the impact on navigation is relatively minor. On the worst day (16th March 99), the L1 code loop lost lock on 1 satellite for approximately 1.7% of the two hour period of interest (roughly 2 minutes in total). For a mask angle of 10°, the minimum number of available satellites during this period was 8. Consequently, even during these two

minutes, the loss of one satellite would not prevent navigation or even seriously degrade the satellite geometry. However, it is clear that the effect of scintillations on the semi-codeless L2 channels was significantly greater. On the 16th March 1999 (a bad day), the L2 carrier loop lost lock on one or more satellites for approximately 27% of the two hour period of interest (a total time of 32 minutes). In addition, two and three satellites were lost simultaneously for about 3% and 0.03% of the time, respectively.

5.4.2. A comparison of models with measurements

The PAQ12™ ISM receiver provides measurements of the four scintillation parameters, S_4 , σ_{ϕ_p} , T and p once every minute. By feeding these parameters into the single link performance models given in Section 5.2, it is possible to predict the probability of an outage on the L2 semi-codeless tracking loops. Unfortunately, because the Millennium™ and ISM receivers are co-located and have approximately the same L1 carrier loop bandwidths, the L1 tracking loops of the Millennium™ would be expected to lose lock at about the same time as the ISM tracking loops (ie. a deep fade will affect both receivers simultaneously). Consequently, it is not possible to check the validity of the tracking thresholds for a full code correlation tracking loop using this approach. Indeed, during the September 1998 equinox, it was found that on average ISM data was missing from 97% of L1 code and 95% of L1 carrier epochs for which the Millennium™ had lost lock. However, as the L2 loops lose lock at much lower levels of scintillation activity, only 54% of L2 code and 52% of L2 carrier loss-of-lock epochs had missing ISM data. Unfortunately, because the S_4 measurements vary so much from epoch to the next, it is not possible to interpolate between valid measurements to eliminate this problem.

In Figure 5.4-2, the percentage of time that the Millennium™ loses lock is plotted as a function of S_4 using data from both the September and March equinoxes (from 6:00pm to local midnight). Data for which the Spectral Strength, T, is greater than -30dBradians² has been ignored to ensure that amplitude scintillations have the predominant effect. Included in the lower panel of this figure is the probability of losing lock on the carrier loop based on the theoretical analysis presented in Section 5.2 and using the ISM measurements of S_4 (the upper and lower error bars represent $\pm 1\sigma$ values of the measured C/N_o from the Millennium™). If the tracking loops re-acquire the signal shortly after the amplitude rises above the tracking threshold, then the measured and theoretical probability of an outage should be comparable. From Figure 5.4-2, this appears

to be true until S_4 becomes large, at which point the measurement curve begins to flatten off. This flattening is believed to be the result of deep fades which result in the simultaneous loss of both Millennium™ L1 and ISM data. Although, these results indicate that the expression for the probability of losing lock, P_L , is relatively accurate, they also suggest that the 1% threshold discussed in Section 3.4 may be relatively conservative.

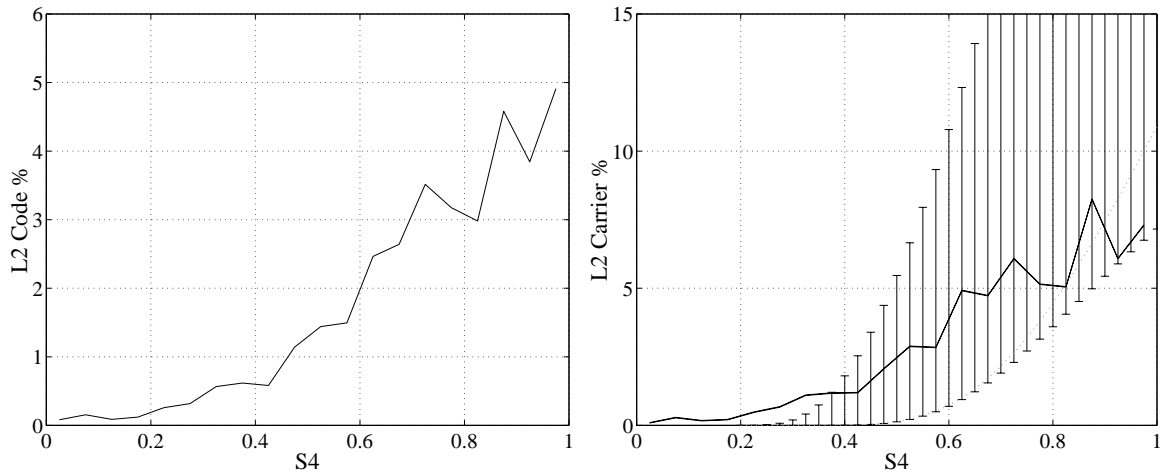


Figure 5.4-2: The percentage of time that the L2 code and carrier loops lose lock as a function of S_4 . Data for which the phase scintillation Spectral Strength, T , is greater than -30dBradians^2 has been ignored. The error bars represent theory based on quiescent L2 C/N_0 values between 34dBHz (upper bars) and 44dBHz (lower bars).

An equivalent analysis of the relationship between loss-of-lock and the spectral strength parameters, T and σ_{ϕ_p} , has not been given because of a lack of confidence in the integrity of the ISM measurements of T and σ_{ϕ_p} .

5.5. Conclusions

Codeless tracking loops are far more susceptible to the effects of scintillations than full code correlation tracking loops. However, the different tracking techniques employed in codeless receivers do have significantly different susceptibilities, with semi-codeless techniques being generally more robust than purely codeless techniques. The poor performance of codeless tracking loops under scintillation conditions may result in a degradation in the accuracy of systems such as the Wide Area Augmentation System (WAAS) which rely on dual frequency SPS receivers for the measurement of ionospheric delays. However, by the time WAAS and equivalent systems become operational, it is

expected that solar activity will have declined to the point where scintillations are no longer regarded as a significant threat. Also, with the imminent introduction of a second C/A-Code signal on the L2 frequency, and with approval being given for a future L5 civil signal, the effects of scintillations on codeless receivers is unlikely to be an issue for future solar maxima.

Measurements of the strength of scintillation activity and loss-of-lock taken during times of strong scintillation activity are generally in quite good agreement with the theory. They also show that because scintillations are very patchy, the chances of losing lock on several channels simultaneously are very small, even under strong scintillation conditions. This issue is discussed further in Chapter 9.

Chapter 6

Navigation data

In this chapter, the effects of scintillations on the process of demodulating the navigation data is examined. In Section 6.1, background theory is given which enables the bit error rates and word error rates to be calculated under quiescent signal conditions. In Sections 6.2 and 6.3, scintillation effects on the navigation data are determined by treating amplitude and phase scintillation effects separately. It is shown that even under very intense scintillation conditions, word error rates increase to only a few percent with amplitude scintillations providing the greatest contribution. The results of these two sections are then used to determine the combined effects of amplitude and phase scintillations on the navigation data. Finally, in Section 6.5 the effects of a slowly varying amplitude waveform on the word error rate is examined.

6.1. Background

The GPS navigation message is broadcast by each satellite and contains information about the satellite ephemerides, clock and ionospheric correction factors, timing information and constellation status. The navigation message consists of 25 data frames, each containing 5 subframes and each subframe containing 10 words of 30 bits. Therefore, at a data rate of 50 bits/s, the complete navigation message takes 12.5 minutes to be downloaded by a receiver. The first three subframes of each frame contain the same clock and ephemeris information which is considered critical to the operation of a receiver. Consequently, this information is made available to a receiver at a rate of once every 30 seconds.

In a GPS receiver, the navigation data is extracted from the in-phase channel of the carrier tracking loop at a point immediately after the pre-detection filters (see Figure 3.1-1). In the analysis that follows, it is assumed that the carrier tracking loop remains locked to the

GPS carrier and synchronised to the navigation data. Under these assumptions, the in-phase signal is given by (from Equation (3.1-2))

$$I_P = \tilde{A}d(t - \tau)\cos(\phi_e) + n_{IP} \quad (6.1-1)$$

where \tilde{A} is the signal amplitude after the pre-detection filters, $d(t - \tau)$ is the navigation data, ϕ_e is the carrier phase error and n_{IP} is distributed $N(0, \sigma_n)$ where $\sigma_n = \sqrt{N_o/T}$. Two new random variables, X_0 and X_1 , can be introduced to represent I_P during the transmission of a binary 0 data bit ($d(t - \tau) = -1$: Hypothesis H_0) and a binary 1 data bit ($d(t - \tau) = 1$: Hypothesis H_1), viz

$$\begin{aligned} H_0 : \quad I_P &= X_0 = -\tilde{A}\cos(\phi_e) + n_{IP} \\ H_1 : \quad I_P &= X_1 = \tilde{A}\cos(\phi_e) + n_{IP} \end{aligned} \quad (6.1-2)$$

Under quiescent conditions (ie. no scintillations), \tilde{A} is approximately constant and ϕ_e is small compared to 1 radian. Consequently, X_0 and X_1 can be approximated by

$$\begin{aligned} X_0 &= -\mathbf{A} + n_{IP} \\ X_1 &= \mathbf{A} + n_{IP} \end{aligned} \quad (6.1-3)$$

where $\mathbf{A} = \tilde{A}$ is a constant. The probability density functions of X_0 and X_1 are therefore

$$\begin{aligned} f_{X_0}(x_0) &= N(-\mathbf{A}, \sigma_n) \\ f_{X_1}(x_1) &= N(\mathbf{A}, \sigma_n) \end{aligned} \quad (6.1-4)$$

and the probability of a bit error is given by (see for example Haykin [39])

$$\begin{aligned} P_e &= p(H_0) \int_0^{\infty} f_{X_0}(x_0) dx_0 + p(H_1) \int_{-\infty}^0 f_{X_1}(x_1) dx_1 \\ &= \int_0^{\infty} f_{X_0}(x_0) dx_0 \\ &= \frac{1}{2} \operatorname{Erfc}\left(\frac{\mathbf{A}}{\sqrt{2}\sigma_n}\right) \end{aligned} \quad (6.1-5)$$

where $\operatorname{Erfc}(\cdot)$ is the Complementary Error Function¹, and $p(H_0)$ and $p(H_1)$ are the

¹ $\operatorname{Erfc}(x) = \frac{2}{\sqrt{\pi}} \int_x^{\infty} \exp(-y^2) dy$

probabilities of binary 0 and 1 data bits respectively². This can also be expressed in terms of the carrier to noise density ratio, $C/N_o = \mathbf{A}^2/(2N_o)$, and the energy per bit, $E_b = T\mathbf{A}^2/2$, as follows

$$\begin{aligned} P_e &= \frac{1}{2} \operatorname{Erfc}\left(\sqrt{T \cdot C/N_o}\right) \\ &= \frac{1}{2} \operatorname{Erfc}\left(\sqrt{\frac{E_b}{N_o}}\right) \end{aligned} \quad (6.1-6)$$

Under normal tracking conditions, $T = 20$ ms and $C/N_o \approx 41.5$ dBHz resulting in a bit error probability of 3.4×10^{-125} (this assumes a nominal satellite signal power level of -160 dBW at the ground and a noise temperature of 530 K).

The probability of a word error, assuming no error correction, is given by (Hegarty [40])

$$\begin{aligned} P_w &= 1 - (1 - P_e)^m \\ &\approx mP_e \quad \text{for } P_e \ll 1 \end{aligned} \quad (6.1-7)$$

where m is the number of bits per word (30 for the GPS navigation message). This results in a word error rate of approximately 10^{-123} under the signal conditions outlined above. Similarly, the probability of a word error in any of the first three subframes (ie. the critical navigation data) is given by $1 - (1 - P_w)^{30} \approx 3.1 \times 10^{-122}$. These results demonstrate that under quiescent signal conditions, the bit error rates and word error rates are negligible for GPS.

In the following sections, the effects of scintillations on the navigation data will be examined by treating the GPS receiver as a BPSK communications system that is subject to non-dispersive fading (ie. frequency and time-flat fading). The principal difference in this analysis over most other analyses is that the signal intensity is assumed to follow the Nakagami-m distribution, and the resulting bit error rates are linked to the scintillation parameters discussed earlier.

² For binary data, $p(H_0) + p(H_1) = 1$.

6.2. The impact of phase scintillations on navigation data

In this section, the effects of phase scintillations on the bit error probability will be examined under the assumption that amplitude scintillations are absent (ie. it will be assumed that the amplitude is constant).

When the satellite signal is modulated by phase scintillations, the phase error, ϕ_e , becomes a random variable. Therefore, the random variables X_0 and X_1 given in Equation (6.1-2) become functions of the two random variables n_{IP} and ϕ_e as follows

$$\begin{aligned} X_0 &= -\mathbf{A}\cos(\phi_e) + n_{IP} \\ X_1 &= \mathbf{A}\cos(\phi_e) + n_{IP} \end{aligned} \quad (6.2-1)$$

where the amplitude \mathbf{A} is assumed to be constant (ie. for the moment, amplitude scintillations have been ignored). If it is assumed that the linearising approximations made in the analysis of the tracking loops are not significantly violated, the variance of ϕ_e can be obtained from the linear model transfer function of the tracking loop as follows (from Equation (3.2-5))

$$\begin{aligned} E\{\phi_e^2\} &= \sigma_{\phi_e}^2 = \int_{-\infty}^{\infty} \frac{f^{2k}}{(f^{2k} + f_n^{2k})} \cdot \frac{\mathbf{T}}{(f_o^2 + f^2)^{p/2}} df + \frac{B_n}{C/N_o} \left[1 + \frac{1}{2TC/N_o} \right] \\ &= \sigma_{\phi_{ep}}^2 + \sigma_{\phi_T}^2 \end{aligned} \quad (6.2-2)$$

where $\sigma_{\phi_{ep}}^2$ and $\sigma_{\phi_T}^2$ are contributions to the phase error variance from phase scintillations and thermal noise respectively. This assumes that the pre-detection filters have a negligible effect on the phase errors produced by phase scintillations. As the integration period of the pre-detection filters coincides with the duration of a navigation data bit, this also implies that the phase errors will remain approximately constant over each data bit. This is an important assumption on which the following analysis is based.

As X_0 is now a function of the phase error, ϕ_e , the new PDF of X_0 is given by

$$f_{X_0}(x_0) = \int_{-\infty}^{\infty} f_{X_0|\phi_e}(x_0|\phi) f_{\phi_e}(\phi) d\phi \quad (6.2-3)$$

where $f_{X_0|\phi_e}(x_0|\phi)$ is the conditional PDF of X_0 given ϕ_e , and $f_{\phi_e}(\phi)$ is the PDF of ϕ_e . The probability of a bit error is thus (from Equation (6.1-5))

$$\begin{aligned}
 P_e &= \int_0^\infty f_{X_0}(x_0)dx_0 \\
 &= \int_0^\infty \int_{-\infty}^\infty f_{X_0|\phi_e}(x_0|\phi).f_{\phi_e}(\phi)d\phi dx_0 \\
 &= \int_{-\infty}^\infty f_{\phi_e}(\phi) \left[\int_0^\infty f_{X_0|\phi_e}(x_0|\phi)dx_0 \right] d\phi \\
 &= \int_{-\infty}^\infty f_{\phi_e}(\phi)P_e(\rho_b,\phi)d\phi
 \end{aligned} \tag{6.2-4}$$

where $\rho_b = T.C/N_o$, and $P_e(\rho_b,\phi)$ is the conditional bit error probability given ρ_b and ϕ . As $f_{X_0|\phi_e}(x_0|\phi)$ is distributed $N(-A\cos(\phi),\sigma_n)$, the conditional bit error probability is given by

$$\begin{aligned}
 P_e(\rho_b,\phi) &= \frac{1}{2} \operatorname{Erfc}\left(\frac{A\cos(\phi)}{\sqrt{2}\sigma_n}\right) \\
 &= \frac{1}{2} \operatorname{Erfc}\left(\cos(\phi)\sqrt{T.C/N_o}\right)
 \end{aligned} \tag{6.2-5}$$

If it is assumed that the phase errors follow the Tikhonov density function for a Costas loop (Equation (C-6)), the probability of a bit error is given by

$$P_e = \int_{-\pi/2}^{\pi/2} \frac{\exp(\rho_e \cos(2\phi))}{\pi I_o(\rho_e)} \cdot \frac{1}{2} \operatorname{Erfc}\left(\cos(\phi)\sqrt{T.C/N_o}\right) d\phi \tag{6.2-6}$$

where $\rho_e = 1/4\sigma_{\phi_e}^2$ and $\sigma_{\phi_e}^2$ is the phase error variance from the linear model (Equation (6.2-2)). Although this result strictly only applies to a system that is based on a first order Costas loop, it is also likely to be quite accurate for higher loop orders, particularly when the spectral index, p , is close to 2. The reasons for this were discussed earlier in Chapter 3. In Figure 6.2-1, the bit error probability and word error probability are plotted as a function of $\sigma_{\phi_e}^2$ for a first order Costas loop with $T = 20\text{ms}$, $C/N_o = 41.5\text{dBHz}$ and $B_n = 2\text{Hz}$. The maximum phase error variance is set to $(\pi/12)^2$ radians 2 which is the rule of thumb tracking threshold for linear operation (Equation (C-3), Appendix C). Notice

that $\sigma_{\phi_{ep}}^2$ can be related to the scintillation parameters T , p and f_o for a specific loop order and bandwidth through Equation (6.2-2).

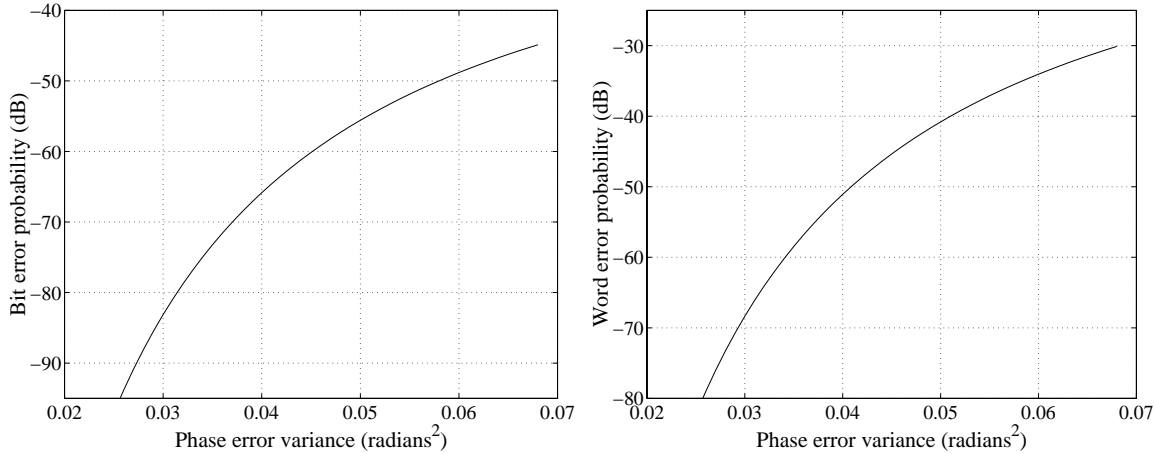


Figure 6.2-1: Probability of a bit error (left panel) and a word error (right panel) as a function of the phase error variance, $\sigma_{\phi_{ep}}^2$, for a first order loop with $T=20ms$, $C/N_o = 41.5dB$ and $B_n = 2Hz$.

The results presented in Figure 6.2-1 suggest that phase scintillations have a relatively minor effect on the process of demodulating the navigation data. Even when the phase error variance is near the carrier loop tracking threshold, the probability of a word error is only 0.1% (-30dB) and the probability of a word error in any of the first three subframes is approximately 3% ($30P_w$). As will be shown in the next section, these are much smaller than the corresponding probabilities under amplitude scintillation conditions with $S_4 = 1$.

6.3. The impact of amplitude scintillations on navigation data

In this section, the effects of amplitude scintillations on the bite error probability will be examined under the assumption that phase scintillations are absent (ie. $\phi_{ep} = \phi_p = 0$).

Under quiescent signal conditions, ϕ_e is extremely small and the simplifying approximation $\cos(\phi_e) \approx 1$ can be made. However, when amplitude scintillations are present, occasional deep fading can result in a significant increase in the thermal noise contributions to ϕ_e , particularly when the tracking loop bandwidth is wide.

Consequently, both the amplitude, \tilde{A} , and the phase error, ϕ_e , will become random variables. X_0 and X_1 can therefore be represented by

$$\begin{aligned} X_0 &= -\tilde{A} \cos(\phi_e) + n_{IP} \\ X_1 &= \tilde{A} \cos(\phi_e) + n_{IP} \end{aligned} \quad (6.3-1)$$

where \tilde{A} is Nakagami-m distributed (Equation (2.1-8)), n_{IP} is distributed $N(0, \sigma_n)$ and ϕ_e is assumed to follow the Tikhonov PDF. In this analysis, it is assumed that the effects of the pre-detection filters on the amplitude are negligible (ie. $\tilde{A} \approx A$, where A is the signal amplitude prior to filtering). For amplitude scintillations, the Tikhonov PDF is considered to be a reasonable choice as the phase errors are driven entirely by white, Gaussian thermal noise. The effective SNR for the Tikhonov PDF is given by $\rho_e = 1/4\sigma_{\phi_e}^2$, where $\sigma_{\phi_e}^2$ is a function of \tilde{A} and is given by (from Equation (3.3-9))

$$\sigma_{\phi_e}^2(\tilde{A}) = \sigma_{\phi_T}^2(\tilde{A}) = \int_{-\infty}^{\infty} |H'(f, \tilde{A})|^2 \frac{S_{n_d}(f)}{\tilde{A}^4} df \quad (6.3-2)$$

For a first order loop, this reduces to (from Equation (3.3-13))

$$\sigma_{\phi_e}^2(\tilde{A}) = \sigma_{\phi_T}^2(\tilde{A}) = \frac{\bar{B}_n}{C/N_o} \left[\frac{1}{g_N} + \frac{1}{2T C/N_o \tilde{A}_N^2 g_N} \right] \quad (6.3-3)$$

where $\tilde{A}_N = \tilde{A}/\mathbf{A}$ is the normalised signal amplitude, and $g_N = g/\mathbf{A}^2$ is the normalised AGC gain factor. These equations assume that the bandwidth of the amplitude scintillations is small compared with the nominal loop noise bandwidth \bar{B}_n . The PDF of X_0 is given by

$$f_{X_0}(x_0) = \int_0^\infty \int_{-\pi/2}^{\pi/2} f_{X_0|\phi_e, \tilde{A}}(x_0|\phi, A) f_{\phi_e|\tilde{A}}(\phi|A) f_{\tilde{A}}(A) d\phi dA \quad (6.3-4)$$

where

$$f_{X_0|\phi_e, \tilde{A}}(x_0|\phi, A) = N(-A \cos(\phi), \sigma_n) \quad (6.3-5)$$

is the conditional PDF of X_0 given ϕ_e and \tilde{A} . Also

$$f_{\phi_e|\tilde{A}}(\phi|A) = \frac{\exp(\rho_e \cos(2\phi))}{\pi I_0(\rho_e)}, \quad |\phi| \leq \frac{\pi}{2} \quad (6.3-6)$$

is the conditional PDF of ϕ_e given \tilde{A} with $\rho_e = \frac{1}{4\sigma_{\phi_e}^2(\tilde{A})}$, and

$$f_{\tilde{A}}(A) = \frac{2m^m A^{2m-1}}{\Gamma(m).(\langle \tilde{A}^2 \rangle)^m} \exp\left(-\frac{mA^2}{\langle \tilde{A}^2 \rangle}\right) \quad A \geq 0 \quad (6.3-7)$$

is the Nakagami-m PDF for amplitude. The probability of a bit error is then (from Equation (6.1-5))

$$\begin{aligned} P_e &= \int_0^\infty f_{X_0}(x_0) dx_0 \\ &= \int_0^\infty \int_0^\infty \int_{-\pi/2}^{\pi/2} f_{X_0|\phi_e, \tilde{A}}(x_0|\phi, A) f_{\phi_e|\tilde{A}}(\phi|A) f_{\tilde{A}}(A) d\phi dA dx_0 \\ &= \int_0^\infty \int_{-\pi/2}^{\pi/2} f_{\phi_e|\tilde{A}}(\phi|A) f_{\tilde{A}}(A) \left[\int_0^\infty f_{X_0|\phi_e, \tilde{A}}(x_0|\phi, A) dx_0 \right] d\phi dA \end{aligned} \quad (6.3-8)$$

By substituting the appropriate PDF expressions from Equations (6.3-5) to (6.3-7) into Equation (6.3-8), the probability of a bit error becomes

$$P_e = \int_0^\infty \int_{-\pi/2}^{\pi/2} \frac{\exp(\rho_e \cos(2\phi))}{\pi I_0(\rho_e)} \cdot \frac{2m^m A^{2m-1}}{\Gamma(m).(\langle \tilde{A}^2 \rangle)^m} \exp\left(-\frac{mA^2}{\langle \tilde{A}^2 \rangle}\right) \frac{1}{2} \operatorname{Erfc}\left(\frac{A \cos(\phi)}{\sqrt{2}\sigma_n}\right) d\phi dA \quad (6.3-9)$$

Although a closed form solution to this integral is difficult to obtain, a numerical solution can be produced for a given nominal (undisturbed) carrier to noise density ratio and noise bandwidth. To obtain a numerical solution, it is convenient to replace the dummy variable A with a variable ρ_o which represents the instantaneous carrier to noise density ratio of the satellite signal. By making the following substitutions

$$\begin{aligned} A &= \sqrt{2N_o\rho_o} \\ \sigma_n^2 &= N_o/T \\ \langle \tilde{A}^2 \rangle &= 2C/N_o * N_o \end{aligned} \quad (6.3-10)$$

where C/N_o is the nominal carrier to noise density ratio, the following expression can be obtained for the probability of a bit error

$$P_e = \int_0^\infty \int_{-\pi/2}^{\pi/2} \frac{\exp(\rho_e \cos(2\phi))}{\pi I_0(\rho_e)} \cdot \frac{m^m \rho_o^{m-1}}{\Gamma(m).C/N_o^m} \exp\left(-\frac{m\rho_o}{C/N_o}\right) \frac{1}{2} \operatorname{Erfc}\left(\sqrt{T\rho_o} \cos(\phi)\right) d\phi d\rho_o \quad (6.3-11)$$

In Figure 6.3-1, P_e is plotted as a function of the intensity scintillation index S_4 ($= 1/m^2$) for a first order loop with $T=20\text{ms}$, $C/N_o = 41.5 \text{ dBHz}$ and $B_n = 2\text{Hz}$ (upper of the two curves). In this case, the AGC is assumed to be ideal (ie. $g_N = \tilde{A}_N^{-2}$), and the effective loop SNR is given by (from Equation (6.3-3))

$$\begin{aligned}\rho_e &= \frac{1}{4\sigma_{\phi_e}^2(\tilde{A})} \\ &= \frac{C/N_o}{4\bar{B}_n \left[\frac{1}{\tilde{A}_N^2} + \frac{1}{2TC/N_o \tilde{A}_N^4} \right]} \\ &= \frac{T\rho_o^2}{2\bar{B}_n [2T\rho_o + 1]}\end{aligned}\quad (6.3-12)$$

If it is assumed that the phase errors are negligible (ie. $\cos(\phi_e) \approx 1$), the PDF of X_0 reduces to

$$f_{X_0}(x_0) = \int_0^\infty f_{X_0|\tilde{A}}(x_0|A) f_{\tilde{A}}(A) dA \quad (6.3-13)$$

The probability of a bit error is then

$$\begin{aligned}P_e &= \int_0^\infty f_{X_0}(x_0) dx_0 \\ &= \int_0^\infty \int_0^\infty f_{X_0|\tilde{A}}(x_0|A) f_{\tilde{A}}(A) dA dx_0. \\ &= \int_0^\infty \frac{m^m \rho_o^{m-1}}{\Gamma(m) C/N_o^m} \exp\left(-\frac{m\rho_o}{C/N_o}\right) \frac{1}{2} \operatorname{Erfc}\left(\sqrt{T\rho_o}\right) d\rho_o\end{aligned}\quad (6.3-14)$$

Wojnar [102], demonstrated that this integral could be expressed in terms of an incomplete Beta function ratio as follows

$$\begin{aligned}P_e &= \frac{1}{2} \frac{\beta_{m/(m+\alpha)}(m, 1/2)}{\beta(m, 1/2)} \\ &= \frac{1}{2} I_{m/(m+\alpha)}(m, 1/2)\end{aligned}\quad (6.3-15)$$

where $\alpha = T.C/N_o$, $\beta(a, b)$ is the Beta function, $\beta_n(a, b)$ is the Incomplete Beta function, and $I_n(a, b) = \beta_n(a, b)/\beta(a, b)$ is the Incomplete Beta function ratio (see for example Gradshteyn [37]). In Figure 6.3-1, the lower curves represent P_e obtained from Equation

(6.3-15) under the assumption that the phase errors are negligible. These curves show that for a narrow bandwidth receiver (in this case 2Hz), the direct effect of amplitude scintillations on the probability of a bit error is far more significant than the effect of an increase in the level of thermal noise in the feedback path. For wider noise bandwidth's, the contributions to P_e from phase errors in the feedback path becomes more significant but are still relatively small (see Figure 6.3-2).

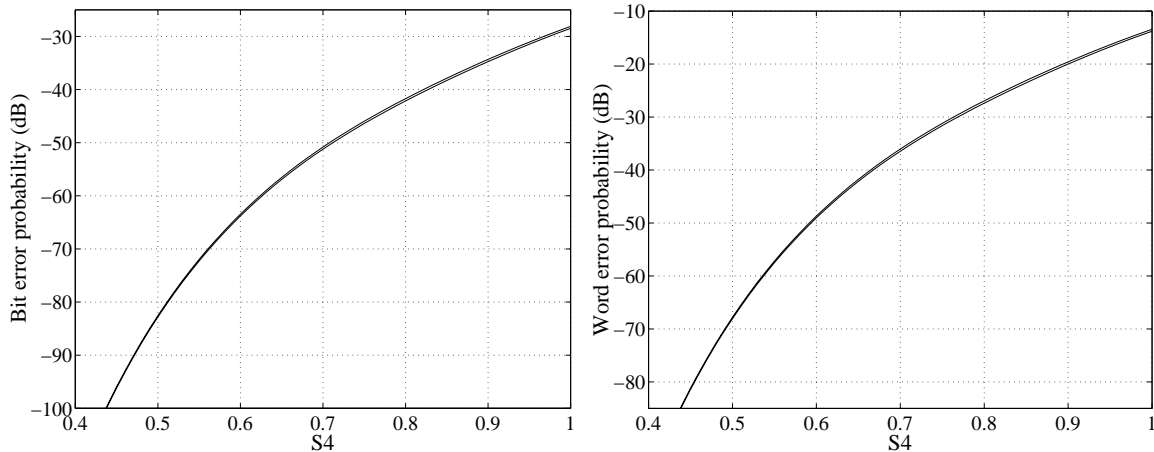


Figure 6.3-1: Probability of a bit error (left panel) and a word error (right panel) as a function of S_4 for $T = 20ms$, $C/N_o = 41.5dB$ and $B_n = 2Hz$. The upper curves represent a situation in which the phase errors have been included (Equation (6.3-11)). The lower curves represent a situation in which they have been ignored (Equation (6.3-15)).

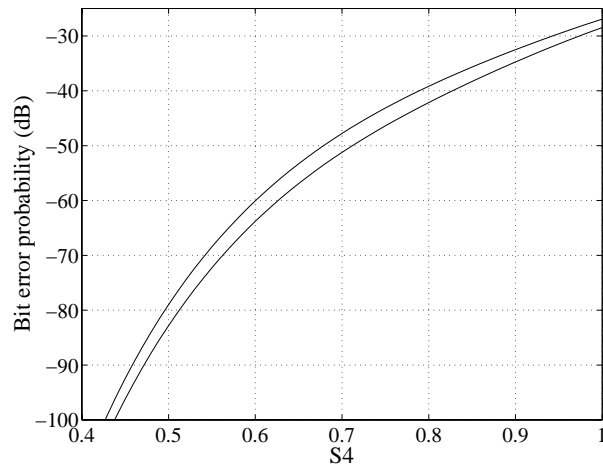


Figure 6.3-2: Probability of a bit error as a function of S_4 for $T=20ms$, $C/N_o = 41.5dB$ and $B_n = 15Hz$. The upper curve represent a situation in which the phase errors have been included. The lower curve represent a situation in which they have been ignored.

So far, only the effects of an ideal AGC have been considered. In order to account for the effects of a non-ideal AGC (either fast or very slow), the linear model variance expression (Equation (6.3-3)) must be modified to include a non-ideal AGC gain factor, g_N . However, as shown in Section 3.3, when the loop is only subject to amplitude scintillations and thermal noise, a non-ideal AGC will result in smaller phase tracking errors. Therefore, the phase errors will have even less of an effect on the bit error rates than has already been discussed. However, this is not necessarily true when the loop is also subject to phase scintillations as its ability to track phase variations will be impaired.

6.4. The combined effect of scintillations on navigation data

When, as is normally the case, amplitude and phase scintillations are present together, their impact on the navigation data can be found using Equation (6.3-11), but with $\sigma_{\phi_e}^2$ based on Equation (3.3-8) rather than Equation (6.3-2). Again, this assumes that the Tikhonov PDF is a valid choice for the phase error density function (ie. it assumes that $p \approx 2$). From Equation (6.3-11), the bit error probability is given by

$$P_e = \int_0^\infty \int_{-\pi/2}^{\pi/2} \frac{\exp(\rho_e \cos(2\varphi))}{\pi I_0(\rho_e)} \cdot \frac{m^m \rho_o^{m-1}}{\Gamma(m) \cdot C/N_o^m} \exp\left(-\frac{m\rho_o}{C/N_o}\right) \frac{1}{2} \operatorname{Erfc}\left(\sqrt{T\rho_o} \cos(\varphi)\right) d\varphi d\rho_o \quad (6.4-1)$$

where $\rho_e = \frac{1}{4\sigma_{\phi_e}^2(\tilde{A})}$ and $\sigma_{\phi_e}^2(\tilde{A}) = \int_{-\infty}^{\infty} \left[|1 - H'(f, \tilde{A})|^2 S_{\phi_p}(f) + |H'(f, \tilde{A})|^2 \frac{S_{n_d}(f)}{\tilde{A}^4} \right] df$ from

Equation (3.3-8). For a first order I.Q Costas loop, this becomes

$$\sigma_{\phi_e}^2(\tilde{A}) = \int_{-\infty}^{\infty} \frac{f^2}{f^2 + (f_n \tilde{A}_N^2 / g_N)^2} \cdot \frac{\mathbf{T}}{(f_o^2 + f^2)^{p/2}} df + \frac{\bar{B}_n}{C/N_o} \left[\frac{1}{g_N} + \frac{1}{2TC/N_o \tilde{A}_N^2 g_N} \right] \quad (6.4-2)$$

For an ideal AGC (or a fast AGC with a large C/N_o and $S_4 \leq 1/\sqrt{2}$), this reduces to

$$\begin{aligned} \sigma_{\phi_e}^2(\tilde{A}) &= \int_{-\infty}^{\infty} \frac{f^2}{f^2 + f_n^2} \cdot \frac{\mathbf{T}}{(f_o^2 + f^2)^{p/2}} df + \frac{\bar{B}_n}{\rho_o} \left[1 + \frac{1}{2T\rho_o} \right] \\ &= \sigma_{\phi_{ep}}^2 + \sigma_{\phi_T}^2(\tilde{A}) \end{aligned} \quad (6.4-3)$$

In Figure 6.4-1, the probability of a bit error is plotted as a function of S_4 and $\sigma_{\phi_{ep}}^2$ for a first order loop with an ideal AGC, $T = 20\text{ms}$, $C/N_o = 41.5\text{dBHz}$ and $B_n = 2\text{Hz}$. Note that $\sigma_{\phi_{ep}}^2$ can be represented in terms of the phase scintillation spectral parameters T , p and f_o for a given loop order and bandwidth.

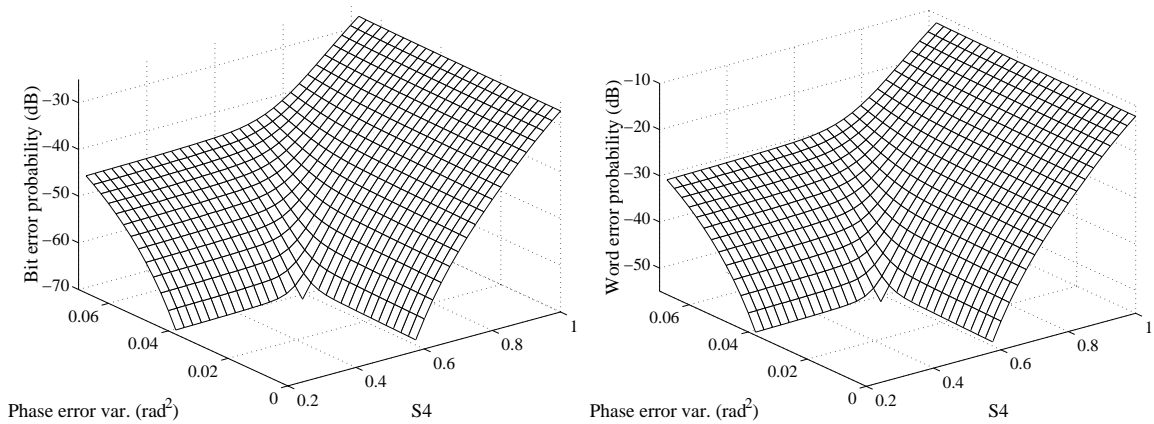


Figure 6.4-1: Probability of a bit error (left panel) and a word error (right panel) as a function of S_4 and $\sigma_{\phi_{ep}}^2$ for $T = 20\text{ms}$, $C/N_o = 41.5\text{dBHz}$ and $B_n = 2\text{Hz}$.

It is clear from Figure 6.4-1 that even under very strong amplitude and phase scintillation conditions (ie. $S_4 \approx 1$ and $\sigma_{\phi_{ep}} \approx \sigma_{\phi_e} \Big|_{T_h}$), the probability of a word error in the navigation data is only a few percent. Because of the high level of redundancy in the navigation data (both within the navigation message and between satellites), it is unlikely that this level of impairment will have much of an impact on a tracking GPS receiver. Indeed, the complete loss of the navigation data will only affect GPS operation if the outage is long enough for the ephemeris data to be significantly in error. As the ephemeris data can be regarded as being accurate for many tens of minutes or more, short losses of a few seconds to minutes would be inconsequential to a receiver (under sever scintillation conditions, loss of code and carrier lock would be of more importance). However, navigation data errors may affect the process of downloading almanac data from a satellite during acquisition, thus extending a receiver's time to first fix.

6.5. A note on word error probabilities

An implicit assumption in the analysis so far has been that the amplitude scintillation waveform remains approximately constant for the duration of a navigation data bit (ie. for 20 ms). Based on a knowledge of the typical fluctuation rates of amplitude scintillations, it is expected that this assumption will be valid under most scintillation conditions.

Word error probabilities were calculated by assuming independence between the bit error probabilities of successive data bits. Consequently, from Equation (6.1-7) the word error probability is given by

$$P_w = 1 - (1 - P_e)^{30} \quad (6.5-1)$$

where P_e is the average bit error probability. As the bit error probability is conditioned on the amplitude, this assumption implies that the amplitude is independent between consecutive data bits. As explained later (see Section 7.3.3 on acquisition) this in turn implies that the amplitude scintillation waveform must be fluctuating at a very rapid rate. However, depending on the cutoff frequency of the amplitude scintillation power spectrum³, f_c , it is known that the amplitude waveform may vary quite slowly in relation to the navigation data. For a slowly varying waveform, there will be fewer, longer duration deep fades over a given interval of time. Therefore, the occasions during which the bit error probabilities are at an elevated level are likely to be clustered and associated with these longer duration deep fades. As the loss of only one data bit is required for the loss of a word, it is expected that this condition will reduce P_w somewhat.

To test this hypothesis, it is assumed that the amplitude remains approximately constant for the 0.6 seconds duration of a word, but may vary between consecutive words (in fact, this result will be the same if the amplitude is assumed to remain constant for longer periods of time). The average word error probability is then

³ f_c is a function of the satellite-receiver geometry and the ionospheric drift velocity (see Appendix G).

$$P_w = \int_0^{\infty} [1 - [1 - P_e(A)]^{30}] f_{\tilde{A}}(A) dA \quad (6.5-2)$$

where $P_e(A) = \int_0^{\infty} f_{X_0|\tilde{A}}(x_0|A) dx_0 = \frac{1}{2} \text{Erfc}\left(\frac{A}{\sqrt{2}\sigma_n}\right)$ is a conditional bit error probability.

Replacing A with ρ_o gives

$$P_w = \int_0^{\infty} \left[1 - \left[1 - 0.5 \text{Erfc}\left(\sqrt{T\rho_o}\right) \right]^{30} \right] \frac{m^m \rho_o^{m-1}}{\Gamma(m).C/N_o^m} \exp\left(-\frac{m\rho_o}{C/N_o}\right) d\rho_o \quad (6.5-3)$$

In Figure 6.5-1, P_w is plotted as a function of S_4 for $T=20\text{ms}$ and $C/N_o = 41.5\text{dBHz}$ using both Equations (6.5-1) and (6.5-3). It is clear that by assuming a slowly varying amplitude waveform, the word error probability is reduced by as much as 5dB for values of S_4 near to one. In practice, it is anticipated that the actual values of P_w will lie somewhere between these two curves.

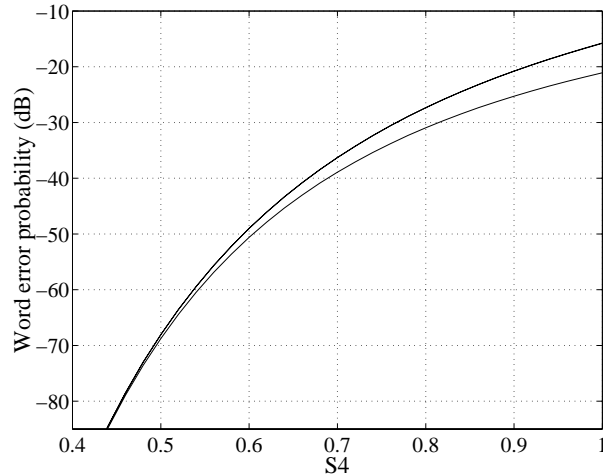


Figure 6.5-1: Probability of a word error as a function of S_4 for $T=20\text{ms}$ and $C/N_o = 41.5\text{dBHz}$. The upper curve represent a situation in which the amplitude is assumed to be independent between successive T second epochs. The lower curve represent a situation in which the amplitude is assumed to be constant during each word.

Although this approach could be extended to include the effects of amplitude scintillations on a subframe, the much greater length of a subframe (10 words = 6s) means that the assumption of a constant amplitude is probably no longer valid.

6.6. Conclusions

In general, phase scintillations have much less of an effect on the navigation data than amplitude scintillations. When phase scintillations are at the tracking threshold of the carrier loop, the word error probability is less than 0.1%, compared to approximately 4% when $S_4 = 1$ (assuming a nominal, quiescent GPS signal level and rapid amplitude fluctuations). However, for a very slowly varying amplitude waveform, the word error probability can fall to only 1% for $S_4 = 1$ under the same quiescent signal conditions. Consequently, even under conditions for which the carrier loop is likely to lose lock, the word error probability will only be a few percent, assuming that amplitude and phase scintillations are uncorrelated.

It is considered unlikely that the small error rates associated with scintillations will cause much of a problem for GPS for the following reasons:

- There is significant redundancy within the navigation message, particularly with regard to the ephemeris data and clock correction factors which are repeated once every frame (ie. every 30 seconds).
- There is also significant redundancy between the navigation messages transmitted by different satellites. Each satellite transmits the same almanac data which contains health, ionospheric correction factors and low precision orbital information etc. for all of the satellites in the constellation.
- As much of the navigation data consists of slowly varying correction factors, loss of the navigation data will only cause a gradual degradation in navigational accuracy.

Nevertheless, during the acquisition process, navigation data errors may have a more significant effect, particularly if the receiver is tracking only one satellite and is attempting to download almanac data following a cold start.

Chapter 7

Acquisition

In this chapter, the effects of scintillations on the acquisition performance of a GPS receiver is examined. In Section 7.2, the effects of scintillations on the probability of detection and the probability of false alarm are investigated for a full code period, square-law, Neyman-Pearson type detector. It is shown that both amplitude and phase scintillations have a negligible effect on the probability of false alarm, but that amplitude scintillations can significantly reduce the probability of detection. The effect of this reduced probability of detection on the mean time to acquire the GPS signal is then examined in Section 7.3 for a single dwell, serial search strategy for which there is assumed to be no *a priori* information about the code phase. This is then extended to a situation in which the correlation time of the amplitude scintillations is much longer than the time required to execute one pass of the search domain. The results show that amplitude scintillations increase the mean time to acquire, and that the effect is more pronounced for longer amplitude correlation times (ie. for slower scintillations).

7.1. Acquisition model

Acquisition is the process of synchronising a local reference signal to the received GPS signal prior to closure of the code and carrier tracking loops. The process involves a two dimensional search for the GPS signal in both Doppler frequency and code phase.

As shown in Figure 7.1-1, the acquisition detector is essentially a square-law detector for the GPS signal where the test statistic is given by

$$Z = \frac{1}{k} \sum_{i=1}^k I_i^2 + Q_i^2 \quad (7.1-1)$$

The output of the detector, Z , is compared with a threshold, η , to determine whether a satellite signal is present and whether it is correctly aligned with the reference signal. If the threshold is exceeded, it is assumed that both the code delay and carrier frequency of

the reference signal are sufficiently close to those of the satellite signal for tracking to begin.

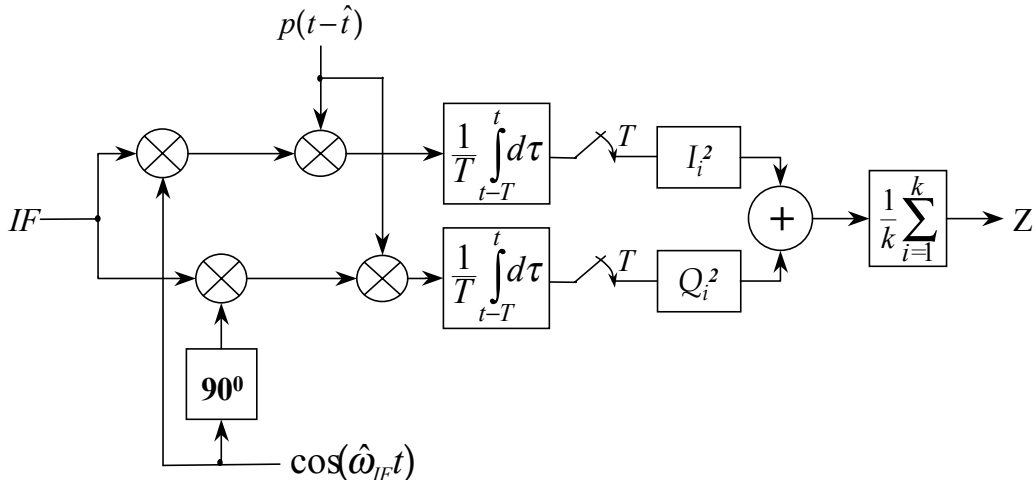


Figure 7.1-1: A square-law acquisition detector for a GPS receiver.

Usually, when the reference is incorrectly aligned, it is assumed that the signal produced at the output of the code and carrier mixers behaves like zero-mean, white Gaussian noise. However, because correlation sidelobes¹ may be present, particularly during C/A-Code acquisition, this model is strictly not correct and a more accurate approach is to assume that a signal of much lower strength is present under these conditions [92]. In the analysis that follows, the white Gaussian noise model will be used predominantly, and the error in this model will be discussed in Section 7.2.2.

7.2. Detection and false alarm probabilities

For an IF signal of the form $A(t)p(t-\tau)d(t-\tau)\cos(\omega_{IF}t + \phi(t)) + n(t)$ and a reference signal of the form $2p(t-\hat{t})\cos(\hat{\omega}_{IF}t + \hat{\phi})$, the I and Q signals immediately after the pre-detection filters are given by [20]

$$\begin{aligned} I &= \tilde{A}(t)d(t-\tau) \frac{\sin(\omega_e T/2)}{\omega_e T/2} R(\tau_e) \cos(\omega_e(t-T/2) + \phi_e(t)) + n_I(t) \\ Q &= \tilde{A}(t)d(t-\tau) \frac{\sin(\omega_e T/2)}{\omega_e T/2} R(\tau_e) \sin(\omega_e(t-T/2) + \phi_e(t)) + n_Q(t) \end{aligned} \quad (7.2-1)$$

where $\omega_e = \omega_{IF} - \hat{\omega}_{IF}$ is the error in the frequency estimate, $\tau_e = \tau - \hat{\tau}$ is the error in the

¹ Correlation sidelobes can result from correlation between the reference signal and another satellite signal, or between an incorrectly aligned reference signal and the desired satellite signal.

code delay estimate, $\phi_e(t) = \phi(t) - \hat{\phi}$ is the phase error, and $R(\tau)$ is the code autocorrelation function (Equation (4.1-1)). These two expressions assume that the amplitude, $\tilde{A}(t)$, and the phase, $\phi(t)$, of the GPS signal do not change appreciably over the T second integration period of the filters, and that the navigation data does not change sign. As T is typically of the order of a few ms, these conditions are usually met, even in the presence of scintillations.

For a typical GPS receiver, the separation between bins in the Code/Doppler search domain is of the order of $1/2$ a chip and $3/(4T)$ Hz respectively [20]. T can be made quite small for strong satellite signals (eg. 1ms for a 750 Hz bin spacing), but must be large for weak signals (eg. 10ms for a 75 Hz bin spacing). Increasing T to account for weak signals will result in longer search times, even if the dwell time in each bin, kT , is kept constant, as the number of Doppler bins required for a given frequency uncertainty will increase. As the signal strength is rarely known *a priori*, assumptions must be made about the receiver antenna gain pattern and the satellite signal power etc. in order to obtain a good estimate of the signal strength. However, such assumptions are unlikely to take into account effects such as obscuration and attenuation by nearby obstacles, nor the effects of scintillations.

In the analysis that follows, it is assumed that if the correct bin is selected in the Code/Doppler search domain, τ_e and ω_e will both be zero. If the bins are separated by τ_Δ chips and ω_Δ radians/s, the maximum error in this assumption will be

$$\xi = \frac{\sin(\omega_\Delta T/4)}{\omega_\Delta T/4} R(\tau_\Delta/2) \quad (7.2-2)$$

To account for this error, the GPS signal power can be multiplied by a correction factor, ξ^2 , prior to calculating the probability of detection. If, $\omega_\Delta = 2\pi*3/4T$ radians/s and $\tau_\Delta = 1/2$ a chip, this correction factor will be -4.6dB.

By assuming $\omega_e = \tau_e = 0$, the I and Q samples produced at the output of the pre-detection filters for a correctly aligned reference signal can be represented by

$$\begin{aligned} I_i &= \tilde{A}_i \cos(\phi_{ei}) + n_{Ii} \\ Q_i &= \tilde{A}_i \sin(\phi_{ei}) + n_{Qi} \end{aligned} \quad (7.2-3)$$

The navigation data, $d(t-\tau)$, has been ignored in these expressions as it will be eliminated by squaring in the subsequent stage. When the reference signal is incorrectly aligned, it is assumed that $I_i = n_{Ii}$ and $Q_i = n_{Qi}$.

The probability density function (PDF) of the test statistic, Z , in the presence of noise only, or in the presence of an incorrectly aligned signal (Hypothesis H_0) is given by the central chi-squared distribution with $2k$ degrees of freedom [84]

$$f_{Z|H_0}(z) = \left[\frac{k}{2\sigma_n^2} \right]^k \frac{z^{k-1}}{\Gamma(k)} \exp\left(-\frac{zk}{2\sigma_n^2}\right), \quad z \geq 0 \quad (7.2-4)$$

where, $\sigma_n^2 = N_o/T$ is the thermal noise variance on either the I or Q channels and k is the order of the post-detection integrator. The PDF of the test statistic in the presence of a correctly aligned satellite signal (Hypothesis H_1) is given by the non-central chi-squared distribution with $2k$ degrees of freedom [84]

$$f_{Z|H_1}(z) = \frac{k}{2\sigma_n^2} \left[\frac{z}{\tilde{A}^2} \right]^{(k-1)/2} I_{k-1} \left(\frac{k\tilde{A}\sqrt{z}}{\sigma_n^2} \right) \exp\left(-\frac{k(z+\tilde{A}^2)}{2\sigma_n^2}\right), \quad z \geq 0 \quad (7.2-5)$$

where $\tilde{A} = \sigma_n \sqrt{2TC/N_o}$ is the signal amplitude immediately after the pre-detection filters, and $I_{k-1}(\cdot)$ is the modified Bessel function of the first kind of order $k-1$. If a detection threshold of η is chosen, the probability of a correct detection is given by

$$\begin{aligned} P_d &= \int_{\eta}^{\infty} f_{Z|H_1}(z) dz \\ &= \int_{\eta}^{\infty} \frac{k}{2\sigma_n^2} \left[\frac{z}{\tilde{A}^2} \right]^{(k-1)/2} I_{k-1} \left(\frac{k\tilde{A}\sqrt{z}}{\sigma_n^2} \right) \exp\left(-\frac{k(z+\tilde{A}^2)}{2\sigma_n^2}\right) dz \end{aligned} \quad (7.2-6)$$

and the probability of a false detection (false alarm) is given by [84]

$$\begin{aligned} P_{fa} &= \int_{\eta}^{\infty} f_{Z|H_0}(z) dz \\ &= \int_{\eta}^{\infty} \left[\frac{k}{2\sigma_n^2} \right]^k \frac{z^{k-1}}{\Gamma(k)} \exp\left(-\frac{zk}{2\sigma_n^2}\right) dz \\ &= \exp(-\eta') \sum_{j=0}^{k-1} \frac{\eta'^j}{j!} \end{aligned} \quad (7.2-7)$$

where $\eta' = k\eta/2\sigma_n^2$. As the random variables, $I_i^2 + Q_i^2$, generated at the output of the square law detector are independent, the Central Limit theorem can be invoked for large values of k to allow Z to be approximated by a Gaussian distribution. The corresponding probabilities of detection and false alarm are then [84]

$$P_d = Q\left(\frac{\beta - \gamma\sqrt{k}}{\sqrt{1+2\gamma}}\right) \quad (7.2-8)$$

$$P_{fa} = Q(\beta) \quad (7.2-9)$$

where Q is the Gaussian probability integral, $\beta = \sqrt{k}\left(\frac{\eta}{2\sigma_n^2} - 1\right)$ and $\gamma = \tilde{A}^2/2\sigma_n^2$ is the signal to noise ratio.

Equations (7.2-8) and (7.2-9) (or (7.2-6) and (7.2-7)) can be used to select the design parameters k and η once the required values of P_d and P_{fa} have been chosen for a given application. σ_n^2 can also be adjusted through the pre-detection integration period, T , but is restricted somewhat by the presence of navigation data and by uncertainties in the carrier Doppler.

From these equations it is clear that P_{fa} is not a function of the GPS signal characteristics, and so will not be affected by scintillations. However, P_d is a function of the GPS signal amplitude, \tilde{A} , and so will be directly affected by amplitude scintillations. In the presence of amplitude scintillations, the PDF of the test statistic Z under Hypothesis H_1 becomes conditional on the amplitude, \tilde{A} , and can be represented by $f_{Z|H_1,\tilde{A}}(z|\mathbf{A})$. The marginal PDF of $Z|H_1$ is thus

$$f_{Z|H_1}(z) = \int_0^\infty f_{Z|H_1,\tilde{A}}(z|\mathbf{A}) f_{\tilde{A}}(\mathbf{A}) d\mathbf{A} \quad (7.2-10)$$

where $f_{\tilde{A}}(\mathbf{A})$ is the Nakagami-m distribution for amplitude (Equation (2.1-8)). The average probability of detection is therefore

$$\begin{aligned}
\bar{P}_d &= \int_{\eta}^{\infty} \left[\int_0^{\infty} f_{Z|H_1, \tilde{A}}(z|A) f_{\tilde{A}}(A) dA \right] dz \\
&= \int_0^{\infty} \left[\int_{\eta}^{\infty} f_{Z|H_1, \tilde{A}}(z|A) dz \right] f_{\tilde{A}}(A) dA \\
&= \int_0^{\infty} P_d(A) f_{\tilde{A}}(A) dA
\end{aligned} \tag{7.2-11}$$

where $P_d(A)$ is the probability of detection as a function of the signal amplitude and can be obtained from either Equation (7.2-6) or (7.2-8). In Figure 7.2-1, \bar{P}_d is plotted as a function of S_4 ($= 1/\sqrt{m}$) for five values of C/N_o and for $P_{fa} = 0.01\%$ (using Equations (7.2-8) and (7.2-9)). It is clear from this figure that the probability of detection decreases as S_4 increases, and that the effect is more pronounced for smaller values of C/N_o . Consequently, satellite links that penetrate the peak of the ionospheric anomaly at low elevation angles are likely to have the poorest acquisition performance (C/N_o is likely to be lower and S_4 larger under these conditions).

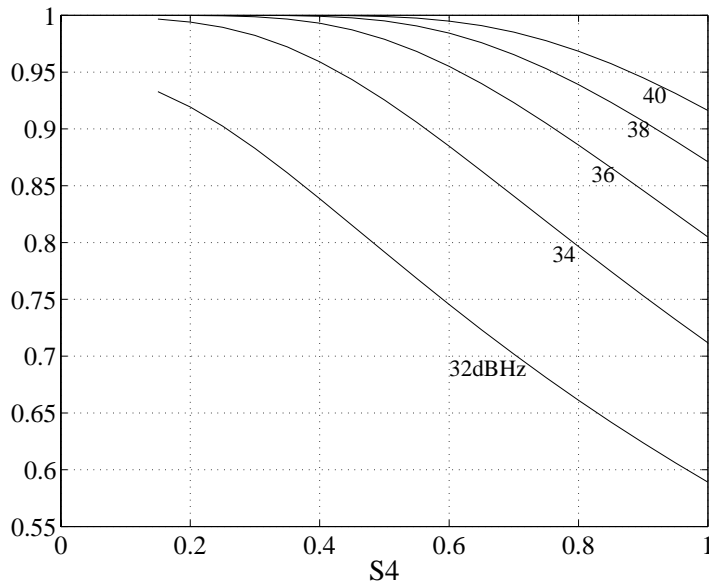


Figure 7.2-1: \bar{P}_d as a function of S_4 for five values of C/N_o (32 to 40dBHz in 2dBHz steps). $T=1ms$, $k=20$, and $P_{fa}=0.01\%$.

By inverting Equation (7.2-8) and solving for the signal to noise ratio, an equivalent C/N_o for quiescent ionospheric conditions can be obtained that will produce the same

probability of detection as Equation (7.2-11). If α is defined as the inverse of Equation (7.2-8) and we let $P_d = \bar{P}_d$, we have

$$\begin{aligned}\alpha &= Q^{-1}(\bar{P}_d) \\ &= \frac{\beta - \gamma' \sqrt{k}}{\sqrt{1 + 2\gamma'}}\end{aligned}\quad (7.2-12)$$

where γ' is the equivalent signal to noise ratio and β is constant for a given P_{fa} . Solving for γ' gives

$$\gamma' = \left[\alpha^2 + \beta \sqrt{k} + |\alpha| \sqrt{\alpha^2 + 2\beta \sqrt{k} + k} \right] / k \quad (7.2-13)$$

from which the equivalent C/N_o' can be obtained using $C/N_o' = \gamma'/T$. In Figure 7.2-2, C/N_o' is plotted as a function of S_4 using the same five values of C/N_o that were used in Figure 7.2-1. It is clear from this figure that C/N_o' decreases as S_4 increases and that the effect is more pronounced for large values of C/N_o .

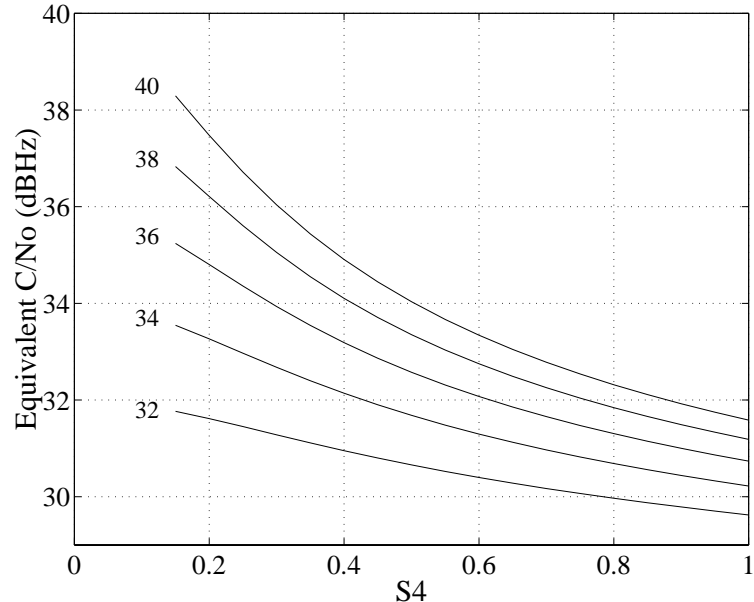


Figure 7.2-2: Equivalent C/N_o as a function of S_4 for five values of C/N_o (32 to 40dBHz in 2dBHz steps). $T=1ms$, $k=20$, and $P_{fa}=0.01\%$.

7.2.1. Phase scintillation effects

If τ_e and ω_e are assumed to be zero when the correct Code/Doppler bin is selected, the test statistic, Z , can be represented by Equation (7.1-1) with I_i and Q_i given by Equation (7.2-3). By making the following substitutions

$$\begin{aligned} n_{Ii} &= n_{ci} \cos(\phi_{ei}) + n_{si} \sin(\phi_{ei}) \\ n_{Qi} &= n_{ci} \sin(\phi_{ei}) - n_{si} \cos(\phi_{ei}) \end{aligned} \quad (7.2-14)$$

where n_{ci} and n_{si} are uncorrelated, zero-mean, baseband Gaussian noise processes with variances of $\sigma_n^2 = N_o/T$, the test statistic becomes

$$Z = \frac{1}{k} \sum_{i=1}^k (\tilde{A}_i + n_{ci})^2 + n_{si}^2 \quad (7.2-15)$$

In this form, it is clear that the carrier phase (and therefore phase scintillations) do not affect Z and so will not influence the detection process for acquisition, provided that the phase does not vary significantly over the integration period of the pre-detection filters. A measure of the phase variation over the integration period of the filters is the expectation of the phase variance over that period. This is given by

$$\sigma_{\phi_{pT}}^2 = E \left\{ \frac{1}{T} \int_{t-T}^t [\phi_p(u) - \bar{\phi}_p]^2 du \right\} \quad (7.2-16)$$

where $\bar{\phi}_p = \frac{1}{T} \int_{t-T}^t \phi_p(u) du$ is the average value of $\phi_p(t)$ over a T second period (which is

also the output of a T second integrate and dump filter which operates directly on the phase). Equation (7.2-16) can be simplified as follows

$$\begin{aligned} \sigma_{\phi_{pT}}^2 &= \frac{1}{T} \int_{t-T}^t [E\{\phi_p(u)^2\} - 2E\{\phi_p(u)\bar{\phi}_p\} + E\{\bar{\phi}_p^2\}] du \\ &= R_{\phi_p}(0) - 2E\left\{\bar{\phi}_p \frac{1}{T} \int_{t-T}^t \phi_p(u) du\right\} + E\{\bar{\phi}_p^2\} \\ &= R_{\phi_p}(0) - E\{\bar{\phi}_p^2\} \end{aligned} \quad (7.2-17)$$

where $R_{\phi_p}(0) = \int_{-\infty}^{\infty} S_{\phi_p}(f) df$ is the power in the phase scintillations prior to filtering,

$E\{\bar{\phi}_p^2\} = \int_{-\infty}^{\infty} |G(f)|^2 S_{\phi_p}(f) df$ is the power in the phase scintillations after a T second

integrate and dump filter which operates directly on the phase, and $G(f) = \text{sinc}(fT) \exp(-j\pi fT)$ is the transfer function of such a filter. Thus,

$$\begin{aligned}\sigma_{\phi_{pT}}^2 &= \int_{-\infty}^{\infty} [1 - |G(f)|^2] S_{\phi_p}(f) df \\ &= \int_{-\infty}^{\infty} [1 - \text{sinc}(fT)^2] \frac{T}{(f_o^2 + f^2)^{p/2}} df\end{aligned}\quad (7.2-18)$$

This can be rearranged to obtain a threshold, T , below which the approximation can be considered to be valid, *viz*

$$T|_{Th} = \frac{\sigma_{\phi_{pT}}^2|_{Th}}{\left[\int_{-\infty}^{\infty} [1 - \text{sinc}(fT)^2] \frac{1}{(f_o^2 + f^2)^{p/2}} df \right]} \quad (7.2-19)$$

where $\sigma_{\phi_{pT}}^2|_{Th}$ is a threshold variance.

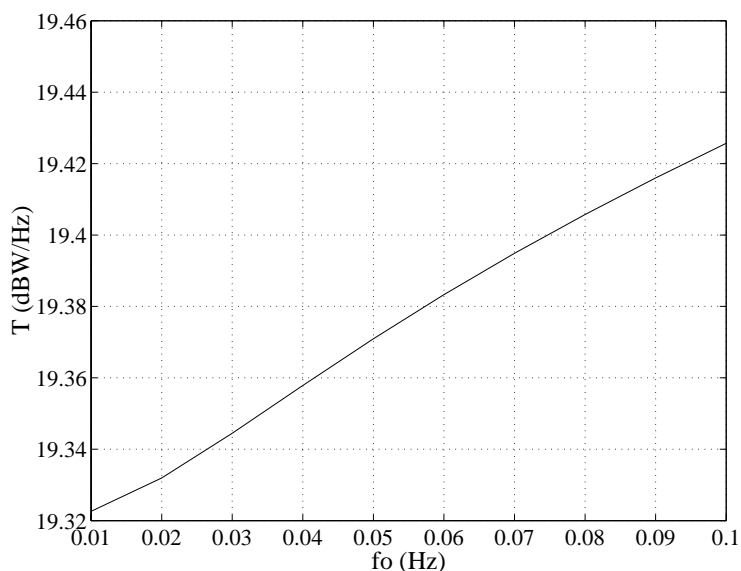


Figure 7.2-3: Threshold T as a function of f_o for a threshold variance of 1 rad^2 , $T=10 \text{ ms}$ and $p=2.5$.

In Figure 7.2-3, the threshold spectral strength, T , is plotted as a function of f_o for a threshold variance of 1 rad², $T=10$ ms (a typical upper limit) and $p=2.5$. It is clear from this figure that the spectral strength must be enormous in order for phase scintillations to cause a significant deviation in the carrier phase over a typical filter integration period. By comparison, a typical large value for the spectral strength parameter in equatorial regions during high solar activity is about -20 dBW/Hz (ie. about 40dB below the values given in Figure 7.2-3). Consequently, for the acquisition model described earlier, the effects of phase scintillations can be ignored.

7.2.2. Correlation sidelobes

The impact of correlation sidelobes on the probability of false alarm can be found by obtaining a new P_{fa} based on the probability of detection equation (Equation (7.2-8)), but using a signal level that is significantly less than the nominal GPS signal level. For the GPS Gold codes (the C/A-Code), the largest sidelobe is approximately 22dB below the correlation peak, although this can vary by several decibels depending on the Doppler offset [87] & [47]. Consequently, the worst case P_{fa} will be associated with a very strong satellite signal that is producing a sidelobe at the maximum level.

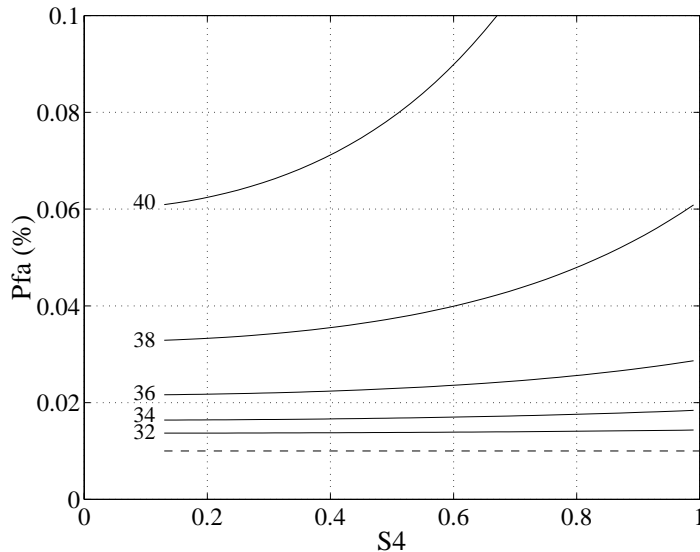


Figure 7.2-4: \bar{P}_{fa} for a peak sidelobe level of -22dB as a function of S_4 for five values of C/N_o (32dBHz to 40dBHz in 2dBHz steps). $T=1ms$, $k=20$, and the design $P_{fa}=0.01\%$.

In Figure 7.2-4, the average false alarm probability, \bar{P}_{fa} , obtained from Equation (7.2-8) using the maximum sidelobe level is plotted as a function of S_4 for the same five values of C/N_o that were used in Figure 7.2-1. The threshold, η , has once again been chosen for a design P_{fa} of 0.01% based on the assumption that the input to the detector is white Gaussian noise when the desired satellite signal is incorrectly correlated. It is clear from these plots that \bar{P}_{fa} increases as S_4 increases, and that the effect becomes more pronounced as the GPS signal level increases. This is because enhancements in the sidelobe levels caused by amplitude scintillations only become a problem when the GPS signal level is relatively large. For small signals, the sidelobe energy remains below the noise floor at the output of the pre-detection filters, even when the signal level has been significantly enhanced.

The results given in Figure 7.2-4 are based on the maximum sidelobe level which will only occur infrequently. In [87], the cumulative probability distribution function of the sidelobe levels is given for the GPS Gold codes for a range of Doppler shifts from 0 to $\pm 5\text{kHz}$. This distribution function is obtained by averaging the results for all 1023 Gold codes in the GPS family, for all possible code time offsets, and for all possible code pairs. By differentiating this function, the PDF of the sidelobe levels, $f_S(s)$, can be found (see Figure 7.2-5, left panel for the case where a Doppler shift of a few kHz is assumed).

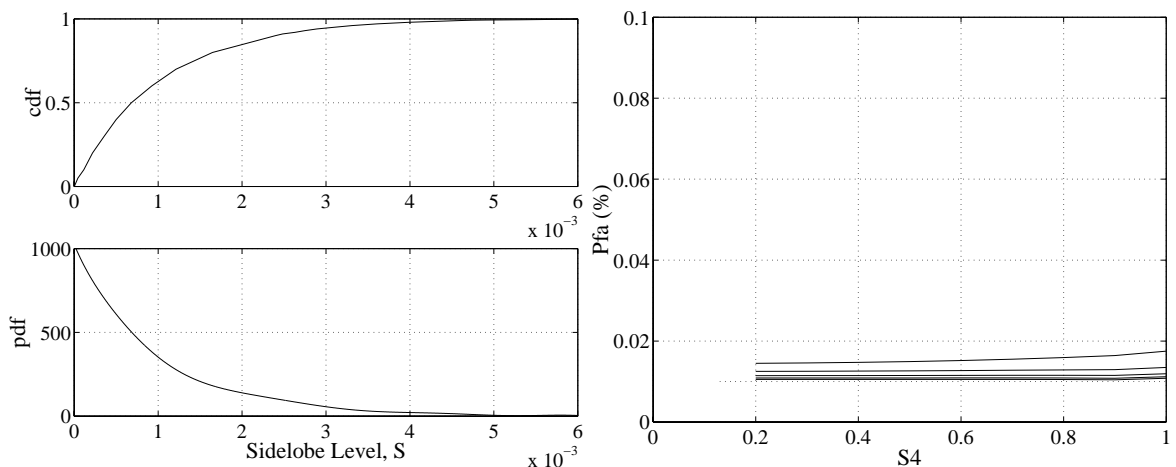


Figure 7.2-5: CDF and PDF of the sidelobe levels for the GPS Gold codes (left panel) and the corresponding \bar{P}_{fa} (right panel). $T=1\text{ms}$, $k=20$, and the design $P_{fa}=0.01\%$. A Doppler shift between the satellite and local codes of a few kHz is assumed.

The average probability of false alarm for a single interfering signal can then be obtained by averaging the probability of detection expression over both the amplitude (to account for scintillations) and the sidelobe levels as follows

$$\bar{P}_{fa} = \int_0^\infty \int_0^\infty P_d(s * A) f_{\tilde{A}}(A) f_S(s) dA ds \quad (7.2-20)$$

where $f_{\tilde{A}}(A)$ is the Nakagami-m PDF for a nominal GPS signal, and s is the sidelobe level (s and A are independent random variables). When Equation (7.2-20) was evaluated for the five values of C/N_o used in Figure 7.2-4, the effects of sidelobes on \bar{P}_{fa} were found to be negligible, even at high S_4 (see Figure 7.2-5, right panel). However, as the sensitivity to sidelobes and scintillations will depend very much on the design parameters P_{fa} , k and T , this result really only applies to this particular example. In addition, these results assume that only one interfering signal is present. In reality, there may be up to 12 satellites visible (possibly more in the future) which will increase the probability that a strong sidelobe will be present.

Van Dierendonck [92] suggests that the detection threshold, η , should be adjusted to account for the worst case sidelobe level while maintaining P_{fa} at a desired level. This can be achieved by solving the probability of detection equations ((7.2-8) or (7.2-6)) for η with $P_d = P_{fa}|_{design}$ and using a signal level that corresponds to the maximum sidelobe level. If this is done, the tracking threshold, η , will be substantially larger and the effects of sidelobes and scintillations will probably be negligible.

Note that because of the extremely low sidelobe levels for the P(Y)-Code, the effect outlined above will not be apparent during direct P(Y)-Code acquisition (at present, direct P(Y)-Code acquisition is only available to the US military).

7.3. Acquisition times

In the previous section, the probability of detection and the probability of false alarm were calculated for a single cell in the code phase / carrier Doppler uncertainty region. The detector type used in this analysis was a fixed integration time, square-law detector based on a Neyman-Pearson detection strategy. In this section, the time required to identify the correct cell will be examined for a single dwell¹, serial search strategy for which there is assumed to be no prior information about the code phase. It will also be assumed that the code Doppler is zero, and that the search is only conducted in the code domain (ie. the frequency of the replica carrier is assumed to be approximately correct).

7.3.1. Acquisition search strategy

In the absence of *a priori* code phase information, a serial search begins at the start of the uncertainty region and progresses through each cell in sequence until a successful detection is made. If a detection is not made before the end of the region is reached, the search returns to the beginning and is repeated. If a false alarm occurs, time will be expended in order to verify that the detection is incorrect before the search can continue. This is usually referred to as *verification* time and may include the time required to re-run the detector on a particular cell, or the time associated with a failed attempt to revert to code tracking mode. The total time required to make a correct detection is therefore a function of the time spent in each cell (the *dwell time*, $T_d = kT$), the number of cells in the uncertainty region, N_C , the probability of detection, P_d , the probability of false alarm, P_{fa} , and the verification time, $T_v = K_v T_d$ where K_v is a factor greater than one.

In the absence of scintillations, the mean time to acquire, \bar{T}_{ACQ} , and the RMS acquisition time, σ_{ACQ} , for a uniform serial search are given by [84]

$$\bar{T}_{ACQ} = N_C T_d \left(K_v P_{fa} + 1 \right) \left[\frac{2 - P_d}{2P_d} \right] \quad (7.3-1)$$

¹ *Single dwell*: The detector's decision is based on a single, fixed time observation of the received signal plus noise. The alternative is *multiple dwell* in which multiple observations are used to verify the first observations

$$\sigma_{ACQ} = N_C T_d \left(K_v P_{fa} + 1 \right) \sqrt{\frac{1}{12} + \frac{1}{P_d^2} - \frac{1}{P_d}} \quad (7.3-2)$$

In Section 7.2, it was shown that when scintillations are present, the probability of detection becomes a function of the signal amplitude, \tilde{A} (if sidelobes are ignored, the probability of false alarm will be unaffected by scintillations). The average mean time to acquire and the RMS acquisition time must then be found by taking an ensemble average of these two parameters over all possible realisations of the amplitude. In order to do this, assumptions must be made about the statistics of the amplitude over the time period required for acquisition. In particular, the joint statistics of the amplitude at time periods separated by $N_C T_d$ seconds must be determined (ie. the time between successive re-visits to the correct code phase cell, assuming that no false alarms have occurred).

In the following sections, it will be assumed that the amplitude is approximately constant during the relatively short dwell time, T_d , in each cell, but that significant variations may occur between the start and end of the acquisition process. As before, it will be assumed that these variations are described by the Nakagami-m distribution.

7.3.2. Mean time to acquire

This analysis closely follows that given by Peterson & Ziemer [72], but has been modified to account for variations in the signal amplitude between successive re-visits to the correct code phase cell. In order to keep the time between re-visits, T_r , constant, it will be assumed that false alarms do not occur, and so $T_r = N_C T_d$. The justification for this assumption is that most acquisition systems are designed to have a very small P_{fa} such that $K_v P_{fa} \ll 1$. Therefore, from Equations (7.3-1) and (7.3-2) it is clear that to a first approximation, the mean and RMS acquisition times are largely unaffected by false alarms. As P_{fa} is also not affected by scintillations (if sidelobes are ignored), it is expected that this approximation will also hold under scintillation conditions. The error in this approximation will be discussed further in Section 7.3.4.

If the n^{th} cell is assumed to be the correct code phase cell, and there are j missed detections, then the total acquisition time is given by

$$T_{ACQ}(n, j) = nT_d + jN_C T_d \quad (7.3-3)$$

where the first term represents the time required to detect the correct cell on the final (successful) pass, and the second term represents the time expended in the j unsuccessful passes. The probability of this event occurring, assuming that there is no prior information about the location of n , is given by ²

$$P_r(n, j | \tilde{A}_{sj}) = \frac{1}{N_C} P_d(\tilde{A}_s) \prod_{i=1}^j [1 - P_d(\tilde{A}_{s-i})] \quad (7.3-4)$$

where $\tilde{A}_{sj} = [\tilde{A}_s, \tilde{A}_{s-1}, \tilde{A}_{s-2}, \dots, \tilde{A}_{s-j}]$ is a vector that represents the amplitude of the GPS signal at the times during which the acquisition detector is testing the correct code phase cell (ie. $\tilde{A}_{s-i} = \tilde{A}(t_{s-i})$ where t_{s-i} is the time corresponding to the $(j-i+1)^{th}$ pass through the correct cell, and $t_{s-i} - t_{s-i-1} = T_r$). As a function of \tilde{A}_{sj} , the mean time to acquire is therefore

$$\begin{aligned} \bar{T}_{ACQ}(\tilde{A}_{sj}) &= E_{n,j} \left\{ T_{ACQ}(n, j) \middle| \tilde{A}_{sj} \right\} \\ &= \sum_{n=1}^{N_C} \sum_{j=0}^{\infty} T_{ACQ}(n, j) P_r(n, j | \tilde{A}_{sj}) \end{aligned} \quad (7.3-5)$$

By taking the expectation over all possible realisations of \tilde{A}_{sj} , this becomes

$$\begin{aligned} \bar{T}_{ACQ} &= E_{\tilde{A}_{sj}} \left\{ \bar{T}_{ACQ}(\tilde{A}_{sj}) \right\} \\ &= \sum_{n=1}^{N_C} \sum_{j=0}^{\infty} E_{\tilde{A}_{sj}} \left\{ T_{ACQ}(n, j) P_r(n, j | \tilde{A}_{sj}) \right\} \end{aligned} \quad (7.3-6)$$

Substituting Equations (7.3-3) and (7.3-4) into the above expression gives

$$\begin{aligned} \bar{T}_{ACQ} &= \frac{T_d}{N_C} \sum_{n=1}^{N_C} \left[n \sum_{j=0}^{\infty} E_{\tilde{A}_{sj}} \left\{ P_d(\tilde{A}_s) \prod_{i=1}^j [1 - P_d(\tilde{A}_{s-i})] \right\} \right] + \\ &\quad N_C \sum_{j=0}^{\infty} j E_{\tilde{A}_{sj}} \left\{ P_d(\tilde{A}_s) \prod_{i=1}^j [1 - P_d(\tilde{A}_{s-i})] \right\} \end{aligned} \quad (7.3-7)$$

² By definition, $\prod_{i=1}^0 f(i) = 1$.

In order to obtain a closed form solution to this expression, it is necessary to simplify the following two terms

$$\text{Term1} = \sum_{j=0}^{\infty} E_{\tilde{A}_{sj}} \left\{ P_d(\tilde{A}_s) \prod_{i=1}^j [1 - P_d(\tilde{A}_{s-i})] \right\} \quad (7.3-8)$$

$$\text{Term2} = \sum_{j=0}^{\infty} j E_{\tilde{A}_{sj}} \left\{ P_d(\tilde{A}_s) \prod_{i=1}^j [1 - P_d(\tilde{A}_{s-i})] \right\} \quad (7.3-9)$$

These terms can only be simplified once the joint statistics of the amplitude scintillations have been established. This will be discussed next.

7.3.2.1. Amplitude correlation times

The correlation time, T_{CT} , of amplitude scintillations is a function of both the Fresnel zone radius, $z_F = \sqrt{h_i \lambda}$ ³, and the relative velocity between the satellite ray path and the irregularity structure (which in turn is a function of the irregularity drift velocity, the receiver velocity, satellite motion and satellite/receiver geometry). T_{CT} is typically of the order of a few seconds, but may extend to a few tens of seconds if the ionospheric pierce point tracks the irregularity drift [50]. For a receiver that is attempting to acquire the GPS signal with no prior information about the code phase (ie. a *cold start*), the number of cells, N_C , is typically of the order of 2046 (ie. 2 x the number of code chips in the C/A-Code assuming a cell spacing of ½ a code chip). For a dwell time of 20ms, this equates to a re-visit time, $T_r = N_C T_d$, of 41 seconds. Consequently, for a cold start it is likely that the correlation time of the amplitude will be much less than the time to re-visit the correct cell. This situation is discussed in Section 7.3.2.2. However, if a receiver is re-acquiring following a relatively short period of loss of lock (ie. a *warm start*), the correlation time may be greater than the re-visit time. The re-acquisition times of modern GPS receivers following a period of signal loss of greater than 1 minute are typically less than a few seconds (GPS World, January 2000, pages 34-54). Consequently, for such receivers, T_r would be expected to be only a few seconds which may be less than T_{CT} . This situation is discussed in Section 7.3.2.3.

³ h_i is the height of the ionospheric pierce point as discussed in Section 2.1.

7.3.2.2. Short amplitude correlation times

If it is assumed that the amplitude correlation time is much less than the re-visit time (ie. during a cold start or in the presence of rapid amplitude scintillations), it is likely that the individual amplitude values in the \tilde{A}_{sj} vector will be independent (see Section 7.3.3 for a justification of this assumption). Consequently, the joint PDF of \tilde{A}_{sj} becomes the product of the individual marginal PDFs as follows

$$f_{\tilde{A}_{sj}}(\tilde{A}_s, \tilde{A}_{s-1}, \tilde{A}_{s-2}, \dots, \tilde{A}_{s-j}) = f_{\tilde{A}_s}(\tilde{A}_s) f_{\tilde{A}_{s-1}}(\tilde{A}_{s-1}) f_{\tilde{A}_{s-2}}(\tilde{A}_{s-2}) \dots f_{\tilde{A}_{s-j}}(\tilde{A}_{s-j}) \quad (7.3-10)$$

where each marginal PDF follows the Nakagami-m distribution. The expectation expressions within Equations (7.3-8) and (7.3-9) can then be simplified as follows

$$\begin{aligned} & E_{\tilde{A}_{sj}} \left\{ P_d(\tilde{A}_s) \prod_{i=1}^j [1 - P_d(\tilde{A}_{s-i})] \right\} \\ &= \int_0^\infty \dots \int_0^\infty P_d(\tilde{A}_s) \prod_{i=1}^j [1 - P_d(\tilde{A}_{s-i})] f_{\tilde{A}_{sj}}(\tilde{A}_s, \dots, \tilde{A}_{s-j}) d\tilde{A}_s \dots d\tilde{A}_{s-j} \\ &= \int_0^\infty \dots \int_0^\infty P_d(\tilde{A}_s) \prod_{i=1}^j [1 - P_d(\tilde{A}_{s-i})] f_{\tilde{A}_s}(\tilde{A}_s) \dots f_{\tilde{A}_{s-j}}(\tilde{A}_{s-j}) d\tilde{A}_s \dots d\tilde{A}_{s-j} \\ &= E_{\tilde{A}_s} \left\{ P_d(\tilde{A}_s) \right\} \prod_{i=1}^j \left[1 - E_{\tilde{A}_{s-i}} \left\{ P_d(\tilde{A}_{s-i}) \right\} \right] \\ &= \bar{P}_d (1 - \bar{P}_d)^j \end{aligned} \quad (7.3-11)$$

This result assumes that the amplitude scintillations are a stationary random process, and so $\bar{P}_d = E_{\tilde{A}_i} \{ P_d(\tilde{A}_i) \} = E_{\tilde{A}_k} \{ P_d(\tilde{A}_k) \}$. Consequently, Equations (7.3-8) and (7.3-9) reduce to

$$\text{Term1} = \sum_{j=0}^{\infty} \bar{P}_d (1 - \bar{P}_d)^j \quad (7.3-12)$$

$$\text{Term2} = \sum_{j=0}^{\infty} j \bar{P}_d (1 - \bar{P}_d)^j \quad (7.3-13)$$

Substituting these two terms back into Equation (7.3-7) results in the following expression

$$\bar{T}_{ACQ} = \frac{T_d}{N_C} \sum_{n=1}^{N_C} \left[n \sum_{j=0}^{\infty} \bar{P}_d (1 - \bar{P}_d)^j + N_C \sum_{j=0}^{\infty} j \bar{P}_d (1 - \bar{P}_d)^j \right] \quad (7.3-14)$$

This expression has the same form as that derived by Peterson & Ziemer [72] (ignoring false alarms), except that the standard probability of detection has been replaced by \bar{P}_d . As shown by Peterson & Ziemer, Equation (7.3-14) can be reduced to

$$\begin{aligned}\bar{T}_{ACQ} &= \frac{T_d}{2} + N_C T_d \left[\frac{2 - \bar{P}_d}{2\bar{P}_d} \right] \\ &\approx N_C T_d \left[\frac{2 - \bar{P}_d}{2\bar{P}_d} \right] \text{ for large values of } N_C \text{ and } \bar{P}_d\end{aligned}\quad (7.3-15)$$

Indeed, as this result assumes that T_r is large enough for the amplitude to be independent between successive re-visits, the additional verification time associated with false alarms will not alter the statistics of \tilde{A}_{sj} . Consequently, the effects of false alarms can readily be incorporated to obtain (see Peterson & Ziemer for a justification of this step)

$$\bar{T}_{ACQ} = N_C T_d (K_v P_{fa} + 1) \left[\frac{2 - \bar{P}_d}{2\bar{P}_d} \right] \quad (7.3-16)$$

The percentage increase in the mean acquisition time as a result of scintillations is then found by dividing Equation (7.3-16) by (7.3-1) as obtain

$$\frac{\bar{T}_{ACQ}|_{\text{scint}}}{\bar{T}_{ACQ}|_{\text{no scint}}} = \frac{P_d(2 - \bar{P}_d)}{\bar{P}_d(2 - P_d)} \quad (7.3-17)$$

where \bar{P}_d and P_d are the probabilities of detection in the presence of scintillations and in the absence of scintillations respectively.

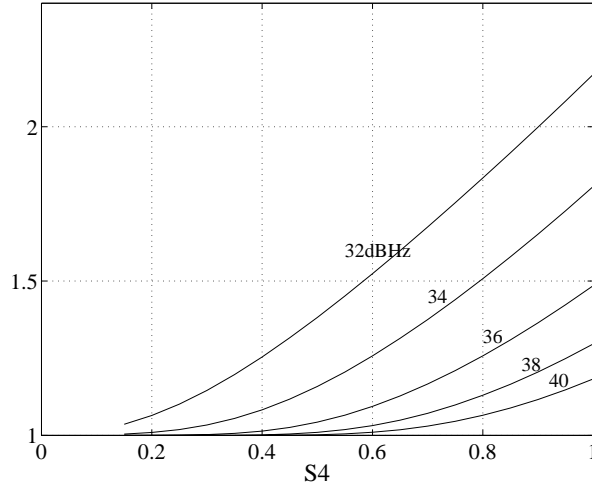


Figure 7.3-1: Mean acquisition time ratio as a function of S_4 for $C/N_o = 32$ to 40 dBHz. $T=1ms$, $k=20$, $P_{fa} = 0.01\%$.

In Figure 7.3-1, Equation (7.3-17) is plotted as a function of S_4 for five values of C/N_o . The worst case increase in the mean acquisition time is by a factor of approximately two, although this corresponds to quite a low quiescent C/N_o . However, at normal signal levels (around 40dBHz) the increase in the acquisition time is relatively small, even under strong scintillation conditions.

A similar argument can be used to demonstrate that the effects of scintillations on the RMS acquisition time can be found by substituting \bar{P}_d in place of P_d in Equation (7.3-2). Again, this only applies to the situation in which T_{CT} is much less than T_r . The corresponding RMS acquisition time ratio is therefore

$$\frac{\sigma_{ACQ}|_{\text{scint}}}{\sigma_{ACQ}|_{\text{no scint}}} = \frac{P_d}{\bar{P}_d} \sqrt{\frac{\bar{P}_d^2 - 12\bar{P}_d + 12}{P_d^2 - 12P_d + 12}} \quad (7.3-18)$$

In Figure 7.3-2, the RMS acquisition time ratio is plotted as a function of S_4 for the same four values of C/N_o that were used in Figure 7.3-1. From these two figures, it is clear that both the mean and the spread of the acquisition times increases.

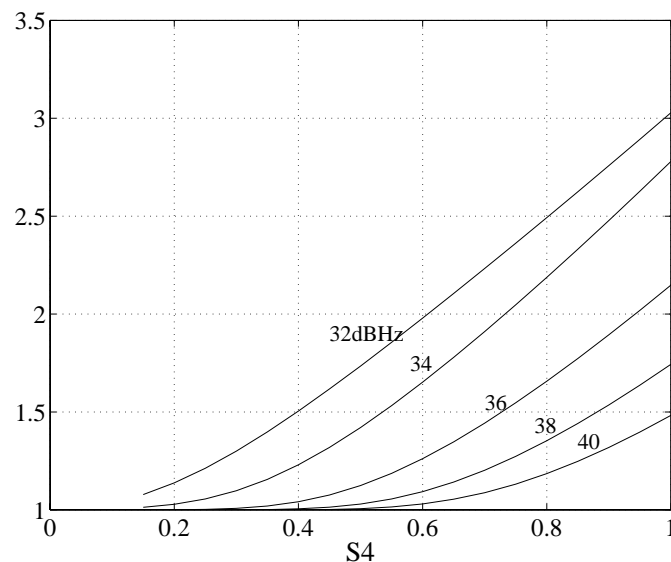


Figure 7.3-2: RMS acquisition time ratio as a function of S_4 for $C/N_o = 32$ to 40 dBHz. $T=1ms$, $k=20$, $P_{fa} = 0.01\%$.

7.3.2.3. Long amplitude correlation times

If the correlation time of the amplitude increases, or conversely the re-visit time decreases, it may no longer be valid to assume that the components of $\underline{\tilde{A}}_{sj}$ are independent. Under these conditions, it is not valid to represent the joint PDF of $\underline{\tilde{A}}_{sj}$ as the product of the individual marginal PDF's, as in Equation (7.3-10). The difficulty that arises under these circumstances is that because the joint PDF is unknown, the two expectation terms in Equations (7.3-8) and (7.3-9) cannot be solved. Therefore, an expression for \bar{T}_{ACQ} cannot be found. Indeed, if the joint PDF were known, it is likely that the complexity involved in attempting to solve Equation (7.3-7) would be so high that a closed form solution would be very difficult to find.

The approach used here to achieve an increase in the correlation time of the amplitude while still allowing \bar{T}_{ACQ} to be solved in closed form is to simply repeat amplitude values within the original sequence. For example, if each amplitude value is repeated once only, the original sequence becomes

$$\underline{\tilde{A}}'_{sj} = \begin{cases} \underline{\tilde{A}}'_{sj}^a = [\tilde{A}_s, (\tilde{A}_{s-1} = \tilde{A}_{s-2}), \tilde{A}_{s-2}, (\tilde{A}_{s-3} = \tilde{A}_{s-4}), \tilde{A}_{s-4}, \dots] & \text{with probability } \frac{1}{2} \\ \underline{\tilde{A}}'_{sj}^b = [(\tilde{A}_s = \tilde{A}_{s-1}), \tilde{A}_{s-1}, (\tilde{A}_{s-2} = \tilde{A}_{s-3}), \tilde{A}_{s-3}, (\tilde{A}_{s-4} = \tilde{A}_{s-5}), \dots] & \text{with probability } \frac{1}{2} \end{cases} \quad (7.3-19)$$

where now only every second amplitude value is independent (ie. $p(\tilde{A}_i, \tilde{A}_{i-n}) = p(\tilde{A}_i)p(\tilde{A}_{i-n})$ for $|n| > 1$). Based on this model, the joint PDF's of the amplitude sequence become

$$\begin{aligned} j=1: \quad p(\tilde{A}_s, \tilde{A}_{s-1}) &= \frac{1}{2} p(\tilde{A}_{s-1}) [p(\tilde{A}_s) + \delta(\tilde{A}_s - \tilde{A}_{s-1})] \\ j=2: \quad p(\tilde{A}_s, \tilde{A}_{s-1}, \tilde{A}_{s-2}) &= \frac{1}{2} p(\tilde{A}_{s-2}) [p(\tilde{A}_s) \delta(\tilde{A}_{s-1} - \tilde{A}_{s-2}) + p(\tilde{A}_{s-1}) \delta(\tilde{A}_s - \tilde{A}_{s-1})] \\ j=3: \quad p(\tilde{A}_s, \tilde{A}_{s-1}, \tilde{A}_{s-2}, \tilde{A}_{s-3}) &= \frac{1}{2} p(\tilde{A}_{s-3}) [p(\tilde{A}_s) \delta(\tilde{A}_{s-1} - \tilde{A}_{s-2}) p(\tilde{A}_{s-2}) + p(\tilde{A}_{s-1}) \delta(\tilde{A}_s - \tilde{A}_{s-1}) \delta(\tilde{A}_{s-2} - \tilde{A}_{s-3})] \\ \text{etc. for } j > 3 & \end{aligned} \quad (7.3-20)$$

where the notation $p(\tilde{A}_i)$ has been used in place of $f_{\tilde{A}_i}(\tilde{A}_i)$ to improve clarity, and $\delta(\)$ is the Dirac Delta function [39]. The joint PDF can be generalised for arbitrary values of j to give

$$p(\tilde{A}_s, \dots, \tilde{A}_{s-j})_{j \text{ even}} = \frac{1}{2} p(\tilde{A}_{s-j}) \left[\prod_{q=1}^{j/2} p(\tilde{A}_{s-2q+1}) \delta(\tilde{A}_{s-2q+2} - \tilde{A}_{s-2q+1}) + \prod_{q=1}^{j/2} p(\tilde{A}_{s-2q+2}) \delta(\tilde{A}_{s-2q+1} - \tilde{A}_{s-2q}) \right] \quad (7.3-21)$$

$$p(\tilde{A}_s, \dots, \tilde{A}_{s-j})_{j \text{ odd}} = \frac{1}{2} p(\tilde{A}_{s-j}) \left[p(\tilde{A}_s) \prod_{q=1}^{(j-1)/2} p(\tilde{A}_{s-2q}) \delta(\tilde{A}_{s-2q+1} - \tilde{A}_{s-2q}) + \delta(\tilde{A}_s - \tilde{A}_{s-1}) \prod_{q=1}^{(j-1)/2} p(\tilde{A}_{s-2q+1}) \delta(\tilde{A}_{s-2q} - \tilde{A}_{s-2q-1}) \right]$$

The sequence $\underline{\tilde{A}}'_{sj}$ is wide sense stationary and the marginal density functions, $p(\tilde{A}_i)$, are again described by the Nakagami-m PDF. The autocorrelation function of $\underline{\tilde{A}}'_{sj}$ is given by

$$\begin{aligned} R(nT_r) &= E\{\tilde{A}_i \tilde{A}_{i-n}\} \\ &= \int_0^{\infty} \int_0^{\infty} \tilde{A}_i \tilde{A}_{i-n} p(\tilde{A}_i, \tilde{A}_{i-n}) d\tilde{A}_i d\tilde{A}_{i-n} \end{aligned} \quad (7.3-22)$$

where n is an integer. As it has been assumed that amplitude values separated by more than one sample are independent, the autocorrelation function reduces to

$$\begin{aligned} R(0) &= E\{\tilde{A}^2\} = \overline{\tilde{A}^2} \\ R(nT_r) &= E\{\tilde{A}\}^2 = (\overline{\tilde{A}})^2, \quad |n| > 1 \\ R(T_r) &= \int_0^{\infty} \int_0^{\infty} \tilde{A}_i \tilde{A}_{i-1} p(\tilde{A}_i, \tilde{A}_{i-1}) d\tilde{A}_i d\tilde{A}_{i-1} \\ &= \int_0^{\infty} \int_0^{\infty} \tilde{A}_i \tilde{A}_{i-1} \frac{1}{2} p(\tilde{A}_{i-1}) [p(\tilde{A}_i) + \delta(\tilde{A}_i - \tilde{A}_{i-1})] d\tilde{A}_i d\tilde{A}_{i-1} \\ &= \frac{1}{2} [\overline{\tilde{A}^2} + (\overline{\tilde{A}})^2] \end{aligned} \quad (7.3-23)$$

where $R(0) \geq R(T_r) \geq R(nT_r)$ as $\overline{\tilde{A}^2} \geq (\overline{\tilde{A}})^2$. Consequently, the correlation time of the amplitude sequence is now between T_r and $2T_r$ seconds (originally, it was less than T_r seconds).

The joint PDF of $\underline{\tilde{A}}'_{sj}$ (Equation (7.3-21)) can be used to obtain closed form expressions for Equations (7.3-8) and (7.3-9), which in turn can be used to derive a simplified expression for \bar{T}_{ACQ} . Expanding Equation (7.3-8) gives

$$\text{term1} = E_{\tilde{\underline{A}}_{s\infty}} \left\{ P_d(\tilde{A}_s) [1 + Q(\tilde{A}_{s-1}) + Q(\tilde{A}_{s-1})Q(\tilde{A}_{s-2}) + Q(\tilde{A}_{s-1})Q(\tilde{A}_{s-2})Q(\tilde{A}_{s-3}) + \dots] \right\} \quad (7.3-24)$$

where $E_{\tilde{\underline{A}}_{s\infty}} = E_{\tilde{\underline{A}}_{sj}}$ for $j \rightarrow \infty$, and $Q(\tilde{A}_i) = [1 - P_d(\tilde{A}_i)]$. By taking account of the two separate amplitude sequences in $\tilde{\underline{A}}'_{sj}$ (see Equation (7.3-19)), this can be reduced to

$$\begin{aligned} \text{term1} &= \frac{1}{2} E_{\tilde{\underline{A}}_{s\infty}^a} \left\{ P_d(\tilde{A}_s) \left[1 + Q(\tilde{A}_{s-2}) + Q(\tilde{A}_{s-2})^2 + Q(\tilde{A}_{s-2})^2 Q(\tilde{A}_{s-4}) + Q(\tilde{A}_{s-2})^2 Q(\tilde{A}_{s-4})^2 + \dots \right] \right\} + \\ &\quad \frac{1}{2} E_{\tilde{\underline{A}}_{s\infty}^b} \left\{ P_d(\tilde{A}_{s-1}) \left[1 + Q(\tilde{A}_{s-1}) + Q(\tilde{A}_{s-1})Q(\tilde{A}_{s-3}) + Q(\tilde{A}_{s-1})Q(\tilde{A}_{s-3})^2 + Q(\tilde{A}_{s-1})Q(\tilde{A}_{s-3})^2 Q(\tilde{A}_{s-5}) + \dots \right] \right\} \end{aligned} \quad (7.3-25)$$

where $E_{\tilde{\underline{A}}_{s\infty}^a} = E_{\tilde{\underline{A}}_{sj}}$ and $E_{\tilde{\underline{A}}_{s\infty}^b} = E_{\tilde{\underline{A}}_{sj}}$ for $j \rightarrow \infty$. Using properties of the expectation such as $E_{\tilde{\underline{A}}_{s\infty}^a} \{P_d(\tilde{A}_s)Q(\tilde{A}_{s-2})\} = E_{\tilde{A}_s} \{P_d(\tilde{A}_s)\} E_{\tilde{A}_{s-2}} \{Q_d(\tilde{A}_{s-2})\}$, Equation (7.3-25) becomes

$$\begin{aligned} \text{term1} &= \frac{1}{2} \left[\bar{P}_d [1 + \bar{Q}] \left[1 + \bar{Q}^2 + \bar{Q}^2 + \dots \text{etc} \right] + \bar{P}_d + \bar{P}_d \bar{Q} [1 + \bar{Q}] \left[1 + \bar{Q}^2 + \bar{Q}^2 + \dots \text{etc} \right] \right] \\ &= \frac{1}{2} \left[\bar{P}_d + [\bar{P}_d + \bar{P}_d \bar{Q}] [1 + \bar{Q}] \sum_{j=0}^{\infty} \bar{Q}^{2j} \right] \\ &= \frac{1}{2} \left[\bar{P}_d + [2\bar{P}_d - \bar{P}_d^2] [2 - \bar{P}_d] \sum_{j=0}^{\infty} \bar{Q}^{2j} \right] \end{aligned} \quad (7.3-26)$$

where $\bar{Q} = 1 - \bar{P}_d$

$$\bar{Q}^2 = E \left\{ [1 - P_d(\tilde{A}_i)]^2 \right\} = 1 - 2\bar{P}_d + \bar{P}_d^2$$

$$\bar{P}_d \bar{Q} = E \left\{ P_d(\tilde{A}_i) [1 - P_d(\tilde{A}_i)] \right\} = \bar{P}_d - \bar{P}_d^2$$

However, as

$$\sum_{j=0}^{\infty} \bar{Q}^{2j} = \sum_{j=0}^{\infty} \left[1 - \left(2\bar{P}_d - \bar{P}_d^2 \right) \right]^j, \text{ and}$$

$$0 \leq \bar{Q}^2 = \int_0^\infty [1 - P_d(\tilde{A}_i)]^2 p(\tilde{A}_i) d\tilde{A}_i \leq \int_0^\infty p(\tilde{A}_i) d\tilde{A}_i = 1$$

we can say that

$$\sum_{j=0}^{\infty} \bar{Q}^{2j} = \frac{1}{2\bar{P}_d - \bar{P}_d^2} \quad (7.3-27)$$

Therefore, Equation (7.3-26) reduces to

$$\begin{aligned} \text{term1} &= \frac{1}{2} \left[\bar{P}_d + \left[2\bar{P}_d - \bar{P}_d^2 \right] \left[2 - \bar{P}_d \right] \frac{1}{\left[2\bar{P}_d - \bar{P}_d^2 \right]} \right] \\ &= 1 \end{aligned} \quad (7.3-28)$$

This result is the same as that obtained for both the constant amplitude and the independent amplitude sequence. In a similar way, Equation (7.3-9) can be expanded using the \tilde{A}'_{sj} model from Equation (7.3-19) to give

$$\begin{aligned} \text{term2} &= \frac{1}{2} E_{\tilde{A}'_{s\infty}^a} \left\{ P_d(\tilde{A}_s) \left[Q(\tilde{A}_{s-2}) + 2Q(\tilde{A}_{s-2})^2 + 3Q(\tilde{A}_{s-2})^2 Q(\tilde{A}_{s-4}) + 4Q(\tilde{A}_{s-2})^2 Q(\tilde{A}_{s-4})^2 + \dots \right] \right\} + \\ &\quad \frac{1}{2} E_{\tilde{A}'_{s\infty}^b} \left\{ P_d(\tilde{A}_{s-1}) \left[Q(\tilde{A}_{s-1}) + 2Q(\tilde{A}_{s-1})Q(\tilde{A}_{s-3}) + 3Q(\tilde{A}_{s-1})Q(\tilde{A}_{s-3})^2 + 4Q(\tilde{A}_{s-1})Q(\tilde{A}_{s-3})^2 Q(\tilde{A}_{s-5}) + \dots \right] \right\} \end{aligned} \quad (7.3-29)$$

By once again evaluating the two expectation terms, this expression reduces to

$$\begin{aligned} \text{term2} &= \frac{1}{2} \left[\bar{P}_d \left[\bar{Q} + 2\bar{Q}^2 + 3\bar{Q}\bar{Q}^2 + 4\bar{Q}^2 + \dots \text{etc} \right] + \bar{P}_d\bar{Q} \left[1 + 2\bar{Q} + 3\bar{Q}^2 + 4\bar{Q}\bar{Q}^2 + \dots \text{etc} \right] \right] \\ &= \frac{1}{2} \left[\bar{P}_d \left[\bar{Q} \sum_{j=0}^{\infty} (1+2j)\bar{Q}^{2^j} + \sum_{j=0}^{\infty} 2j\bar{Q}^{2^j} \right] + \bar{P}_d\bar{Q} \left[\bar{Q} \sum_{j=0}^{\infty} (2+2j)\bar{Q}^{2^j} + \sum_{j=0}^{\infty} (1+2j)\bar{Q}^{2^j} \right] \right] \\ &= \frac{1}{2} \left[[\bar{P}_d\bar{Q} + \bar{P}_d\bar{Q}(2\bar{Q}+1)] \sum_{j=0}^{\infty} \bar{Q}^{2^j} + 2(\bar{Q}+1)[\bar{P}_d + \bar{P}_d\bar{Q}] \sum_{j=0}^{\infty} j\bar{Q}^{2^j} \right] \\ &= \frac{1}{2} \left[[4\bar{P}_d - 3\bar{P}_d^2 - 3\bar{P}_d^2 + 2\bar{P}_d\bar{P}_d^2] \sum_{j=0}^{\infty} \bar{Q}^{2^j} + 2[4\bar{P}_d - 2\bar{P}_d^2 - 2\bar{P}_d^2 + \bar{P}_d\bar{P}_d^2] \sum_{j=0}^{\infty} j\bar{Q}^{2^j} \right] \end{aligned} \quad (7.3-30)$$

Also,

$$\begin{aligned} \sum_{j=0}^{\infty} j\bar{Q}^{2^j} &= \sum_{j=0}^{\infty} j \left[1 - \left(2\bar{P}_d - \bar{P}_d^2 \right) \right]^j \\ &= \frac{1 - 2\bar{P}_d + \bar{P}_d^2}{\left[2\bar{P}_d - \bar{P}_d^2 \right]^2} \end{aligned} \quad (7.3-31)$$

By substituting Equations (7.3-27) and (7.3-31) into Equations (7.3-30), it is possible to show after some manipulation that term 2 reduces to

$$\text{term2} = \frac{1}{2} \left[\frac{[\bar{P}_d - 2]^2}{2\bar{P}_d - \bar{P}_d^2} - 1 \right] \quad (7.3-32)$$

Consequently, although the amplitude sequence \tilde{A}'_{sj} is somewhat artificial, it does allow Equations (7.3-8) and (7.3-9) to be reduced to simple closed form expressions while still obeying the requirements that the marginal density functions are Nakagami-m distributed and the correlations time is greater than that of an independent amplitude sequence.

By substituting these reduced expressions for terms 1 and 2 back into Equation (7.3-7), the mean acquisition time becomes

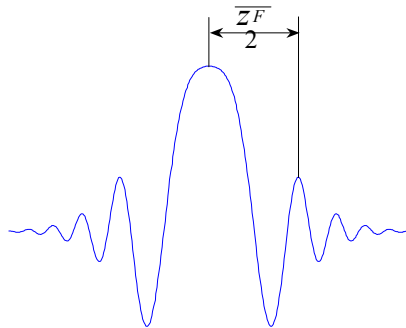
$$\begin{aligned} \bar{T}_{ACQ} &= \frac{T_d}{N_C} \sum_{n=1}^{N_C} \left[n + N_C \frac{1}{2} \left[\frac{[\bar{P}_d - 2]^2}{2\bar{P}_d - \bar{P}_d^2} - 1 \right] \right] \\ &= \frac{T_d}{N_C} \left[\frac{N_C(N_C+1)}{2} + \frac{N_C^2}{2} \left[\frac{[\bar{P}_d - 2]^2}{2\bar{P}_d - \bar{P}_d^2} - 1 \right] \right] \quad (7.3-33) \\ &= \frac{T_d}{2} + \frac{N_C T_d [\bar{P}_d - 2]^2}{2 [2\bar{P}_d - \bar{P}_d^2]} \end{aligned}$$

It is relatively straightforward to prove that this new mean acquisition time is greater than or equal to the mean acquisition time obtained by assuming an independent amplitude sequence (ie. \bar{T}_{ACQ} from Equation (7.3-33) $\geq \bar{T}_{ACQ}$ from Equation (7.3-15)). This implies that as the rate of the amplitude scintillations decreases, the mean time to acquire increases, at least for the amplitude model used in this analysis. However, this effect is only likely to be important when the time taken to re-visit the correct cell, T_r , is relatively small. This will generally be the case when the receiver is re-acquiring following a short outage and has a good knowledge of the code phase and carrier frequency. When T_r is large, such as during a cold start, the probability that a typical amplitude scintillation sequence will be correlated between successive re-visits is likely to be quite small.

7.3.3. Independence

The analysis given in the previous section was based on the assumption that if the amplitude scintillation sequence was sampled at a sufficiently low rate, successive samples would be independent. This section provides a justification for this assumption.

As discussed in Appendix A, the majority of the amplitude scintillation energy is created by irregularities of the order of the first Fresnel zone radius. For GPS, this is approximately 300m or so depending of the height and elevation angle of the irregularities. Irregularities much larger or much smaller than this produce negligible diffraction energy, although large, extremely dense irregularities may produce refractive fading effects. However, generally it can be assumed that amplitude scintillation patterns are produced by the composite effect of numerous irregularities of the order of the first Fresnel zone radius. The amplitude diffraction pattern produced by an isolated irregularity has the following general form



where z_F is the first Fresnel zone radius. It is clear from this diagram that the pattern decays very rapidly beyond $z_F/2$, and that the spacing between the peaks is independent of the irregularity size (as z_F is not a function of irregularity size). Consequently, if the amplitude scintillation waveform produced by an isolated irregularity is sampled with a spacing in excess of z_F , it is likely that only one sample will contain a significant amount of energy from the scintillation pattern. Adjacent irregularities will produce similar patterns, and superposition can be used to determine the combined effects of these irregularities (ie. a composite pattern can be obtained). As the sizes and locations of the irregularities within a larger plume structure can be assumed to be random, it is reasonable to assume that samples of the pattern taken more than z_F m apart will be approximately independent. If it is then assumed that the irregularities are part of a *frozen flow*, and that motion of the frozen flow causes the pattern to move past the receiver with a relative velocity of v_e m/s, then samples taken more than z_F/v_e seconds apart can be

assumed to be independent. For example, for $v_e = 100 \text{ m/s}$, $z_F = 275 \text{ m}$, and $\tau_d = 20 \text{ ms}$ (typical values), then samples taken more than 2.75s apart ($N_C > 125$ cells) will be approximately independent.

7.3.4. False alarms

If the amplitude values are assumed to be independent between successive re-visits (ie. the amplitude correlation time is relatively short), \bar{T}_{ACQ} can be calculated as the sum of two parts; one associated with detecting the correct cell assuming no false alarms, the other associated with the false alarm verification time (see for example [84]). Consequently, under these conditions \bar{T}_{ACQ} becomes (based on Equations (7.3-1) and (7.3-15))

$$\bar{T}_{ACQ} = N_C T_d \left(K_v P_{fa} + 1 \right) \left[\frac{2 - \bar{P}_d}{2\bar{P}_d} \right] \quad (7.3-34)$$

However, if the amplitude correlation time is long enough for the amplitude sequence to be correlated between re-visits, the additional verification time associated with false alarms may shift the sequence more towards an independent sequence by increasing the average re-visit time. This will tend to reduce \bar{T}_{ACQ} somewhat. In this section, it will be demonstrated that the probability that the amplitude sequence statistics are significantly affected by false alarms is extremely small, even for quite large verification times. This assumes that scintillations do not greatly affect the false alarm rate, even when sidelobe enhancements are considered (this is justified in Section 7.2.2).

If we let:

K_v = false alarm verification time factor,

$T_v = K_v T_d$ = false alarm verification time,

q = the number of false alarms between successive re-visits (ie. in N_C cells),

N_{fa} = the number of cells in which false alarms can occur,

then,

$N_C T_d$ is the time taken for one unsuccessful pass of the uncertainty region with no false alarms,

$N_{fa} = N_C - 1$ as one cell out of N_C in the uncertainty region is the correct cell,

$T_p = qK_v T_d$ is the false alarm penalty time for one pass,

$T_r = N_C T_d + T_p$ is the total re-visit time,

$$\begin{aligned} P(q|N_{fa}) &= \binom{N_C - 1}{q} P_{fa}^q (1 - P_{fa})^{N_C - 1 - q}, \\ E\{q|N_{fa}\} &= \sum_{q=0}^{N_C - 1} q * P(q|N_{fa}), \\ &= (N_C - 1)P_{fa} \\ E\{T_p|N_{fa}\} &= (N_C - 1)P_{fa} * K_v T_d \end{aligned}$$

Consequently, the average false alarm penalty time for one pass of the uncertainty region is $\bar{T}_p = (N_C - 1)P_{fa} * K_v T_d$ seconds. As a proportion of the total time, this is

$$\begin{aligned} \frac{(N_C - 1)P_{fa} * K_v T_d}{N_C T_d} &= \frac{(N_C - 1)K_v P_{fa}}{N_C} \\ &\approx K_v P_{fa} \end{aligned} \quad (7.3-35)$$

Thus, if $K_v P_{fa} \ll 1$, false alarms will have a negligible impact on both the average re-visit time and the statistics of the amplitude sequence. For example, if $P_{fa} = 0.01\%$ (a typical level), $K_v \ll 10,000$ is required. In general, this condition is expected to be met, although the actual value of K_v will depend on the verification methodology. For example, re-checking the cell once will result in $K_v = 1$, whereas attempting to establish carrier lock immediately will probably result in $K_v \gg 1$ (Campanile [20] suggests that $K_v \gg 10$).

If $K_v P_{fa} \ll 1$, false alarms can be ignored and Equation (7.3-33) can be used to give the mean acquisition time for the amplitude model described by Equation (7.3-19). However, if $K_v P_{fa} \ll 1$ is violated, the additional verification time will tend to increase \bar{T}_{ACQ} somewhat, while the increase in the degree of independence of the amplitude sequence will tend to reduce \bar{T}_{ACQ} slightly. As the two effects are linked, it is difficult to account for them correctly.

7.4. Conclusions

Scintillations increase acquisition times by reducing the probability of detection while searching the code phase / carrier Doppler uncertainty region. For satellite signals which have a relatively low signal to noise ratio, the mean time to acquire may increase by a

factor of two or more, and the RMS acquisition time by a factor of three, depending on the characteristics of the detector and the precise value of the carrier to noise density ratio, C/N_o . Amplitude scintillations have by far the greatest impact on detection probabilities. For example, the probability of detection can drop from almost one to approximately 0.8 at $S_4 = 1$ for a C/N_o of 36 dBHz (this represents an equivalent C/N_o of only 31 dBHz under quiescent signal conditions). It was also found that for a slowly varying amplitude waveform (ie. slow in relation to the time required to search the uncertainty region), the increase in the mean time to acquire may be larger than for a rapidly varying amplitude waveform.

Phase scintillations, on the other hand, were found to have virtually no effect on detection probabilities for the square-law detector studied in this chapter. Similarly, correlation sidelobes produced by competing satellite signals or by an incorrectly aligned signal were found to have a negligible impact on false alarm probabilities, even under severe scintillation conditions.

This chapter examined the effects of scintillations on the time to locate the correct code phase and carrier Doppler for a square-law acquisition detector. However, the problems that may be encountered when attempting to transition to a state of code and carrier tracking under scintillation conditions have not been addressed. From earlier chapters, it seems likely that under very intense scintillation conditions, it may not be possible to achieve code and carrier lock, even though the correct code phase and carrier Doppler may be known. Consequently, the acquisition time may effectively be extended to include the time required for the scintillation patch to pass, or at least for the level of scintillation activity to drop to the point where carrier tracking can begin.

Chapter 8

Optimum tracking of the carrier phase

The objective of this Chapter is to determine an optimum phase locked loop for the GPS carrier that provides minimum phase tracking error under the specified ionospheric scintillation and dynamic conditions. In Section 8.1, this is achieved by finding an optimum filter using Wiener filter theory, and then mapping this filter into the structure of an equivalent phase locked loop. Although in practice it is unlikely that GPS receivers will be designed with scintillations in mind, this exercise nevertheless gives some insight into the benefits that may arise from adopting an optimum loop configuration, and the sensitivity of this optimum to receiver dynamics (normally, the characteristics of a tracking loop are based solely on the dynamics and nominal signal to noise ratios). In Section 8.2, the optimum bandwidth for minimum mean square tracking error is determined directly for each loop order. Although this approach is not as generic as the Wiener filter approach (ie. it assumes that the filter is a phase locked loop), it nevertheless allows the optimum to be determined for arbitrary values of the spectral index, p .

8.1. Wiener filter approach

If the GPS signal is modelled as the sum of a phase process, $\phi(t)$, and thermal noise, $w(t)$, which are assumed to be jointly stationary, the Wiener filter is the filter that minimises the mean-square carrier phase tracking error, $E\left\{\left[\phi(t) - \hat{\phi}(t)\right]^2\right\}$. Figure 8.1-1 is an illustration of the relationship between the Wiener filter (represented by the dotted box) and the equivalent phase locked loop filter, $F(s)$.

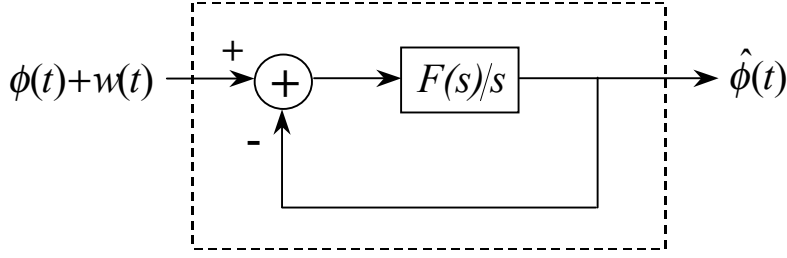


Figure 8.1-1: Wiener filter model of a phase locked loop.

8.1.1. Causal Wiener filters

As the carrier tracking loop is causal (ie. future phase measurements are unavailable), the Wiener filter must also be causal. The causal Wiener filter for the tracking loop illustrated in Figure 8.1-1 is given by (see for example Brown & Hwang [19], Van Trees [95])

$$H_o(s) = \frac{1}{[S_{\phi+w}(s)]^+} \left[\frac{S_{\phi+w,\phi}(s)}{[S_{\phi+w}(s)]^-} \right]_{pos} \quad (8.1-1)$$

where $S_{\phi+w}(s)$ is the power spectral density of the combined signal $\phi(t) + w(t)$, $S_{\phi+w,\phi}(s)$ is the cross-spectral density of $\phi(t) + w(t)$ with $\phi(t)$, + and - denotes all poles and zeros in the left and right half of the complex s plane respectively (ie. $X(s) = X^+(s)X^-(s)$ where $X^+(s) = X^-(s)^*$), and $[]_{pos}$ denotes the transform of a positive-time function $f(t)$ such that $f(t) = 0$ for $t < 0$. If it is assumed that $\phi(t)$ and $w(t)$ are uncorrelated, then $S_{\phi+w}(s) = S_\phi(s) + S_w(s)$ and $S_{\phi+w,\phi}(s) = S_\phi(s)$. The Wiener filter then becomes

$$H_o(s) = \frac{1}{[S_\phi(s) + S_w(s)]^+} \left[\frac{S_\phi(s)}{[S_\phi(s) + S_w(s)]^-} \right]_{pos} \quad (8.1-2)$$

When $w(t)$ is white with a power spectral density of βN_o (where β is a constant), the Wiener filter reduces to (based on the result by Yovits and Jackson [104])

$$H_o(s) = 1 - \frac{\sqrt{\beta N_o}}{[S_\phi(s) + \beta N_o]^+} \quad (8.1-3)$$

The transfer function of the optimum loop filter is then

$$\begin{aligned}
F_o(s) &= s \left[\frac{H_o(s)}{1 - H_o(s)} \right] \\
&= s \left[\frac{[S_\phi(s) + \beta N_o]^+}{\sqrt{\beta N_o}} - 1 \right]
\end{aligned} \tag{8.1-4}$$

Initially, it is assumed that the input phase process is produced entirely by phase scintillations with a power spectral density of $S_{\phi_p}(f) = T(f_o^2 + f^2)^{-p/2}$ (ie. dynamics and other sources of phase noise are ignored for the moment). This is representative of a situation in which the receiver is either stationary or INS aided and phase scintillations are the dominant source of phase noise. It is also assumed that the thermal noise term, $w(t)$, is zero-mean and white, but with a power spectral density that is scaled by the effects of amplitude scintillations. A justification for this assumption is given below:

If it is assumed that the filter is a phase locked loop with an imperfect AGC, then the thermal noise at the loop input can be represented by

$$w(t) = \frac{n(t)}{\sqrt{g(t)}} \tag{8.1-5}$$

where $n(t)$ is zero-mean, white Gaussian thermal noise at the loop input (ie. on the IF signal from Equation (3.1-1)), and $g(t)$ is the AGC gain factor from Section 3.2 which has been translated back to the IF (ie. $g(t) = \tilde{A}(t)^2 + 2N_o/T > 0$ for an imperfect AGC – see Equation (3.3-16)). If $n(t)$ is assumed to be independent of $g(t)$ ¹, the mean value of $w(t)$ is given by

$$\begin{aligned}
E\{w(t)\} &= E\left\{ \frac{n(t)}{\sqrt{g(t)}} \right\} \\
&= E\{n(t)\} E\left\{ \frac{1}{\sqrt{g(t)}} \right\} \\
&= 0.
\end{aligned} \tag{8.1-6}$$

Therefore, $w(t)$ is zero-mean.

¹ This implies that the amplitude fades are not too deep (ie. $\tilde{A}(t)$ does not become too small), or the AGC time constant is relatively large.

The autocorrelation function of $w(t)$ is

$$\begin{aligned}
R_w(\tau) &= E\{w(t)w(t+\tau)\} \\
&= E\left\{\frac{n(t)}{\sqrt{g(t)}} \frac{n(t+\tau)}{\sqrt{g(t+\tau)}}\right\} \\
&= E\{n(t)n(t+\tau)\}E\left\{\frac{1}{\sqrt{g(t)}\sqrt{g(t+\tau)}}\right\} \\
&= N_o \delta(\tau)E\left\{\frac{1}{g(t)}\right\} \\
&= N_o \delta(\tau)\beta
\end{aligned} \tag{8.1-7}$$

where $N_o = E\{n(t)^2\}$ is the power spectral density of the thermal noise on the IF, $\delta(\tau)$ is the Dirac Delta function and β is a constant. The power spectral density of $w(t)$ is thus

$$\begin{aligned}
S_w(f) &= F\{N_o \delta(\tau)\beta\} \\
&= \beta N_o
\end{aligned} \tag{8.1-8}$$

where $F\{\}$ denotes the Fourier Transform. This result demonstrates that $w(t)$ is white, although it is not necessarily Gaussian. For an ideal AGC (ie. $g = \tilde{A}(t)^2$), the power spectral density of $w(t)$ reduces to

$$\begin{aligned}
S_w(f) &= N_o E\left\{\frac{1}{\tilde{A}(t)^2}\right\} \\
&= \frac{1}{2C/N_o(1-S_4^2)}.
\end{aligned} \tag{8.1-9}$$

In Section 3.2, it was shown that this result is only likely to be accurate for S_4 less than about $1/\sqrt{2}$. As $n(t)$ is assumed to be independent of $g(t)$ and $\phi_p(t)$, it is straightforward to show that $w(t)$ is uncorrelated with $\phi_p(t)$, viz

$$\begin{aligned}
E\{\phi_p(t)w(t)\} &= E\left\{\phi_p(t)\frac{n(t)}{\sqrt{g(t)}}\right\} \\
&= E\{n(t)\}E\left\{\frac{\phi_p(t)}{\sqrt{g(t)}}\right\} \\
&= 0.
\end{aligned} \tag{8.1-10}$$

However, as $A(t)$ and $\phi_p(t)$ are produced by the same ionospheric processes, it cannot also be said that $w(t)$ and $\phi_p(t)$ are independent. Nevertheless, these results are sufficient to make use of Equation (8.1-3) to find an optimum Wiener filter.

The power spectral density of $w(t)$ and $\phi_p(t)$ can be represented in terms of the complex frequency variable $s = j2\pi f$ as follows

$$\begin{aligned} S_w(s) &= \beta N_o \\ S_{\phi_p}(s) &= \frac{(2\pi)^p T}{(\omega_o^2 - s^2)^{p/2}} \end{aligned} \quad (8.1-11)$$

where $\omega_o = 2\pi f_o$ is the outer scale size angular frequency. The causal Wiener filter is then

$$\begin{aligned} H_o(s) &= 1 - \frac{\sqrt{\beta N_o}}{[S_{\phi_p}(s) + \beta N_o]^{1/2}} \\ &= 1 - \frac{1}{\left[\frac{(2\pi)^p T / \beta N_o + (\omega_o^2 - s^2)^{p/2}}{(\omega_o^2 - s^2)^{p/2}} \right]^{1/2}} \\ &= 1 - \frac{1}{X(s)} \end{aligned} \quad (8.1-12)$$

The denominator of $X(s)$ can be separated into two factors which represent repeated poles at $s = \pm\omega_o$. These are $(\omega_o - s)^{p/2}$ and $(\omega_o + s)^{p/2}$. However, the numerator is more difficult to factorise. The zeros can be found by solving

$$(2\pi)^p T / \beta N_o + (\omega_o^2 - s^2)^{p/2} = 0$$

to give

$$s = \pm \sqrt{\omega_o^2 - (2\pi)^2 \left(\frac{T}{\beta N_o} \right)^{2/p} \cdot \exp(2\pi j(1+2n)/p)} \quad (8.1-13)$$

where n is an integer. Consequently, depending on the value of p , there are potentially an infinite number of zeros and so no unique solution to the factorisation problem. When m zeros are present, the Wiener filter can be represented by

$$\begin{aligned}
H_o(s) &= 1 - \frac{1}{\left[\frac{\prod_{i=1}^m (z_i + s)}{(\omega_o + s)^{p/2}} \cdot \frac{\prod_{i=1}^m (z_i - s)}{(\omega_o - s)^{p/2}} \right]^+} \\
&= 1 - \frac{(\omega_o + s)^{p/2}}{\prod_{i=1}^m (z_i + s)}
\end{aligned} \tag{8.1-14}$$

where z_i are the zeros which are given by Equation (8.1-13). In order to proceed, two integer values are chosen for the spectral index, p . These are $p=2$ and $p=4$.

Case 1: $p = 2$

For $p = 2$, the Wiener filter simplifies considerably as shown below

$$\begin{aligned}
H_o(s) &= 1 - \frac{(\omega_o + s)}{(z + s)} \\
&= \frac{z - \omega_o}{z + s}
\end{aligned} \tag{8.1-15}$$

where $z = \sqrt{\omega_o^2 + (2\pi)^2 T / \beta N_o}$. The loop filter then becomes

$$F_o(s) = \left[\frac{s}{s + \omega_o} \right] (z - \omega_o) \tag{8.1-16}$$

Consequently, in the limit as ω_o approaches zero (ie. for an infinitely large ionospheric outer scale size), the Wiener filter approaches a first order loop with a loop natural frequency of

$$\begin{aligned}
\omega_n|_o &= \lim_{\omega_o \rightarrow 0} F_o(s) \\
&= 2\pi \sqrt{\frac{T}{\beta N_o}}
\end{aligned} \tag{8.1-17}$$

As the spectral index, p , at equatorial latitudes is typically equal to 2.5 [82], a first order loop gives a good approximation to the optimum tracking loop at these latitudes. The corresponding phase error variance is given by (from Equation (3.2-1))

$$\sigma_{\phi_e}^2 = \int_{-\infty}^{\infty} [1 - H_o(f)^2 S_{\phi_p}(f) + |H_o(f)|^2 S_w(f)] df \quad (8.1-18)$$

A simplified version of this expression for the case where $w(t)$ is white is (Van Trees [95])

$$\sigma_{\phi_e}^2 = \beta N_o \sum_{i=1}^n (z_i - p_i) \quad (8.1-19)$$

where p_i and z_i are the poles and zeros of $S_{\phi_p}(s) + \beta N_o$. For $p=2$, this becomes

$$\sigma_{\phi_e}^2 = \beta N_o (z - \omega_o) \quad (8.1-20)$$

Therefore, in the limit as ω_o approaches zero, the phase error variance becomes

$$\begin{aligned} \lim_{\omega_o \rightarrow 0} \sigma_{\phi_e}^2 &= \beta N_o \omega_n|_o \\ &= 2\pi \sqrt{T \beta N_o} \end{aligned} \quad (8.1-21)$$

Consequently, the variance increases equally with both the phase scintillation energy, T , and the amplitude scintillation energy, β . However, as would be expected, the optimum loop bandwidth increases with the phase scintillation energy, but decreases with the amplitude scintillation energy (the optimum loop bandwidth is proportional to $\omega_n|_o$).

Case 2: p=4

For $p=4$, the Wiener filter is given by

$$\begin{aligned} H_o(s) &= 1 - \frac{(\omega_o + s)^2}{(z_1 + s)(z_2 + s)} \\ &= \frac{z_1 z_2 - \omega_o^2 + s[z_1 + z_2 - 2\omega_o]}{z_1 z_2 + s[z_1 + z_2] + s^2} \end{aligned} \quad (8.1-22)$$

where z_1 and z_2 are the zeros which are given by (from Equation (8.1-13))

$$z_1, z_2 = \sqrt{\omega_o^2 \mp j(2\pi)^2 \sqrt{\frac{T}{\beta N_o}}} \quad (8.1-23)$$

If we let $\omega_o^2 \mp j(2\pi)^2 \sqrt{\frac{\mathbf{T}}{\beta N_o}} = k \exp(\mp j\theta)$, where $k = \sqrt{\omega_o^4 + (2\pi)^4 \frac{\mathbf{T}}{\beta N_o}}$ and

$\theta = \text{atan}\left(\frac{(2\pi)^2}{\omega_o^2} \sqrt{\frac{\mathbf{T}}{\beta N_o}}\right)$, the zeros become

$$\begin{aligned} z_1, z_2 &= \sqrt{k} \exp(\mp j\theta/2) \\ &= \sqrt{k} [\cos(\theta/2) \mp j \sin(\theta/2)] \\ &= \sqrt{k/2} [\sqrt{1+\cos(\theta)} \mp j \sqrt{1-\cos(\theta)}] \\ &= \left[\sqrt{k + \omega_o^2} \mp j \sqrt{k - \omega_o^2} \right] / \sqrt{2} \end{aligned} \quad (8.1-24)$$

By substituting Equation (8.1-24) into (8.1-22), the Wiener filter becomes

$$H_o(s) = \frac{k - \omega_o^2 + s \left[\sqrt{2(k + \omega_o^2)} - 2\omega_o \right]}{k + s \sqrt{2(k + \omega_o^2)} + s^2} \quad (8.1-25)$$

In the limit as ω_o approaches zero, this reduces to

$$H_o(s) = \frac{\sqrt{2}\omega_n s + \omega_n^2}{s^2 + \sqrt{2}\omega_n s + \omega_n^2} \quad (8.1-26)$$

where $\omega_n|_o = 2\pi \sqrt{\frac{\mathbf{T}}{\beta N_o}}$. In this form, the Wiener filter represents an active second order

loop with a damping factor of $\zeta = 1/\sqrt{2}$ and a loop natural frequency of ω_n (see Table 3-2). As 4 is the upper limit for the spectral index parameter [27], this result suggests that a third order loop will not provide an optimum solution unless dynamics are also present. The corresponding phase error variance is given by (from Equation (8.1-19))

$$\begin{aligned} \sigma_{\phi_e}^2 &= \beta N_o [(z_1 - \omega_o) + (z_2 - \omega_o)] \\ &= \beta N_o \left[\sqrt{2(k + \omega_o^2)} - 2\omega_o \right] \end{aligned} \quad (8.1-27)$$

In the limit as ω_o approaches zero, this simplifies to

$$\begin{aligned} \lim_{\omega_o \rightarrow 0} \sigma_{\phi_e}^2 &= \sqrt{2} \beta N_o \omega_n|_o \\ &= 2\pi \sqrt[4]{4\mathbf{T}(\beta N_o)^3} \end{aligned} \quad (8.1-28)$$

Consequently, for $p=4$ the variance is far more sensitive to amplitude scintillation energy, β , than to phase scintillation energy, T .

8.1.2. Non-causal Wiener filters

Although the non-causal Wiener filter is not a practical filter structure for a phase locked loop, it does provide a lower bound on the phase tracking error which cannot be surpassed by any filter type (Van Trees [95]). As $\phi_p(t)$ and $w(t)$ are uncorrelated, the non-causal Wiener filter for arbitrary values of p is given by

$$\begin{aligned} H_o(s) &= \frac{S_{\phi_p}(s)}{S_{\phi_p}(s) + S_w(s)} \\ &= \frac{(2\pi)^p T}{(2\pi)^p T + \beta N_o (\omega_o^2 - s^2)^{p/2}} \end{aligned} \quad (8.1-29)$$

and the corresponding phase error variance is

$$\begin{aligned} \sigma_{\phi_e}^2 &= \int_{-\infty}^{\infty} [1 - H_o(f)^2 S_{\phi_p}(f) + |H_o(f)|^2 S_w(f)] df \\ &= \int_{-\infty}^{\infty} \frac{S_{\phi_p}(f) S_w(f)}{S_{\phi_p}(f) + S_w(f)} df \\ &= \int_{-\infty}^{\infty} \frac{T \beta N_o}{T + \beta N_o (f^2 + f_o^2)^{p/2}} df \end{aligned} \quad (8.1-30)$$

In the limit as f_o approaches zero, this expression reduces to

$$\lim_{f_o \rightarrow 0} \sigma_{\phi_e}^2 = \frac{2\pi \beta N_o}{p \sin(\pi/p)} \left[\frac{T}{\beta N_o} \right]^{1/p}, \quad p > 1 \quad (8.1-31)$$

Although a closed form expression for the transfer function of an optimum causal filter cannot be obtained for arbitrary values of p , it is possible to determine the variance for arbitrary p without the need to factor the input spectrum. This given by (Van Trees [95])

$$\begin{aligned}
\sigma_{\phi_e}^2 &= \beta N_o \int_{-\infty}^{\infty} \ln \left[1 + \frac{S_{\phi_p}(f)}{\beta N_o} \right] df \\
&= \beta N_o \int_{-\infty}^{\infty} \ln \left[1 + \frac{T}{\beta N_o (f_o^2 + f^2)^{p/2}} \right] df
\end{aligned} \tag{8.1-32}$$

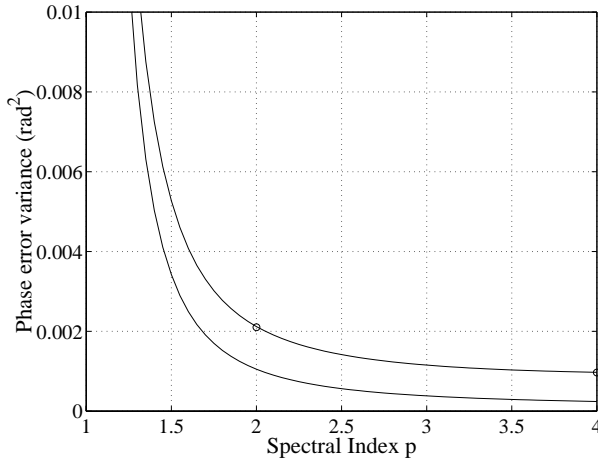


Figure 8.1-2: Phase error variance as a function of the spectral index p for $T = -25 \text{ dBW/Hz}$, $S_4 = 0$, $C/N_o = 41.5 \text{ dBHz}$ and $f_o \approx 0$. The lower line represents the non-causal Wiener filter, the upper line represents the causal Wiener filter. The two circles correspond to the variance values obtained from Equations (8.1-21) and (8.1-28) for $p=2$ and $p=4$ respectively.

A comparison between these two variance measures is given in Figure 8.1-2 for $T = -25 \text{ dBW/Hz}$, $S_4 = 0$ (ie. $\beta = 1/\mathbf{A}^2$), $C/N_o = 41.5 \text{ dBHz}$ and $f_o \approx 0$. It is clear from these plots that the errors associated with the causal Wiener filter are always larger than those associated with the non-causal filter (as would be expected).

8.1.3. Doppler errors

The optimum filters obtained in the previous sections were based on the assumption that the tracking loops are only subject to scintillations and thermal noise. However, the tracking loops of a real GPS receiver will also encounter Doppler errors resulting from relative motion between the satellite and the receiver. An optimum filter which takes account of Doppler errors can be obtained by adding a Doppler term to the power spectral density of the input phase process, $S_\phi(s)$.

In the approach taken by Jaffe and Rechtin [45], optimum loop filters were obtained for a phase locked loop that was subject to thermal noise and dynamics consisting of a step in position, velocity and acceleration. This resulted in 1st, 2nd, and 3rd order tracking loops respectively. An equivalent approach can be taken here by adding the power spectral densities of a step in position, velocity and acceleration to the phase scintillation terms. From Appendix E, the power spectral density of the dynamics, $S_{\phi_d}(s)$, is given by

$$\begin{aligned} S_{\phi_d}(s) &= E\{\Phi_d(s) \times \Phi_d(s)^*\} \\ &= -\frac{\Theta^2}{s^2}, \quad \text{position step} \\ &= +\frac{\Omega^2}{s^4}, \quad \text{velocity step} \\ &= -\frac{\Lambda^2}{s^6}, \quad \text{acceleration step} \end{aligned} \quad (8.1-33)$$

where Θ , Ω and Λ are the magnitudes of the dynamic processes in radians, radians/s and radians/s² respectively (note that these can be related to the quantities given in Appendix E through $\Theta = 2\pi r_o/\lambda$, $\Omega = 2\pi v_o/\lambda$, and $\Lambda = 2\pi a_o/\lambda$, where λ is the carrier wavelength).

Equation (8.1-33) can be generalised as follows

$$S_{\phi_d}(s) = (-1)^n \frac{\Gamma^2}{s^{2n}} \quad (8.1-34)$$

where Γ is either Θ , Ω or Λ , and n is the order of the dynamics (1, 2 or 3 for position, velocity and acceleration respectively). The total power spectral density of the input phase process is therefore

$$\begin{aligned} S_\phi(s) &= S_{\phi_p}(s) + S_{\phi_d}(s) \\ &= \frac{(2\pi)^p \mathbf{T}}{(\omega_o^2 - s^2)^{p/2}} + (-1)^n \frac{\Gamma^2}{s^{2n}} \end{aligned} \quad (8.1-35)$$

Assuming $\omega_o = 0$ and letting $s = j2\pi f$ gives

$$S_\phi(f) = \frac{\mathbf{T}}{|f|^p} + \frac{\Gamma^2}{(2\pi f)^{2n}} \quad (8.1-36)$$

The corresponding closed loop transfer function is therefore (from Equation (8.1-3))

$$H_o(f) = 1 - \frac{\sqrt{\beta N_o}}{[S_\phi(f) + \beta N_o]^+} \quad (8.1-37)$$

In the analysis that follows, four cases are considered corresponding to $p=2$ and $p=4$, and steps in both position and velocity (other values of p result in filters that do not map into phase locked loop structures).

Case 1: Position step ($n=1$), $p=2$

For a position step with $p=2$, $S_\phi(f)$ becomes

$$S_\phi(f) = \frac{T}{f^2} + \frac{\Theta^2}{(2\pi f)^2} \quad (8.1-38)$$

Consequently, the optimum tracking loop is 1st order with a loop natural frequency of

$$\omega_n|_o = 2\pi \sqrt{\frac{T + (\Theta/2\pi)^2}{\beta N_o}} \quad (8.1-39)$$

Note that this reverts to Equation (8.1-17) when dynamics are absent (ie. $\Theta=0$).

Case 2: Velocity step ($n=2$), $p=2$

For a velocity step with $p=2$, $S_\phi(f)$ becomes

$$S_\phi(f) = \frac{T}{f^2} + \frac{\Omega^2}{(2\pi f)^4} \quad (8.1-40)$$

Consequently,

$$\begin{aligned} [S_\phi(f) + \beta N_o]^+ &= \left[\frac{T}{f^2} + \frac{\Omega^2}{(2\pi f)^4} + \beta N_o \right]^+ \\ &= \left[\frac{f^4 + Tf^2/\beta N_o + \Omega^2/[(2\pi)^4 \beta N_o]}{f^4/\beta N_o} \right]^+ \\ &= \left[\left(\frac{(j2\pi f)^2 + (j2\pi f)A + B}{C(j2\pi f)^2} \right) \left(\frac{(-j2\pi f)^2 + (-j2\pi f)A + B}{C(-j2\pi f)^2} \right) \right]^+ \\ &= \frac{(j2\pi f)^2 + (j2\pi f)A + B}{C(j2\pi f)^2} \end{aligned} \quad (8.1-41)$$

where $B = \frac{\Omega}{\sqrt{\beta N_o}}$, $A = \sqrt{D+2B}$, $C = \frac{1}{\sqrt{\beta N_o}}$, $D = \frac{(2\pi)^2 T}{\beta N_o}$. The optimum closed loop filter is therefore

$$\begin{aligned} H_o(f) &= 1 - \frac{\sqrt{\beta N_o}}{\left[\frac{(j2\pi f)^2 + (j2\pi f)A + B}{C(j2\pi f)^2} \right]} \\ &= \frac{(j2\pi f)A + B}{(j2\pi f)^2 + (j2\pi f)A + B} \\ &= \frac{(j2\pi f)2\zeta\omega_n + \omega_n^2}{(j2\pi f)^2 + (j2\pi f)2\zeta\omega_n + \omega_n^2} \end{aligned} \quad (8.1-42)$$

which is the transfer function of a 2nd order loop with a loop natural frequency, ω_n , and damping factor, ζ , given by

$$\begin{aligned} \omega_n|_o &= \sqrt{B} = 2\pi \sqrt[4]{\frac{\Omega^2/(2\pi)^4}{\beta N_o}} \\ \zeta &= \frac{A}{2\sqrt{B}} = \frac{1}{\sqrt{2}} \sqrt{\frac{(2\pi)^2 T}{2\Omega\sqrt{\beta N_o}} + 1} \end{aligned} \quad (8.1-43)$$

Consequently, the loop natural frequency (and thus bandwidth) depends only on the magnitude of the dynamics and the amplitude scintillations. However, the damping factor is greater than the normal critical damping factor of $1/\sqrt{2}$ by a factor which depends on all three effects (ie. dynamics and both the amplitude and phase scintillation characteristics).

Case 3: Position step ($n=1$), $p=4$

For a position step with $p=4$, $S_\phi(f)$ becomes

$$S_\phi(f) = \frac{T}{f^4} + \frac{\Theta^2}{(2\pi f)^2} \quad (8.1-44)$$

Consequently, by inspection from Case 2 it is clear that the optimum tracking loop is 2nd order with

$$\omega_n|_o = 2\pi \sqrt[4]{\frac{T}{\beta N_o}}$$

$$\zeta = \frac{1}{\sqrt{2}} \sqrt{\frac{\Theta^2}{8\pi^2 \sqrt{T\beta N_o}} + 1} \quad (8.1-45)$$

Consequently, the loop natural frequency depends only on the magnitude of the scintillation activity, and the damping factor depends on all three effects.

Case 4: Velocity step ($n=2$, $p=4$)

For a velocity step with $p=4$, $S_\phi(f)$ becomes

$$S_\phi(f) = \frac{T}{f^4} + \frac{\Omega^2}{(2\pi f)^4} \quad (8.1-46)$$

And the optimum tracking loop is a 2nd order loop with

$$\omega_n|_o = 2\pi \sqrt[4]{\frac{T + \Omega^2/(2\pi)^4}{\beta N_o}} \quad (8.1-47)$$

$$\zeta = \frac{1}{\sqrt{2}}$$

Consequently, phase scintillations and dynamics affect the loop bandwidth equally.

Although this analysis has not been continued for higher order dynamics, it appears that if the order of the dynamics is expected to be large (ie. $2n \gg p$), the order of the optimum tracking loop will be determined solely by the dynamics. Indeed, at equatorial latitudes where $p \approx 2$, it appears that the strength of phase scintillations will only affect the damping factor, ζ , for a velocity step. The loop order will be determined by the dynamics, and the loop bandwidth will be a function of both the dynamics and the strength of amplitude scintillations.

8.1.4. Optimum post-loop filters

The optimum loop filters discussed so far have been designed to minimise the phase errors in the carrier tracking loop. To reduce the effects of scintillations on the phase estimates without compromising this first design objective, a second filter can be placed in cascade with the tracking loop. This can be done in one of two ways as shown in Figure 8.1-3.

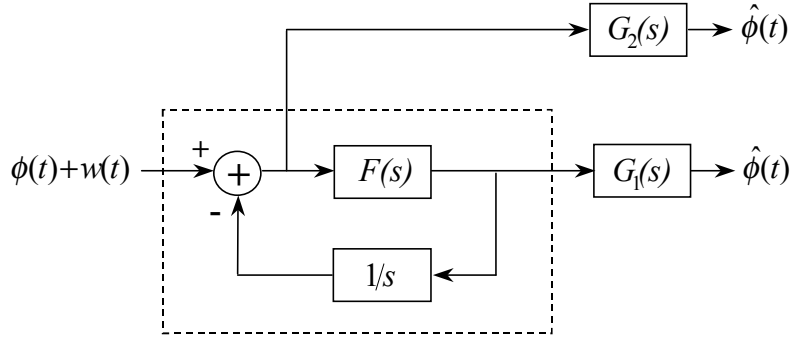


Figure 8.1-3: Post-loop filtering schemes to reduce scintillation phase noise in the loop phase estimates.

The transfer functions of the resulting cascaded systems are

$$\text{Case 1: } K_1(s) = s.H_o(s).G_1(s), \text{ and} \quad (8.1-48)$$

$$\text{Case 2: } K_2(s) = [1 - H_o(s)]G_2(s). \quad (8.1-49)$$

The causal Wiener filter for either system is given by (from Equation (8.1-2))

$$K_{oc}(s) = \frac{1}{[S_\phi(s) + \beta N_o]^+} \left[\frac{S_{\phi_d}(s)}{[S_\phi(s) + \beta N_o]^-} \right]_{pos} \quad (8.1-50)$$

where $S_{\phi_d}(s)$ is the power spectral density of the dynamics (ie. the desired signal for a GPS receiver) and $S_\phi(s) = S_{\phi_d}(s) + S_{\phi_p}(s) + S_{\phi_o}(s)$ is the power spectral density of the input phase process. Notice that Equation (8.1-3) cannot be used in this case as the noise is no longer white (ie. it is of the form $w(t) + \phi_p(t) + \phi_o(t)$). The Wiener filter represented by Equation (8.1-50) is designed to minimise the errors from all noise sources while providing a best estimate of the dynamics $\phi_d(t)$. By substituting Equation (8.1-50) into Equations (8.1-48) and (8.1-49), the following optimum post-loop filters can be obtained for a causal system

$$\text{Case 1: } G_{1o}(s) = \frac{1}{s[S_\phi(s) + \beta N_o]^+ - \sqrt{\beta N_o}} \left[\frac{S_{\phi_d}(s)}{[S_\phi(s) + \beta N_o]^-} \right]_{pos}, \text{ and} \quad (8.1-51)$$

$$\text{Case 2: } G_{2o}(s) = \frac{1}{\sqrt{\beta N_o}} \left[\frac{S_{\phi_d}(s)}{[S_\phi(s) + \beta N_o]^-} \right]_{pos}. \quad (8.1-52)$$

As the cascaded system does not necessarily need to be causal, equivalent non-causal filters can also be found. The non-causal Wiener filter is given by

$$K_{oNC}(s) = \frac{S_{\phi_d}(s)}{S_\phi(s) + \beta N_o} \quad (8.1-53)$$

The non-causal filter applies to systems that are not required to provide range and velocity estimates in real time and so may have access to future phase estimates. Consequently, filter of this sort may be approximated arbitrarily closely by introducing a processing delay. Notice that although the cascade represented by $K_{oNC}(s)$ may be non-causal, the loop filter, $H_o(s)$, must always be causal. The two non-causal post-loop filters are given by

Case 1: $G_{1o}(s) = \frac{S_{\phi_d}(s)}{s[S_\phi(s) + \beta N_o - \sqrt{\beta N_o}[S_\phi(s) + \beta N_o]]}, \text{ and}$ (8.1-54)

Case 2: $G_{2o}(s) = \frac{S_{\phi_d}(s)}{\sqrt{\beta N_o}[S_\phi(s) + \beta N_o]}.$ (8.1-55)

The error associated with the estimate of the Doppler process, $\phi_d(t)$, is given by

$$\phi_{\varepsilon_d}(t) = \hat{\phi}(t) - \phi_d(t) \quad (8.1-56)$$

The corresponding mean square error is therefore

$$E\{\phi_{\varepsilon_d}(t)^2\} = \frac{1}{2\pi j} \int_{-\infty}^{\infty} S_{\phi_{\varepsilon_d}}(s) ds \quad (8.1-57)$$

where $S_{\phi_{\varepsilon_d}}(s) = |1 - K_o(s)|^2 S_{\phi_d}(s) + |K_o(s)|^2 [S_{\phi_p}(s) + \beta N_o]$ is the power spectral density of the Doppler estimate error. Using Equation (8.1-57), the mean-square error can be found for the optimum loop filter, $H_o(s)$, the optimum causal cascaded filter, $K_{oC}(s)$, and the optimum non-causal cascaded filter, $K_{oNC}(s)$. Although a comparison of these errors has not been carried out here, it is expected that the optimum non-causal cascaded filter will produce the minimum error as it has access to both past and future information.

8.2. Direct determination of the MMSE

The principal advantage of the Wiener filter approach is that it allows the optimum filter for minimum mean square error (MMSE) to be found without regard for the filter structure. However, a drawback with this approach is that it results in a filter which does not readily map into a phase locked loop unless the spectral index, p , is either 2 or 4. By minimising the mean square error for each loop order directly, it is possible to determine an optimum loop bandwidth and MMSE for all values of p . The optimum loop order can then be found by comparing the MMSE's for each of the three loop orders and selecting the minimum. In this section, an expression will be derived for the optimum loop bandwidth for MMSE for all three loop orders in the presence of scintillations and thermal noise. It will also be demonstrated that dynamics may strongly influence the choice of an optimum loop bandwidth and order, and will in many cases take precedence over scintillation effects.

The variance of the phase tracking error for a phase locked loop in the presence of scintillations is given by (from Equation (3.2-5))

$$\sigma_{\phi_e}^2 = \sigma_{\phi_{ep}}^2 + \sigma_{\phi_T}^2 \quad (8.2-1)$$

where (based on Equation (8.1-8))

$$\begin{aligned} \sigma_{\phi_T}^2 &= 2B_n S_w(f) \\ &= 2B_n \beta N_o \end{aligned} \quad (8.2-2)$$

and (from Equation (3.2-8))

$$\sigma_{\phi_{ep}}^2 = \frac{\pi T}{kf_n^{p-1} \sin([p-1]\pi/2k)}, \quad 1 < p < 2k \quad (8.2-3)$$

and (from Table 3-2)

$$B_n = \begin{cases} \pi f_n / 2, & 1^{\text{st}} \text{ Order} \\ 3\pi f_n / 2\sqrt{2}, & 2^{\text{nd}} \text{ Order} \\ 5\pi f_n / 3, & 3^{\text{rd}} \text{ Order} \end{cases} \quad (8.2-4)$$

$$= \alpha f_n$$

Therefore, the derivative of $\sigma_{\phi_e}^2$ with respect to the loop natural frequency, f_n , is given by

$$\frac{\partial \sigma_{\phi_e}^2}{\partial f_n} = \frac{(1-p)\pi T}{kf_n^p \sin([p-1]\pi/2k)} + 2\alpha\beta N_o \quad (8.2-5)$$

Letting $\frac{\partial \sigma_{\phi_e}^2}{\partial f_n} = 0$ gives

$$\begin{aligned} f_n|_o &= \left[\frac{(p-1)\pi T}{2\alpha\beta N_o k \sin([p-1]\pi/2k)} \right]^{1/p} \\ &= \frac{\omega_n|_o}{2\pi} \\ &= \frac{B_n|_o}{\alpha} \end{aligned} \quad (8.2-6)$$

$B_n|_o$ is the optimum loop bandwidth for MMSE for all three loop orders. As shown in Figure 8.2-1, Equation (8.2-5) is guaranteed to return the bandwidth for MMSE as the variance of the tracking error consists of a monotonically increasing component due to thermal noise added to a monotonically decreasing component due to phase scintillations. It can also be shown that for a 1st order loop and $p=2$, or a 2nd order loop and $p=4$, $\omega_n|_o$ reduces to the two results given in Section 8.1 for the Wiener filter solution.

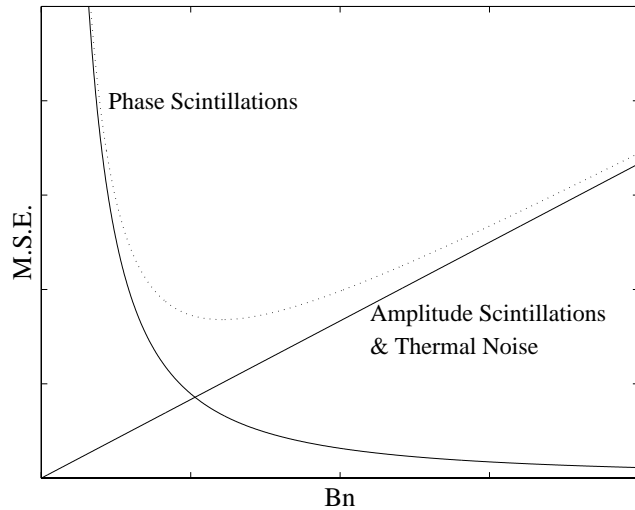


Figure 8.2-1: Illustration of the relationship between the two components of the mean square tracking error as a function of the loop noise bandwidth, B_n . The dotted line represents the sum, $\sigma_{\phi_e}^2$.

The corresponding MMSE can be found by substituting Equation (8.2-6) back into Equation (8.2-1) to give

$$\sigma_{\phi_e}^2 \Big|_o = \frac{2\alpha\beta N_o p}{(p-1)} \left[\frac{(p-1)\pi T}{2\alpha\beta N_o k \sin([p-1]\pi/2k)} \right]^{1/p} \quad (8.2-7)$$

8.2.1. Doppler errors

The effects of dynamics on the optimum loop bandwidth can be treated in one of two ways; (i) assume that the dynamics are constant and the loop is in steady state, or (ii) assume that the dynamics are introduced suddenly and produces a transient error in the tracking loop. In the first case, the dynamics will either produce a constant error if the order of the dynamics is equal to the order of the tracking loop, or zero error if the order of the dynamics is less than the order of the tracking loop (see Appendix E, Section E.1). In the second case, the transient error can be accounted for by introducing a term referred to as the Total Transient Distortion, ε_T^2 . This is based on the approach taken by Jaffee and Rechtin [45] that was discussed in Section 8.1.3.

Using Jaffee and Rechtin's approach, the optimisation problem becomes one of minimising the following variance expression

$$\sigma_{\phi_e}^2 = \sigma_{\phi_{ep}}^2 + \sigma_{\phi_T}^2 + \varepsilon_T^2 \quad (8.2-8)$$

From Appendix E, the Total Transient Distortion is given by

$$\varepsilon_T^2 = \int_{-\infty}^{\infty} |1 - H(f)|^2 S_{\phi_d}(f) df \quad (8.2-9)$$

where $S_{\phi_d}(f) = \frac{\Gamma^2}{(2\pi f)^{2n}}$ from Section 8.1.3. ε_T^2 can be expanded to give

$$\begin{aligned} \varepsilon_T^2 &= \int_{-\infty}^{\infty} \frac{f^{2k}}{f^{2k} + f_n^{-2k}} \times \frac{\Gamma^2}{(2\pi f)^{2n}} df \\ &= \frac{\Gamma^2}{2k(2\pi f_n)^{2n-1} \sin([2n-1]\pi/2k)}, \quad 0.5 < n < k + 0.5 \end{aligned} \quad (8.2-10)$$

The condition $0.5 < n < k + 0.5$ implies that the loop order must be greater than or equal to the order of the dynamics in order for ε_T^2 to be finite (eg. either a position or velocity step for a 2nd order loop, but not an acceleration). In principle, the optimum loop bandwidth for MMSE can once again be found by minimising Equation (8.2-8) with Equation (8.2-10) used in place of ε_T^2 . However, in practice a simple analytical expression cannot readily be obtained for all values of n , k and p as the derivative of Equation (8.2-8) is a polynomial with a non-integer order. What can be done is to solve the polynomial using numerical techniques for a specific set of conditions, or obtain an analytical solution for integer values of p . Alternatively, it is possible to determine a value for the spectral strength, T , above which the phase scintillation component dominates over the dynamics component. This can be found by equating Equations (8.2-3) and (8.2-10) to give

$$T = \frac{\Gamma^2 \sin([p-1]\pi/2k) f_n^{p-2n}}{(2\pi)^{2n} \sin([2n-1]\pi/2k)}, \quad 0.5 < n < k + 0.5 \text{ and } 1 < p < 2k \quad (8.2-11)$$

In Figure 8.2-2, T (in decibels) is plotted as a function of Γ for a 2nd order loop that is subject to both a position step ($\Gamma=\Theta$) and a velocity step ($\Gamma=\Omega$). In addition, two loop bandwidths are considered that represent typical upper and lower values for a phase locked loop.

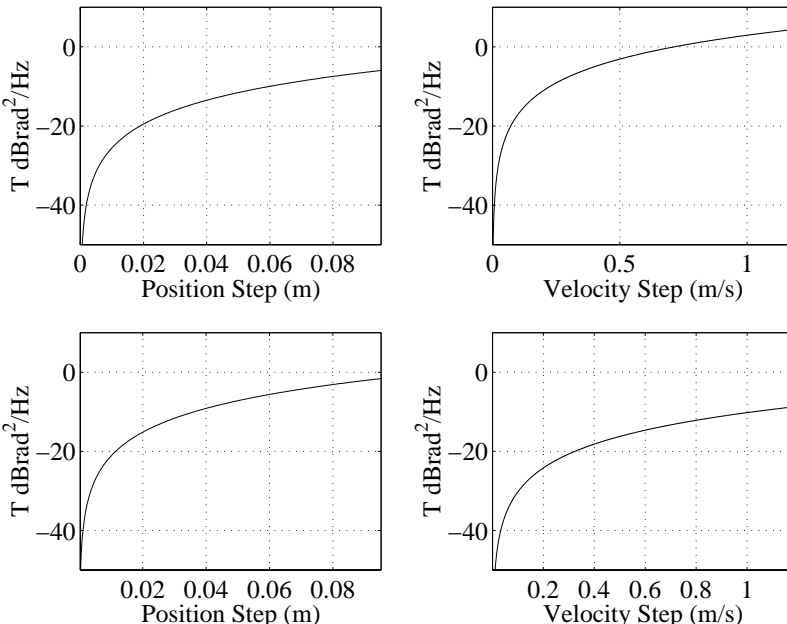


Figure 8.2-2: Threshold values of T above which phase scintillation energy will dominate over dynamics in the selection of an optimum loop bandwidth. The upper two panels represent a loop bandwidth of 2Hz. The lower two panels represent a loop bandwidth of 15Hz. $p=2.5$.

Also note that because of the ambiguity in a sinusoid, it is only necessary to look at instantaneous phase steps of less than $\frac{1}{2}$ a cycle (~ 0.095 m at the GPS L1 frequency). For this reason, Θ is often modelled as a uniform random variable on $(-\pi, \pi)$ such that

$$S_{\phi_d}(f) = \frac{E\{\Theta^2\}}{(2\pi f)^2} = \frac{\pi^2/3}{(2\pi f)^2}. \text{ The corresponding value of } T \text{ can then be found from the two}$$

left panels of Figure 8.2-2 by assuming a position step of $\pi/\sqrt{3}$ radians or 0.055m at GPS L1. Notice that this implies that T must be greater than about -10 dBradians 2 /Hz in the presence of a random phase step before it will begin to dominate over dynamics in the selection of an optimum loop bandwidth.

8.3. Conclusions

Using Wiener filter theory, it can be shown that the optimum causal filter for minimum carrier phase tracking error has the same structure as a first order phase locked loop when the spectral index, p , is equal to two, and a second order loop when $p = 4$. Therefore, as p is usually close to 2.5 at equatorial latitudes, it seems likely that a first order loop will be the best choice for carrier tracking in an equatorial scintillation environment. However, this result is predicated on the assumption that amplitude scintillations can be treated as a scaling factor for the thermal noise power spectral density, and that other direct phase processes such as dynamics are absent.

For $p = 2$ (close to the typical equatorial value) and for a step in position, the optimum phase locked loop structure is a first order loop with a bandwidth that depends on both the strength of scintillation activity (ie. T and S_4), and the magnitude of the phase step. However, for $p = 2$ and a step in velocity, the optimum loop order is determined by the dynamics (ie. it is second order) and the bandwidth is a function of the magnitude of the velocity step and the strength of amplitude scintillations only. Although this analysis has not been carried out for dynamics with higher orders, it appears that if the order of the dynamics is large (ie. $2n \gg p$), the order of the optimum tracking loop will be decided by the dynamics.

Based on a direct determination of the optimum bandwidth for a second order phase locked loop, it appears that the strength of phase scintillations must be extremely large before it begins to dominate over dynamics, even when the magnitude of the dynamics is quite modest. Consequently, in practice the choice of loop order and bandwidth should

be based on the dynamics, the quiescent GPS signal level and perhaps the anticipated strength of amplitude scintillation activity. The level of phase scintillation activity is only likely to be important when dynamics are greatly minimised through the use of inertial aiding, or in the case of codeless and semi-codeless receivers, through L1 aiding of the L2 carrier loop.

Chapter 9

Scintillation effects on navigation

In this thesis, a number of receiver performance measures have been derived by combining a stochastic ionospheric scintillation model with various receiver tracking loop models. By linking these measures with a climatological scintillation model such as the Wide Band Scintillation Model, WBMOD, the performance of individual satellite-receiver links can be predicted for a given time and location. This is discussed further in Section 9.1. However, because WBMOD does not account for large scale structures such as *equatorial plumes* which affect the distribution of irregularities in the sky, it is unable to model the spatial and temporal patchiness of scintillations, nor the night-to-night variability that is frequently observed on scintillating links. Consequently, it is not well suited to predicting the performance of multiple satellite links simultaneously, and so cannot easily be used to assess the impact of scintillations on navigational accuracy. This is discussed in more detail in Sections 9.2 and 9.3. Nevertheless, in Section 9.4 it is shown that WBMOD can be used to determine the number of links that may be stressed to the point of losing lock for a given time, location and percentile. Although this does not indicate the likelihood of simultaneous losses of lock, it does illustrate when and where significant scintillation events are likely to occur for a given receiver type.

9.1. Predicting the performance of a single link

For any given satellite-receiver geometry, time and date, uncertainty will exist about the size and density of the irregularities along a specified propagation path. In WBMOD, this uncertainty is accounted for by providing a probability density function (PDF) for the height integrated irregularity strength parameter¹, $C_k L$. Based on Equations (3.4-9) and (3.4-10), it is clear that T and S_4 can be related to $C_k L$ through the expressions

¹ $C_k L$ is the height-integrated strength of the irregularity spatial power spectrum at a scale size of 1km (see Equation (2.1-2) and [82] and [76]).

$$\begin{aligned} T &= \alpha C_k L, \text{ and} \\ S_4^2 &= 1 - \exp(-\beta C_k L) \end{aligned} \tag{9.1-1}$$

where α and β are based on a combination of deterministic geometrical factors and accurately modelled random parameters (see for example [82] and [76]). T and S_4 can also be related to each other through the expression $T = -\ln(1 - S_4^2)/\gamma$ where $\gamma = \beta/\alpha$ (Equation (3.4-7)). Therefore, for a given set of conditions (ie. time, date and satellite-receiver geometry), WBMOD's internal models provide information from which the parameters α , β , and γ and the distribution functions of T and S_4 , $f_T(T)$ and $f_{S_4}(S_4)$, can be deduced. These functions can then be used to determine average values for many of the receiver performance measures derived in earlier chapters. These include the variance of the code and carrier phase range errors, the probability of losing lock, P_L , the probability of a navigation data bit error, P_e , and the probability of detection for acquisition, \bar{P}_d . Also, because T can be expressed as a function of S_4 and the geometry factor γ , it is only necessary to determine the PDF of S_4 (or T) in order to find average values for the specified performance measures (ie. the joint PDF of T and S_4 can be expressed as $f_{T,S_4}(T, S_4) = \delta(T - T')f_{S_4}(S_4)$ where $T' = -\ln(1 - S_4^2)/\gamma$).

In WBMOD, the PDF of $\log(C_k L)$ in equatorial regions is modelled as the sum of two Gaussians [82]. In principle, this allows Equation (9.1-1) to be used to determine the PDF of S_4 for a given value of β . In practice, however, WBMOD does not provide this information as part of its standard output. Nevertheless, it is possible to deduce the PDF of S_4 directly by differentiating the cumulative distribution function of S_4 which can be obtained from WBMOD's predictions of S_4 over a range of different percentiles.

If the PDF of S_4 is known for a particular link, the average probability of losing lock can be found as follows

$$\begin{aligned} \bar{P}_L &= \int_0^\infty \int_0^1 P_L(T, S_4) f_{T,S_4}(T, S_4) dS_4 dT \\ &= \int_0^1 P_L(T', S_4) f_{S_4}(S_4) dS_4 \end{aligned} \tag{9.1-2}$$

where $P_L(T, S_4)$ is the probability of losing lock as a function of T and S_4 (from Equation

(3.4-3) with $m = 1/S_4^2$, $T' = -\ln(1 - S_4^2)/\gamma$, $f_{S_4}(S_4)$ is the PDF of S_4 , $T \geq 0$ and $0 \leq S_4 \leq 1$.

In a similar way, the average values of P_e and \bar{P}_d can be found for each visible satellite link (ie. from Equation (6.3-11) and (6.3-15) we have $P_e(S_4)$, and from Equation (7.2-11) we have $\bar{P}_d(S_4)$).

9.2. Predicting the performance of multiple links

In order to determine the impact of scintillations on navigational accuracy, it is necessary to find the probability of losing lock on multiple satellite links simultaneously. The average probability of losing lock on n satellite links simultaneously is given by

$$\bar{P}_n = \int_0^1 \dots \int_0^1 \left[\prod_{k=1}^n P_{L_k}(T'_k, S_{4_k}) \right] * f_{S_{4_1} \dots S_{4_n}}(S_{4_1}, \dots, S_{4_n}) dS_{4_1} \dots dS_{4_n} \quad (9.2-1)$$

where $P_{L_k}(T'_k, S_{4_k})$ is the probability of losing lock on link k as a function of the S_4 index on that link, and $f_{S_{4_1} \dots S_{4_n}}(S_{4_1}, \dots, S_{4_n})$ is the joint PDF of S_4 on the n links. Equation (9.2-1) implies that for a given set of S_4 values, the individual probabilities of losing lock are independent of one another. In other words, the probability of losing lock on n links simultaneously is simply the product of the probabilities of losing lock on each link. This is based on the observation that although the strength of scintillation activity may be correlated between the links (perhaps as a result of a large plume structure that is penetrated by several links simultaneously), the individual scintillation patterns, and in particular the deep fades that give rise to loss-of-lock, are likely to be independent. The justification for this assumption is that scintillation patterns are produced by small scale irregularities of the order of the Fresnel zone radius or smaller (< 300m or so), and so it is unlikely that two propagation paths will penetrate the same group of irregularities at the same time. This assumption may, however, break down if the ionospheric pierce points of the two propagation paths happen to be extremely close.

Although WBMOD does not provide information about the joint PDF of S_4 on multiple satellite links, if it is assumed that the links are independent (ie. the irregularity regions are assumed to be highly "patchy"), then the average probability of losing lock on n links simultaneously is simply the product of the average probability of losing lock on each link, *viz*

$$\bar{P}_n = \prod_{k=1}^n \bar{P}_{L_k} \quad (9.2-2)$$

where $f_{S_{4_1}, \dots, S_{4_n}}(S_{4_1}, \dots, S_{4_n}) = \prod_{k=1}^n f_{S_{4_k}}(S_{4_k})$ has been assumed. Under these conditions, the probability of simultaneously losing lock on n links is expected to be very small, given that the individual probabilities are also likely to be quite small. Measurements of loss-of-lock taken from a Novatel Millennium™ receiver during the September 1998 and March 1999 equinoxes tends to support this view. In Figure 5.4-1 from Chapter 5, the percentage of time between 8:00pm and 10:00pm that the Novatel Millennium™ loses lock on both the L1 and semi-codeless L2 channels is plotted as a function of day. It is clear from these plots that the percentage of time that one link was lost (represented by the white sections of the bars) was always much greater than the percentage of time that two or more links were lost simultaneously (represented by the solid sections). Indeed, on days during which significant scintillation activity occurred, the average ratio of the percentage of time that two or more links were lost simultaneously compared to only one link was 4.7% for the semi-codeless L2 carrier loop. Again, this supports the view that the simultaneous loss of multiple links becomes much less common as the number of links, n , increases.

9.3. Predicting navigational accuracy

Equation (9.2-1) gives the average probability of losing lock on n satellite-receiver links based on the joint PDF of S_4 on those links. However, on its own this provides no information about the navigational accuracy, nor the probability of a complete navigation outage. In this section, an approach is outlined which addresses these problems by assuming that the joint statistics of scintillation on multiple satellite-receiver links are known.

Consider a situation in which any n of m visible links have lost lock, and let i index the different ways in which this can occur. The probability of any one of these is denoted as \bar{P}_{n_i} and is given by (based on Equation (9.2-1))

$$\bar{P}_{n_i} = \int_0^1 \dots \int_0^1 \left[\prod_{k=1}^n P_{L_k}(\mathbf{T}'_k, S_{4_k}) \prod_{k=n+1}^m [1 - P_{L_k}(\mathbf{T}'_k, S_{4_k})] \right] \times f_{S_{4_1}, \dots, S_{4_m}}(S_{4_1}, \dots, S_{4_m}) dS_{4_1} \dots dS_{4_m} \quad (9.3-1)$$

If it is assumed that a navigation outage occurs when less than four satellites are tracking, and a RAIM² failure occurs when less than six are tracking, the probabilities of these two events are given by

$$P(\text{Navigation outage}) = \sum_{j=0}^3 \left[\sum_{i=1}^{\binom{m}{j}} \bar{P}_{(m-j)i} \right] \quad (9.3-2)$$

$$P(\text{RAIM outage}) = \sum_{j=0}^5 \left[\sum_{i=1}^{\binom{m}{j}} \bar{P}_{(m-j)i} \right]$$

where $\binom{m}{j} = \frac{m!}{(m-j)!j!}$ represents the number of different satellite-receiver combinations for which j of the m visible satellites are tracking, and $\bar{P}_{(m-j)i}$ are the probabilities associated with each possible satellite-receiver combination (ie. the i^{th} satellite combination for which $m-j$ satellite links have lost lock).

Unfortunately, Equation (9.3-2) cannot be evaluated as the joint PDF of S_4 is unknown. However, if it is assumed that the probability of losing lock on each satellite link is the same (and given by \bar{P}_L), then

$$\bar{P}_n = \bar{P}_L^n (1 - \bar{P}_L)^{m-n} \quad (9.3-3)$$

where $\bar{P}_n = \bar{P}_{ni}$ as all combinations associated with the loss of n satellites now have the same probability. In practice, this is an extremely unlikely situation given the inhomogeneous nature of the ionosphere and the vastly different satellite-receiver geometries on each link. Nevertheless, this assumption allows Equation (9.3-2) to be simplified and evaluated for a given value of \bar{P}_L . It also illustrates the sensitivity of Equation (9.3-2) to the number of satellites, m , and the single link probability of losing lock, \bar{P}_L . Under this assumption, Equation (9.3-2) simplifies to

² Receiver Autonomous Integrity Monitoring or RAIM is a technique whereby six or more satellite pseudorange measurements are cross-checked to determine their integrity. As RAIM is performed within a receiver, it eliminates the need for external integrity information. Although five satellites are required for fault detection, an additional satellite is needed for both the detection and exclusion of faults [47], page 313.

$$P(\text{Navigation outage}) = \sum_{j=0}^3 \left[\binom{m}{j} \bar{P}_L^{(m-j)} (1-\bar{P}_L)^j \right] \quad (9.3-4)$$

$$P(\text{RAIM outage}) = \sum_{j=0}^5 \left[\binom{m}{j} \bar{P}_L^{(m-j)} (1-\bar{P}_L)^j \right]$$

In Figure 9.3-1, the probability of a navigation outage and a RAIM outage are given for different values of \bar{P}_L and m based on Equation (9.3-4). Although these results must be treated with caution, they do show that a small increase in m , perhaps as a result of improved satellite visibility or the use of a supplementary navigation system such as GLONASS, will greatly reduce the risk of navigation or RAIM outages. They also shows that RAIM is far more vulnerable to failure than a loss of navigation.

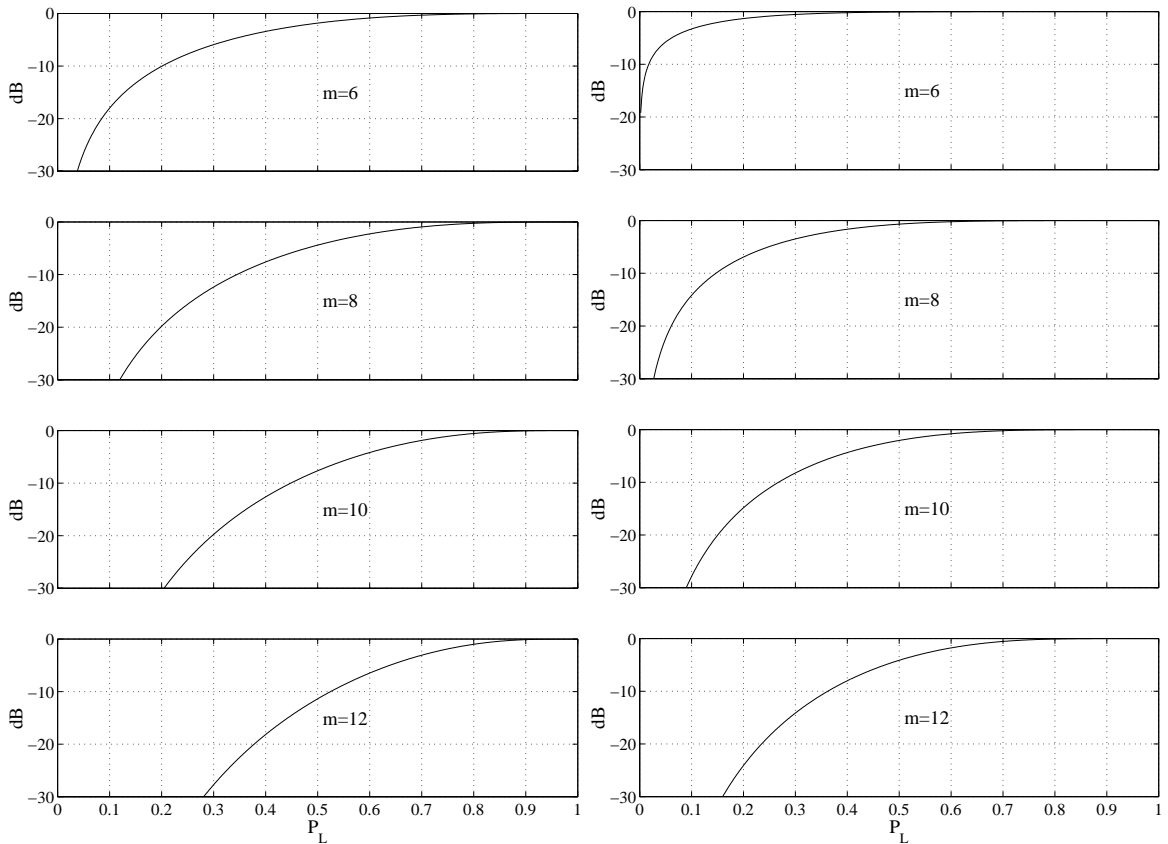


Figure 9.3-1: The probability of a navigation outage (left panel) and a RAIM outage (right panel) as a function of both the single link probability of losing lock, \bar{P}_L , and the number of visible satellites, m .

Although a navigation outage is very unlikely, it is still possible for scintillations to reduce navigational accuracy by degrading the satellite-receiver geometry. For example, if a receiver is located slightly to the North of the anomaly peak, it may lose several satellites towards the South in the direction of the anomaly. Consequently, the satellites available to the receiver will be skewed towards the North which will probably degrade the horizontal accuracy of the receiver in a North-South direction.

In order to assign probabilities to different levels of navigational accuracy, it is necessary to determine a DOP³ value for each satellite-receiver combination. If a probability is assigned to each satellite combination, \bar{P}_{n_i} , and a DOP value is assigned, DOP_{n_i} , the probability of the DOP exceeding some acceptable level, β , can be represented by

$$P(DOP > \beta) = \sum_{DOP_{n_i} > \beta} \bar{P}_{n_i} (DOP_{n_i}) \quad (9.3-5)$$

However, as this expression cannot be evaluated without a knowledge of the joint statistics of S_4 and T , it will not be considered any further.

³ The Dilution of Precision or DOP is a factor which converts the average pseudorange error into equivalent navigation and time errors by taking into account the geometry of the satellite constellation. DOP factors exist for horizontal position error, vertical position error, 3 dimensional position error, time error, and position and time error.

9.4.Predictions based on WBMOD

Although WBMOD does not provide information about the PDF of S_4 and T , or the joint statistics of scintillations on multiple satellite links, it does allow the scintillation stresses on individual links to be predicted for a given time, location and percentile. This enables areas to be identified within a broader region of interest in which significant scintillation effects may occur for a given receiver type. It also allows factors such as the sunspot number (SSN), the magnetic activity index (K_p), the carrier loop bandwidth, the quiescent signal level, and the elevation mask angle¹ etc. to be varied and the resulting impact on carrier loop performance to be examined. In Figure 9.4-1, the percentage of links above an elevation angle of 10° that may be stressed to the point of losing lock is plotted over an area that encompasses both the northern and southern anomalies in the South East Asia / Australian region. These plots were obtained by passing WBMOD's predictions of the scintillation indices, S_4 and T , into the carrier loop model from Section 3.4. For each satellite-receiver link, the tracking state was then found by comparing the predicted probability of losing lock, P_L (obtained from S_4 and T), with a 1% threshold. In this particular plot, the following parameter values were chosen:

Date:	23/09/2000 (the Sept. equinox nearest to the current solar maximum)
Time:	12:00 UTC (approximately 8:00pm local time at a longitude of 120°E)
Duration:	~ 20 minutes
Percentile:	90%
SSN:	135 (based on predictions for September 2000 obtained from the IPS ²)
K_p :	4.3 (a moderate level of geomagnetic activity)
Mask angle:	10°
C/N_o :	41.5 dBHz
B_n :	15 Hz

It is important to realise that this plot does not indicate the likelihood of simultaneous losses of lock, merely the number of links that may be stressed to the point of losing lock for a given percentile. Nevertheless, it could be said that if many links are stressed, and

¹ The elevation mask angle is the satellite elevation angle below which receiver measurements are ignored. It is primarily intended to reduce contamination of the navigation solution by multipath and thermal noise.

² IPS: the Australian Ionospheric Prediction Service.

the chosen percentile is relatively small, the probability of simultaneous losses of lock should become much larger.

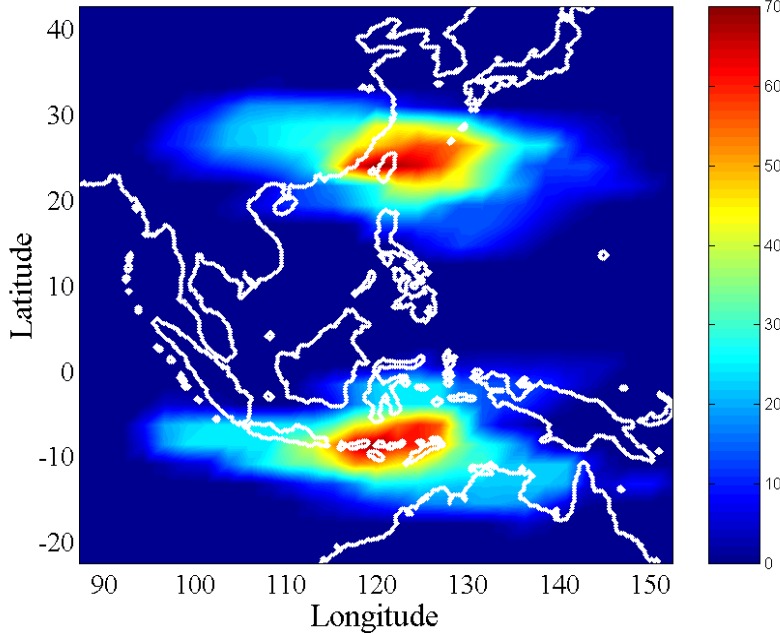


Figure 9.4-1: The percentage of links that may be stressed to the point of losing lock from WBMOD. Parameter values are: 23 Sept. 2000, 12:00 noon UTC, 90th percentile, SSN=135, $K_p = 4.3$, 10° elevation angle mask, $C/N_o = 41.5\text{dBHz}$, $B_n = 15\text{Hz}$, Loop order = 3, Coded L1 loop.

It is clear from Figure 9.4-1 that scintillations are only likely to be a problem between 6:00pm and 10:00pm local time³ and within the region of the anomaly. It is also apparent that directly beneath the anomaly crest at approximately 120°E (~ 8:00pm local time), the percentage of affected links increases to about 70%. However, care must be taken in drawing too many conclusions from this result as it only applies to WBMOD predictions at the 90th percentile and is based on the rather conservative threshold of 1% for P_L . Additional simulations (not shown) revealed that if the percentile was reduced to 65%, the percentage of links affected by scintillations dropped to zero at all times and locations. Therefore, based on WBMOD, it can be said that under the specified conditions, the probability of losing lock on any satellite-receiver link in the region would be less than 35%.

In Figure 9.4-2, the quiescent carrier to noise density ratio was raised to 44dBHz with all other parameters left unchanged. By comparing this with Figure 9.4-1, it is clear that the

³ Because of Earth rotation, 90°E and 150°E represent 6:00pm and 10:00pm local time respectively for a simulation time of 12:00 noon UTC.

signal to noise ratio has a significant influence on the tolerance of wide bandwidth receivers to scintillations. From Figure 3.4-3, it is apparent that this is because wide bandwidth receivers have a greater susceptibility to amplitude scintillations which are strongly influenced by the quiescent signal level (essentially, an increase in C/N_o will reduce the probability of the amplitude falling below the tracking threshold).

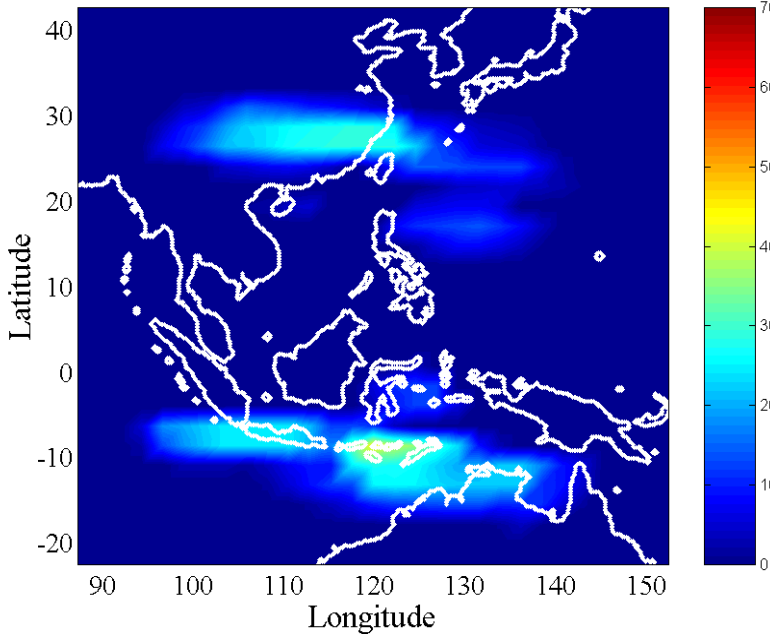


Figure 9.4-2: The percentage of links that may be stressed to the point of losing lock from WBMOD. Parameter values are: 23 Sept. 2000, 12:00 noon UTC, 90th percentile, SSN=135, $K_p = 4.3$, 10° elevation angle mask, $C/N_o = 44\text{dBHz}$, $B_n = 15\text{Hz}$, Loop order = 3, Coded L1 loop.

In Figure 9.4-3 and Figure 9.4-4, the predictions are repeated for a 2Hz bandwidth receiver for both $C/N_o = 41.5\text{dBHz}$ and 44dBHz respectively. It is clear from these figures that variations in the carrier to noise density ratio have much less of an effect on narrow bandwidth receivers than on wide bandwidth receivers. This suggests that the majority of the predicted outages in these figures are due to phase scintillations which are not influenced by the quiescent signal level. Again, this conclusion is consistent with Figure 3.4-3 for a narrow bandwidth receiver.

In the four figures presented so far, the elevation mask angle was set to 10°. In Figure 9.4-5, the effect of reducing the mask angle to 0° is examined. By comparing Figure 9.4-5 with Figure 9.4-1, it is apparent that a reduced mask angle increases the extent of the region affected by scintillations, but also reduces the impact of scintillations directly beneath the anomaly peak. This second effect is a result of an increase in the number of satellite-receiver links that are directed away from the anomaly peak when the additional

low elevation angle links are included (ie. directly beneath the anomaly peak, the low elevation angle links all point away from the peak and will therefore be largely unaffected by scintillations).

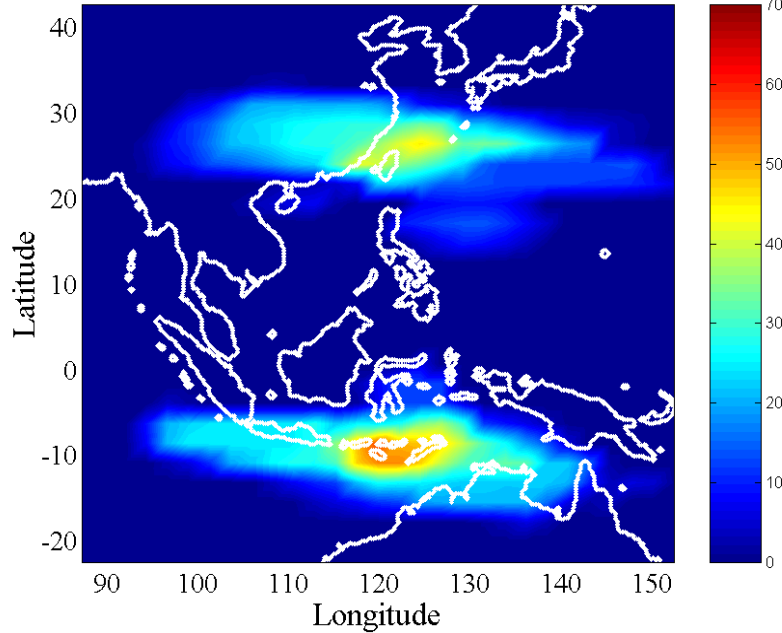


Figure 9.4-3: The percentage of links that may be stressed to the point of losing lock from WBMOD. Parameter values are: 23 Sept. 2000, 12:00 noon UTC, 90th percentile, SSN=135, $K_p = 4.3$, 10° elevation angle mask, $C/N_o = 41.5\text{dBHz}$, $B_n = 2\text{Hz}$, Loop order = 3, Coded L1 loop.

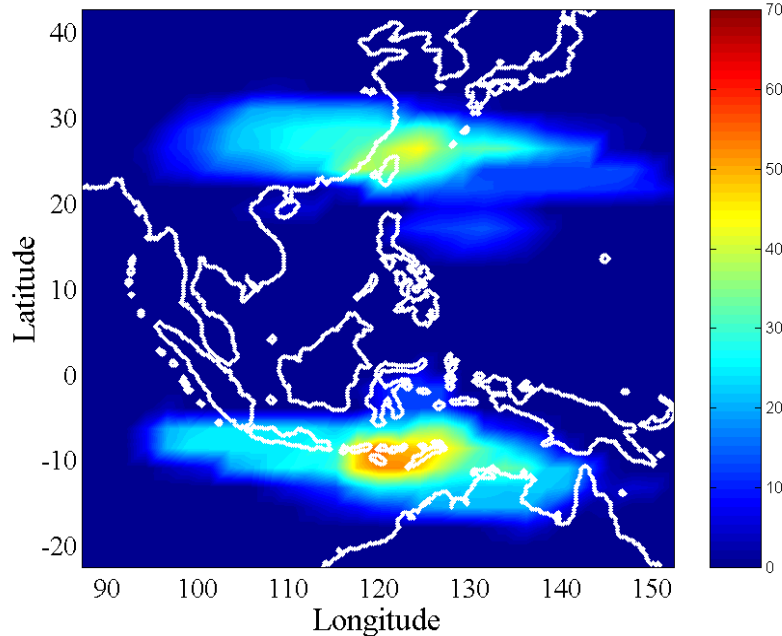


Figure 9.4-4: The percentage of links that may be stressed to the point of losing lock from WBMOD. Parameter values are: 23 Sept. 2000, 12:00 noon UTC, 90th percentile, SSN=135, $K_p = 4.3$, 10° elevation angle mask, $C/N_o = 44\text{dBHz}$, $B_n = 2\text{Hz}$, Loop order = 3, Coded L1 loop.

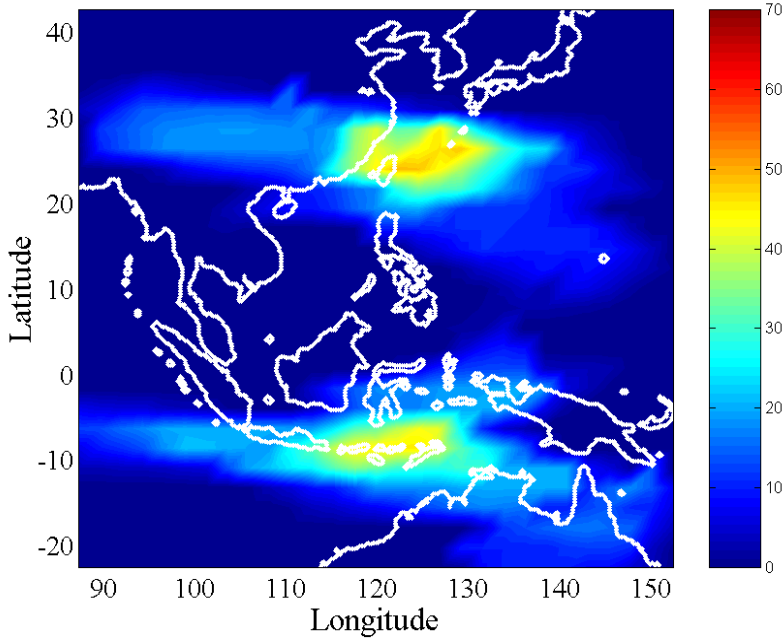


Figure 9.4-5: The percentage of links that may be stressed to the point of losing lock from WBMOD. Parameter values are: 23 Sept. 2000, 12:00 noon UTC, 90th percentile, SSN=135, $K_p = 4.3$, 0° elevation angle mask, $C/N_o = 41.5\text{dBHz}$, $B_n = 15\text{Hz}$, Loop order = 3, Coded L1 loop.

So far, all simulations have been conducted for the equinox of the 23rd September 2000. Simulations conducted under the conditions outlined in Figure 9.4-1 and Figure 9.4-3, but for days that were two months removed from the September and March equinoxes revealed no evidence of scintillation effects at all, even at a reduced signal level (30 dBHz). Also, simulations conducted on days that were one month removed from the equinoxes showed that scintillation effects were significantly reduced. An example of this is given in Figure 9.4-6 which is based on the 23rd October 2000 (all other parameters are the same as Figure 9.4-1). Therefore, according to WBMOD, it appears that receivers are unlikely to suffer any effects from scintillations beyond about one month from the equinoxes, even near solar maximum. Obviously, more simulations would need to be conducted in order to rigorously test this observation.

In Figure 9.4-7, the impact of reducing the sunspot number to 100 is given. Based on current predictions, this level of solar activity is unlikely to be reached until about October 2002. When the sunspot number was reduced to 70 (approximately August 2003), the observed effects were negligible, and when reduced further to 50 (approximately March 2004), no effects were observed at all under the specified conditions.

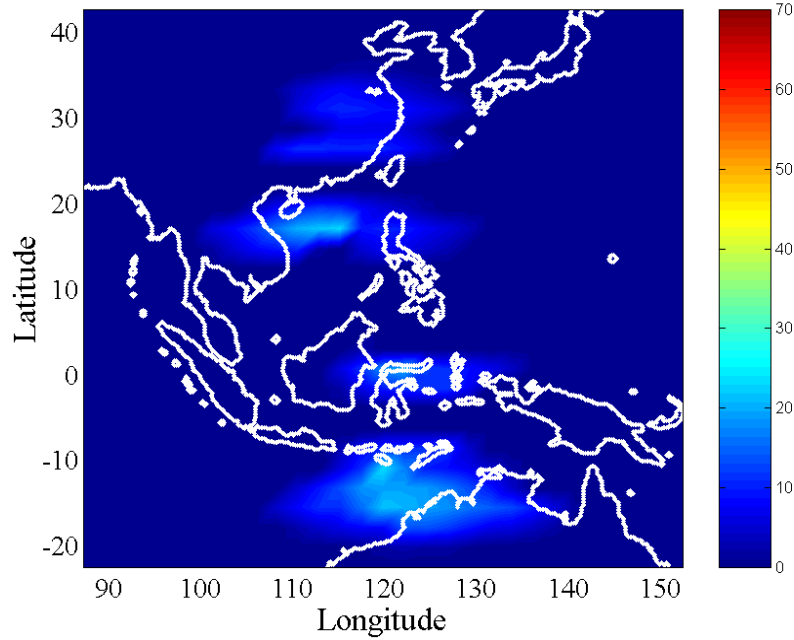


Figure 9.4-6: The percentage of links that may be stressed to the point of losing lock from WBMOD. Parameter values are: 23 Oct. 2000, 12:00 noon UTC, 90th percentile, SSN=135, $K_p = 4.3$, 10° elevation angle mask, $C/N_o = 41.5\text{dBHz}$, $B_n = 15\text{Hz}$, Loop order = 3, Coded L1 loop.

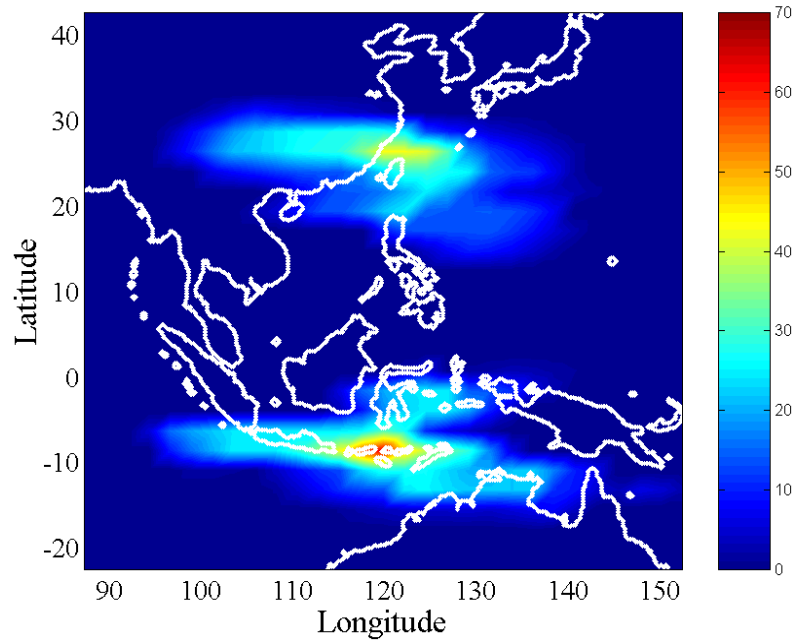


Figure 9.4-7: The percentage of links that may be stressed to the point of losing lock from WBMOD. Parameter values are: 23 Sept. 2000, 12:00 noon UTC, 90th percentile, SSN=100, $K_p = 4.3$, 10° elevation angle mask, $C/N_o = 41.5\text{dBHz}$, $B_n = 15\text{Hz}$, Loop order = 3, Coded L1 loop.

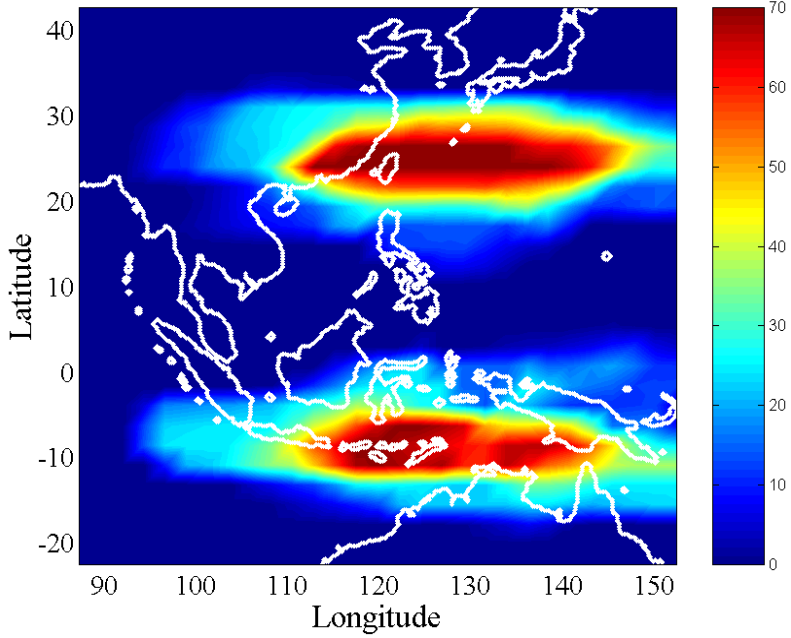


Figure 9.4-8: The percentage of links that may be stressed to the point of losing lock from WBMOD. Parameter values are: 23 Sept. 2000, 12:00 noon UTC, 90th percentile, SSN=135, $K_p = 4.3$, 10° elevation mask angle, $C/N_o = 41.5\text{dBHz}$, $B_n = 0.2\text{Hz}$, Loop order = 3, Semi-codeless L2 tracking loop.

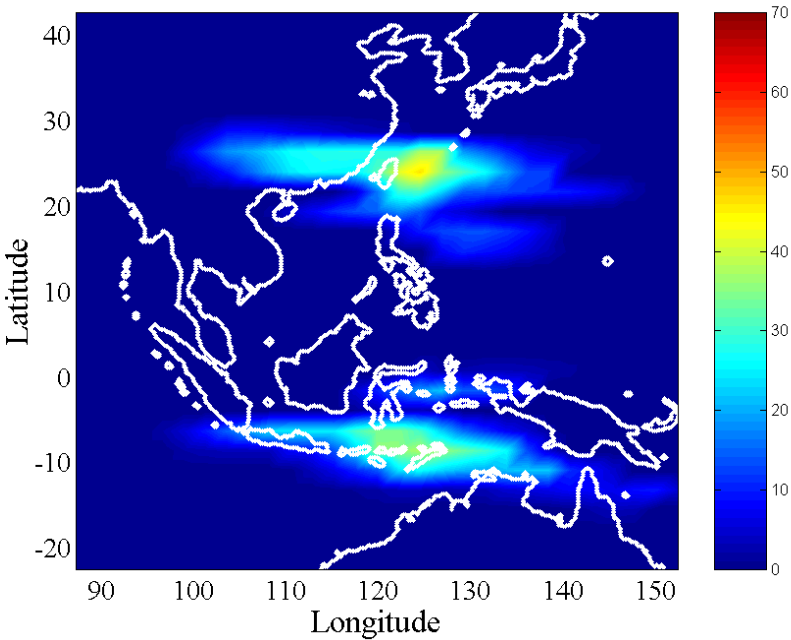


Figure 9.4-9: The percentage of links that may be stressed to the point of losing lock from WBMOD. Parameter values are: 23 Sept. 2000, 12:00 noon UTC, 65th percentile, SSN=135, $K_p = 4.3$, 10° elevation angle mask, $C/N_o = 41.5\text{dBHz}$, $B_n = 0.2\text{Hz}$, Loop order = 3, Semi-codeless L2 tracking loop.

In Figure 9.4-8, the effects of scintillations on a semi-codeless tracking loop of the sort discussed in Chapter 5 are given. By comparing this with Figure 9.4-1, it is clear that the predicted effects are much more severe than for a full correlation L1 tracking loop. Indeed, even at the 65th percentile, significant effects were observed on the semi-codeless tracking loops when virtually no effects were observed on a full correlation tracking loop (see Figure 9.4-9). Consequently, it would be expected that the probability of simultaneously losing two or more satellites would be much greater for the semi-codeless channels (the measurements reported in Section 5.3.1.1 for lower levels of solar activity tend to support this view).

9.5. Conclusions

WBMOD provides information from which the PDF's of the two principal scintillation indices, S_4 and T , can be deduced. Using these functions, it is possible to determine the average values of various receiver performance measures such as the variance of the code and carrier phase range errors, the probability of losing lock, the probability of a navigation data bit error, and the probability of detection for acquisition.

However, WBMOD is not well suited to predicting the performance of multiple channels simultaneously, and so cannot be used to determine the overall impact of scintillations on navigational accuracy. This is because it does not account for the large scale structures such as equatorial plumes which tend to restrict scintillation activity to certain parts of the sky. The statistics that are required from a scintillation model in order to determine navigational accuracy are the joint PDF's of S_4 and T on each of the propagation paths. Although this information is not available at present, it is clear that if scintillations are assumed to be independent between the individual propagation paths, the probability of losing lock simultaneously on multiple channels would be expected to be quite small, given that the individual probabilities are also quite small. Consequently, the probability of a navigation outage or a loss of RAIM is likely to be very small, even under conditions for which all links are affected by scintillations (ie. when the irregularities cover the entire sky).

Predictions of the percentage of links that may be stressed to the point of losing lock based on WBMOD clearly show that scintillation effects are mainly restricted to:

- Solar maximum (or at least high sunspot numbers).
- The equinox.
- Approximately 6:00pm to 10:00pm local time.
- The Northern and Southern anomalies.

However, even under these conditions, the probability of losing lock simultaneously on multiple links would be very small.

Chapter 10

Summary

In Section 10.1, a brief overview of the thesis is given and the main results from each chapter are summarised. In Section 10.2, conclusions are drawn about the overall performance of GPS in a scintillation environment by drawing together the results from all previous chapters. Finally, in Section 10.3, future research directions are examined including areas in which the scintillation model can be improved, and the potential impact of new developments in GPS on the susceptibility of GPS to scintillations.

10.1. Overview

In this thesis, a stochastic model of scintillation activity was combined with various receiver tracking and acquisition models to determine the likely impact of scintillations on GPS. A summary of the key points to come out of this work is given below:

- In general, the carrier tracking loops of full code correlation GPS receivers are quite robust to scintillations, even under very strong scintillation conditions.
- An optimum bandwidth exists for minimum probability of losing lock which depends on the relative contributions of amplitude and phase scintillation activity, as well as the quiescent signal level and the presence of dynamics.
- For a given level of ionospheric disturbance, the geometry of the propagation path affects the ratio of amplitude to phase scintillation activity as well as the absolute levels of scintillation activity. Therefore, geometry will affect both the optimum bandwidth of a tracking loop and its overall susceptibility to scintillations.
- Carrier tracking loops are generally very robust to signal fades of short duration, particularly if the bandwidth of the tracking loop is narrow.
- RMS carrier phase errors of several centimetres can be introduced into satellite range measurements by scintillations. These may have a significant impact on carrier phase DGPS observations made in equatorial regions during solar maximum, particularly for baselines of a kilometre or more.

- Frequency locked loops are more robust to phase scintillations but slightly less robust to amplitude scintillations than phase locked loops for the same loop bandwidth and pre-detection integration period. Therefore, receivers that make use of frequency locked loops, either as a primary means of carrier tracking or as a fall-back strategy to phase locked loops, are likely to be more tolerant to scintillations than receivers that employ only phase locked loops.
 - Phase scintillations have a negligible effect on code tracking loops and the additional thermal noise associated with amplitude scintillations is only small, unless S_4 is close to unity. Nevertheless, under strong amplitude scintillation conditions, it is likely that error spikes will exist in the code pseudorange measurements during times when the amplitude is deeply faded.
 - Codeless tracking loops are far more susceptible to the effects of scintillations than full code correlation tracking loops. The poor performance of codeless tracking loops may result in a degradation in the accuracy of systems such as WAAS which rely on dual frequency SPS receivers for the measurement of ionospheric delays.
 - Even under conditions for which the carrier loop is likely to lose lock, the probability of a word error in the navigation data will only be a few percent. Therefore, because of the high levels of redundancy that exist in the navigation data, it is expected that scintillations will have negligible effect on a receiver's ability to acquire the navigation information.
 - Scintillations increase acquisition times by reducing the probability of detection. For satellite signals which have a relatively low signal to noise ratio, the mean time to acquire may increase by a factor of two or more, and the RMS acquisition time by a factor of three, depending on the characteristics of the detector and the signal to noise ratio.
 - Wiener filter theory was used to determine the optimum structure of a phase locked loop that is subject to both scintillations and dynamics. It was found that in the absence of line of sight dynamics, the optimum loop order was determined by the slope of the phase scintillation power spectrum. However, in the presence of dynamics, the order of the dynamics would usually determine the optimum loop order. It was also found that the magnitude of the dynamics and the strength of amplitude scintillation activity would determine the optimum loop bandwidth, unless phase scintillation activity was very strong.
 - WBMOD provides information from which the probability of occurrence of scintillations at different levels can be determined for individual satellite-receiver propagation paths. This information can be used to determine average values for many of the receiver performance measures derived in earlier chapters. However, WBMOD is not
- 248

well suited to predicting the performance of multiple receiver channels simultaneously, and so cannot be used to determine the overall impact of scintillations on navigational accuracy.

- Although information about the joint statistics of scintillations on multiple propagation paths is not available, it is clear that if scintillations are assumed to be independent between the individual paths, the probability of losing lock simultaneously on multiple channels would be very small, given that the individual probabilities are also quite small.

10.2. Conclusions

The analysis carried out in this thesis suggests that equatorial scintillations will have a relatively minor effect on the navigation performance of stand-alone GPS receivers. This is partly because the patchy nature of scintillations introduces a degree of independence between the individual satellite-receiver links, and partly because the coverage of satellites in the equatorial region is generally very good. Consequently, the probability of simultaneously losing lock on enough satellites to significantly degrade the satellite geometry is relatively small. Also, on the satellite links that remain in lock, the additional noise introduced into the code tracking loops by amplitude scintillations is unlikely to contribute significantly to the overall pseudorange error. Data obtained from GPS receivers deployed throughout South East Asia during the past three equinoxes strongly supports this view.

However, if the visible constellation is reduced, either through an increase in the elevation mask angle or obscuration from nearby obstacles, fewer satellite losses would be required before navigational performance was significantly degraded. In addition, Receiver Autonomous Integrity Monitoring or RAIM requires at least six visible satellites in order to be effective. Consequently, under conditions of limited sky coverage, strong scintillation activity may degrade the performance of RAIM.

The combination of conditions under which a receiver is likely to experience the greatest stresses from equatorial scintillations are as follows:

- High solar activity.
- Low geomagnetic activity.
- During the months of the equinoxes (March/April and September/October).
- For several hours following local sunset.

- Within bands approximately 15° wide and centred on the crests of the northern and southern anomalies.

However, simulations based on WBMOD reveal that scintillation effects may extend well beyond the nominal northern and southern boundaries of the anomaly. This is caused by a few satellite-receiver links penetrating the peak of the anomaly at low elevation angles, even when the receiver is well removed from the region of the anomaly. Consequently, areas of Northern Australia that are generally considered to be south of the southern anomaly may still be affected by scintillations on certain low elevation angle links. In addition, plume structures are known to reach enormous heights near the equator and may extend the influence of scintillations well beyond that predicted by WBMOD (the WBMOD model assumes that all irregularities are concentrated at height that is typical of the F2-layer peak height).

The analysis carried out in Chapters 3 and 9 suggests that narrow bandwidth receivers, such as those used in tightly coupled GPS-INS systems, are more susceptible to the effects of phase scintillations than wide bandwidth receivers. Consequently, narrow bandwidth receivers are more sensitive to factors that influence the phase scintillation rate such as receiver dynamics. Wide bandwidth receivers, on the other hand, are more susceptible to the effects of amplitude scintillations and thermal noise, and so are affected more by factors that influence the signal to noise ratio such as the antenna gain pattern and electromagnetic interference (EMI).

Most military and some civilian aircraft are likely to be fitted with tightly coupled GPS-INS systems to improve their immunity to EMI and high dynamics. Although the GPS receivers in such systems will adopt a narrow bandwidth and so will become more susceptible to phase scintillations, the INS units will be unaffected by scintillations and so will continue to provide a navigation solution during any scintillation induced GPS outages. This will also help the GPS receiver to recover when the scintillation activity has eventually passed. It is also likely that the high velocities of jet aircraft will allow the satellite-receiver links to pass through the scintillation patches much more rapidly. Again, the reduced dwell time within the patches will help to mitigate their effects on GPS.

It should also be mentioned that under high velocity conditions, the amplitude scintillation rate will increase on many satellite links causing the assumption $B_n > f_c$ ¹ to be violated (ie. the duration of deep fades will be reduced on many links). This is likely to reduce the impact of amplitude scintillations somewhat, particularly for narrow bandwidth receivers for which B_n is already quite small. However, as phase scintillations are likely to be the principal factor causing loss of lock at high receiver velocities, this effect may be negligible in terms of the number of satellites lost.

Although the higher chipping rate of the P-Code offers P(Y)-Code receivers greater resistance to interference, it does not afford them any protection against scintillations. Indeed, the lower power levels of the P(Y)-Code tends to make P(Y)-Code receivers slightly more susceptible to the effects of amplitude scintillations. Added to this is the higher level of scintillation activity on the L2 frequency as a result of the inverse frequency scaling of scintillations. However, military P(Y)-Code receivers are likely to be designed and constructed much better than civilian receivers, which may give them superior performance under conditions of reduced signal level (ie. in the presence of amplitude scintillations).

Codeless and semi-codeless tracking loops are considerably more susceptible to the effects of scintillations than full correlation tracking loops. The very narrow bandwidths of codeless tracking loops increases their susceptibility to phase scintillations, despite a reduction in phase scintillation energy through carrier aiding from the L1 C/A-Code carrier loops. Similarly, the reduced signal to noise ratio of codeless channels greatly increases their susceptibility to amplitude scintillations, despite their very narrow loop bandwidths. Therefore, it seems likely that systems which rely on codeless and semi-codeless receivers such as the Wide Area Augmentation System (WAAS) may suffer very adverse effects under strong scintillation conditions. However, by the time these systems are actually operational, the expectation is that the second civil signal on the L2 frequency will be available which will mitigate the need for codeless and semi-codeless processing.

RMS carrier phase errors of several centimetres can be introduced onto individual satellite-receiver links by phase scintillations. Generally, these errors will become decorrelated over distances of a few km, depending upon the ionospheric outer scale size

¹ Where B_n is the loop bandwidth and f_c is the cutoff frequency of the amplitude scintillation power spectrum.

parameter, f_o , and the direction of the baseline. This may have a significant impact on carrier phase DGPS measurements taken in equatorial regions during solar maximum. Unfortunately, the modelling of f_o in WBMOD is very primitive at this stage.

Under very intense scintillation conditions, the mean time to acquire the GPS signal may increase by a factor of two or more, although only when the carrier to noise density ratio of the GPS signal is at a reduced level. However, under these conditions it is uncertain whether a channel will have the ability to transition to a stable tracking state anyway. Nevertheless, as only a few of the satellites in a receiver's field of view are likely to be subject to such high levels of activity, even during solar maximum, this effect is not expected to be overly important.

The impact of scintillations on the navigation data also appears to be negligible. It is likely that a tracking loop will lose lock or become unreliable well before navigation data demodulation errors become significant. Indeed, much of the navigation data is repeated on each satellite-receiver link and the update rate required from such information is relatively low anyway.

The performance measures discussed in this thesis have been based on a number of assumptions and approximations, some of which have already been discussed. However, other sources of loop stress such as oscillator phase noise, multipath, foliage attenuation, obscuration, antenna gain pattern variations, the elevation angle dependence of C/N_o , and EMI etc. have largely been ignored. Each of these effects is likely to reduce a receiver's tolerance to the effects of scintillations.

10.3. Further research

Research into the effects of ionospheric scintillations on GPS is by no means complete. Possible areas for further research include:

1. *Determining the joint statistics of scintillations on multiple satellite links.* Data obtained from scintillation monitoring receivers located in equatorial regions could be used to determine the correlation between scintillation activity on different satellite-receiver links. Factors that may influence this correlation include the separation between individual ionospheric pierce points (IPPs), the location and local solar time

at the IPPs, and other factors that affect the overall levels of scintillation activity such as the sunspot number and the magnetic activity index.

2. *The correlation between signal amplitude and the strength of phase scintillations.* If the amplitude is negatively correlated to the rate of change of the carrier phase (ie. the rate of change of carrier phase increases when the amplitude decreases), then the combined effects of amplitude and phase scintillations on GPS may be more severe than is predicted in this thesis.
3. *The impact of highly dense ionospheric structures, or plasma lenses, on the performance of GPS receivers.* Structures of this sort produce refractive focusing and de-focusing effects which can alter the statistics of scintillations and drive S_4 values well above one. Predicting the occurrence of lenses and developing models of the resulting signal statistics at L-band frequencies are two areas that could be looked at further. In [56], the effects of a collection of discrete, Gaussian shaped ionospheric lenses on the performance of carrier tracking loops was investigated using the diffraction model from Appendix A and the tracking loop simulator from Appendix B. However, an analytical approach to this problem has yet to be developed. Also, it has not been established whether naturally occurring ionospheric lenses will have a sufficiently short focal length at L-band frequencies to cause significant scintillation effects for GPS.
4. *The development of a model to account for the non-stationary nature of scintillations.* In this thesis, it has been assumed that scintillations can be described by wide-sense stationary random processes. However, scintillations tend to occur in patches, the duration of which will depend on the dimensions of the irregularity patch and the speed with which the satellite-receiver ray path scans through the patches. Also, statistics such as S_4 and T may change with time as the ray path scans through a particular patch. Models that account for the resulting non-stationarity will not only help with the analysis of single link performance, but will also assist in the development of models of the joint statistics of scintillations on multiple satellite links.
5. *The validation and extension of models such as WBMOD and SCINDA for the South East Asia / Australian region.* The WBMOD and SCINDA models are based largely on data obtained from the American longitude sector. Consequently, it is necessary to determine whether these models also apply to the South East Asia / Australian region by analysing scintillation data obtained from this region. DSTO in conjunction with

the AFRL², LAPAN³, and DSTC⁴ have deployed a network of ionospheric scintillation monitoring receivers in Indonesia, Malaysia and Papua & New Guinea to measure scintillations and to compare their occurrence statistics with models such as WBMOD (see for example [57], [22]). The data obtained from these sites is also being used to investigate the probability of scintillation activity occurring simultaneously on multiple satellite links.

6. *The validation of analytical results against hardware simulations.* For the past few years, various groups within the United States⁵ have been investigating the effects of simulated scintillation data on real GPS receivers by appropriately modulating the signals produced by satellite signal simulators. However, these tests have yet to include the effects of high receiver velocities, inertial aiding, and EM interference on receivers that are subject to scintillations.
7. *Accounting for new developments in GPS,* including:
 - Alternative tracking and acquisition architectures.
 - The use of beamforming antennas. Antennas that are capable of steering beams towards the GPS satellites will gain a significant advantage under amplitude scintillation conditions as a result of an increase in the signal to noise ratio. Antennas of this sort are already in existence (eg. the Navsys Corporation High gain Advanced GPS Receiver or HAGR™ [18]).
 - The introduction of a second civil signal at 1176.45 MHz (referred to as the L5 signal), the new military code or M-Code signals, the addition of a C/A-Code signal at the L2 frequency, and a general increase in satellite signal power levels following the launch of the modified block IIR and new generation block IIF satellites. Under the current launch schedule, it is anticipated that the constellation will consist primarily of block IIF and the proposed new block III satellites by the time the next solar maximum occurs in 2011.
 - Increased satellite coverage through the use of supplementary satellite navigation systems such as the Russian GLONASS system, the European Geostationary Navigation Overlay System (EGNOS), and the proposed European Galileo system.

² AFRL: The Air Force Research Laboratory, USA.

³ LAPAN: The Ionospheric Research and Development Centre, Indonesia.

⁴ DSTC: The Defence Science and Technology Centre, Malaysia.

⁵ The GPS & Navigation Systems division of the SPAWAR Systems Center in San Diego, and the Air Force Research Laboratory and Wright Patterson Laboratory, AFRL and WPL, in Cambridge Massachusetts and Dayton Ohio respectively.

Appendix A

Scintillation model

The scintillation model used in this study is essentially that of Titheridge [89] and Davies [28] and is based on the solution of the Fresnel-Kirchoff integrals for an assembly of field aligned irregularities. The irregularities are assumed to produce variations in TEC in directions normal to the earth's magnetic field lines, but no variations along the field lines. For convenience, the phase perturbations are assumed to be concentrated within a thin phase screen located at a typical F2 layer peak height. In reality, such perturbations would result from the cumulative effect of numerous small irregularities located along the ray path.

A.1 Deterministic phase screen

The deterministic model, which is essentially that described by Titheridge and Davies, assumes that the irregularities are discrete rod like lenses which are aligned with the Earth's magnetic field and produce Gaussian phase perturbations normal to the field. The phase perturbation produced by k such lenses is given by

$$\Phi(x) = \sum_{i=1}^k \Phi_{0i} \cdot \exp\left[\frac{-(x - x_{0i})^2}{l_i^2}\right] \quad (A-1)$$

where x is the horizontal position in a direction normal to the Earth's magnetic field lines (ie. in an East-West direction), and Φ_{0i} , l_i , and x_{0i} are the peak phase variations, scale sizes, and centres of the irregularities respectively. The peak phase variations, Φ_{0i} , are related to the peak TEC variations, ΔTEC_{0i} , through the expression (Davies [27])

$$\Phi_{0i} = 40.3 * 2\pi \frac{\Delta TEC_{0i}}{cf} \quad (\text{radians}) \quad (A-2)$$

where f is the GPS carrier frequency and c is the speed of light. If it is assumed that the variations in plasma density are Gaussian in both the x and y (vertical) directions, ΔTEC_{0i} can be found as a function of the scale sizes and peak density variations. The variation in

plasma density over the background is given by¹

$$\Delta N(x, y) = \Delta N_0 \exp \left[-\frac{(x - x_0)^2}{l_x^2} - \frac{(y - y_0)^2}{l_y^2} \right] \quad (A-3)$$

where ΔN_0 is the peak density variation. As TEC is the vertical integral of the electron density,

$$\begin{aligned} \Delta TEC(x) &= \int_{-\infty}^{\infty} \Delta N(x, y) dy \\ &= \Delta N_0 l_y \sqrt{\pi} \exp \left[-\frac{(x - x_0)^2}{l_x^2} \right] \end{aligned} \quad (A-4)$$

The peak TEC variation is therefore

$$\Delta TEC_0 = \Delta N_0 l_y \sqrt{\pi} \quad (A-5)$$

ΔN_0 can then be defined as a fraction, p , of the background electron density, N_b , as follows

$$\Delta N_0 = p N_b, \quad p \geq -1 \quad (A-6)$$

An additional constraint which can be applied in order to establish a relationship between the scale sizes, l_x and l_y , and ΔN_0 is the maximum permissible electron density gradient, N_{gm} . From Equation (A-3), the maximum density gradients in both the x and y directions are

$$\left. \frac{\partial \Delta N}{\partial x} \right|_{\max} = \frac{\Delta N_0 \sqrt{2/e}}{l_x}, \quad y=y_0 \quad (A-7)$$

$$\left. \frac{\partial \Delta N}{\partial y} \right|_{\max} = \frac{\Delta N_0 \sqrt{2/e}}{l_y}, \quad x=x_0 \quad (A-8)$$

The maximum peak density variation which will ensure that N_{gm} is not exceeded is then

¹ This assumes that the density profile is symmetrical in both the x (horizontal) and y (vertical) planes.

$$\Delta N_0 = \min(l_x, l_y) \cdot N_{gm} \sqrt{e/2} \quad (A-9)$$

By combining Equations (A-1), (A-2), (A-5), (A-6) and (A-8), an irregularity layer can be defined once values for N_b and N_{gm} are assigned. If it is assumed that the irregularities are located at the F2 layer peak, N_b will be equal to the peak density of the F2 layer, NmF2.

The peak phase variations can either be positive, which corresponds to an enhancement in TEC (a defocusing type irregularity), or negative which corresponds to a depletion in TEC (a focusing type irregularity). Both types of irregularity have been shown to exist in the ionosphere [90]. The radio wave is also assumed to experience no attenuation as it passes through the phase screen. Consequently, any amplitude fluctuations are caused entirely by the effects of interference across the wavefront as it propagate towards the ground.

At the ground, and relative to the undisturbed wave, the in-phase, I , and quadrature, Q , components of a vertically propagating plane wave² can be found by solving the Fresnel-Kirchoff integrals (see for example [89] & [28]). This results in the following two terms

$$I = 1 - 2 \int_{ir} \sin(P_o + \Phi/2) \sin(\Phi/2) dx / \sqrt{r\lambda} \quad (A-10)$$

$$Q = 2 \int_{ir} \cos(P_o + \Phi/2) \sin(\Phi/2) dx / \sqrt{r\lambda} \quad (A-11)$$

where $\Phi = \Phi(x)$, $P_o = -\pi/4 - 2\pi(r-h)/\lambda$, h is the screen height and r joins the elements dx on the phase screen to a point on the ground (see Figure A-1). As these two integrals contain a $\sin(\Phi/2)$ term which approaches zero when the emergent wave is unperturbed, the integrals need only be calculated over the region of the irregularities in the plane of the phase screen. This region is denoted as ir .

² In this analysis it is assumed that the GPS satellites are at sufficiently high altitudes to make the simplifying assumption that the all incident waves are plane waves.

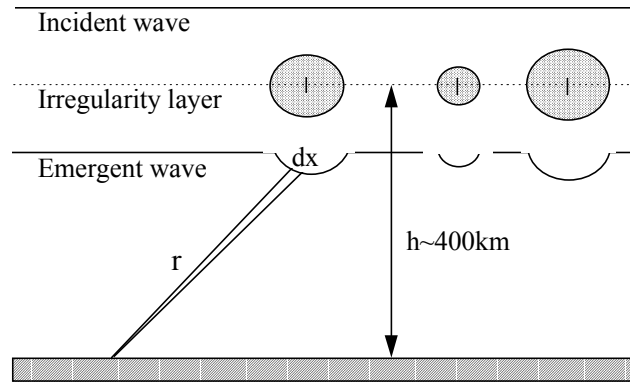


Figure A-1: Geometry of the thin phase screen diffraction model.

The resulting phase and amplitude variations are obtained from the I and Q components as follows

$$\begin{aligned} \text{Phase} &= \text{Atan}(Q/I) \\ \text{Amplitude} &= \sqrt{Q^2 + I^2} \end{aligned} \quad (A-12)$$

For irregularities much larger than the first Fresnel zone radius, z_F , diffraction effects are minimal and a geometric optics solution can be employed. As a result, phase variations on the ground will closely resemble those in the ionosphere and amplitude variations will be negligible. On the other hand, for scale sizes of the order of the Fresnel zone radius or smaller, or for very large plasma density gradients, rapid variations in both amplitude and phase will occur. Irregularities smaller than z_F produce diffraction effects, whereas those containing large density gradients produce significant refraction and hence interference effects. Both cause rapid variations in the amplitude and phase of the GPS signals on the ground. For a Gaussian shaped irregularity, the threshold conditions for diffraction and interference are (from [89])

$$\text{Diffraction: } l < z_F = \sqrt{\frac{\lambda z_1 z_2}{z_1 + z_2}} \approx \sqrt{\lambda z_2} \quad (A-13)$$

$$\text{Interference: } l < \sqrt{\frac{\Phi_0 h}{37 f}} \quad (A-14)$$

where Φ_0 is the peak phase variation, z_1 and z_2 are the distances between the ionospheric irregularity layer and the satellite and receiver respectively. Typical upper limits on the scale sizes of irregularities which are likely to produce these effects are

<i>Diffraction:</i>	300m (L2), 275m (L1)
<i>Interference:</i>	220m (L2), 190m (L1)

where it has been assumed that $h_i = 400\text{km}$ and $\Delta TEC_0 = 1 \text{TECu}$ (approximately 1% of a typical equatorial TEC value during solar maximum). This analysis also assumes that the irregularities are directly overhead and that propagation is vertical. For E-region irregularities ($h \sim 100 \text{ km}$), the equivalent dimensions are approximately one half.

It is expected that irregularities of the order of the Fresnel Zone radius or slightly smaller will produce the most significant scintillation effects. Larger irregularities are unlikely to produce fully developed diffraction effects and would require very large peak densities in order to produce significant interference effects. Irregularities much smaller than the Fresnel zone radius will produce prolific diffraction effects, but with very small peak phase variations. Examples of the effects of different scale sizes on the amplitude and phase diffraction patterns is given in Section 2.1.5.

The phase and amplitude fluctuations derived from this model are a function of position in an East-West direction. Because the irregularities are assumed to be field aligned, fluctuations do not exist in a North-South direction. Consequently, the temporal variations in phase and amplitude experienced by a GPS receiver will depend on the East-West component of the irregularity velocity, the GPS platform velocity and the satellite velocity. These velocity components are encapsulated in the effective scan velocity, v_e , which was discussed in Section 2.1.3.

A.2 Random phase screen

A more realistic model for the phase screen based on in-situ measurements³ of electron density fluctuations is the power law phase screen model. This model assumes that the phase perturbations on the emergent wave are random with a Gaussian distribution and a power law wavenumber power spectrum which is given by

$$S_\Phi(k) = A \left(k_o^2 + k^2 \right)^{-p/2} \quad (\text{A-15})$$

where k is the wavenumber, A determines the strength of scintillation activity, $k_o = 2\pi/l_o \text{ m}^{-1}$ is an outer scale wavenumber, l_o is the outer scale size, and p is the

³ In-situ measurements of electron density are made with probes flown on rockets and satellites.

spectral index. The in-situ wavenumber power spectrum of phase (or equivalently of TEC) has the same spectral index as the power spectrum of scintillations measured on the ground ([16] and [49]). Consequently, p is in the range 1 to 4 and is typically 2.5 at equatorial latitudes.

Realisations of a random phase screen $\Phi(x)$ with the desired spectral characteristics can be obtained from an N^{th} order Autoregressive (AR) process of the form

$$\Phi(nX) = w(nX) + \sum_{i=1}^N h_i \Phi([n-i]X) \quad (A-16)$$

where n is an integer, X represents the spacing between successive points on the phase screen, $w(nX)$ is a white Gaussian noise process and h_i are the coefficients of the AR model. Equation (A-16) can be rearranged as follows

$$\Phi(nX) - \sum_{i=1}^N h_i \Phi([n-i]X) = w(nX) \quad (A-17)$$

Multiplying (A-17) through by $\Phi(nX)$ and taking the expectation gives

$$r_0 - \sum_{i=1}^N h_i r_i = \sigma_w^2 \quad (A-18)$$

where $r_j = R_\Phi(jX)$ is the Autocorrelation function of phase at a separation of jX m and σ_w^2 is the variance of the white noise process. In a similar way, multiplying through by $\Phi([n-1]X)$ and taking the expectation gives

$$r_1 - \sum_{i=1}^N h_i r_{i-1} = 0 \quad (A-19)$$

By repeating this process $N+1$ times, the following matrix expression can be obtained

$$\begin{bmatrix} r_0 & r_1 & \cdots & r_N \\ r_1 & r_0 & & \vdots \\ \vdots & & \ddots & \vdots \\ r_N & \cdots & \cdots & r_0 \end{bmatrix} \begin{bmatrix} 1 \\ -h_1 \\ \vdots \\ -h_N \end{bmatrix} = \sigma_w^2 \begin{bmatrix} 1 \\ 0 \\ \vdots \\ 0 \end{bmatrix} \quad (A-20)$$

which can also be expressed as

$$P \cdot \bar{h} = \sigma_w^2 \bar{\delta} \quad (A-21)$$

The coefficients of the AR model are therefore

$$\bar{h} = \sigma_w^2 \cdot P^{-1} \cdot \bar{\delta} \quad (A-22)$$

Consequently, in order to determine \bar{h} , the autocorrelation function of phase $R_\Phi(x)$ must be found. As the wavenumber power spectrum of phase is an even function, $R_\Phi(x)$ is given by

$$\begin{aligned} R_\Phi(x) &= \int_{-\infty}^{\infty} S_\Phi(k) \cdot e^{j k x} \cdot dk \\ &= 2 \int_0^{\infty} S_\Phi(k) \cdot \cos(kx) \cdot dk \end{aligned} \quad (A-23)$$

Substituting (A-15) into (A-23) gives

$$R_\Phi(x) = 2A \int_0^{\infty} \frac{\cos(kx)}{(k_o^2 + k^2)^{p/2}} \cdot dk \quad (A-24)$$

This is a general expression for the autocorrelation function of phase for a power law wavenumber power spectrum. Unfortunately, it is difficult to solve in closed form for arbitrary p . Consequently, numerical techniques must be used in order to determine $R_\Phi(x)$ and P^{-1} for any p .

However, for the special case of $p=2$, the following simple solution for $R_\Phi(x)$ can be obtained from a table of integrals

$$\begin{aligned} R_\Phi(x) &= 2A \int_0^{\infty} \frac{\cos(kx)}{k_o^2 + k^2} \cdot dk \\ &= \frac{A\pi}{k_o} e^{-k_o x} \end{aligned} \quad (A-25)$$

Giving

$$P = \frac{A\pi}{k_o} \begin{bmatrix} 1 & e^{-k_o X} & \dots & e^{-Nk_o X} \\ e^{-k_o X} & 1 & & \vdots \\ \vdots & & \ddots & \vdots \\ e^{-Nk_o X} & \dots & \dots & 1 \end{bmatrix} \quad (A-26)$$

Substituting (A-26) into (A-22) and solving for the AR coefficients gives $h_1 = e^{-k_o X}$ and $h_2 \cdots h_N = 0$. Therefore, for $p=2$ a first order AR process will generate suitable realisations, *viz*

$$\Phi(nX) = w(nX) + \Phi([n-1]X) \cdot e^{-k_o X} \quad (A-27)$$

An example of simulated scintillation data obtained from the Fresnel-Kirchoff diffraction model using the AR process from Equation (A-27) is given in Figure A-2. Parameter values for the AR process are $l_o = 1\text{km}$ (outer scale size), $X = 1\text{m}$ (step size), and $h_i = 400\text{km}$ (ionospheric height). In addition, it was assumed that the velocity of the propagation path normal to the receiver was 150m/s and that the L1 frequency was being used. Consequently, for this example, the AR process is of the form

$$\Phi(nX) = w(nX) + 0.994\Phi([n-1]X) \quad (A-28)$$

where $w(nX)$ is assumed to have a variance of 0.0025 radians².

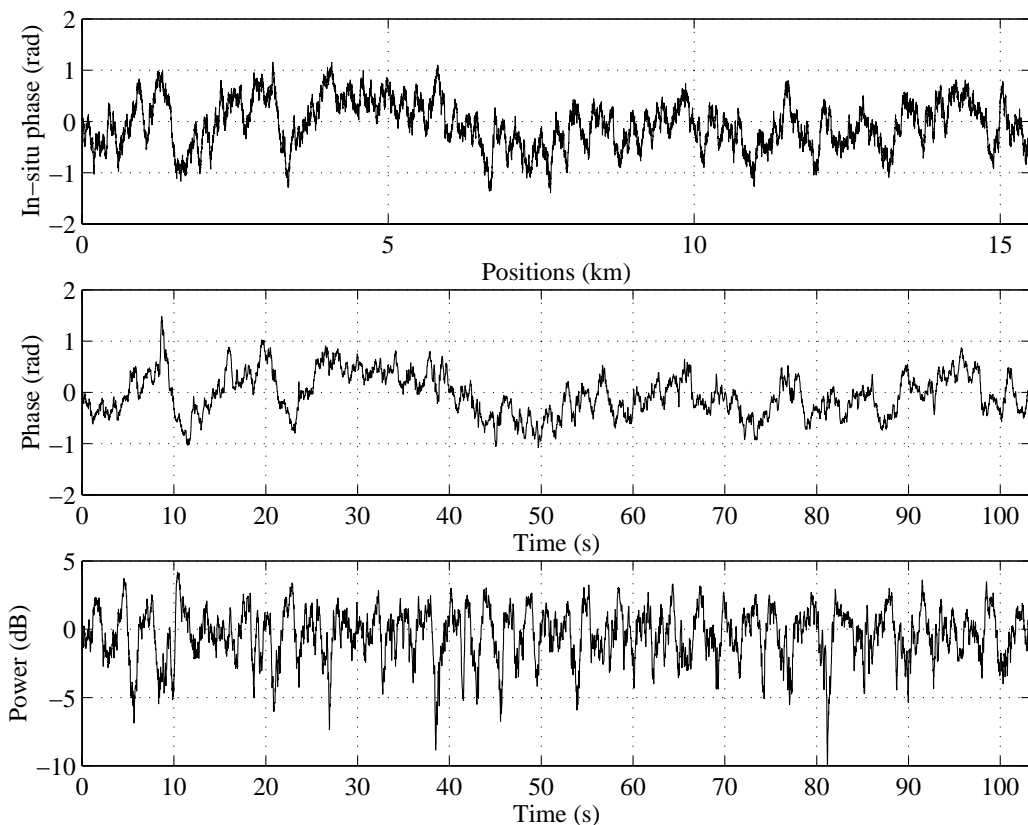


Figure A-2: A sample realisation of the In-situ phase (upper panel), phase scintillations (middle panel), and amplitude scintillations (lower panel) obtained from the Fresnel-Kirchoff diffraction model.

Notice that the phase process at the receiver (middle panel) bears only a vague resemblance to the in-situ phase process (upper panel). For much larger in-situ phase gradients, the two phase processes would become even more different. The RMS phase and S_4 values for this particular example are 0.41 radians and 0.39 respectively. These were obtained by averaging numerous different realisations based on Equation (A-28) and the phase screen model.

Appendix B

GPS tracking loop simulators

In this thesis, software simulations of GPS receiver code and carrier tracking loops are used to validate analytical results and to determine where the analytical results begin to fail. The advantage of simulation over a purely analytical approach is that it allows the loop non-linearities to be taken into account without the need to introduce any approximations. These non-linearities include the discriminator, the I and Q channel mixers and the code correlators. Although the majority of the work described in this thesis is based on stand-alone code and carrier tracking loops, the behaviour of a combined code and carrier tracking loop channel can be investigated relatively easily through the simulation approach described here.

The tracking loop simulators are based on Simulink™ for Matlab™ and are driven by amplitude and phase scintillation data produced by the model described in Appendix A. Simulink™ diagrams of a stand-alone Costas carrier tracking loop and a delay locked loop are given in Figures B-1 and B-2. An equivalent diagram of a combined tracking loop is given in Figure B-3. In all cases, the simulated scintillation data is stored in amplitude and phase lookup tables and is extracted at a rate which depends on the value of v_e chosen for the simulation.

For the Costas loop simulator, it is assumed that the prompt code estimate is perfectly aligned with the satellite code (ie. $\tau_e = 0$) and is therefore removed completely from the GPS signal. It is also assumed that the pre-detection filters are correctly synchronised to the navigation data. Similarly, for the delay locked loop it is assumed that the carrier phase error is negligible (ie. $\phi_e = 0$) and so the Q channel consists only of thermal noise (ie. $A_p(t)\sin(\phi_e) + n_Q \approx n_Q$). In the combined simulator, the code and carrier phase errors affect both tracking loops. In addition, because of the dispersive nature of scintillations, the effects of phase scintillations on the code delay is assumed to be equal in magnitude but opposite in sign to the effect on the carrier phase.

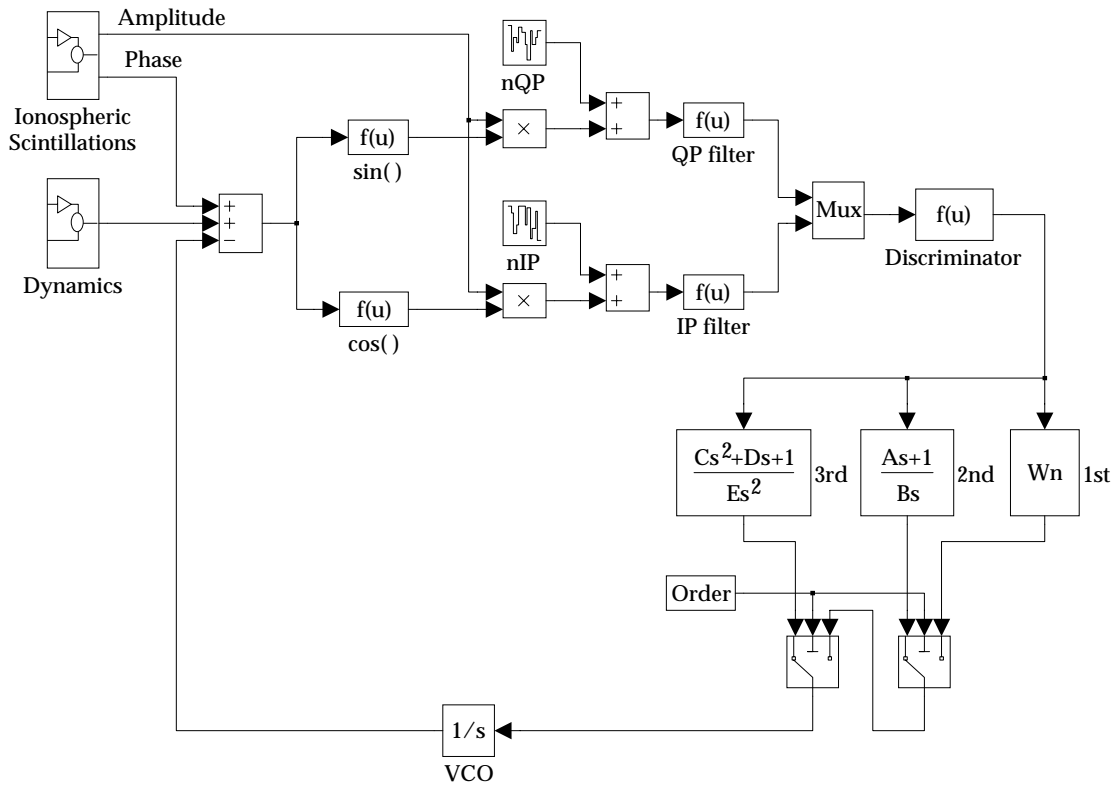


Figure B-1: Simulink™ model of a Costas phase locked loop.

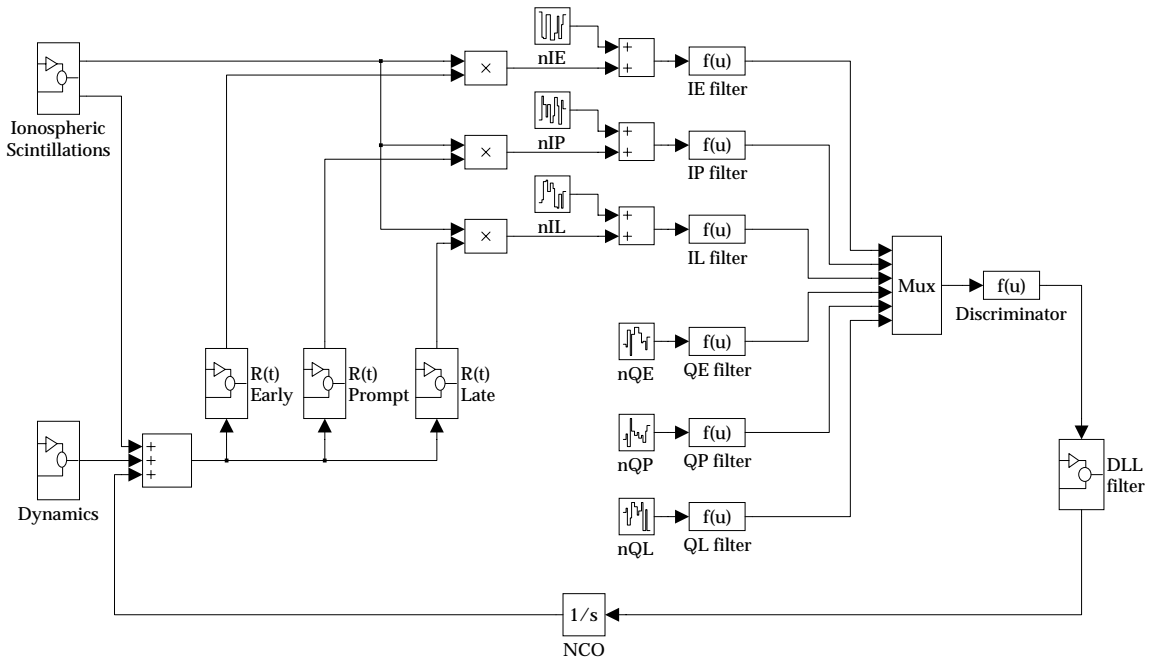


Figure B-2: Simulink™ model of a delay locked loop.

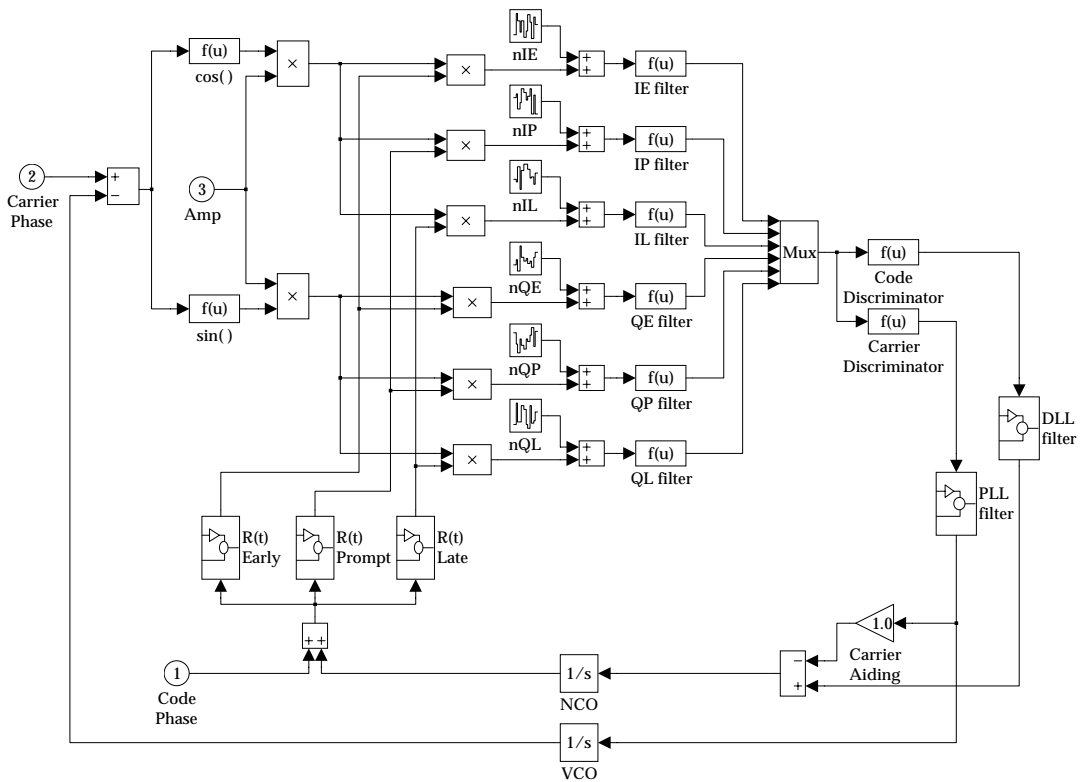
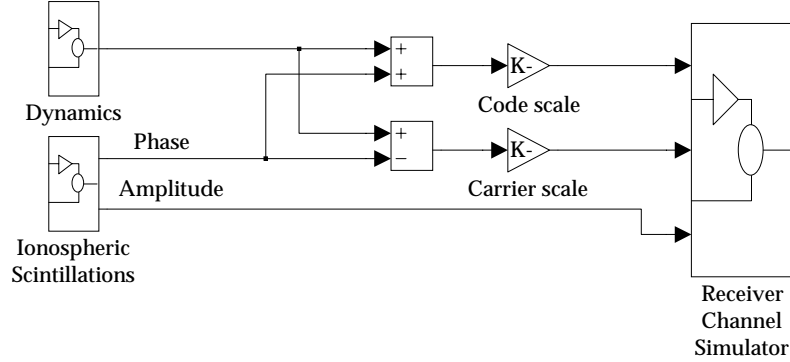


Figure B-3: Simulink model of a combined Costas phase locked loop / Delay locked loop channel. The upper panel represents the environment model. The lower panel represents the tracking loops.

In all simulations, the thermal noise blocks are based on Gaussian distributed random number generators which are fed with different seeds. This helps to ensure that the individual noise sequences are uncorrelated, or at least approximately so. For the delay locked loop, this implies that the separation between the Early, Prompt and Late signals must be $1/2$ chips or greater (see Appendix D). The code spacing is set within Early, Prompt and Late autocorrelation functions which replicate the behaviour of the three code correlators in a delay locked loop. In addition, all simulators provide the capacity to vary the loop order, the loop bandwidth and the discriminator type.

Appendix C

Tracking thresholds and cycle slips

Tracking thresholds define the point at which a tracking loop transitions from a state of stable tracking to one of loss-of-lock. When a tracking loop loses lock, the VCO frequency drifts away from the signal frequency and the loop phase estimates become meaningless. This is qualitatively different from a condition of frequent cycle slips during which the loop continues to track the phase and frequency of the signal between successive slips. In practice, however, it is difficult to distinguish between the two states, particularly when the cycle slipping rate is very high. Consequently, it is often useful to define tracking thresholds in terms of acceptable tracking performance. This may take the form of a maximum acceptable probability of a cycle slip based on the non-linear analysis described in Section C.2, or a maximum acceptable phase error variance based on the linear model analysis described in Section C.1. The second of these threshold measures is based on the assumption that a loop will lose lock when the magnitude of the phase tracking error exceeds a certain boundary. This is generally set at a fairly conservative level under the assumption that the probability of losing lock increases sharply when the linear model approximations are significantly violated.

Because tracking loops are highly non-linear in the threshold region, Monte Carlo simulation techniques are usually required in order to establish the true tracking performance. The code and carrier tracking loop simulator described in Appendix B takes account of the non-linearities in a tracking loop and provides an indication of where loss-of-lock is likely to occur for various noise and dynamic conditions.

For an unaided GPS receiver, loss of carrier lock is usually followed soon after by a loss of code lock. Consequently, the tracking threshold of such a receiver is typically set by the carrier tracking loop. However, when a receiver is aided with Doppler measurements from an Inertial Navigation System (INS), the tracking threshold will be determined by the code loop. This is because Doppler aiding allows the VCO to continue tracking the frequency of the desired signal ⁴, even when the carrier loop has been forced to lose lock.

⁴ For a prolonged outage, changes in the carrier frequency as a result of satellite motion will eventually cause the VCO frequency to drift away from the carrier frequency.

However, in the analysis that follows, the receiver is assumed to be unaided and the loop threshold is assumed to be determined by the carrier loop.

C.1 Linear analysis

The tracking loop threshold derived from the linear loop model is based on the assumption that loss of lock occurs when the linearising approximations are significantly violated. If the carrier phase errors are modelled as zero-mean, Gaussian⁵ random variables, the probability of a phase error exceeding some threshold Φ_T is given by

$$p(|\phi_e| > \Phi_T) = 1 - \int_{-\Phi_T}^{\Phi_T} \frac{1}{\sqrt{2\pi}\sigma_{\phi_e}} \exp\left(-\frac{(\phi - \phi_{eSS})^2}{2\sigma_{\phi_e}^2}\right) d\phi \quad (C-1)$$

where ϕ_{eSS} is the steady state phase error resulting from relative motion between the satellite and the receiver (see Appendix E). This can also be expressed in terms of the complementary error function as follows

$$p(|\phi_e| > \Phi_T) = \frac{1}{2} \left[\operatorname{Erfc}\left(\frac{\Phi_T - \phi_{eSS}}{\sqrt{2}\sigma_{\phi_e}}\right) + \operatorname{Erfc}\left(\frac{\Phi_T + \phi_{eSS}}{\sqrt{2}\sigma_{\phi_e}}\right) \right] \quad (C-2)$$

A widely used rule of thumb tracking threshold for a Costas loop is that the 3-sigma phase jitter from all sources other than dynamic stress errors must be less than 45° for the loop to remain in lock (Ward [47], page 157). This corresponds to an error in the linear loop model of approximately 36% for an I.Q Costas loop (ie. the phase error estimate from the discriminator is in error by a factor of $1 - [0.5\sin(2\Phi_T)/\Phi_T] \approx 0.36$). Thus for $\phi_{eSS} = 0$, the tracking threshold can be represented by $3\sigma_{\phi_e} = \Phi_T = 45^\circ$. From Equation (C-2), this corresponds to a probability of approximately 0.27% of the phase error exceeding Φ_T , which is the probability of a Gaussian random variable lying more than 3 standard deviations from the mean. In Figure C.1, the RMS phase error from all sources other than dynamic stress errors, σ_{ϕ_e} , is plotted as a function of the steady state phase tracking error, ϕ_{eSS} , for $\Phi_T = 45^\circ$ and $p(|\phi_e| > \Phi_T) = 0.27\%$. This curve represents the locus of points for which the loop is on the verge of losing lock under the specified threshold conditions (from Equation (C-2)). Notice that for a zero steady state error, the threshold

⁵ This is based on the assumption that the thermal noise and ionospheric phase scintillations are both zero-mean and Gaussian distributed.

RMS jitter is approximately 15^0 ($\pi/12$ radians) which is consistent with the initial assumption. Also, notice that the straight section of Figure C.1 implies that the following approximate relationship holds between the RMS phase error and the steady state dynamic phase error for the loop to remain in lock

$$3\sigma_{\phi_e} + \phi_{eSS} \leq 45^0 \quad (C-3)$$

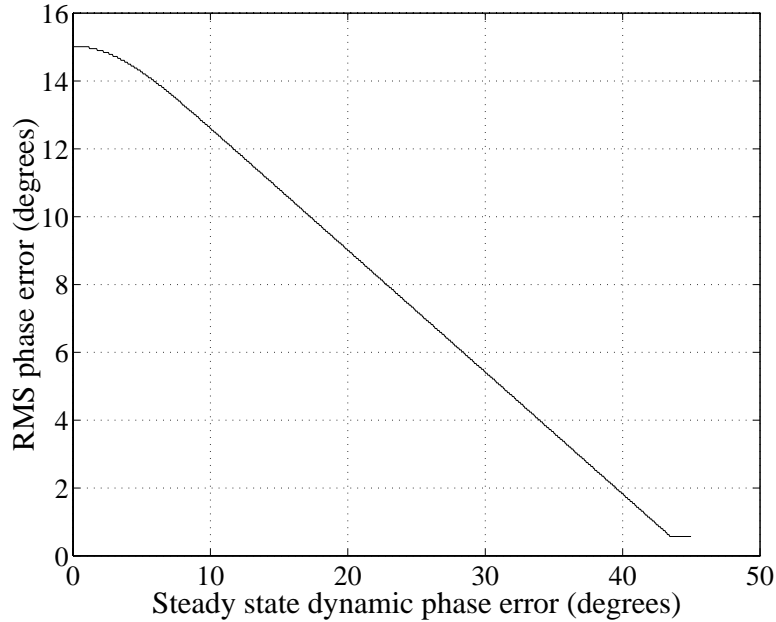


Figure C.1: 1σ phase error from all sources other than dynamics versus the steady state dynamic phase error at the tracking threshold of an I.Q Costas loop.

C.2 Non-linear analysis

In this section, various results from the non-linear analysis of tracking loops are presented without proof. Closed form expressions are given for the PDF of phase errors, the mean time to cycle slip and the probability of a cycle slip for a Costas loop. Although these expressions have only been obtained for a 1st order tracking loop under fairly restrictive signal conditions, various researchers have shown that the performance of higher order loops can be closely approximated by these expressions with only minor adjustments to the SNR . The principal drawback in the use of results from the non-linear model is that they assume that the system is driven by additive white Gaussian thermal noise only. However, in the presence of scintillations, coloured phase noise will also be present. Nevertheless, Van Trees ([96], pages 55-56) demonstrated that by a simple translation of the phase noise process back through the loop integrator, phase noise with a power

spectral density of the form Tf^{-2} could be considered to behave like additive white Gaussian thermal noise at the input (also see Section 3.3.3).

The non-linear analysis is based on the solution of the non-linear stochastic differential equation which defines the operation of a standard phase locked loop. This is given by

$$\phi = \phi_e + \frac{F(s)}{s} [A \sin(\phi_e) + n_d] \quad (C-4)$$

The origin of this equation can be understood by referring to Figure 3.1-2 with the non-linear element $0.5\tilde{A}^2 \sin(2\phi_e)$ replaced with $A \sin(\phi_e)$ for a standard phase locked loop. By assuming a first order loop with the input phase process, ϕ , constant (ie. the system is driven by additive white thermal noise only), the following PDF for the phase errors reduced modulo 2π can be obtained (for proof, see Holmes [43], pages 114-118)

$$f_\vartheta(\varphi) = \frac{\exp(\rho \cos(\varphi))}{2\pi I_0(\rho)}, \quad |\varphi| \leq \pi \quad (C-5)$$

where $I_0(\)$ is the modified Bessel function of the first kind of order zero, ρ is the loop SNR which is given by $\rho = 1/\sigma_{\phi_e}^2 = A^2/(2N_o B_n)$ for a standard phase locked loop, and ϑ is the phase error reduced modulo 2π (ie. $\vartheta = \phi_e \bmod 2\pi$). This PDF is usually referred to as the "Tikhonov density function". For a first order Costas loop with an I.Q discriminator, the Tikhonov density function is given by (Holmes [43], page 274)

$$f_\vartheta(\varphi) = \frac{\exp(\rho_e \cos(2\varphi))}{\pi I_0(\rho_e)}, \quad |\varphi| \leq \frac{\pi}{2} \quad (C-6)$$

where ρ_e is the effective loop SNR which is given by $\rho_e = 1/4\sigma_{\phi_e}^2$, and ϑ is the phase error reduced modulo π (ie. $\vartheta = \phi_e \bmod \pi$). For an I.Q loop in the presence of white Gaussian thermal noise only, the variance of the phase errors is given by the following expression (Appendix D)

$$\sigma_{\phi_T}^2 = \frac{B_n}{C/N_0} \left[1 + \frac{1}{2TC/N_0} \right] \quad (C-7)$$

The variance of the phase errors reduced modulo π for a first order I.Q Costas loop can be obtained from the Tikhonov PDF as follows (assuming that the errors are zero-mean)

$$\sigma_\vartheta^2 = E\{\vartheta^2\} = \int_{-\pi/2}^{\pi/2} \varphi^2 f_\vartheta(\varphi) d\varphi \quad (C-8)$$

where $\sigma_\vartheta^2 \approx \sigma_{\phi_e}^2$ when the phase errors are small (ie. when they rarely exceed $\pm\pi/2$ radians).

For a standard phase locked loop in the presence of white Gaussian thermal noise, the mean time to cycle slip is given by (Homes [43], page 95, Gardner [36], page 38)

$$\bar{T} = \frac{\pi^2 \rho I_o^2(\rho)}{2B_n} \quad (C-9)$$

where B_n is the single sided noise bandwidth of the tracking loop. For a standard phase locked loop, a cycle slip is defined as an increase in the magnitude of the phase error by 2π radians. This usually leads to a jump in the loop's estimate of carrier phase by an integer number of carrier cycles.

A more generalised expression for the mean time to cycle slip which includes the steady-state phase tracking error, ϕ_{eSS} , is [59]

$$\bar{T} = \frac{\pi \tanh(\pi \phi_{eSS} \rho)}{2B_n \phi_{eSS}} \left[I_o^2(\rho) + 2 \sum_{n=1}^{\infty} \frac{(-1)^n I_n^2(\rho)}{1 + (n/\rho \phi_{eSS})^2} \right] \quad (C-10)$$

where $I_n()$ is the modified Bessel function of the first kind of order n .

For an I.Q Costas loop, the mean time to cycle slip includes the effective loop SNR and is given by (Holmes [43], page 200)

$$\bar{T} = \frac{\pi^2 \rho_e I_o^2(\rho_e)}{2B_n} \quad (C-11)$$

where for a Costas loop, a cycle slip is defined as an increase in the magnitude of the phase error by π radians (leading to an integer number of half cycle jumps in the carrier phase). The corresponding expression for the mean time to cycle slip in the presence of a steady-state phase tracking error, ϕ_{eSS} , is

$$\bar{T} = \frac{\pi \tanh(2\pi\phi_{eSS}\rho_e)}{4B_n\phi_{eSS}} \left[I_o^2(\rho_e) + 2 \sum_{n=1}^{\infty} \frac{(-1)^n I_n^2(\rho_e)}{1 + (n/2\rho_e\phi_{eSS})^2} \right] \quad (C-12)$$

Equations (C-11) and (C-12) can be obtained from the standard phase locked loop expressions by doubling both σ_{ϕ_e} and ϕ_{eSS} . This simple relationship holds because the phase error characteristic of an I.Q Costas loop discriminator is $\sin(2\phi_e)/2$, while the corresponding characteristic for a standard phase locked loop is $\sin(\phi_e)$. Consequently, the carrier phase tracking errors of an I.Q Costas loop need only be half as large as those of a standard phase locked loop to have the same impact in terms of cycle slips.

By applying the linear model tracking threshold for σ_{ϕ_e} (Equation (C-3)) to Equation (C-11), the mean time to cycle slip becomes $\bar{T} = 1260/B_n$ seconds. This demonstrates that the tracking threshold obtained from the linear model analysis is quite conservative. For example, for a noise bandwidth of 10Hz, the mean time to cycle slip is more than 2 minutes.

If it is assumed that the slipping process is approximately Poisson distributed, then the probability of a slip within t seconds from a condition of zero error is (Holmes [43], page 95)

$$p_s = 1 - \exp\left(-\frac{t}{\bar{T}}\right) \quad (C-13)$$

Appendix D

Thermal noise errors

In this Appendix, the statistics of thermal noise errors on the code and carrier tracking loops are examined. A method is outlined for obtaining the standard expression for the variance of the thermal noise errors on a Costas carrier loop. This is then extended to include the effects of amplitude scintillations on an I.Q Costas loop that is normalised by an AGC.

D.1 Thermal noise prior to the discriminator

From Equation (3.1-1), the IF signal at the input of the receiver tracking loops is given by

$$IF(t) = A(t)p(t - \tau(t))d(t - \tau(t))\sin(\omega_{IF}t + \phi(t)) + n(t)$$

where $n(t) = n_c(t)\cos(\omega_{IF}t) + n_s(t)\sin(\omega_{IF}t)$ is a narrowband representation of thermal noise at the IF stage. $n(t)$ is assumed to be a wideband, stationary, zero-mean Gaussian random process with a power spectral density of N_o W/Hz within the IF band. Similarly, the two baseband noise processes, $n_c(t)$ and $n_s(t)$, are wideband, stationary, zero-mean, Gaussian noise processes with power spectral densities of N_o W/Hz at baseband. After mixing with the VCO reference signals, the noise is separated into I and Q components as follows (note that the double frequency terms have been ignored as they will be eliminated by filtering in the pre-detection filters).

$$\begin{aligned} n_I &= n_c(t)\sin(\hat{\phi}(t)) + n_s(t)\cos(\hat{\phi}(t)) \\ n_Q &= n_c(t)\cos(\hat{\phi}(t)) - n_s(t)\sin(\hat{\phi}(t)) \end{aligned} \tag{D-1}$$

where n_I and n_Q are again uncorrelated noise processes with the same statistics as $n_c(t)$ and $n_s(t)$. The I and Q signals are mixed with Early, Prompt and Late replica codes from the code generator and filtered by pre-detection integrate and dump filters to produce the three I and Q pairs given by Equation (4.1-6). These are then converted into phase tracking errors by the code and carrier tracking loop discriminators. The noise on the six I and Q signals after filtering can be represented by the following vector

$$\mathbf{n} = [n_{IE}, n_{QE}, n_{IP}, n_{QP}, n_{IL}, n_{QL}] \quad (D-2)$$

The covariance between any two of these six signals is given by

$$\sigma_{\alpha X} \sigma_{\beta Y} = E\{ (n_{\alpha X} - E\{n_{\alpha X}\})(n_{\beta Y} - E\{n_{\beta Y}\}) \} \quad (D-3)$$

where α and β represents either I or Q , and X and Y represents either E , P or L . As all of these noise terms are zero-mean, the covariance simplifies to

$$\begin{aligned} \sigma_{\alpha X} \sigma_{\beta Y} &= E\{n_{\alpha X} n_{\beta Y}\} \\ &= E\left\{ \left[\frac{1}{T} \int_{t-T}^t n_{\alpha}(u) p(u-x).du \right] \left[\frac{1}{T} \int_{t-T}^t n_{\beta}(v) p(v-y).dv \right] \right\} \\ &= \frac{1}{T^2} \int_{t-T}^t \int_{t-T}^t E\{n_{\alpha}(u) n_{\beta}(v) p(u-x) p(v-y)\} du.dv \end{aligned} \quad (D-4)$$

where n_{α} and n_{β} are given by Equation (D-1), $p(u-x)$ and $p(v-y)$ represent the PRN codes with delays of $u-x$ and $v-y$ seconds respectively, and x and y represent the delays associated with either the Early, Prompt or Late codes. As n_{α} and n_{β} are uncorrelated and independent of the PRN codes, the covariance expression can be simplified as follows

$$\begin{aligned} \sigma_{\alpha X} \sigma_{\beta Y} &= \frac{1}{T^2} \int_{t-T}^t \int_{t-T}^t E\{n_{\alpha}(u) n_{\beta}(v)\} E\{p(u-x) p(v-y)\} du.dv \\ &= \begin{cases} \frac{1}{T^2} \int_{t-T}^t E\{n_{\alpha}(u)^2\} E\{p(u-x) p(u-y)\} du, & \alpha = \beta \\ 0, & \alpha \neq \beta \end{cases} \\ &= \begin{cases} \frac{1}{T^2} \int_{t-T}^t N_o R(x-y) du, & \alpha = \beta \\ 0, & \alpha \neq \beta \end{cases} \\ &= \begin{cases} \frac{N_o}{T} R(x-y), & \alpha = \beta \\ 0, & \alpha \neq \beta \end{cases} \end{aligned} \quad (D-5)$$

where $E\{p(u-x) p(u-y)\} = R(x-y)$ is the autocorrelation function of the PRN code (given by Equation (4.1-1)), and $E\{n_{\alpha}(u)^2\} = R_n(0) = N_o$ is the power spectral density of n_{α} (or n_{β}). This result also relies on n_I and n_Q being sufficiently wideband for

$$E\{n_\alpha(u)n_\alpha(v)\}=0 \text{ for } u \neq v.$$

Based on Equation (D-5), the covariance matrix of the six noise terms for an Early-Late spacing of $2d$ code chips⁶ is given by

$$E\{\mathbf{n}^T \mathbf{n}\} = \frac{N_o}{T} \begin{bmatrix} 1 & 0 & R(d) & 0 & R(2d) & 0 \\ 0 & 1 & 0 & R(d) & 0 & R(2d) \\ R(d) & 0 & 1 & 0 & R(d) & 0 \\ 0 & R(d) & 0 & 1 & 0 & R(d) \\ R(2d) & 0 & R(d) & 0 & 1 & 0 \\ 0 & R(2d) & 0 & R(d) & 0 & 1 \end{bmatrix} \quad (D-6)$$

For an Early-Late spacing of 1 code chip ($d = 1/2$; typical of most GPS receivers), the covariance matrix becomes

$$E\{\mathbf{n}^T \mathbf{n}\} = \frac{N_o}{T} \begin{bmatrix} 1 & 0 & 0.5 & 0 & 0 & 0 \\ 0 & 1 & 0 & 0.5 & 0 & 0 \\ 0.5 & 0 & 1 & 0 & 0.5 & 0 \\ 0 & 0.5 & 0 & 1 & 0 & 0.5 \\ 0 & 0 & 0.5 & 0 & 1 & 0 \\ 0 & 0 & 0 & 0.5 & 0 & 1 \end{bmatrix} \quad (D-7)$$

Consequently, when the Early-Late spacing is greater than or equal to 1 code chip, the noise on all Early and Late signals is uncorrelated (ie. $R(2d)=0$). However, this is not the case for narrow correlator spacing receivers such as the Novatel GPSCard™ for which $d < 1/2$ chips.

D.2 Thermal noise errors in the absence of scintillations

For a phase locked loop, the mean-square phase tracking error resulting from thermal noise is given by

$$\begin{aligned} E\{\phi_e^2\} &= \sigma_{\phi_T}^2 \\ &= \int_{-\infty}^{\infty} |H(f)|^2 S_{n_d}(f) df \end{aligned} \quad (D-8)$$

⁶ The spacing between the Early and Prompt codes and between the Prompt and Late codes is assumed to be d chips.

where $H(f)$ is the closed loop transfer function (Table 3.1-2), and $S_{n_d}(f)$ is the power spectral density of the discriminator noise term (labelled n_d in Figures 3.1-2 and 4.1-3). In the analysis that follows, it is assumed that amplitude scintillations are absent and that n_d is a zero-mean random variable. Also, the sample-and-hold circuits which form part of the pre-detection filters will maintain n_d at a constant level for a period of T seconds. However, between successive T second epochs, the values of n_d will be uncorrelated. As will be shown in Equation (D-24), this is a result of n_{IP} and n_{QP} being uncorrelated between epochs.

The discriminator noise can be viewed as the output of a sample-and-hold circuit fed by a white noise sequence, $w(t)$. Therefore, we can express $n_d(t)$ in the following way (from Haykin [39], Section 7.3)

$$n_d(t) = w_\delta(t) \otimes g_h(t) \quad (D-9)$$

where $w_\delta(t) = \sum_{k=-\infty}^{\infty} w(kT)\delta(t-kT)$ is an instantaneously sampled version of $w(t)$, $g_h(t) = \text{rect}\left(\frac{t-T/2}{T}\right)$ represents the “hold” function of the sample-and-hold, and \otimes represents the convolution integral. The corresponding power spectral density of $n_d(t)$ is

$$\begin{aligned} S_{n_d}(f) &= E\left\{|F\{w_\delta(t) \otimes g_h(t)\}|^2\right\} \\ &= S_{w_\delta}(f)|G_h(f)|^2 \end{aligned} \quad (D-10)$$

where $S_{w_\delta}(f)$ is the power spectral density of $w_\delta(t)$, and $G_h(f) = T \text{sinc}(fT) \exp(-j\pi fT)$ is the Fourier transform of $g_h(t)$. As $w(t)$ is a white noise sequence, $w_\delta(t)$ is also white. Therefore, $S_{w_\delta}(f) = N_{w_\delta}$ which is a constant. The variance of $n_d(t)$ is given by

$$\begin{aligned} \sigma_{n_d}^2 &= \int_{-\infty}^{\infty} S_{n_d}(f) df \\ &= \int_{-\infty}^{\infty} S_{w_\delta}(f) |G_h(f)|^2 df \\ &= \int_{-\infty}^{\infty} N_{w_\delta} T^2 \text{sinc}^2(fT) df \\ &= N_{w_\delta} T \end{aligned} \quad (D-11)$$

Consequently, $S_{w\delta}(f) = \sigma_{n_d}^2 / T$ and Equation (D-10) becomes

$$S_{n_d}(f) = \sigma_{n_d}^2 T \operatorname{sinc}^2(fT) \quad (D-12)$$

Therefore, from Equation (D-8), the thermal noise variance of the phase errors is given by

$$\begin{aligned} \sigma_{\phi_T}^2 &= \int_{-\infty}^{\infty} |H(f)|^2 \sigma_{n_d}^2 T \operatorname{sinc}^2(fT) df \\ &= 2\sigma_{n_d}^2 T \left[\frac{1}{2} \int_{-\infty}^{\infty} |H(f)|^2 \operatorname{sinc}^2(fT) df \right] \end{aligned} \quad (D-13)$$

The closed loop transfer function, $H(f)$, is a low-pass filter with a bandwidth much smaller than the bandwidth of the $\operatorname{sinc}(fT)$ function⁷. Consequently, $\operatorname{sinc}^2(fT)$ can be approximated by one, giving

$$\begin{aligned} \sigma_{\phi_T}^2 &\approx 2\sigma_{n_d}^2 T \left[\frac{1}{2} \int_{-\infty}^{\infty} |H(f)|^2 df \right] \\ &= 2TB_n \sigma_{n_d}^2, \quad \text{radians}^2 \end{aligned} \quad (D-14)$$

where $B_n = \frac{1}{2} \int_{-\infty}^{\infty} |H(f)|^2 df$ is the single-sided noise equivalent bandwidth of the tracking

loop. Noise equivalent bandwidth's for the three loop orders are given in Table 3.1-2 as a function of the loop natural frequency, ω_n .

Equation (D-14) is independent of the algorithm chosen for the Costas loop discriminator. In order to proceed, however, it is necessary to specify a discriminator algorithm so that $\sigma_{n_d}^2$ can be found. For the I.Q Costas loop, the discriminator noise term n_d is given by (from Equation (3.1-3))

$$n_d = \tilde{A}d(t-\tau)[\cos(\phi_e)n_{QP} + \sin(\phi_e)n_{IP}] + n_{QP}n_{IP} \quad (D-15)$$

⁷ The single-sided noise equivalent bandwidth of $H(f)$ is normally less than 20Hz, whereas the equivalent bandwidth for the $\operatorname{sinc}(fT)$ function is $1/2T$ Hz = 25Hz for $T=20\text{ms}$.

If it is assumed that the signal amplitude is constant (ie. $\tilde{A} = \mathbf{A}$ where \mathbf{A} is a constant), and the discriminator is normalised by an ideal post-detection AGC (ie. $g = \mathbf{A}^2$), the noise term will become

$$n'_d = \frac{n_d}{\mathbf{A}^2} = \frac{1}{\mathbf{A}} d(t-\tau) [\cos(\phi_e) n_{QP} + \sin(\phi_e) n_{IP}] + \frac{1}{\mathbf{A}^2} n_{QP} n_{IP} \quad (D-16)$$

As n_{QP} and n_{IP} are uncorrelated and zero-mean, the variance of n'_d is given by

$$\begin{aligned} \sigma_{n'_d}^2 &= E\{n'_d^2\} \\ &= \frac{1}{\mathbf{A}^2} \cos^2(\phi_e) E\{n_{QP}^2\} + \frac{1}{\mathbf{A}^2} \sin^2(\phi_e) E\{n_{IP}^2\} + \frac{1}{\mathbf{A}^4} E\{n_{QP}^2\} E\{n_{IP}^2\} \end{aligned} \quad (D-17)$$

Letting $E\{n_{QP}^2\} = E\{n_{IP}^2\} = N_o/T$ (from the diagonal elements of Equation (D-6)) gives

$$\begin{aligned} \sigma_{n'_d}^2 &= \frac{N_o}{T\mathbf{A}^2} \left[1 + \frac{N_o}{T\mathbf{A}^2} \right] \\ &= \frac{1}{2TC/N_o} \left[1 + \frac{1}{2TC/N_o} \right] \end{aligned} \quad (D-18)$$

where $C/N_o = \mathbf{A}^2/2N_o$ is the nominal carrier to noise power density ratio of the GPS signal⁸. Consequently, the phase error variance of a normalised I.Q Costas loop is given by (from Equations (D-14) and (D-18))

$$\begin{aligned} \sigma_{\phi_T}^2 &= 2TB_n \sigma_{n'_d}^2 \\ &= \frac{B_n}{C/N_o} \left[1 + \frac{1}{2TC/N_o} \right], \quad \text{radians}^2 \end{aligned} \quad (D-19)$$

Equivalent expressions for the thermal noise variance of both the Delay Locked Loop (DLL) and the Frequency Locked Loop (FLL) are given below (see for example Kaplan [47]).

$$\text{DLL: } \sigma_{\tau_T}^2 = \frac{4F_1 d^2 B_n}{C/N_o} \left[2(1-d) + \frac{4F_2 d}{TC/N_o} \right] \quad \text{chips}^2 \quad (D-20)$$

⁸ If it is assumed that the nominal satellite signal power at the ground is -160dBW [81] and the noise temperature is 530K, the nominal carrier to noise density ratio is $C/N_o = 41.5$ dBHz.

$$\text{FLL: } \sigma_{v_T}^2 = \frac{F_3 B_n}{\pi^2 T^2 C/N_o} \left[1 + \frac{1}{T C/N_o} \right] \text{ Hz}^2 \quad (D-21)$$

where F_1 is the discriminator correlator factor (1 for time shared tau-dithered early/late correlators, 1/2 for dedicated early/late correlators), F_2 is the discriminator type factor (1 for early/late discriminators, 1/2 for dot product discriminators), F_3 is 1 at high C/N_o and 2 at low C/N_o and d is the correlator spacing (in chips). Although the discriminator algorithms are quite different for the DLL and FLL, it is clear that the variance expressions have the same general form as Equation (D-19).

D.3 Thermal noise errors in the presence of amplitude scintillations

In the presence of an AGC, the discriminator noise term is given by (based on Eqⁿ (3.1-3))

$$n'_d = \frac{n_d}{g} = \frac{1}{g} \left[\tilde{A} d(t-\tau) [\cos(\phi_e) n_{QP} + \sin(\phi_e) n_{IP}] + n_{QP} n_{IP} \right] \quad (D-22)$$

where $g = \frac{1}{k} \sum_{i=1}^k I_i^2 + Q_i^2$ is the AGC gain factor. If n_{QP} and n_{IP} are assumed to be independent of \tilde{A} and g (ie. independent of amplitude scintillations), and both n_{QP} and n_{IP} are uncorrelated and zero-mean, the noise term n'_d will also be zero-mean. This is demonstrated below

If we let $n_x = \cos(\phi_e) n_{QP} + \sin(\phi_e) n_{IP}$ and $n_y = n_{QP} n_{IP}$, it can easily be shown that $E\{n_x\} = 0$, $E\{n_y\} = 0$ and $E\{n_x n_y\} = 0$. Therefore

$$\begin{aligned} E\{n'_d\} &= E\left\{ \frac{1}{g} \left[\tilde{A} d(t-\tau) n_x + n_y \right] \right\} \\ &= E\left\{ \frac{\tilde{A} d(t-\tau)}{g} \right\} E\{n_x\} + E\left\{ \frac{1}{g} \right\} E\{n_y\} \\ &= 0. \end{aligned} \quad (D-23)$$

and so n'_d is zero-mean. It is can also be shown that under the assumptions outlined above, n'_d is uncorrelated between successive T second epochs. The autocorrelation function of n'_d for a lag of T seconds is given by

$$\begin{aligned}
R_{n'_d}(T) &= E\{n'_d(t)n'_d(t+T)\} \\
&= E\left\{\frac{1}{g(t)}[\tilde{A}(t)d(t-\tau)n_x(t)+n_y(t)]^*\frac{1}{g(t+T)}[\tilde{A}(t+T)d(t+T-\tau)n_x(t+T)+n_y(t+T)]\right\} \\
&= E\left\{\frac{\tilde{A}(t)d(t-\tau)\tilde{A}(t+T)d(t+T-\tau)}{g(t)g(t+T)}\right\}E\{n_x(t)n_x(t+T)\}+ \\
&\quad E\left\{\frac{\tilde{A}(t)d(t-\tau)}{g(t)g(t+T)}\right\}E\{n_x(t)n_y(t+T)\}+ \\
&\quad E\left\{\frac{\tilde{A}(t+T)d(t+T-\tau)}{g(t)g(t+T)}\right\}E\{n_y(t)n_x(t+T)\}+ \\
&\quad E\left\{\frac{1}{g(t)g(t+T)}\right\}E\{n_y(t)n_y(t+T)\}
\end{aligned} \tag{D-24}$$

As $E\{n_x n_y\}=0$, the second and third terms in this expression are zero. Also, as n_x and n_y are uncorrelated between epochs, $E\{n_x(t)n_x(t+T)\}=0$ and $E\{n_y(t)n_y(t+T)\}=0$. Consequently, $R_{n'_d}(T)=0$ and so n'_d is also uncorrelated between successive epochs (note that $R_{n'_d}(\tau)=0$ for $\tau>T$ also). The variance of n'_d is given by

$$\begin{aligned}
\sigma_{n'_d}^2 &= E\{n'_d(t)^2\} \\
&= E\left\{\frac{\tilde{A}^2}{g^2}\right\}E\{n_x^2\}+E\left\{\frac{1}{g^2}\right\}E\{n_y^2\} \\
&= E\left\{\frac{\tilde{A}^2}{g^2}\right\}E\{n_{QP}^2 \cos^2(\phi_e) + n_{IP}^2 \sin^2(\phi_e) + 2n_{QP}n_{IP} \cos(\phi_e)\sin(\phi_e)\}+E\left\{\frac{1}{g^2}\right\}E\{n_{QP}^2 n_{IP}^2\} \\
&= E\left\{\frac{\tilde{A}^2}{g^2}\right\}[E\{n_{QP}^2\}\cos^2(\phi_e)+E\{n_{IP}^2\}\sin^2(\phi_e)]+E\left\{\frac{1}{g^2}\right\}E\{n_{QP}^2\}E\{n_{IP}^2\}
\end{aligned} \tag{D-25}$$

Letting $E\{n_{QP}^2\}=E\{n_{IP}^2\}=N_o/T$ (from the diagonal elements of Equation (D-7)), the variance expression reduces to

$$\sigma_{n'_d}^2 = \frac{N_o}{T}\left[E\left\{\frac{\tilde{A}^2}{g^2}\right\}+\frac{N_o}{T}E\left\{\frac{1}{g^2}\right\}\right] \tag{D-26}$$

The signal amplitude \tilde{A} can be normalised by dividing by the nominal (unperturbed) signal amplitude \mathbf{A} as follows

$$\tilde{A}_N = \frac{\tilde{A}}{\mathbf{A}} \quad (D-27)$$

where $E\{\tilde{A}_N^2\} = E\{\tilde{A}^2\}/\mathbf{A}^2 = 1$ under amplitude scintillation conditions. By substituting $\tilde{A} = \mathbf{A}^* \tilde{A}_N$ and $C/N_o = \mathbf{A}^2/2N_o$ into the variance expression, the following result is obtained

$$\sigma_{n_d}^2 \approx \frac{1}{2TC/N_o} \left[E\left\{\frac{\tilde{A}_N^2}{g_N^2}\right\} + \frac{1}{2TC/N_o} E\left\{\frac{1}{g_N^2}\right\} \right] \quad (D-28)$$

where $g_N = g/\mathbf{A}^2$ is a normalised AGC gain factor, and C/N_o is the carrier power to noise density ratio of the GPS signal.

Equation (D-28) represents the noise variance at the output of a normalised I.Q discriminator. The only assumptions made in this analysis are that the amplitude and AGC gain factor are independent of the thermal noise terms, n_{QP} and n_{IP} . However, no assumptions have been made about the bandwidth of the amplitude scintillations.

D.3 A note on sample-and-hold circuits

The outputs of the pre-detection integrate-and-dump filters will generally be held constant for T seconds by a zero-order sample-and-hold circuit. The purpose of the sample-and-hold is to maintain the I and Q signals at a constant level so that $\hat{\phi}(t)$ is fixed for the subsequent T second integrate-and-dump period. Using arguments similar to those given in Equations (D-9) to (D-12), it is relatively straightforward to show that the sample-and-hold does not change the variances or power spectral densities of the six noise terms from Equation (D-2), although it may alter their appearance in the time domain (ie. they will become stepped rather than continuous). Therefore, if $n_{\alpha X}(t)$ represents one of the noise terms from Equation (D-2), $S_{n_{\alpha X}}(f) = N_o \text{sinc}(fT)^2$ and $\sigma_{n_{\alpha X}}^2 = N_o/T$, irrespective of whether a sample-and-hold circuit is present after the integrate-and-dump filters.

Appendix E

Doppler errors

The effects of satellite and receiver motion on the phase of the GPS signal can be represented by the following Doppler expressions

$$\text{Carrier: } \phi_d(t) = u(t) \frac{2\pi}{\lambda} \left[r_o + v_o t + \frac{1}{2} a_o t^2 + \frac{1}{6} j_o t^3 + \dots \right] \quad \text{radians} \quad (E-1)$$

$$\text{Code: } \tau_d(t) = u(t) \frac{1}{c} \left[r_o + v_o t + \frac{1}{2} a_o t^2 + \frac{1}{6} j_o t^3 + \dots \right] \quad \text{seconds} \quad (E-2)$$

where $u(t)$ is the unit step function, r_o, v_o, a_o and j_o are constants which define the range, velocity, acceleration and jerk components of the relative motion between the satellite and receiver, λ is the carrier wavelength and c is the speed of light. These equations assume that the dynamics are applied at time $t=0$, and that prior to $t=0$ there is no relative motion between the satellite and receiver. The Laplace transforms of $\phi_d(t)$ and $\tau_d(t)$ are given by the following generalised expression

$$\theta_d(s) = k \left[\frac{r_o}{s} + \frac{v_o}{s^2} + \frac{a_o}{s^3} + \frac{j_o}{s^4} + \dots \right] \quad (E-3)$$

where $\theta_d(s)$ represents either $\phi_d(s)$ or $\tau_d(s)$, and k is a constant which equals $2\pi/\lambda$ for the carrier tracking loop and $1/c$ for the code tracking loop. The phase errors at the output of the tracking loop are given by

$$\theta_e(s) = [1 - H(s)]\theta_d(s) = \frac{s\theta_d(s)}{s + F(s)} \quad (E-4)$$

where $F(s)$ is the loop filter and $H(s)$ is the closed loop transfer function (from Table 4.2-2). The phase error as a function of time, $\theta_e(t)$, can be obtained from Equation (E-4) by taking the inverse Laplace transform.

E.1 Steady state errors

The steady state tracking error is given by the Final Value Theorem of Laplace transform theory as follows

$$\theta_{\varepsilon SS} = \lim_{t \rightarrow \infty} \theta_{\varepsilon}(t) = \lim_{s \rightarrow 0} s\theta_{\varepsilon}(s). \quad (E-5)$$

where $\theta_{\varepsilon}(t)$ is the inverse Laplace transform of $\theta_{\varepsilon}(s)$. For the generalised Doppler process of Equation (E-3), the steady state tracking error becomes

$$\theta_{\varepsilon SS} = k * \lim_{s \rightarrow 0} \left[\frac{r_o s}{s + F(s)} + \frac{v_o}{s + F(s)} + \frac{a_o}{s(s + F(s))} + \frac{j_o}{s^2(s + F(s))} + \dots \right]. \quad (E-6)$$

Equation (E-6) results in the following steady state phase errors as a function of the loop order and the specified component Doppler processes.

	$u(t)r_o$	$u(t)v_o t$	$u(t)\frac{a_o t^2}{2}$	$u(t)\frac{j_o t^3}{6}$
1 st Order	1 st Order	2 nd Order	3 rd Order	4 th Order
1 st Order	0	$k \frac{v_o}{\omega_n}$	∞	∞
2 nd Order	0	0	$k \frac{a_o}{\omega_n^2}$	∞
3 rd Order	0	0	0	$k \frac{j_o}{\omega_n^3}$

Table E.1: Steady state tracking errors as a function of the loop order and loop natural frequency ω_n for the specified Doppler process.

It is clear from Table E.1 that if the loop order is less than the order of the Doppler process minus one, the loop will lose lock. However, when the loop order is greater than or equal to the order of the Doppler process, the steady state tracking error will be zero (assuming that the loop filter is active). When the loop order is equal to the order of the Doppler process minus one, the steady state phase error is given by (based on Table E.1)

$$\theta_{eSS} = \frac{\frac{d^k \theta_d(t)}{dt^k}}{\omega_n^k} \quad (E-7)$$

where k is the loop order. This expression implies that the steady state error can be reduced by increasing the loop bandwidth (ie. increasing ω_n). For the frequency locked loop, the steady state error is given by the first derivative of the phase error as follows

$$f_{eSS} = \frac{d\theta_{eSS}(t)}{dt} = \frac{\frac{d^{k+1} \theta_d(t)}{dt^{k+1}}}{\omega_n^k} \quad \text{radians/s} \quad (E-8)$$

Consequently, an FLL will in general be more robust to Doppler effects than a PLL of the same order.

E.2 Transient errors

For a typical GPS receiver closed loop transfer function, the transient errors will overshoot the steady state error by only a small amount ([92], page 390). Nevertheless, the contribution to the loop phase error from transient dynamic effects can be accounted for by including a Total Transient Distortion term in the phase error variance expression [45]. The Total Transient Distortion is given by

$$\varepsilon_T^2 = \int_0^\infty \theta_e(t)^2 . dt \quad (E-9)$$

If we replace $\theta_d(s)$ with a truncated version of the series given in Equation (E-3), and we assume that $\theta_e(t)$ is bounded (ie. The loop remains in lock), then $\theta_e(t)$ is a deterministic power signal and its power spectral density is defined by

$$\begin{aligned} S_{\theta_e}(f) &= E\left\{|\theta_e(f)|^2\right\} \\ &= E\left\{[1 - H(f)]\theta_d(f)\right\}^2 \\ &= |1 - H(f)|^2 E\left\{|\theta_d(f)|^2\right\} \\ &= |1 - H(f)|^2 S_{\theta_d}(f) \end{aligned} \quad (E-10)$$

The Total Transient Distortion then becomes

$$\begin{aligned}
 \varepsilon_T^2 &= \int_{-\infty}^{\infty} S_{\theta_e}(f) df \\
 &= \int_{-\infty}^{\infty} |1 - H(f)|^2 S_{\theta_d}(f) df
 \end{aligned} \tag{E-11}$$

Equation (E-11) assumes that the steady state tracking error is zero (ie the order of the loop is greater than the order of the Doppler process). If this assumption is violated, the Total Transient Distortion will become infinite.

Appendix F

Ionospheric pierce point velocity

Satellite motion

The steps required in order to determine the Ionospheric Pierce Point (IPP) velocity due to satellite motion, \bar{v}_s , are outlined below. It is assumed that suitable algorithms are available to convert between the geodetic coordinate system (latitude, longitude and height) and the Cartesian Earth Centred Earth Fixed (ECEF) coordinate system.

Step 1

Using the satellite Almanac (or Ephemeris) parameters, calculate the satellite ECEF coordinates, $\bar{r}_S = (x_S, y_S, z_S)$. The appropriate equations can be found in Appendix II of ICD-GPS-200 [81].

Step 2

Convert the satellite ECEF coordinates to local level coordinates as follows:

The ECEF line of sight coordinates of the satellite from the receiver are

$$\bar{r}_{LS} = (x_{LS}, y_{LS}, z_{LS}) = \bar{r}_S - \bar{r}_R$$

where $\bar{r}_R = (x_R, y_R, z_R)$ are the ECEF coordinates of the receiver. Convert the receiver ECEF coordinates to latitude and longitude coordinates, (ϕ_R, λ_R) , using an appropriate transform. Convert the line of sight satellite coordinates to local level coordinates using the following matrix

$$R = \begin{bmatrix} -\sin(\lambda_R) & \cos(\lambda_R) & 0 \\ -\sin(\phi_R)\cos(\lambda_R) & -\sin(\phi_R)\sin(\lambda_R) & \cos(\phi_R) \\ \cos(\phi_R)\cos(\lambda_R) & \cos(\phi_R)\sin(\lambda_R) & \sin(\phi_R) \end{bmatrix}$$

The local level coordinates are then

$$\bar{r}_L' = R * \bar{r}_{LS}'$$

where $\bar{r}_L = (x_L, y_L, z_L)$ are in the East, North and Up directions respectively, and the $x_L y_L$ plane is tangent to the Earth at the receiver location.

Step 3

Determine the elevation and azimuth angles of the satellite using local level coordinates. Only those satellites for which the elevation angles are above some low elevation angle mask are considered further (a typical mask angle is 5^0)

$$\text{Elevation, } e = \arctan\left(\frac{z_L}{\sqrt{x_L^2 + y_L^2}}\right)$$

$$\text{Azimuth, } a = \arctan\left(\frac{x_L}{y_L}\right)$$

Step 4

Calculate the earth centred angle, Ψ (the angle between a line joining the centre of the Earth and the receiver, and a line joining the centre of the Earth and the IPP).

$$\Psi = 90 - e - \arcsin\left(\frac{\cos(e)R_e}{R_e + h_I}\right)$$

where $R_e = 6378$ km is the Earth's radius, and $h_I = 350$ km is the mean ionospheric height.

Step 5

Calculate the IPP in geodetic coordinates. The IPP is the point below which the line of sight vector penetrates the mean ionospheric height.

$$\phi_I = \phi_R + \Psi \cos(a)$$

$$\lambda_I = \lambda_R + \frac{\Psi \sin(a)}{\cos(\phi_I)}$$

where (ϕ_I, λ_I) are the IPP latitude and longitude respectively.

Step 6

Determine the velocity of the IPP in ECEF coordinates as follows:

Convert the IPP geodetic coordinates (ϕ_I, λ_I, h_I) to ECEF coordinates, $\bar{r}_I = (x_I, y_I, z_I)$, using an appropriate transform. Perform this step at two time instants separated by a small time increment, τ , to obtain the two coordinates, \bar{r}_{I1} and \bar{r}_{I2} . The ECEF velocity of the IPP is then approximately

$$\bar{v}_I = (v_{xI}, v_{yI}, v_{zI}) = \frac{\bar{r}_{I2} - \bar{r}_{I1}}{\tau}$$

(An alternative approach is to solve the expression $R_e + h_I = |\bar{r}_R + \beta \bar{r}_{LS}|$ for the scalar factor β ($0 < \beta < 1$) at two different satellite locations separated in time by τ seconds. The IPP in ECEF coordinates is then $\bar{r}_I = \bar{r}_R + \beta \bar{r}_{LS}$ and the IPP velocity, \bar{v}_I , is once again found using the equation given above. This approach by-passes steps 2 to 5. However, if this approach is used, it is still necessary to find the local level vector, \bar{r}_L , in order to obtain the satellite elevation angle for masking purposes.)

Step 7

Translate the IPP ECEF velocity into a local level velocity as follows:

Form a translation/rotation matrix based on the first IPP coordinate \bar{r}_{I1} (or $(\phi_{I1}, \lambda_{I1}, h_{I1})$ in geodetic coordinates)

$$R_1 = \begin{bmatrix} -\sin(\lambda_{I1}) & \cos(\lambda_{I1}) & 0 \\ -\sin(\phi_{I1})\cos(\lambda_{I1}) & -\sin(\phi_{I1})\sin(\lambda_{I1}) & \cos(\phi_{I1}) \\ \cos(\phi_{I1})\cos(\lambda_{I1}) & \cos(\phi_{I1})\sin(\lambda_{I1}) & \sin(\phi_{I1}) \end{bmatrix}$$

Convert the velocity vector to a local level vector as follows

$$\bar{v}_{LI}' = R_1 * \bar{v}_I'$$

where $\bar{v}_{LI} = (v_{LxI}, v_{LyI}, v_{LzI})$ are the velocity components in the East, North and Up directions respectively. The IPP velocity due to satellite motion is then $\bar{v}_s = \bar{v}_{LI}$ and the speed of the IPP is simply $v_s = |\bar{v}_{LI}|$ m/s.

Receiver motion

The steps required to determine the IPP velocity due to receiver motion, \bar{v}_r , are outlined below.

Step 1

Determine the ECEF coordinates of two receiver locations separated by τ seconds in time.

The receiver must be characterised in terms of its location \bar{r}_R (in ECEF coordinates), and its velocity in local level coordinates, $\bar{v}_R = (v_{xR}, v_{yR}, v_{zR})$ (East, North and Up directions respectively). Following τ seconds of motion, the location of the receiver in local level coordinates (with respect to \bar{r}_R) is given by $\bar{v}_R * \tau$. Consequently, the ECEF line of sight vector from \bar{r}_R to the new receiver location is

$$\bar{r}_{LS}' = R^{-1} * \bar{v}_R' * \tau$$

where R^{-1} is the inverse of the transformation matrix given earlier. Therefore, the two receiver locations in ECEF coordinates will become

$$\begin{aligned}\bar{r}_{R1} &= \bar{r}_R \\ \bar{r}_{R2} &= \bar{r}_R + \bar{r}_{LS}'\end{aligned}$$

Step 2

If it is assumed that the satellite position, \bar{r}_S , remains fixed over the τ second period of interest, the procedures outlined earlier for satellite motion can be repeated in order to derive the two IPP coordinates corresponding to the two receiver locations (ie. repeat step's 2 to 6 for satellite motion). As before, these two coordinates can then be combined in order to obtain ECEF, and finally local level IPP velocity measures (ie. \bar{v}_r).

Combined motion

It is quite straightforward to combine the effects of satellite and receiver motion by calculating two values of \bar{r}_S (\bar{r}_{S1} and \bar{r}_{S2}) and two values of \bar{r}_R (\bar{r}_{R1} and \bar{r}_{R2}) which represent the two time instants of interest. Steps 2 to 7 of the analysis of satellite motion can then be used to determine \bar{v}_I based on combined motion.

However, to a first approximation, the IPP velocity can simply be found by summing the two velocity vectors obtained by treating the satellite and receiver motion separately.

Equivalent satellite velocity

For GPS calculations, the WBMOD model is called using the *FILE* option. This requires that the receiver be stationary at a known location, and that the satellite position and velocity vectors be specified in a file that is passed to WBMOD. Unfortunately, WBMOD does not include an option in which both the satellite and receiver are capable of moving independently of one another. To account for this, it is possible to determine an equivalent satellite velocity vector that includes the effects of both satellite and receiver motion. The receiver is then considered to be stationary and the equivalent velocity vector is passed to WBMOD within the satellite file. The equivalent satellite velocity vector is calculated as follows:

The ECEF satellite vector can be described in terms of the ECEF receiver and IPP vectors as follows

$$\bar{r}_S = \bar{r}_R + \frac{1}{\beta}(\bar{r}_I - \bar{r}_R)$$

where β is the scalar factor described earlier. If \bar{r}_R is considered to be stationary, and β is assumed to be constant, the time derivative of the above expression is given by

$$\begin{aligned}\bar{v}_{SE} &= \frac{\partial \bar{r}_R}{\partial t} + \frac{1}{\beta} \left(\frac{\partial \bar{r}_I}{\partial t} - \frac{\partial \bar{r}_R}{\partial t} \right) \\ &= \frac{\bar{v}_I}{\beta}\end{aligned}$$

where \bar{v}_I is the IPP ECEF velocity which includes the effects of both satellite and receiver motion, and \bar{v}_{SE} is the equivalent satellite velocity. The value of \bar{v}_{SE} given by this expression will ensure that WBMOD creates an IPP velocity vector which accounts for both satellite and receiver motion, and that β is a constant over some small time interval, ∂t . The \bar{v}_{SE} vector must then be transformed into a local level velocity vector for WBMOD by multiplying by the following matrix

$$R_S = \begin{bmatrix} -\sin(\lambda_S) & \cos(\lambda_S) & 0 \\ -\sin(\phi_S)\cos(\lambda_S) & -\sin(\phi_S)\sin(\lambda_S) & \cos(\phi_S) \\ \cos(\phi_S)\cos(\lambda_S) & \cos(\phi_S)\sin(\lambda_S) & \sin(\phi_S) \end{bmatrix}$$

where ϕ_S, λ_S are the satellite latitude and longitude respectively.

Appendix G

WBMOD predictions of f_c

Many of the results derived in this thesis are based on the assumption that the bandwidth of the amplitude scintillations is much less than the bandwidth of the tracking loops. This assumption greatly simplifies the problem of analysing tracking errors and allows analytical expressions to be obtained for measures such as phase error variance and the probability of losing lock. The cutoff frequency of the amplitude scintillation power spectrum, f_c , is an important indicator of the validity of this assumption as the majority of the amplitude scintillation energy is expected to be concentrated near to f_c (above f_c , the PSD of amplitude scintillations falls off according to a power law expression of the form $k_A f^{-p}$ where k_A is a constant). From Equation (2.1-3), f_c is given by

$$f_c = \frac{v_e}{\sqrt{2z_F}} \text{ Hz} \quad (G-1)$$

where v_e is the effective velocity, $z_F \approx \sqrt{\lambda z}$ is the Fresnel zone radius, λ is the carrier wavelength, and z is the distance to the irregularity layer. For a given satellite-receiver geometry, WBMOD provides predictions of v_e based on internal models of the ionospheric drift velocity, v_d . In addition, simple geometry can be used to determine z as a function of the elevation angle, e , for an assumed ionospheric height of h_i , *viz*

$$z = r_e \left[\sqrt{\sin(e)^2 + (1 + h_i/r_e)^2 - 1} - \sin(e) \right] \quad (G-2)$$

where r_e is the radius of the Earth. In Figure G-1, WBMOD predictions of v_e under the same conditions as those used in Figure 3.4-5 were used to obtain f_c as a function of the elevation angle for $h_i = 350$ km. Each point in the upper panel of this figure represents one propagation path at one instant in time between 12:00 noon and 14:00 hours GMT. It is clear from this figure that on average, f_c tends to be slightly larger at low elevation angles. This implies that the increase in z_F at low elevation angles tends to be outweighed by a larger increase in v_e on some of the low angle links. It is also clear that f_c is generally less than about 0.3 Hz (often considerably less), which is well below the

bandwidth of a typical carrier loop. However, it is possible that in the presence of high platform velocities, f_c may increase significantly on some links. If the carrier loop bandwidth is also very narrow, perhaps due to INS aiding, the assumptions made about the amplitude bandwidth may be violated, particularly for the narrower bandwidth code loops.

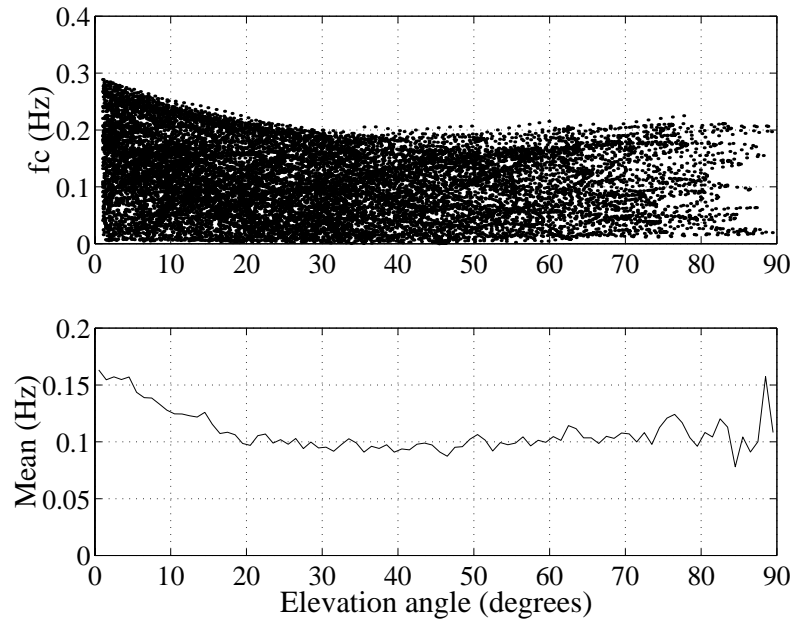


Figure G-1: f_c as a function of the elevation angle from WBMOD.

Bibliography

- [1] Aarons, J. A., "Equatorial Scintillations: A Review", IEEE Transactions on Antennas and Propagation, vol. AP-25, No. 5, pp. 729-736, 1977.
- [2] Aarons, J. A., Basu, S., "Ionospheric Amplitude and Phase Fluctuations at the GPS Frequencies", Proceedings of ION GPS-94, Seventh International Technical Meeting of the Satellite Division of the Institute of Navigation, pp. 1569-1578, 1994.
- [3] Aarons, J. A., et al., "Gigahertz scintillations associated with equatorial patches", Radio Science, vol. 18, No. 3, pp. 421-434, 1983.
- [4] Ashjaee, J., Lorenz, R., "Precision GPS Surveying After Y-Code", Proceedings of ION GPS-92, Fifth International Technical Meeting of the Satellite Division of the Institute of Navigation, pp. 657-659, 1992.
- [5] Bandyopadhyay, T., Guha, A., DasGupta, A., Banerjee, P., Bose, A., "Degradation of navigational accuracy with global positioning system during periods of scintillation at equatorial latitudes", Electronics Letters, vol. 33, No. 12, pp. 110-111, 1997.
- [6] Barrow, B. B., "Error probabilities for data transmission over fading radio paths", SHAPE Air Defence Technical Centre, Den Haag, Report TM-26, 1962.
- [7] Basu, S., et al., "250MHz/GHz scintillation parameters in the equatorial, polar, and auroral environments", IEEE Journal on Selected Areas in Communications, vol. SAC-5, No. 2, pp. 102-115, 1987.
- [8] Basu, S., Basu, S., "Equatorial scintillations - a review", Journal of Atmospheric and Terrestrial Physics, vol. 43, No. 5/6, pp. 473-489, 1981.
- [9] Bishop, G. J., Basu, S., "Impacts of Ionospheric Fading on GPS Navigation Integrity", Proceedings of ION GPS-94, Seventh International Technical Meeting of the Satellite Division of the Institute of Navigation, pp. 577-585, 1994.
- [10] Bishop, G. J., Bullet, T. W., Holland, E. A., "GPS Measurements of L-Band Scintillation and TEC in the Northern Polar Cap Ionosphere at Solar Maximum", Proceedings of the International Beacon Satellite Symposium, 1994.
- [11] Bishop, G. J., Mazella, A. J., Holland, E. A., Rao, S., "An Overview of Ionospheric Effects and Mitigation in RF Communication, Navigation and Surveillance", Ionospheric Effects Symposium IES-96, 1996.
- [12] Bishop, G. J., et al., "Test Bed for Evaluation of GPS Receivers' Performance in Ionospheric Scintillation - A Progress Report", Proceedings of the ION 1998 National Technical Meeting, pp. 637-648, 1998.

- [13] Bishop, G. J., et al., "GPS Applications to Global Ionospheric Monitoring: Requirements for a Ground-Based System", Proceedings of ION GPS-92, Fifth International Technical Meeting of the Satellite Division of the Institute of Navigation, pp. 393-353, 1992.
- [14] Bishop, G. J., et al., "Upcoming Ionospheric Impacts on GPS at Solar Maximum, what do we know / what do we need?", Proceedings of ION GPS-96, Ninth International Technical Meeting of the Satellite Division of the Institute of Navigation, pp. 595-604, 1996.
- [15] Blanchard, A., "Phase-Locked Loops, Application to Coherent Receiver Design", John Wiley & sons, 1979.
- [16] Bogusch, R. L., Guiglano, F. W., Knepp, D. L., Michelet, A. H., "Frequency Selective Propagation Effects on Spread-Spectrum Receiver Tracking", Proceedings of the IEEE, vol. 69, No. 7, pp. 787-796, 1981.
- [17] Bogusch, R. L., Guiglano, F. W., Knepp, D. L., "Frequency-Selective Scintillation Effects and Decision Feedback Equalization in High Data-Rate Satellite Links", Proceedings of the IEEE, vol. 71, No. 6, pp. 754-767, 1983.
- [18] Brown, A., Holm, E., Groves, K., "GPS Ionospheric Scintillation Measurements using a Beam Steering Antenna Array for improved Signal/Noise", Proceedings of the 54th Annual Meeting of the Institute of Navigation, 1998.
- [19] Brown, R. G., Hwang, P. Y. C., "Introduction to random signals and applied Kalman filtering - Second Edition", John Wiley & sons, New York, 1992.
- [20] Campanile, J., et al., "GPS Acquisition Performance in the Presence of Jamming", Proceedings of ION GPS-92, Fifth International Technical Meeting of the Satellite Division of the Institute of Navigation, pp. 1569-1578, 1992.
- [21] Caton, R. G., McNeil, W. J., Groves, K. M., Basu, S., Sultan, P., "Real-Times UHF and L-Band Scintillation Measurements with the Scintillation Network Decision Aid (SCINDA)", Proceedings of the Ionospheric Effects Symposium - IES 99, pp. 1A6-1 to 1A6-8, 1999.
- [22] Cervera, M. A., et al., "Validation of WBMOD in the South-East Asian Region", paper submitted to Radio Science journal in June 2000.
- [23] Chyttil, B., "The distribution of amplitude scintillation and the conversion of scintillation indices", Journal of Atmospheric and Terrestrial Physics, vol. 29, pp. 1175-1777, 1967.
- [24] Coco, D. S., Coker, C., Valladares, C. E., Bishop, G. J., Mazzella, A. J., Fremouw, E. J., Howell, D., "High Speed GPS Scintillation Measurements", Proceedings of the Ionospheric Effects Symposium - IES 99, pp. 2A6-1 to 2A6-6, 1999.

- [25] Crepeau, P. J., "Uncoded and coded performance of MFSK and DPSK in Nakagami fading channels", IEEE Transactions on Communications, vol. COM-40, No. 3, pp. 487-493, 1992.
- [26] Crepeau, P. J., "Performance of FH/BFSK with Generalised Fading in Worst Case Partial-Band Gaussian Interference", IEEE Journal in Selected Areas of Communications, vol. SAC-8, No. 5, pp. 884-886, 1990.
- [27] Davies, K., "Ionospheric Radio", vol. 31, IEE Electromagnetic Waves Series, Peter Peregrinus Ltd., 1990.
- [28] Davies, K., Whitehead, J. D., "A radio lens in the ionosphere", Journal of Atmospheric and Terrestrial Physics, vol. 39, pp. 383-387, 1977.
- [29] Doherty, P. H., Klobuchar, J. A., "Expected Ionospheric Scintillation Effects During the Next Solar Maximum – Observations From Previous Solar Cycles", Proceedings of the Ionospheric Effects Symposium - IES 99, 1999.
- [30] Eng, T., Milstein, L. B., "Partially Coherent DS-SS Performance in Frequency Selective Multipath Fading", IEEE Transactions on Communications, vol. 45, No. 1, pp. 110-118, 1997.
- [31] Eng, T., Milstein, L. B., "Coherent DS-CDMA Performance in Nakagami Multipath Fading", IEEE Transactions on Communications, vol. 43, pp. 1134-1143, 1995.
- [32] Esposito, R., "Error probabilities for the Nakagami channel", IEEE Transactions on Information Theory, vol. IT-13, pp. 145-148, 1967.
- [33] Fremouw, E. J., "DSTO Workshop on Ionospheric and Atmospheric effects on Spaced Based Assets", private correspondence, DSTO, Jan 1999.
- [34] Fremouw, E. J., Livingston, R. C., Miller, D. A., "On the statistics of scintillating signals", Journal of Atmospheric and Terrestrial Physics, vol. 42, pp. 717-731, 1980.
- [35] Fremouw, E. J., et al., "Early results from the DNA Wideband satellite experiment - Complex-signal scintillation", Radio Science, vol. 13, No. 1, pp. 167-187, 1978.
- [36] Gardner, F. M., "Phaselock Techniques, 2nd Ed.", John Wiley & sons, 1979.
- [37] Gradshteyn, I. S., Ryzhik, I. M., "Table of Integrals, Series, and Products: Fourth Ed.", Academic Press, New York, 1965.
- [38] Groves, K. M., et al., "Equatorial scintillation and system support", Radio Science, vol. 32, No. 5, pp. 2047-2064, 1997.
- [39] Haykin, S., "Communication Systems ", Second Edition, John Wiley and sons Inc., 1983.
- [40] Hegarty, J. C., "Analytical Derivation of Maximum Tolerable In-Band Interference Levels for Aviation Applications of GNSS", NAVIGATION, Journal of the Institute of Navigation, vol. 44, No. 1, pp. 25-34, 1997.

- [41] Hegarty, C., Bakry El-Arini, M., Kim, T., Ericson, S., "Scintillation Modelling for GPS/WAAS Receivers", Proceedings of the Ionospheric Effects Symposium - IES 99, pp. 3A6-1 to 3A6-8, 1999.
- [42] Heron, M., L., "Diffraction from discrete and homogeneously structured ionospheric irregularities", Radio Science, vol. 14, No. 1, pp. 97-102, 1979.
- [43] Holmes, J. K., "Coherent Spread Spectrum Systems", Krieger Publishing Company, 1990.
- [44] Hurd, W. J., Statman, J. I., Vilnrotter, V. A., "High Dynamic GPS Receiver Using Maximum Likelihood Estimation and Frequency Tracking", IEEE Transactions on Aerospace and Electronic Systems, vol. AES-23, No. 4, pp. 425-437, 1997.
- [45] Jaffe, R., Rechtin, E., "Design and Performance of Phase-Lock Loops Capable of Near-Optimum Performance Over a Wide Range of Input Signal and Noise Levels", IRE Transactions, IT-1, pp. 66-76, 1955.
- [46] Kam, P. Y., Teo, S. K., Some, Y. K, Tjhung, T.T., "Approximate results for the bit error probability of binary phase shift keying with noisy phase reference", IEEE Transactions on Communications, vol. 41, No. 7, pp. 1020-1022, 1993.
- [47] Kaplan, E. D., "Understanding GPS: Principles and Applications", Mobile Communications Series, Artech House, 1996.
- [48] Kaplan, G., Ram, U., "Bounds on performance for the noisy reference PSK channel", IEEE Transactions on Communications, vol. 38, No. 10, pp. 1699-1707, 1990.
- [49] Kelly, M. C., "The Earth's Ionosphere; Plasma Physics and Electrodynamics", vol. 43, International Geophysics Series, Academic Press Inc., 1989.
- [50] Kintner, P. M., Kil, H., "Fading time scales associated with GPS signals and potential consequences", Proceedings of the Ionospheric Effects Symposium - IES 99, pp. 5A3-1 to 5A3-7, 1999.
- [51] Klobuchar, J. A., "Ionospheric Time-Delay Algorithm for Single-Frequency GPS Users", IEEE Transactions on Aerospace and Electronic Systems, vol. AES-23, No. 3, pp. 325-331, 1987.
- [52] Klobuchar, J. A., "Ionospheric Effects on GPS", GPS World, pp. 48-51, April 1991.
- [53] Klobuchar, J. A., "Global Positioning System: Theory and Applications, Volume I", Progress in Astronautics and Aeronautics, vol. 163, Chapter 12, pp. 485-515, 1996.
- [54] Knepp, D. L., "Multiple Phase-Screen Calculation of the Temporal Behaviour of Stochastic Waves", Proceedings of the IEEE, vol. 71, No. 6, pp. 722-737, 1983.
- [55] Knepp, D. L., Houpis, H. L. F., "Altair VHF/UHF Observations of Multipath and Backscatter Enhancement", IEEE Transactions on antennas and propagation, vol. 39, No. 4, pp. 528-534, 1991.

- [56] Knight, M. F., Finn, A., "The Impact of Ionospheric Scintillations on GPS Performance", Proceedings of ION GPS-96, The Ninth International Technical Meeting of the Satellite Division of the Institute of Navigation, pp. 555-564, 1996.
- [57] Knight, M. F., Cervera, M., Finn, A., "A Comparison of Predicted and Measured GPS Performance in an Ionospheric Scintillation Environment", Proceedings of ION GPS-99, The Twelfth International Technical Meeting of the Satellite Division of the Institute of Navigation, pp. 1437-1450, 1999.
- [58] Kumar, R., Munjal, P., "Simulation Studies for Ionospheric Scintillation", Proceedings of the 54th Annual Meeting of the Institute of Navigation, 1998.
- [59] Lindsey, W. C., Charles, F. J., "A Model Distribution for the Phase Error in Second-Order Phase-Locked Loops", IEEE Transactions on Communication Technology, vol. COM-14, pp. 662-664, 1966.
- [60] McDonough, R. N., Whalen, A. D., "Detection of Signals in Noise, Second Ed.", Academic Press, 1995.
- [61] Miyagaki, Y., Morinaga, N., Namekawa, T., "Error Probability Characteristics for CPSK Signal Through m -Distributed Fading Channel", IEEE Transactions on Communications, vol. COM-26, No. 1, pp. 88-100, 1978.
- [62] Morris, J. M., "Burst Error Statistics of Simulated Viterbi Decoded BPSK on Fading and Scintillating Channels", IEEE Transactions on communications, vol. 40, No. 1, pp. 34-41, 1992.
- [63] Morrissey, T. N., et al, "GPS Receiver Performance Characterization Under Simulated Ionospheric Scintillation Environments", Proceedings of the IAIN World Congress, 2000.
- [64] Nakagami, M., "The m -distribution - A general formula of intensity distribution of rapid fading", in Statistical Methods in Radio Wave Propagation, W.C. Hoffman Ed., Symposium Publications Division, Pergamon Press, 1960.
- [65] Nesenbergs, M., "Binary error probability due to an adaptable fading model", IEEE Transactions on Communications, vol. COM-12, pp. 64-73, 1964.
- [66] Nichols, J., Hansen, A., Walter, T., Enge, P., "High Latitude Measurements of Ionospheric Scintillation Using the NSTB", Proceedings of the ION 1999 National Technical Meeting, 1999.
- [67] Nichols, J., Hansen, A., Walter, T., Enge, P., "Observations of Equatorial Scintillations Using GPS Receivers", Proceedings of ION GPS-99, The Twelfth International Technical Meeting of the Satellite Division of the Institute of Navigation, pp. 1451-1460, 1999.

- [68] NovAtel Communications Ltd., "GPSCard™ Command Description Manual Revision 2.0, Software Version 3.3", 1995.
- [69] Ossakow, S. L., Chaturvedi, P. K., "Morphological studies of rising equatorial spread F bubbles", Journal of Geophysical Research, vol. 83, 1978.
- [70] Parkinson, B. W., "Global Positioning System: Theory and Applications, Volume I", Progress in Astronautics and Aeronautics, vol. 163, Chapter 1, pp. 3-28, 1996.
- [71] Peterson, B., Hartnett, R. J., Fiedler, R., Nebrich, A., "Frequency Domain Techniques for Fast GPS Acquisition and Interference Detection/Rejection", NAVIGATION, Journal of the Institute of Navigation, vol. 43, No. 3, pp. 237-255, 1996.
- [72] Peterson, R. L., Ziemer, R. E., Borth, D. E., "Introduction to Spread Spectrum Communications", Prentice-Hall, New Jersey, 1995.
- [73] Pullen, S., et al., "A Preliminary Study of the Effect of Ionospheric Scintillation on WAAS User Availability in Equatorial Regions", Proceedings of ION GPS-98, Eleventh International Technical Meeting of the Satellite Division of the Institute of Navigation, pp. 687-699, 1998.
- [74] Proakis, J. G., "Digital Communications, 2nd Edition", Mc Graw Hill, New York, 1989.
- [75] Proakis, J. G., Salehi, M., "Communication Systems Engineering", Prentice Hall, 1994.
- [76] Rino, C. L., "A power law phase screen model for ionospheric scintillation: 1. Weak scatter", Radio Science, vol. 14, No. 6, pp. 1135-1145, 1979a.
- [77] Rino, C. L., "A power law phase screen model for ionospheric scintillation: 2. Strong scatter", Radio Science, vol. 14, No. 6, pp. 1147-1155, 1979b.
- [78] Rino, C.L., "On the application of phase screen models to the interpretation of ionospheric scintillation data", Radio Science, vol. 17, No. 4, pp. 855-867, 1982.
- [79] Rino, C. L., Gonzalez, V. H., Hessing, A. R., "Coherence bandwidth loss in transitionospheric radio propagation", Radio Science, vol. 16, No. 2, pp. 245-255, 1981.
- [80] Rishbeth, H., "Basic physics of the ionosphere: a tutorial review", Journal of the Institution of Electronic and Radio Engineers, vol. 58, No. 6, pp. S207-S223, 1988.
- [81] Rockwell International Corporation, Satellite Systems Division, "ICD-GPS-200, NAVSTAR GPS Space Segment / Navigation User Interfaces", 1987.
- [82] Secan, J. A., Bussey, R. M., Fremouw, E. J., Basu, S., "An improved model of equatorial scintillation", Radio Science, vol. 30, No. 3, pp. 607-617, 1995.
- [83] Shanmugan, K. S., "Modelling and Simulation of Wireless and Satellite Communication Systems", Course presented at the Institute for Telecommunications Research, the University of South Australia, April 2000.
- [84] Simon, M. K., Omura, J. K., Scholtz, R. A., Levitt, B. K., "Spread Spectrum Communications Handbook, Revised Edition", McGraw-Hill, 1994.

- [85] Spatz, D. E., Franke, S. J., Yeh, K. C., "Analysis and interpretation of spaced receiver scintillation data recorded at an equatorial station", Radio Science, vol. 23, No. 3, pp. 347-361, 1988.
- [86] Spiegel, M. R., "Mathematical Handbook", Mc Graw-Hill, New York, 1968.
- [87] Spilker, J. J., "Signal Structure and Performance Characteristics", Global Positioning System papers published in Navigation, The Institute of Navigation, pp. 29-54, 1980.
- [88] Steele, R., "mobile Radio Communications", IEEE Press N.Y. and Pentech Press London.
- [89] Titheridge, J. E., "The diffraction of satellite signals by isolated ionospheric irregularities", Journal of Atmospheric and Terrestrial Physics, vol. 33, pp. 47-69, 1971.
- [90] Tsunoda, R. T., Livingston, R. C., McClure, J. P., Hanson, W. B., "Equatorial Plasma Bubbles: Vertically Elongated Wedges From the Bottomside F Layer", Journal of Geophysical Research, vol. 87, No. A11, pp. 9171-9180, 1982.
- [91] Van Dierendonck, A. J., "Understanding GPS Receiver Terminology: A Tutorial", GPS World, pp. 34-44, January 1995.
- [92] Van Dierendonck, A. J., "Global Positioning System: Theory and Applications, Volume I", Progress in Astronautics and Aeronautics, vol. 163, Chapter 8, pp. 329-407, 1996.
- [93] Van Dierendonck, A. J., Hua, Q., Fenton, P., Klobuchar, J. A., "Commercial Ionospheric Scintillation Monitoring Receiver Development and Test Results", Proceedings of the 52nd Annual Meeting, The Institute of Navigation, pp. 573-582, 1996.
- [94] Van Dierendonck, A. J., Reddan, P., Nicholson, M. J., "GPS Receiver Performance Characterization under Simulated Ionospheric Scintillation Environments", Proceedings of the Ionospheric Effects Symposium - IES 99, pp. 3A7-1 to 3A7-8, 1999.
- [95] Van Trees, H. L., "Detection, Estimation , and Modulation Theory, Part I", John Wiley & sons, New York, 1968.
- [96] Van Trees, H. L., "Detection, Estimation , and Modulation Theory, Part II", John Wiley & sons, New York,
- [97] Viterbi, A. J., "Principles of Coherent Communications", McGraw-Hill, New York, 1966.
- [98] Wanninger, L., "Effects of the Equatorial Ionosphere on GPS", GPS World, pp. 48-54, 1993.
- [99] Ward, P. W., "Performance Comparisons Between FLL, PLL and a Novel FLL-Assisted-PLL Carrier Tracking Loop Under RF Interference Conditions", Proceedings of ION

- GPS-98, The Eleventh International Technical Meeting of the Satellite Division of the Institute of Navigation, pp. 783-795, 1998.
- [100] Weber, W. J., "Performance of phase-locked loops in the presence of fading communications channels", IEEE Transactions on Communications, vol. COM-24, No. 5, pp. 487-499, 1976.
 - [101] Whitney, H. E., Aarons, J. A., Allen, R. S., Seemann, D. R., "Estimation of the cumulative amplitude probability distribution function of ionospheric scintillations", Radio Science, vol. 7, No. 12, pp. 1095-1104, 1972.
 - [102] Wojnar, A. H., "Unknown bounds on performance in Nakagami channels", IEEE Transactions on communications, vol. COM-34, No. 1, pp. 22-24, 1986.
 - [103] Yeh, K. C., Liu, C. H., "Radio wave scintillation in the ionosphere", Proceedings of the IEEE, vol. 70, pp. 324-360, 1982.
 - [104] Yovits, M. C., Jackson, J. L., "Linear Filter Optimization with Game-Theoretic Considerations", IRE National Convention Record, part 4, pp. 193-199, 1955.